THE TRIBOLOGY OF LINEAR TAPE RECORDING SYSTEMS

Erwan Sourty

Doctor of Philosophy

THE UNIVERSITY OF ASTON IN BIRMINGHAM

August 2002

Summary

This thesis is devoted to the tribology at the head-to-tape interface of linear tape recording systems, OnStream ADR™ system being used as an experimental platform. Combining experimental characterisation with computer modelling, a comprehensive picture of the mechanisms involved in a tape recording system is drawn. The work is designed to isolate the mechanisms responsible for the physical spacing between head and tape with the aim of minimising spacing losses and errors and optimising signal output. Standard heads—used in ADR current products—and prototype heads—DLC and SPL coated and dummy heads built from a Al_2O_3-TiC and alternative single-phase ceramics intended to constitute the head tape-bearing surface—are tested in controlled environment for up to 500 hours (exceptionally 1000 hours).

Evidences of wear on the standard head are mainly observable as a preferential wear of the TiC phase of the Al_2O_3-TiC ceramic. The TiC grains are believed to delaminate due to a fatigue wear mechanism, a hypothesis further confirmed *via* modelling, locating the maximum von Mises equivalent stress at a depth equivalent to the TiC recession (20 to 30 nm). Debris of TiC delaminated residues is moreover found trapped within the pole-tip recession, assumed therefore to provide three-body abrasive particles, thus increasing the pole-tip recession.

Iron rich stain is found over the cycled standard head surface (preferentially over the pole-tip and to a lesser extent over the TiC grains) at any environment condition except high temperature/humidity, where mainly organic stain was apparent. Temperature (locally or globally) affects staining rate and aspect; stain transfer is generally promoted at high temperature. Humidity affects transfer rate and quantity; low humidity produces thinner stains at higher rate. Stain generally targets preferentially head materials with high electrical conductivity, *i.e.* Permalloy and TiC.

Stains are found to decrease the friction at the head-to-tape interface, delay the TiC recession hollow-out and act as a protective soft coating reducing the pole-tip recession. This is obviously at the expense of an additional spacing at the head-to-tape interface of the order of 20 nm.

Two kinds of wear resistant coating are tested: diamond like carbon (DLC) and super-protective layer (SPL), 10 nm and 20 to 40 nm thick, respectively. DLC coating disappears within 100 hours due possibly to abrasive and fatigue wear. SPL coatings are generally more resistant, particularly at high temperature and low humidity, possibly in relation with stain transfer. 20 nm coatings are found to rely on the substrate wear behaviour whereas 40 nm coatings are found to rely on the adhesive strength at the coating/substrate interface. These observations seem to locate the wear-driving forces 40 nm below the surface, hence indicate that for coatings in the 10 nm thickness range—*i.e.* compatible with high-density recording—the substrate resistance must be taken into account.

Single-phase ceramic as candidate for wear-resistant tape-bearing surface are tested in form of full-contour dummy-heads. The absence of a second phase eliminates the preferential wear observed at the Al_2O_3-TiC surface; very low wear rates and no evidence of brittle fracture are observed.

Key words: Magnetic tape recording, Al_2O_3-TiC subsurface stress numerical modelling, pole-tip recession, stain transfer, chromium oxide protective coating.

Dedication

Dedicated to John Jansen

Acknowledgments

Thanks are due to Prof. John Sullivan my supervisor, for trusting me right from the beginning and all through my PhD. It would be impossible to express all my gratitude for his guidance, his availability, his patience and friendship.

Neither could I express all my gratitude to Dr. Sayah Saied, for having supported me well beyond the work context, with the consideration of a sensitive Kurdish mother.

I am also grateful to Dr. Martin Bijker for his support, dynamism and friendship all along the project, and making my stay in Eindhoven during my early PhD such a unique experience.

I am grateful to Andrew Abbot, for his essential assistance and availability. I am also grateful to the other members of the surface science group, in particular Mark Wild, Jill Collins, Cristina Surdu-Bob, Tudor Zaharia, and Baogui Shi for contributing to the friendly atmosphere within the group.

I am grateful to the people at OnStream for being so cooperative and enthusiast along the project, and especially while I was working there. I want particularly to thank Sep Bastiaens, Eddie Draaisma, and Marcel de Jong.

At the beginning was my family: thank-you to the four of them. In the meantime, I met Shuhui to whom I express my love and gratitude for fulfilling my life with such beauty, and in this way making a major contribution to this work.

Table of contents

Figure captions

Figure captions

Figure captions

Figure captions

Figure captions

Figure captions

Figure captions

Table captions

Table captions

1 Chapter I—Introduction and theoretical background

The project reported here was concerned with the tribology of linear data tape systems. As an experimental platform, the advanced digital recording (ADR™) system manufactured by OnStream MST was used. The aim of the project was the understanding of the tribological phenomena in relation with the wear and material transfer mechanisms occurring at the head-to-tape interface, in particular those interactions that resulted in "spacing" loss and hence signal degradation and errors. Of particular interest was the assessment of limiting tribological factors on ADR technology and identification of viable solutions to minimize or possibly eliminate their effects, in view of developing the future generation products with advanced tape formulations and new heads.

The project started with the characterisation of the wear behaviour of current ADR data heads and tapes. This included finding the right analysis tools for characterisation and a reference for next head and tape materials / configuration. Followed the characterisation of prototype data heads intended for the next generations. Based on the previous characterisation, a comprehensive and predictive model for head-tape surface interaction was developed.

This thesis first introduces the theoretical background (Chapter I), then describes the materials, analytical tools and techniques used in the project (Chapter II). Experimental results (Chapter III) and a numerical modelling of the head / tape surface interaction (Chapter IV) are subsequently presented. Follow the overall discussion (Chapter V) and the conclusion (Chapter VI).

1.1 Overview

First implemented a hundred years ago [1], magnetic storage has since been the major technology for storing audio, video and computer data. Increasing demands on storage volumes conjugated to rapid advances in technology have caused a strong market growth over the past 20 years. The share of magnetic recording in the market for magnetic materials—worth about 30B$ a year in 1999 with an overall growth of 10% a year [2, 3]—is indicated in Figure 1.

Figure 1. Global market for magnetic materials: 30B$ in 1999 [2].

Hard disk drive (HDD) market has put the highest demand on capacity, data rate and access time. Since its introduction in 1956, HDD storage density has increased 20 million fold from 2 kb/in^2 up to nearly 40 Gb/in^2 for today's most advanced systems; 106 Gb/in^2 has been demonstrated in laboratory [4]. Compound annual growth rate (CGR) in disk surface densities have increased from 30% in the eighties to 60% in the nineties as the thin-film magneto-resistive (MR) heads was introduced (Figure 2). With the introduction of giant magneto-resistive (GMR) heads, the storage density has further increased at a rate of over 100% annually [5, 6, 7]. Typical values for the density in current products are a track pitch of 1 μm and a bit length of 0.1 μm, corresponding to an order of magnitude for the storage density of ~ 10 Gb/in^2 (for comparison: compact disk (CD): 0.65 Gb/in^2; digital versatile disk (DVD): 3.28 Gb/in^2 [8, 9]; helical scan tape system: ~ 1 Gb/in^2 [10, 11]—up to 11.5 Gb/in^2 demonstrated [12]).

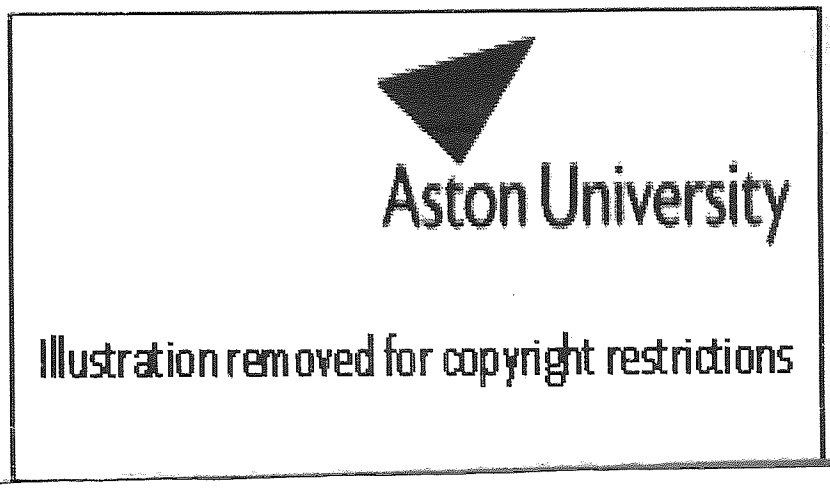

Figure 2. Density increase for HDD (left) and helical scan tape drives (right) systems in the last decades [13,14].

Magnetic tape storage lacks the rapid access of HDD. The interest in this product rests rather on its ultra-high capacities, respectable data rate, all at an extremely low-cost per bit (respectively 55 GB, 25 Mb/s and 1.5 $/GB for digital video (DV) [15], corresponding to track pitch and bit length of 10 μm and 0.25 μm, respectively [16]. Two formats are available: helical scan recorders (*e.g.* DDS, DV and D-VHS) and linear scan recorders (*e.g.* QIC and LTO). If linear recording systems offer lower capacities (typically 100 Mb/in^2), they have the advantage of small form factors and low-cost manufacturing, due to less complicated mechanics.

Inspired by the integrated circuit technology, thin-film heads emerged in the early sixties [17], solving major drawbacks inherent to ferrite bulk heads, such as high inductance, mechanically defined track width and throat height, low permeability at high frequency, and low saturation magnetisation [18]. Multi-channel thin-film heads with separate read and write elements has then made possible the integration of MR heads, which produce a high signal per unit track width independent of media speed, are relatively simple to make and allow very high areal storage density.

In order to overcome the thermal noise, wear, corrosion and electrostatic burn-out inherent to 'shielded heads' common in hard disk and some tape head technologies, Philips has developed a yoke type MR head (YMRH) concept, in which a magneto-resistive element (MRE) bridges a gap in the yoke of the thin-film head (Figure 3) [8].

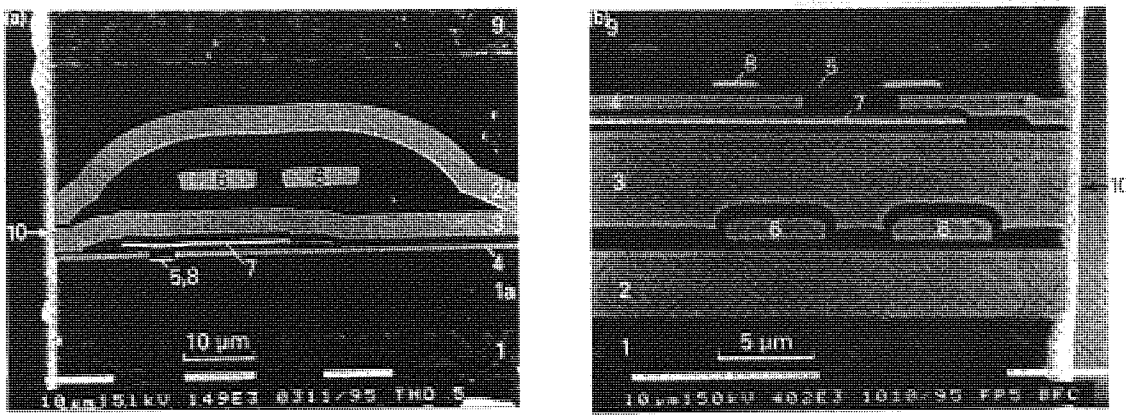

(a) (b)

Figure 3. YMRH, cross section: 1. ceramic substrate, 1a. oxide base coat, 2. write flux guide, 3. shared flux guide, 4. read flux guide, 5. MRE, 6. write coil, 7. bias coil, 8. overlay, 9. cover bar, 10. tape bearing surface (TBS). (a) non-planar head, sensor-first design; (b) planar head, sensor-last design (see following sections for details).

The YMRH concept was first constructed in 1993 in the digital compact cassette (DCC) audio system, first multi-track thin-film tape head (Figure 3 (a)) for consumer use. The advent of 'sensor-last' technology, using chemical and mechanical polishing (CMP), has since made possible the conception of heads (Figure 3 (b)) with higher efficiency combined to lower consumption, use of high temperatures to optimise magnetic flux guide properties, and the reduction of smaller dimensions, risks of short-circuit and mechanical stress. The sensor-last technology is used in the ADR system conception, which first generation, initially referred as DigaMax™ uses multi-track heads and active servo tracking [19], for a track pitch of 37.5 µm, a recording wavelength of 0.7 µm, and a bit length of 0.35 µm, yielding a native capacity of 15/25 GB at a data rate of 2 MB/s. The second generation—introduced to the market in September 2001—has a native capacity of 30/50 GB, a track pitch of 18.75 µm, a recording wavelength of 0.7 µm, and a bit length 0.35 µm, at a data rate of 2.5 MB/s (native) [20].

This chapter intend to review firstly the fundamental concepts inherent to magnetic recording—particularly the ones relevant to linear magnetic tape recording (1.2), and secondly aspects of the tribology at the head-to-media interface with a potential impact on the recorded signal (1.3).

1.2 Foundation of magnetic recording

1.2.1 Recording and reproducing processes

In its most simple form, a magnetic head consists of a ring shaped electro-magnet, combining a conductive coil to a soft magnetic core with a gap facing the magnetic coating of the magnetic medium (Figure 4).

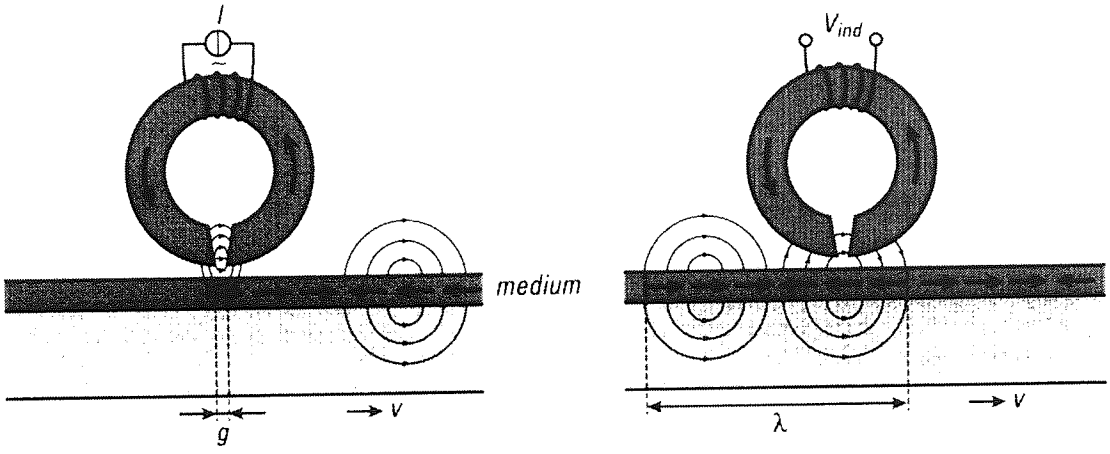

Figure 4. The recording (or write) process (left) and reproducing (or read-back) process (right) with a ring head. g: gap, v: sliding direction, and λ: recording wave-length.

A recording ('write') current in the coil causes a *fringing* field (or *stray* field) to protrude outside the gap and to (re-) direct the magnetisation in the medium as it moves along the head. The hard magnetic coating retains the induced recording pattern, until it experiences a recording field larger than the coercive field of the medium. During reproduction, (playback or 'reading') magnetic transitions in the medium induce flux reversal in the soft magnetic core, resulting in an induced read voltage at the coil terminals. The presence or absence of a transition corresponds respectively to a one or zero binary digit (or 'bit') used to encode the digital information.

1.2.2 Recording media

Recording media come in two categories: *particulate media* and *thin-film media*. In particulate media, magnetic particles are dispersed in a polymeric matrix binder and coated onto a polymeric flexible substrate or rigid substrate (aluminium or glass). In thin-film media, continuous films of magnetic material are deposited onto the substrate by (electro-) plating, sputtering or evaporation. Thin-films have higher remanence and coercivity

(the packed fraction of magnets is closer to 1) than particulate films, hence lower transition lengths and higher recording densities.

1.2.2.1 *Magnetic properties*

The recording performance of the coating is governed by magnetic properties such as the coercivity H_c, the magnetisation remanence M_r and saturation M_s, and their ratio or squareness M_r/M_s. High coercivity is determinant for the coating to resist demagnetisation. High remanence (meaning eventually high pigment packing densities for particulate media) is desirable in that it gives high output signals. Increasing the remanence however, increases the demagnetising fields H_d, which in turn lowers the effective M_r.

Coatings loaded with magnetically oriented particles result in increased squareness and reduced switching field distribution (SFD). The SFD measures the slope of the hysteresis loop near H_c (Figure 5); a lower SFD (that is a steeper loop) corresponds to narrower magnetic transitions and therefore permits higher recording density.

Figure 5. Hysteresis loop of oriented (1) and non-oriented (2) MP tapes [21].

1.2.2.2 *Particulate media*

In particulate media, the magnetic coating consists of a polymeric resin (binder) filled with acicular magnetic particles (typical particle volume concentration ~ 37-50%, *i.e.* weight concentration ~ 60-80%). Head cleaning agents (HCA—typically about 4 to 8%

by weight of a relatively large abrasive particle such as Al, Cr or Zr oxide), a possible combination of wetting, cross-linking and anti-fungal agents, solvents and carbon black (to prevent surface charging) are also added. It is usual to incorporate the lubricant (typically fatty acid esters) in the magnetic layer. However, as the latter become thinner, the lubricant would be incorporated into the undercoat, and reach the surface through pores in the magnetic layer [22].

The most commonly used magnetic particles are listed in Table 1. With the exception of barium ferrite (BaFe), they all come needle-shaped, shape anisotropy partly contributing to their coercivity. A typical particle size in a high-density dual layer tape is 40 ~ 60 nm with between 4 and 8% aspect ratio [23]. The particle size is critical: the highest coercivity is achieved in single-domain particles (in the 100 nm range). Too large particles lower their magnetic energy by creating multiple magnetic domains, decreasing both their remanence and coercivity. In return, the media output loss increases *via* the particle-length term with decreasing particle length, making too small particles incompatible with high-density recording [24]. Towards the sub-nm size range, the particles magnetic moments experience thermal instability or superparamagnetism. At the boundary of superparamagnetism the particles may acquire a viscous magnetisation in the signal field of neighbouring layers in a reel of tape, giving rise to echo or *print-through* effects.

Table 1. Properties of hard magnetic materials for recording media [25, 26].

The absolute output signal versus frequency has been measured for four different types of magnetic tapes on a rotating tape setup with an inductive head at 3.08 m/s [27]. The increase at short wavelength (up to 10 MHz) from a Co-γFe_2O_3 particle tape (H_c = 72 kA/m) to a metal powder MP^{++} (H_c = 140 kA/m) tape was 10~15 dB, to a thin MP^{+++} DVCPro tape (H_c = 160 kA/m), ~ 20 dB, and to an advanced metal evaporated (AME) tape (H_c = 200 kA/m), more than 25 dB.

The particles embedded in a coating act as a discrete array of magnets, which discontinuous stray field generates a background noise proportional to $n^{1/2} \cdot v \cdot M_s$; n and v are the number density and volume of the particles, respectively. Making the particles smaller to reduce noise means moving the small size tail of the distribution towards the superparamagnetic threshold, thereby increasing the print-through. A compromise must therefore be found depending on both the degree of perfection and size distribution of the particles.

The size range of particles suitable for magnetic recording is further confined by additional restrictions at both boundaries. At the lower limit (towards the superparamagnetic threshold), too small particles may have a high frequency coercivity exceeding the maximum head recording-field. At the upper limit (towards the multi-domain threshold), high-frequency signals are reduced as the particle size becomes comparable to the recorded wavelength, which causes the magnetic pattern to be smeared out. This latter length-loss effect constrains typically the particle to be shorter than $\lambda/3$.

Single-domain particles are always magnetised to saturation, M_s, and induce an external stray field H_s and internal demagnetising field $H_d = -N \cdot M_s$, where N is the *demagnetising factor*. The shape anisotropy of acicular particles is proportional to M_s and to the difference between the demagnetising factor along and perpendicular to the long axis of the particle (Figure 6). Particles commercially used have aspect ratios greater than 6:1, which provide high shape anisotropy, hence high H_c and narrow SFD.

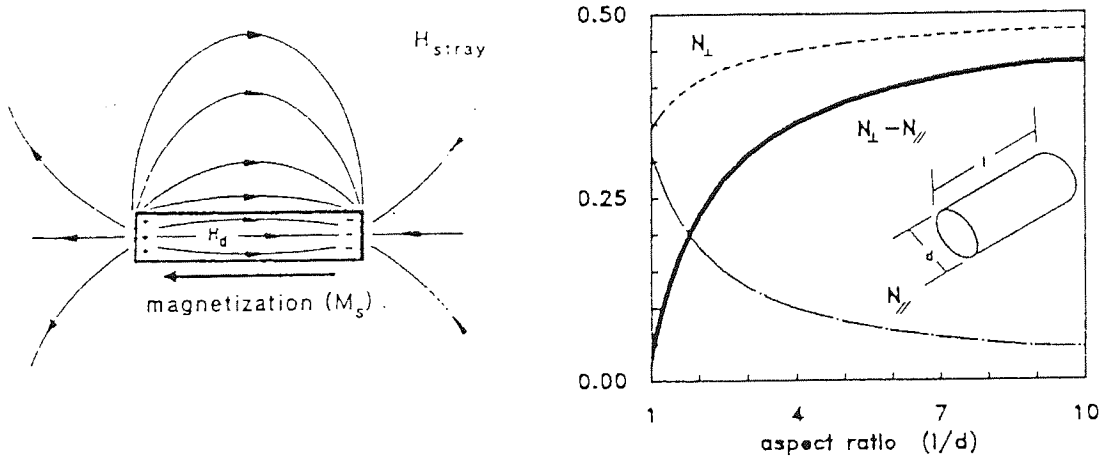

Figure 6. Demagnetising factor as a function of the aspect ratio.

Magnetocrystalline anisotropy also contributes to the particle coercivity, although unlike shape anisotropy, it is independent of the particle size and shape and produces very nar-

row SFD. γFe_2O_3 and MP coercivity relies almost exclusively on shape anisotropy, FeBa on magnetocrystalline anisotropy and CrO_2 on both.

Since γFe_2O_3, Co-γFe_2O_3 and MP have cubic crystallographic structures, their synthesis as needle-shaped particles must proceed *via* at least two steps, which may result in irregular and porous particles. Irregularities make the particles cumbersome to pack and orient, reducing the tape remanence, and due to local fluctuations in the demagnetising field, decreasing the coercivity.

CrO_2, Co-γFe_2O_3 and MP have a layered structure. Co-γFe_2O_3 is coated with cobalt ferrite, which increases its magnetocrystalline anisotropy hence coercivity, whereas CrO_2 and MP have protective coatings to provide durable stability.

Systems based on quarter inch cartridge (QIC) technology, including most of the existing linear recorders, are in transition from using Co-γFe_2O_3 particles to using passivated MP (Fe) tapes with higher coercivity and squareness.

In order to meet the requirements of high magnetic loading, good wear resistance, good substrate and particle adhesion, low surface energy (low friction), resistance to temperature and humidity effects and sufficient flexibility, polymeric binders are normally a blend of two phases. A 'hard' glassy phase will give the system mechanical integrity, and a 'soft' rubbery phase, will give flexibility. Cross-linking further increases phase separation and ensures that the glass transition temperature stays below the operating temperature of the media. The addition of wetting or dispersing agents encourages polymer-particle adhesion and homogeneous dispersion. Self-wetting polymers are also in use.

Flexible magnetic media are traditionally based on polyethylene teraphtalate (PET), but materials with higher elastic modulus such as polyaramide and polyethylene naphtalate (PEN) are developed [28]. Thickness of the magnetic coating and base film may be as low as 0.2 and 5 μm, respectively. A backside coating may be applied to give the tape the desired mechanical and tribological properties, to prevent adhesion when rolled and to give anti-static protection.

Additional load-bearing filler particles or HCA—typically α-Al_2O_3—are added to the coating. These particles protect the coating from damage by the head, prevent adhesion between the head and the tape surface and keep the head surface clean from staining. Filler particles with diameters from 0.5 to 1.0 μm are added to the coating in concentrations that varies from 2% to 6% [29]. Coarse filler making large non-magnetic voids

within the coating generates noise and increases the spacing between the head and the tape. On the other hand, small filler particles lack polishing effectiveness and therefore must be added to a high concentration, competing with the magnetic pigments. Small angular fillers with a certain degree of agglomeration are therefore found as the best option.

Many current tapes have a dual layer structure where a titanium oxide layer is sandwiched between the magnetic coating and the base.

1.2.2.3 Thin-film media

Thin-film or metal evaporated (ME) media was commercially introduced by Sony in 1989 for high areal recording density in Hi-8 video systems. Unlike particulate media, film media require nonmagnetic processing or coating layers, and non-magnetic wear or load bearing particles cannot be used.

Thin magnetic film media are usually cobalt-based alloys (Table 1) - exceptionally sputtered iron oxide - that have been electroplated, chemically plated, evaporated, and sputtered in thickness ranging from 25 to 200 nm. They have high coercivity, often due to the magnetocrystalline anisotropy of a hexagonal crystal structure. Because of their high magnetisation, they can be deposited as thinner recording layers while maintaining high signal amplitude, leading to better-defined magnetisation reversals and thus, higher recording densities [25]. By modifying the thin-film deposition process or substrate preparation, it is possible to tailor the magnetic properties (*e.g.* isotropy, coercivity).

In particulate media, the binder porosity acts as a reservoir from which surface lubricant can be constantly replenished and as due to low polymer surface energy, incomplete coverage can be afforded without catastrophic failure to occur. However, new concepts in lubrication are necessary for film media. Surface coverage by lubricant (usually perfluoropolyethers with end group modification) must indeed remain complete for the projected lifetime of the media, must afford complete corrosion protection and should not be more than 5 nm thick to keep spacing losses at an acceptable level. Gradual breakdown of ME film lubricant allows metal-to-metal contact, causing work hardening of the metal surface. Subsurface fatigue cracks are subsequently nucleated and propagate, leading to the delaminative removal of the material [30].

1.2.3 Recording heads

This section intends to describe a magnetic recording MR thin-film head. Although many concepts introduced are general and apply to most MR thin film heads, linear tape head and more specifically ADR head will be given a more particular attention, every time an overall consideration would be unnecessarily long within the scope of this thesis. The reader seeking more in-depth information is referred to the "Special Issue on Heads for Magnetic Tape Recording" of *Philips J. Res.* (vol. 51) and more particularly to references [9], [18] [19] [31] and [32].

1.2.3.1 Types of recording elements

Almost all head designs for audio, video and computer data recording products are based on inductive recording heads. The trend is to smaller dimension in gap length, track width and core volume to keep up with the increase in recording densities and bandwidth. Whilst for stationary-head applications such as tape drives, reading, writing and often erasing are usually performed by separate inductive heads, moving-heads have emphasised designs with single inductive elements performing all functions, with lower head mass and simpler connection technology.

A write head must be able to generate fields that are strong enough to overcome the coercive field H_c of the tape (*c.f.* Figure 7). Because soft-magnetic materials have low coercive field H_c and high relative permeability μ_r, any reversal of the magnetic field H will be translated in a reversal of the magnetization M in the gap of a soft-magnetic fluxguide causing a field large enough to change the magnetization in the hard-magnetic recording medium. The fluxguide geometry and materials are designed to provide adequate field strength at the signal frequency, with rapid decrement to a value well below H_c at the trailing edge of the gap.

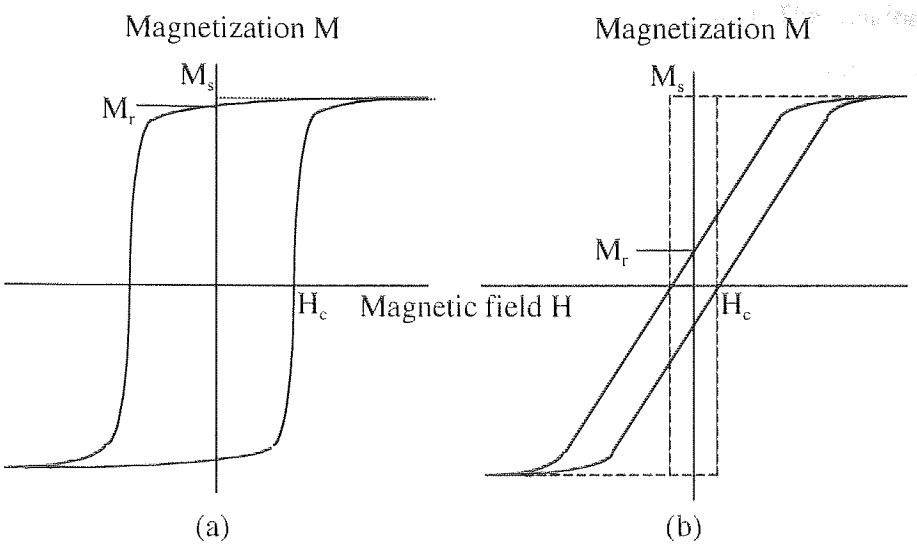

Figure 7. Hysteresis loop of (a) a hard magnetic tape particle and (b) a soft magnetic head yoke—the continuous and discontinuous lines correspond to yokes with and without gap, respectively.

Inductive reproducing heads are inherently low flux-density devices; hence, uncontrolled domain switching can be a source of Barkhausen noise, accentuated for low volume heads [32].

Magneto-resistive (MR) reading heads are flux sensitive heads that unlike inductive heads are independent of the rate of flux changes, hence of the medium speed. The sensing element is a narrow thin-film stripe made of a material such as NiFe (Permalloy), Ni-Co and Co-Fe, laid perpendicularly to the plane of the recorded medium. The sensing element width matches the track width. The stripe is connected to leads at each end carrying a sense current; as a result of the MR effect, the resistivity of each portion of this stripe will be function of the angle θ between the direction of magnetisation and the current-density vector [33]:

$$\rho = \rho_0 + \Delta\rho \cos^2\theta, \qquad (1)$$

For most materials of interest, $\Delta\rho / \rho_0 \sim$ 2-6% [34].

The origin of the MR effect in Permalloy lies in the differing electron scattering rates when electron flow is either parallel or perpendicular to the magnetisation. For a sensor of width w, height h, and thickness t, the voltage development across the sensor by a current I, is:

$$V = I \cdot \rho \cdot (w/t \cdot h) \cdot (\Delta\rho/\rho) \cdot \langle \cos^2\theta \rangle, \qquad (2)$$

where the brackets <...> denote an average over the element. The quadratic form of the MR response is linearised by applying a DC field to the element and holding the magnetisation at a constant angle (~ 45°) to the sense current. Several methods have been devised to produce the DC bias field, most of which use self-biasing [18].

The parameters that have the largest influence on the output are indicated in Figure 8 for a thin-film MR read and write-head. The output is proportional to M_r as long as the MR element does not saturate. When larger than H_c, the internal field in the transition causes demagnetisation to occur. The transition length can be expressed as [35]:

$$a = \sqrt{M_r \delta \left(d + \frac{\delta}{2} \right) \Big/ \pi H_c}, \tag{3}$$

where δ is the thickness for thin media, or the penetration depth of the write field for thicker storage layers, approximated by:

$$\delta = \frac{g_w /2}{\tan\left(\frac{\pi H_c}{2 H_g} \right)} - d, \tag{4}$$

where H_g is the field in the gap of the write head.

The smallest transition length a_s allowed in the case of the demagnetisation limit is given by [36]:

$$a_s = \frac{M_r \delta}{\pi H_c}, \tag{5}$$

Figure 8. Three-dimensional (top) and schematic (bottom) view of magnetic recording by a thin-film yoke-type MR head and inductive write head [9].

A general expression for the playback amplitude is given for an inductive head by the Wallace equation [37]:

$$e(t) = 10^{-8} Un\eta 4\pi M_r T(\lambda) S(\lambda) G(\lambda) A(\lambda) GS(\lambda) \cos(2\pi Ut/\lambda), \qquad (6)$$

Table 2. Parameters used in Wallace equation (6).

Parameter	Description
$\eta = R_g/(R_g+R_c)$	Head efficiency factor
R_g and R_c	Gap and core *reluctance*
n	Number of turns in the head
w	Width of the head (mm)
μ_r	Relative permeability of the core
U	Sliding speed (m/s)
t	Time (s)
λ	Recorded wavelength (μm)
θ	Angle between the gap line and the transition
s	Standard deviation from the gap edge ideal position
$T(\lambda) = [1 - \exp(-2\pi\delta / \lambda)]$	Thickness loss
$S(\lambda) = \exp(-2\pi d / \lambda)$	Separation loss
$G(\lambda) = \frac{\sin(\pi g_r / \lambda)}{(\pi g_r / \lambda)}$	Read gap length loss
$A(\lambda) = \frac{\sin(\pi w\theta / \lambda)}{(\pi w\theta / \lambda)}$	Azimuth loss
$GS(\lambda) = \exp(-2\pi^2 s^2 / \lambda^2)$	Gap scatter loss

Computed loss functions are plotted in Figure 9.

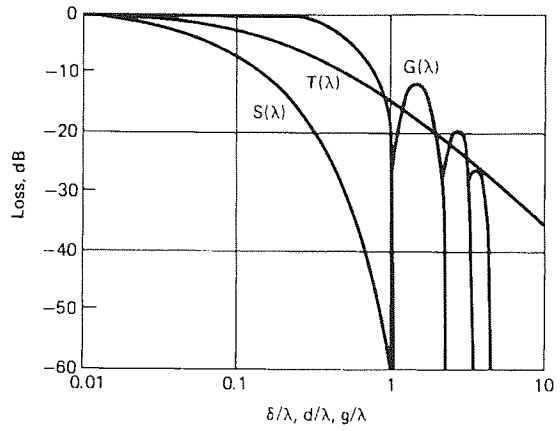

Figure 9. Thickness loss, T(λ); separation loss, S(λ); and gap loss, G(λ).

The output for the MR head is similar to that of the inductive head, where the MR effect has been transposed to the Faraday effect:

$$e(t) = 2I_s R_0(\Delta\rho/\rho)\eta 4\pi M_r(2\pi\delta/\lambda)T(\lambda)S(\lambda)G(\lambda)A(\lambda)GS(\lambda)\cos(2\pi Ut/\lambda). \qquad (7)$$

The gap length loss however, is somewhat more complex, depending on the configuration in which the MR element is used: unshielded head, shielded head or yoke type head (YMRH) [38].

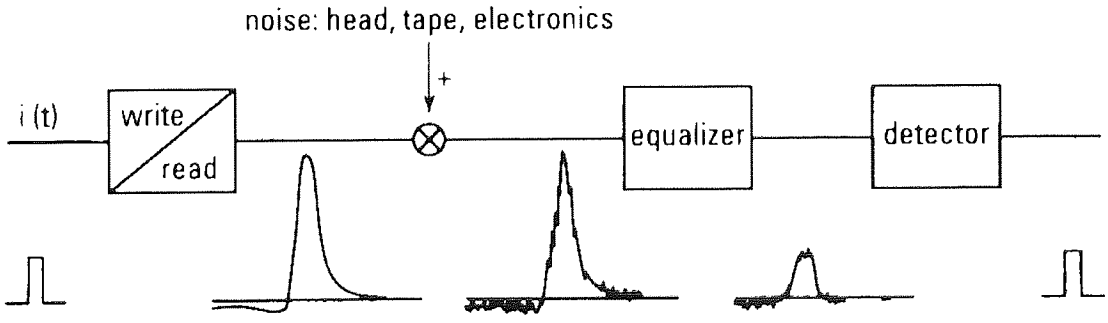

Figure 10. Digital magnetic recording. i(t) represents one bit of information. The shape of the output signal will depend on the head geometry.

To restore the written data, an equaliser first reshapes the read-back waveform, and then a detector decides whether or not a transition (a 'one' bit) is present (Figure 10). The equaliser function depends critically upon parameters like a, d, g_r, whereas the equaliser quality, the signal level, and the noise level strongly influence the detector's decision. The signal-to-noise ratio must be kept high to produce low enough bit error rate. Sources of noise are the random nature of the magnetic units in the medium, thermal and Bark-hausen noises in the MR element, and electronic noise from the read amplifier.

1.2.3.2 Head materials

Thin-film MR head layout consists of the assembly of soft-magnetic layers, electrical conductors, insulation layers and the MR element. Examples of thin-film MR heads used for linear-tape recording are illustrated below: the MR part is of the yoke-type for ADR systems (Figure 11) and the shield type—inherited from the hard disk technology—for Travan (Figure 12). The deposition processes will not be described here; the reader interested in the details involved is referred to [18] and [39].

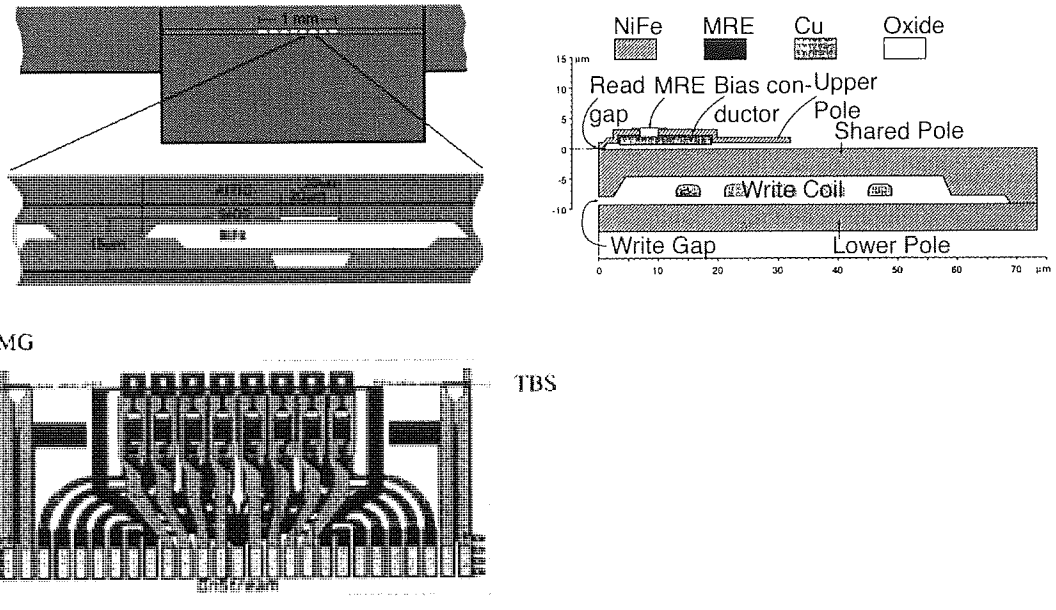

Figure 11. Top view (upper right), cross-section (upper left) and thin-film layout (bottom right) of the head design of an ADR head.

Figure 12. Schematic diagram of a Travan NS20 read write head [40].

Demands on soft-magnetic layers regard magnetic, electrical, mechanical and chemical properties and deposition techniques. The magnetic properties of interest are the coercivity H_c (soft-magnetic behaviour), saturation magnetisation M_s (determines the maximum write field), permeability μ_r (determines the head efficiency η), the magnetostriction (represents the coupling stress / soft-magnetic properties), anisotropy and the magnetic domain structure. The important electrical properties are the resistivity, ideally as high as possible to minimise the reduction in permeability (more sensitive at high frequency) due to eddy currents. Mechanical properties such as thermal expansion coefficient (stress), hardness (differential wear), adhesion and machinability should match more or less those of the other head materials. Most determinant chemical properties are the ability to be structured wet-chemically and the corrosion resistance. Sputter deposition or electro deposition are the deposition techniques commonly applied, the latter being favourably cheaper and faster [18].

The soft-magnetic materials in use are Permalloy ($Ni_{80}Fe_{20}$), electro-deposited in a magnetic field, amorphous Co alloys and nanocrystalline Fe alloys [41, 42], sputter-deposited in a magnetic field, and further annealed in a magnetic field at temperatures above 350°C. As shown in Table 3, Permalloy remanence and resistivity are rather low for high frequency (*i.e.* high-density) recording, making the two other alternatives more suitable.

Table 3. Three classes of soft-magnetic materials, applicable in the flux guides of thin-film heads [31].

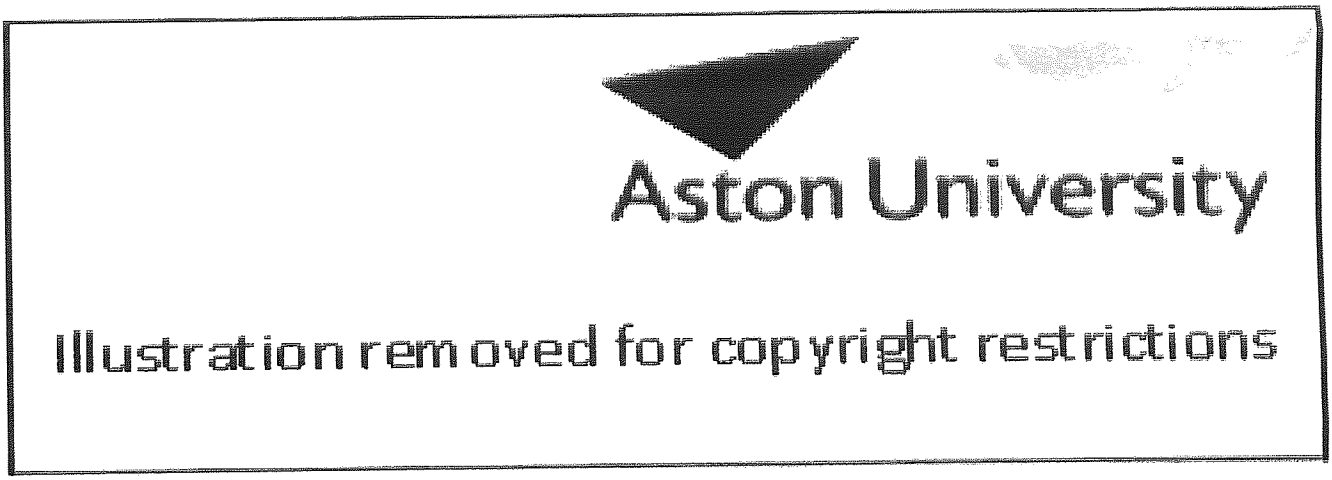

Cu (ρ = 1.68 μΩ.cm) and Au (ρ = 2.24 μΩ.cm) are the choice for thin-film head conductors in general, Cu for the writer coil, and Au for barber-pole, overlay and bias-coil.

They either can be electro-deposited or sputtered (sputtering increases their resistivity by ~ 10%).

Insulating layer materials commonly used are SiO_2 and Al_2O_3. SiO_2 can be deposited by plasma-enhanced chemical vapour deposition (PE-CVD). This offers higher deposition rates and better step coverage than sputtering, used for Al_2O_3. SiO_2 also offers better wet-chemical behaviour and mechanical hardness. In counterpart, Al_2O_3 has a higher thermal coefficient and is required for thick layers to minimise thermal stress.

The head thin-film layout, including the fluxguides, insulating layers, MR element and write coil, are generally sandwiched between Al_2O_3-TiC (sintered ceramic: 20 to 30% TiC embedded as ~ 1 μm grains within an Al_2O_3 matrix) substrate and coverbar. The Al_2O_3-TiC ceramic is selected for its extreme hardness to constitute a wear-resistance structure protecting the head thin-film structure against abrasion resulting from the medium motion.

1.2.3.3 Machining and assembly

Thousands of thin-film head layouts (Figure 11) are deposited on top of a single Al_2O_3-TiC wafer (substrate). Once the deposition process is completed, the wafer has to be diced in its individual components, and each thus produced chip integrated to a complete head structure. Contouring is another necessary step intended to allow the magnetic tape motion along the magnetic gaps. The machining procedure followed for an ADR head are step by step [18]:

i. Thin-film wafer sliced into bars; coverbar cut and lapped at one side.

ii. Coverbars bonded to thin-film bars.

iii. Head contour formed *via* grinding and lapping.

iv. Bars cut into individual pieces.

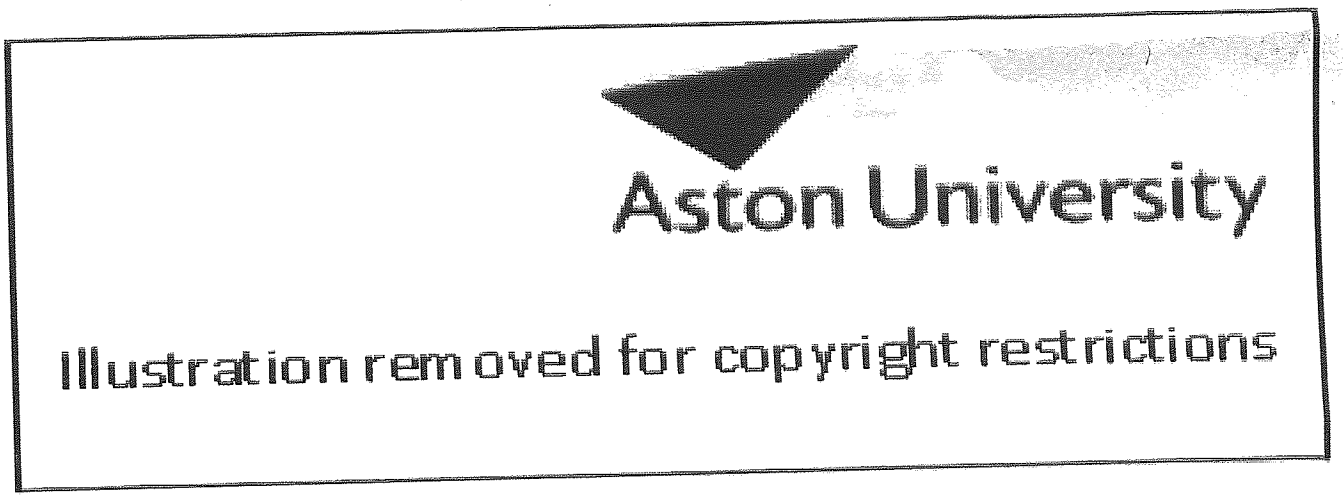

Figure 13. ADR thin-film head machining process flow [18].

The ultimate head contour is realised *via* precision lapping controlled by means of machining guides embodied within the thin-film technology. Two types of machining guides are used (Figure 14):

i. Optical machining guides (OMG): the lapping progress is assessed in controlling the number of embedded structures—which culminate at incremental heights—visible at the tape-bearing surface.

ii. Electrical machining guides (EMG): the lapping progress is assessed in controlling the resistance increase of resistive structures flush with the tape-bearing surface.

Figure 14. Optical (left) and electrical (right) machining guides [18].

After the ultimate lapping step, the machined thin-film device is ready to be connected to a flex foil and mounted into the head housing.

1.3 Tribology of the head / tape interface

Tribology is the science and technology of interacting surfaces in relative motion. First used in U.K. in 1966 [43], the term was an attempt to combine friction, lubrication and wear in an interdisciplinary manner. Tribology is of immense economic importance [44, 45]: an improvement in the engineering practice of tribology through better understanding of a contact mechanics problem may involve savings in the billions of dollars.

The theme of this thesis is the tribology of magnetic storage devices, more specifically linear tape recoding systems, which main concern is to reduce the magnetic spacing between the head and the medium within a few tens of nanometers. This requires the understanding at nanoscopic scale of the contact geometry, dynamics, thermodynamics, and wear processes involved at the head-to-tape interface.

1.3.1 Solid surface characterisation

The solid surface (strictly the solid-gas or solid-liquid interface) properties depend on the nature of solid, the method of surface preparation, and the interaction between the surface and the environment. In turn, these properties will determine how (nature of the contact), where (real area of contact) and with what consequences (friction, stress and material transfer) will the contact take place.

A surface is usually formed of successive layers having different physical or chemical properties than the bulk material. These layers can be classified as:

i. Chemisorbed: typically one monomolecular layer, bound to the surface *via* covalent bonding.

ii. Physisorbed: typically mono or polymolecular layer bound to the surface *via* van der Waals forces.

iii. Chemically reacted: oxide, nitride, sulphide, chlorine, etc., depending on the environment; the thickness depends on the reactivity of the material to the environment and is typically 10~100 nm

iv. Beilby and deformed: produced during lapping, grinding, machining, polishing or during the friction process; may be amorphous/microcrystalline due to melting or

surface flow of molecular layers hardened by quenching, or strained by plastic deformation; typically 1~100 nm (Beilby), 1~100 μm (deformed). Beilby or severely deformed layers of a magnetic material would become magnetically dead.

Figure 15. Sketch of surface texture [46].

The repetitive or random deviation from the nominal surface that forms the three-dimensional topography of the surface is designated as the surface *texture*. The important features (Figure 15) are:

i. *Surface roughness*: short wave-length fluctuations, mainly intrinsic to the production process;

ii. *Waviness*: longer wave-length fluctuations; may result from machine or work piece deflection, vibration, chatter, heat treatment, or wrapping strains;

iii. *Lay*: principal direction of the predominant surface pattern, determined by the production method;

iv. *Flaws*: unexpected interruptions in the topography,

The typical limit between roughness and waviness occurs according to Robbe-Valloire [47] at a period of 800 μm, whereas Broese van Groenou [48] defines as waviness asperities with wavelengths ranging from 50 to 200 μm.

Surface height distribution may be either *isotropic* or *non-isotropic*, whether it has been processed using non-directional (*e.g.* electro-polishing and lapping) or directional (turning, milling and planning) methods, respectively. The distribution is *Gaussian* at the height end of most engineering surfaces, whilst the bottom 1 to 5% of the distribution is generally found to be *non-Gaussian* [49]. The surface roughness of a Co-γFe_2O_3 magnetic tape—measured *via* a WYKO optical surface profilometer with a 40 times objective, on a 150 × 110 μm area—was found to follow a Gaussian distribution [50].

Surface roughness, as referred to the variation in the height of the surface $z(x)$ relative to a reference plane, is commonly measured statistically using:

the arithmetic average,

$$R_a = \frac{1}{L}\int_0^L |z - m| dx, \tag{8}$$

the standard deviation,

$$\sigma^2 = \frac{1}{L}\int_0^L (z - m)^2 dx, \tag{9}$$

the root mean square or rms,

$$R_q = \frac{1}{L}\int_0^L (z^2) dx = \sigma^2 + m^2, \tag{10}$$

where $m = \frac{1}{L}\int_0^L z dx$. For Gaussian surfaces: $\sigma \sim \left(\sqrt{\pi}/2\right) R_a$.

Other standard parameters for roughness and waviness measurement are advocated by The International Organization for Standardization (ISO) [51]. Amongst these, three extreme value descriptors R_t, R_p and R_z are commonly used, in particular by image analysis software [52]. They are defined as the vertical (z-) distance between:

i. The highest peak and lowest valley: R_t

ii. The highest peak and mean line: R_p

iii. The average of five highest peaks and five lowest valleys: R_z

It must be pointed out that asperity densities and curvatures are not intrinsic properties of surfaces but varies in their numerical value with the scale of measurement [53]. Based on fractal analysis, methods to describe the surface using intrinsic parameters have been proposed and applied to the contact between rough surfaces [54, 55, 56, 57, 58]. Such methods are beyond the scope of this thesis; it should only be emphasized that whenever the surface texture is to be considered, one should keep in mind the roughness scale-dependence, and choose a sampling interval relevant to the specific tribological aspect regarded.

1.3.2 Contact between solid surfaces

To quantify *where* and *how* the contact between two solids—here the head and the magnetic medium—takes place, two parameters are introduced: the real area of contact (determining the load distribution at the interface), the plasticity index (determining the mode of deformation). Other parameters are introduced, used in the analysis of the subsurface stress distribution due first to a single asperity, then generalised to a rough (multiple asperity) contact.

1.3.2.1 Real area of contact and plasticity index

Two nominally flat surfaces put together are in contact only at some discrete spots (asperity junctions). The sum of the junction areas, designated as the real area of contact, is only a fraction of the apparent (nominal) area of contact [59].

Deformation occurs at the asperity junctions. The mode of deformation, either *elastic* or *plastic*, depends on the nominal stress (load / apparent contact area), the surface roughness and the material constants. A plasticity index is defined as [60, 61]:

$$\psi = \frac{E_c}{Y}\left(\frac{\sigma}{R}\right)^{1/2}, \qquad (11)$$

where Y is the tensile yield stress (for polymer contacts; for metallic contacts Y is replaced by the hardness H), $\frac{1}{R} = \frac{1}{R_1} + \frac{1}{R_2}$, is the equivalent curvature, $\sigma = \sqrt{\sigma_1^2 + \sigma_2^2}$, the standard deviation of the equivalent peak-height distribution and E_c is the composite modulus, given by $\frac{1}{E_c} = \frac{1-\nu_1^2}{E_1} + \frac{1-\nu_2^2}{E_2}$, with E_1, E_2 and ν_1, ν_2 respectively the moduli of elasticity (complex moduli) and Poisson ratios of the mating surfaces. For polymers, the

contact is *plastic* (respectively *elastic*) if $\psi > 2.6$ (respectively $\psi < 1.8$). For metals, the contact is *plastic* (respectively *elastic*) if $\psi > 1$ (respectively $\psi < 0.6$) [61].

The plasticity index can be perceived as a compound characteristic of the interface, combining constitutive properties via E_c / Y and surface topography via σ / R [62]. For most materials, except elastomers $E_c / Y >> 1$, while for most rough surface of interest $\sigma / R << 1$. Therefore for a great majority of materials the order of magnitude of ψ is not known *a priori*. As an illustration, for metal surfaces ψ lies in the range 0.1-100 [44].

Since wear is more severe for plastic rather than pure elastic asperity contacts, machine components designed withψ close to the elastic contact limit ($\psi \sim 1.8$) are desirable. For a given load, high E_c and σ_p, and low R_p produce high contact stresses and result in a lower real area of contact.

Typical head media contact were experimentally determined as elastic, the ratio real to apparent area of contact expressed as:

$$A_r / A_a = 3.2(W / \psi Y), \tag{12}$$

where W stands for the applied load [63, 64].

For plastic contact, the same ratio would be expressed as:

$$A_r / A_a = \left(\frac{W}{H}\right)^b, \tag{13}$$

where b = 1 [65] or according to some authors, b < 1 [66, 67].

Polymers are a special case where the mode of deformation may be complicated by particular physical properties. Depending on their temperature polymers exhibit very different physical properties. Below glass transition temperature, polymers behave like a rigid solid, either amorphous (glassy) or crystalline; in this case the deformation is determined by the plasticity index. Above flow temperature, that is above the melting point, the polymer behaves like a liquid of high molecular weight, hence of high viscosity. Between glass transition and flow temperature, the polymer behaves in a viscoelastic manner, responding elastically to rapidly applied stress, while flowing as a viscous fluid in case the applied stress is maintained, a behaviour known as creep.

1.3.2.2 *Single asperity contact*

The solution to the problem of a single asperity contact was developed by Hertz [68] for frictionless elastic contact. Each body is approximated by an elastic half-space loaded over a plane elliptical contact area, of which the dimensions must be small compared to the dimensions of each body and to the radii of curvature of the surfaces.

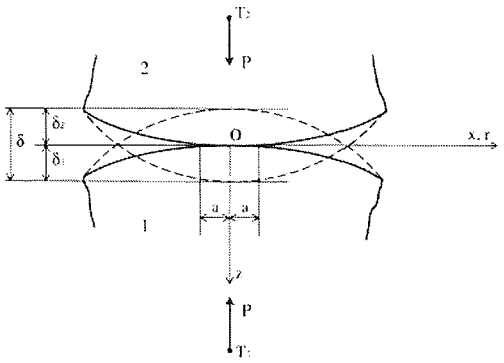

Figure 16. Hertzian contact of two non-conforming elastic bodies.

Figure 16 shows the two contacting solids after deformation. The quantity $\delta \equiv \delta_1 + \delta_2$ is called the *normal approach* or the *interference*. For the Hertz contact of two spheres [69, 70]:

$$\delta = \sqrt[3]{\frac{9P^2}{16RE^{*2}}}, \quad a = \sqrt[3]{\frac{3PR}{4E^*}}, \quad p_0 = \sqrt[3]{\frac{6PE^{*2}}{\pi^3 R^2}},$$
$$\frac{1}{E^*} \equiv \frac{1-\nu_1^2}{E_1} + \frac{1-\nu_2^2}{E_2}, \quad \frac{1}{R} \equiv \frac{1}{R_1} + \frac{1}{R_2}, \tag{14}$$

where a, p_0, $E_{1,2}$, $\nu_{1,2}$ and $R_{1,2}$ are the contact radius, the maximum contact pressure (at $r = 0$), the Young modulii, Poisson's ratios and radii of curvature, respectively.

The analogous expressions for the contact of two cylindrical bodies whose long axii are parallel to the y-axis is:

$$a = \sqrt{\frac{4P'R}{\pi E^*}}, \quad p_0 = \sqrt{\frac{P'E^*}{\pi R}}, \tag{15}$$

where P' is the applied load per unit length of y-direction.

In the case of two-dimensional cylindrical indenter in frictional contact with a semi-infinite solid, the Hertzian model assumes elliptically distributed normal and tangential loads at the interfacial contact, *i.e.*

$$\sigma_{zz} = \begin{cases} 0 & |x| > a \\ -p_0\sqrt{1-\dfrac{x^2}{a^2}} & |x| \le a \end{cases} \tag{16}$$

$$\sigma_{xz} = \begin{cases} 0 & |x| > a \\ \mu p_0\sqrt{1-\dfrac{x^2}{a^2}} & |x| \le a \end{cases} \tag{17}$$

where μ is the friction coefficient. Hence, the stress components in the semi-infinite solid can be expressed as [71]

$$\sigma_{xx} = \mu\frac{p_0}{\pi}\left[\left(2x^2-2a^2-3z^2\right)\psi + 2\pi\frac{x}{a} + 2\left(a^2-x^2-z^2\right)\frac{x}{a}\overline{\psi}\right] - \frac{p_0}{\pi}z\left(\frac{a^2+2x^2+2z^2}{a}\overline{\psi} - \frac{2}{a} - 3x\psi\right) \tag{18}$$

$$\sigma_{zz} = \mu\frac{p_0}{\pi}z^2\psi - \frac{p_0}{\pi}z\left(a\overline{\psi} - x\psi\right) \tag{19}$$

$$\sigma_{xz} = \mu\frac{p_0}{\pi}\left[\left(a^2+2x^2+2z^2\right)\frac{z}{a}\overline{\psi} - 2\pi\frac{z}{a} - 3xz\frac{x}{a}\psi\right] - \frac{p_0}{\pi}z^2\psi \tag{20}$$

with

$$\psi \equiv \frac{\pi}{k_1}\frac{1-\sqrt{k_1/k_2}}{\sqrt{k_1/k_2}\sqrt{2\sqrt{k_1/k_2}+\left[\left(k_1+k_2-4a^2\right)/k_1\right]}}$$

$$\overline{\psi} \equiv \frac{\pi}{k_1}\frac{1+\sqrt{k_1/k_2}}{\sqrt{k_1/k_2}\sqrt{2\sqrt{k_1/k_2}+\left[\left(k_1+k_2-4a^2\right)/k_1\right]}} \tag{21}$$

$$k_1 \equiv (a+x)^2+z^2, \quad k_2 \equiv (a-x)^2+z^2$$

σ_{zz} and σ_{xz} are plotted in Figure 17 and Figure 18 for a friction coefficient $\mu = 0.1$.

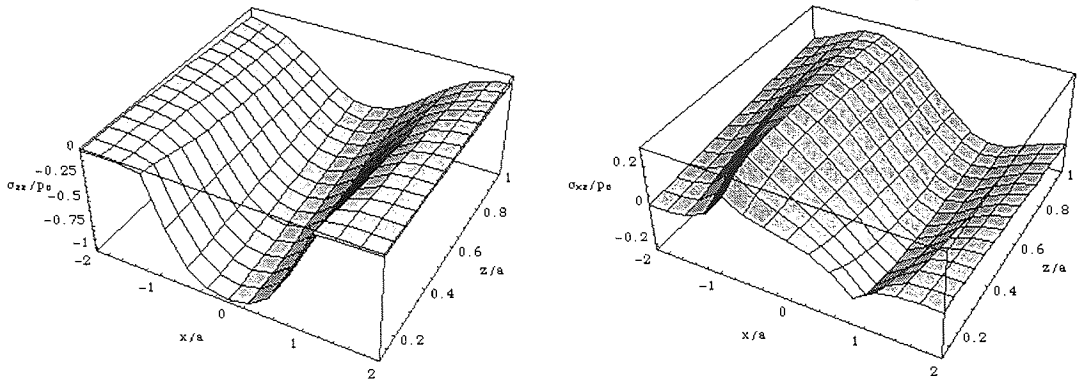

Figure 17. Two-dimensional cylindrical indenter in frictional Hertzian contact: compressive stress σ_{zz} and shear stress σ_{xz} at the subsurface of the semi-infinite solid; the friction coefficient was chosen as μ=0.1.

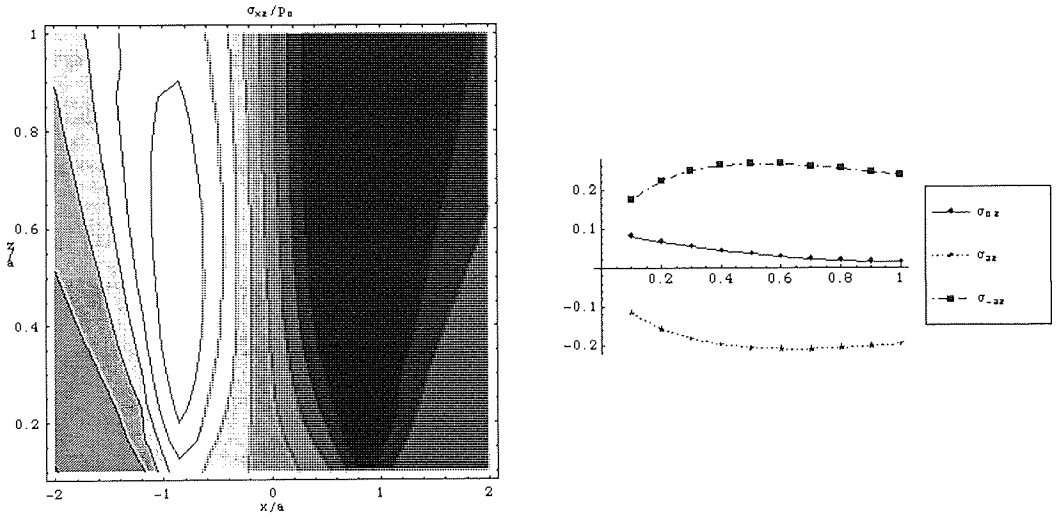

Figure 18. Two-dimensional cylindrical indenter in frictional Hertzian contact: shear stress σ_{xz} at the subsurface of the semi-infinite solid; the friction coefficient was chosen as μ=0.1.

The *Tresca* maximum shear stress theory state that plastic deformation begins at a point in the body at which the maximum shear stress reaches a critical value, *i.e.*

$$\max\left(|\sigma_1-\sigma_2|,|\sigma_2-\sigma_3|,|\sigma_3-\sigma_1|\right)=Y \qquad (22)$$

where σ_i, i = 1, 2, 3 are the principal stresses and Y is the yield stress in the simple tension test. Another theory, the *von Mises* criterion, states the yielding occurs when the distortional strain energy reaches a critical value,

$$(\sigma_1-\sigma_2)^2+(\sigma_2-\sigma_3)^2+(\sigma_3-\sigma_1)^2=2Y^2 \qquad (23)$$

which, for pure shear, predicts yielding at a stress 15.5% higher than does the Tresca criterion [72].

For the Hertz contact of two spheres, the maximum shear stress for $\nu = 0.3$ occurs at a depth of 0.48 a and has a value of 0.31 p_0. Thus, both the Tresca and von Mises theories predict the onset of yielding when

$$(p_0)_Y = 1.60Y, \quad P_Y = 21.2\frac{R^2Y^3}{E^{*2}}, \quad \delta_Y = 6.32R\left(\frac{Y}{E}\right)^2. \tag{24}$$

Yielding will initiate in the material with the lower yield strength.

1.3.2.3 *Rough surfaces contact*

Because real surfaces have roughness, it is necessary to combine the effects of a large number of asperity contacts. The only existing method that accurately accounts for so-called microcontact interaction effects is the direct numerical solution of contact problems for samples of real rough surfaces [73, 74, 75, 76, 77, 78, 79, 80].

Practical application of this approach poses serious difficulties inherent to the multi-scale (fractal) nature of surface roughness and roughness samples having both a sufficiently short sampling interval and a sufficiently long sample length must be considered. Consequently, the number of data will often be extremely large, especially in the more realistic and technologically significant 3D case. AFM typically produce data sets of about 500×500 points, and a system of about 2.5×10^5 equations arises from the corresponding contact problem.

Two modelling routines (one in two, another in three dimensions) are implemented in the modelling chapter (Chapter IV) later in this thesis.

1.3.3 Friction

Controlling and ideally minimizing the friction at the head / tape interface is of major concern for tape drive designers in their effort to increase recording densities. Friction occurs at any contact between the tape and the drive components along the tape path.

Friction is the resistive force generated between two solid surfaces in sliding contact:

$$F = f \cdot W. \tag{25}$$

W is the normal load. The friction coefficient f is a constant, given a pair of sliding materials and a set of operating conditions (temperature, relative humidity, normal pressure and sliding velocity). A pertinent review on the significance of the friction coefficient is due to Blau [81].

The friction force work can be converted to heat, vibration (*e.g.* sound), material deformation, or generation of new surfaces. Alternatively, it can be stored in association with microstructural defects (work hardening, dislocations, etc.).

Frictional heat increases the head-to-tape temperature, thus changing the mechanical properties and reactivity of the surface, with significant consequences on wear (*e.g.* see [82], [83] or [84]). It may also cause perturbation of the output signal [11].

The force required to initiate sliding is called static friction or stiction, as opposed to dynamic friction. Stiction is generally higher than dynamic friction. A marked difference between both or a friction coefficient decreasing with increasing sliding velocity causes the so-called stick-slip phenomena, which results in jerky and uneven motion [85]. This has consequences on the tape speed regularity and head-to-tape conformation hence may result in signal degradation.

In many metals and non-metals (such as polymers), an increase in the sliding velocity causes the shear strain rate to increase, with the consequence of higher strength, hence lower real area of contact and coefficient of friction in a dry contact [86, 87]. In well-lubricated contacts, the shear is localised within the lubricant film therefore the shear stress, hence the coefficient of friction increases with the sliding speed or acceleration [88, 89].

The contribution to intrinsic frictional resistance consists of a *deformation* component (plastic deformation or ploughing term plus a hysteresis loss term) plus an *adhesive* component [65, 90, 91, 92, 93].

1.3.3.1 *Deformation friction*

The deformation friction takes different aspects depending on the material considered. In metal, it results in ploughing, grooving or cracking of the softer surface by asperities of the harder mating material. In rigid plastics, stress beyond the yield point produces permanent deformation with no energy feedback. In viscoelastic materials, a delayed recovery after indentation by a particular asperity causes hysteresis friction.

Considering the viscoelastic nature of magnetic layers, the nature of the contact, and the surface topography, the total deformation component is small as compared to the adhesion component, and can be neglected [94].

1.3.3.2 Adhesion friction

Tabor's classical theory of adhesion defines the adhesion friction force as [65]:

$$F_A = A_r \tau_a, \tag{26}$$

for a dry contact,

$$F_A = A_r\left[\alpha\tau_a + (1-\alpha)\tau_l\right], \tag{27}$$

for a lubricated contact, with

$$\tau_l = \eta_l U/h, \tag{28}$$

where A_r is the real area of contact, α is the fraction of the lubricated area, τ_a and τ_l are the shear strength of the dry contact and of the lubricated film, respectively, η_l is the absolute viscosity of the lubricant, U is the relative sliding velocity, and h the lubricant film thickness.

Adhesive forces may be physical, involving Van der Waals bonds [95] (about 0.02 to 0.2 eV / atom), or chemical, involving electrostatic / ionic, covalent (about 2 to 10 eV / atom) or hydrogen bonding (0.2 to 0.5 eV / atom). Covalent bonding are likely to occur at polymer / metal contacts [96], whereas ion-dipole bonds occurs usually at polymer / ceramic contacts [97], both giving strong adhesive junctions. For an in-depth review on interfacial interactions between low-energy surfaces, the reader is further referred to [98].

1.3.3.3 Stiction

Tapes loaded at high pressures on smooth surfaces for long periods of time (when wound on reel or stationary over the magnetic head), their asperities will creep with time resulting in higher real area of contact, hence increasing the initial friction value.

High humidity conditions are found responsible for high friction forces, possibly due to meniscus effect, but more likely due to hydrolysis and plasticization taking place. High hardness and high complex modulus, as well as hydrophobic nature are therefore desirable properties for polymers [99].

1.3.4 Temperature at the head / tape interface

Friction and temperature are intimately related. A large proportion of the mechanical energy involved in friction is dissipated in form of frictional heat [100], which immediate effect is to increase the head-to-tape interface temperature. In turn, the temperature affects the mechanical properties of the materials exposed at the head-to-tape interface, with particular severity as polymer with low flow temperatures are involved. At temperatures just above room temperature, the binder is therefore prone to pyrolysis, and eventually mixed to the lubricant, will polymerise onto the head surface to form a transfer film (staining). Depending on the adhesive strength between the transfer film and the tape coating, friction may further be enhanced or reduced [82].

Heat is generated at the head-to-tape interface by the friction or impact of the tape on to the head surface. Between two surfaces sliding against each other, contacts at numerous asperities induce high transient temperature flashes of a few hundred degrees over surfaces of a few μm in diameter, within a few ns to a few μs. The maximum contact temperature for a particular linear tape systems has been calculated to be over 100°C [101]. However, considering isolated contacts between magnetic particles and a ferrite head surface, Bhushan [102, 103] estimated the average and maximum temperature as ~ 600°C and ~ 900°C, respectively. The resulting average temperature increase may causes pyrolysis of the binder polymer of the magnetic tape, which in turn may give rise to head staining. Moreover, considering the Curie temperature of most common magnetic materials (Table 1), the mean flash temperature is likely to affect the magnetic performance of the tape.

Models have been developed to predict the temperature at the interface between two sliding bodies (*e.g.* [104] and [105], the latter applied to a head-to-tape interface). We here refer to a model proposed by Bhushan [102, 103] that considers the temperature increase at each individual asperity due to both intermittent contacts (flash temperature) and steady state interaction between asperities:

Two configurations are considered for the head-to-tape interface:

1. *Rough-smooth* interface: one of the two mating surfaces is much rougher than its counterpart; the former behaves as a slider on an effectively stationary (smoother) surface. Because the magnetic head is much harder than the tape, the rough-smooth

case applies for tape-head (non-stained) contacts, even though the mating surfaces have comparable roughness.

2. *Rough-rough* interface: the two mating surfaces are of comparable roughness. The contact involves a pair of asperity tips, sliders to each other, the centre of the contact moving at about half the sliding speed ($U/2$).

The frictional heat liberated at the interface is expressed as

$$q = f \cdot p_a \cdot U \cdot \left(\frac{A_a}{A_r}\right). \tag{29}$$

f, p_a and U are the friction coefficient, the apparent pressure and the sliding speed, respectively. $\frac{A_a}{A_r}$ as well as all the parameters relevant to the considered model are defined below in chapter III, Table 18.

Two cases are further distinguished on the basis of a dimensionless speed parameter named the *Peclet number*, and defined as

$$L = \frac{Ul}{\kappa}. \tag{30}$$

where U, l and κ stand for the characteristic speed, length and thermal diffusivity, respectively.

Solutions for the temperature increase (average and maximum) at the interface are given in chapter 3, Table 19 for the following four different cases (the relevant characteristic parameters used to determine L are also indicated in the table):

i. Rough-smooth surface and $L < 0.5$ (low speed).

ii. Rough-smooth surface and $L > 10$ (high speed).

iii. Rough-rough surface and $L < 0.5$ (low speed).

iv. Rough-rough surface and $L > 10$ (high speed).

The intermediate case $0.5 < L < 10$ must be interpolated from the boundary cases [106].

The temperature increase is typically of the order of 10°C, therefore at least one order of magnitude lower than the above prediction for flash temperature.

1.3.5 Generic wear mechanisms

Two solid surfaces in sliding, rolling or impact contacts are susceptible to produce wear. Wear is traditionally classified in adhesive, abrasive, fatigue, impact, and chemical.

1.3.5.1 Adhesive Wear

Adhesive wear occurs at the asperity contact on the interface where fragments are pulled out from one surface to adhere to its counterpart. These fragments may later on be transferred back to the original surface or form loose wear particles. For plastic contacts, the worn volume may be expressed according to Archard's law [107]:

$$V = k\frac{Wx}{H}, \tag{31}$$

with k, W, x and H, respectively the wear coefficient, the normal load, the sliding distance and the hardness of the surface being worn. The non-dimensional wear coefficient depends on the materials in contact and their exact degree of cleanliness.

The equivalent for elastic contacts has been derived as [26]:

$$V = k'\frac{Wx}{E_c\sqrt{\sigma/R}}, \tag{32}$$

with E_c, σ and R, the composite modulus of elasticity, standard deviation and mean curvature radius of the summit, respectively, of the mating surfaces. From this equation, it can be noticed that the elastic modulus and surface roughness govern the worn volume. Repeated elastic contacts can result in surface / subsurface fatigue, and detached material transferred by adhesion to the harder surface.

Adhesive wear is of great importance at the head-to-medium interface in magnetic recording: it is mainly responsible for transfer film and debris particle formation. The binder polymer chains are built on covalent bonding, chains being mutually bound by dipole-dipole bounding. Since the adhesive forces at the interface are of the same nature as the binding forces within the material, the shearing process may actually tear out fragments of the material during sliding.

Introduction of a boundary lubricant at the head-to-medium interface while reducing the polar molecule content of the binder was found to reduce adhesive wear [108]. Reversely, the formation of surface transfer films may enhance adhesive wear [109].

1.3.5.2 Abrasive Wear

Abrasive wear is related to a ploughing action caused either by rough hard surface asperities (two body abrasion) or entrapped hard particles (three body abrasion) drawing a series of grooves in a softer surface, and which upon repetition, induce low-cycle fatigue mechanism promoting material removal. A simple quantitative expression for abrasive wear has been derived by Rabinowicz [110]. Assuming a conical asperity on the hard surface, the volume of wear is expressed as:

$$V = k \cdot W \cdot x \cdot \overline{\tan\theta}/H \qquad (33)$$

W, x and H are respectively the normal load, sliding distance and worn surface hardness; $\overline{\tan\theta}$ is a weighted average of the $\tan\theta$ values of all the individual cones; the dimensionless factor k takes into account the geometry and probability of a cutting (rather than ploughing) action by the asperity.

For polymeric materials the abrasive wear rate is inversely proportional to $S{\cdot}e$—S is the breaking strength of the material and e the elongation to break [111]—which represents the work to fracture (related to the impact strength of the material). Filling the polymer with particles will both increase S and reduce e, therefore will have little effect on its resistance to abrasion.

Plastic deformation beneath the abrasive asperity or particle is essential for abrasion to take place. Since polymers will deform plastically only in contact with very rough (roughness ~ 2 μm) opposing hard surfaces, two-body abrasion is unlikely to affect magnetic tape [60, 112]. Moreover, although head materials are not ideally brittle and may flow plastically, the surface roughness and particle size associated with current tape format prevents two-body abrasion from taking place [113, 114]. Abrasion will therefore imply a third body in form of wear or contamination debris agglomerates.

1.3.5.3 Fatigue Wear

Structural materials are rarely designed with compositions and microstructure optimized for fatigue resistance: metallic alloys generally designed for strength, intermetallics for ductility and ceramics for toughness. However, over 80% of all service failures derive from mechanical fatigue, in association with cyclic plasticity, physical contact (sliding, fretting or rolling contact fatigue), environment (corrosion fatigue), or temperature (creep fatigue) [115].

Fatigue wear mechanism relies on the growth of surface or subsurface crack. These cracks elongate and propagate until the surface eventually breaks up, pulled out as large fragments leaving large pits in the surface. Crack growth mechanism is described by Ritchie [116] as a mutual competition between *intrinsic* microstructural damage, promoting crack propagation ahead of the tip and *extrinsic* crack-tip shielding, retarding crack propagation behind the tip. In that perspective, crack growth in metallic materials is mainly intrinsic—involving creation of microcracks and voids, possibly by dislocation or interface decohesion in the highly stressed region ahead of the tip, and leading to failure by cleavage, intergranular cracking or microvoid coalescence—, whereas in brittle materials, crack growth is mainly extrinsic—resulting from the creation of inelastic zones around the crack wave or from physical contact between the crack surfaces.

Improving the fracture resistance of low-ductility materials such as ceramics has included over the years the design of microstructures that develop zones of inelasticity, microcracking or most predominantly bridging (by grains, particulate, fibres or layers) that surround the crack. However, it has been demonstrated that fatigue loading can severely degrade such toughening, which hence provide the critical mechanism promoting fatigue-cracks growth in materials showing *a priori* no intrinsic mechanism of cyclic crack advance [115]. In that respect, in Al_2O_3-TiC—applied as a wear-resistant material to most magnetic head structures—the TiC phase is precisely added to the Al_2O_3 to exhibit extensive plastic stretching, in an attempt to inhibit crack opening [117, 118]. Consequences of such combination will be further illustrated in the next section.

Crack propagation at the subsurface is intimately related to the stress distribution in connection with potential mechanical failure. The determinant quantities are then the location of any region of failure predicted by the yield criterion (*c.f. 1.3.2.2*) and the appearance of large tensile stresses [119]. In high precision mechanical components with smooth surfaces and good lubrication (small coefficient of friction), the largest contact stress always appear at a certain depth under the contacting surfaces [120]. It is furthermore assumed that the fatigue crack will then be initiated at the point of maximum von Mises equivalent stress [121]. The appearance of tensile stress plays a more essential role for brittle materials and predetermines the destructive development even more than the yield criterion [122]. An illustration of this is found in the ring cracks typically found on ceramic surfaces at the trailing edge of an indenter [123].

Unlike ductile materials, fatigue cracks do not appear to initiate naturally in ceramics, but are invariably associated with some pre-existing defect [115, 124].

Fatigue wear is equally applicable to polymers [125]. Cyclic compression and tension of an isolated asperity by an opposing asperity would lead to the initiation and propagation of subsurface cracks eventually resulting in delaminative removal of material, leaving crater-like recesses behind [22]. This has been observed in both metal particle (MP) tapes [30, 126] and floppy disks [108]. In flexible magnetic recording the effect is twofold: loss of bits of information contained in the delaminated material and, *via* transfer (combination with adhesive wear), hence head-to-media increased spacing, signal dropout.

1.3.5.4 *Impact Wear*

Impact wear can be either erosive (jets and streams of solid particles, liquid droplets, and implosion of bubbles formed in the fluid) or percussive (repetitive solid body impact).

The erosion by solid particles is induced by the kinetic energy of particle flowing in an air or liquid stream.

The volume lost from the surface due to the impact of *unit mass* of erodent particles at velocity v can be expressed as [127]:

$$V = \frac{\kappa}{2} v^2 \qquad (34)$$

κ is the 'dimensional wear coefficient' ($mm^3 \cdot m^{-1} \cdot N^{-1}$), often effectively constant over large ranges of experimental conditions. In practice, V is usually found to depend on a higher power of v (~ 2.4), and on the impact angle θ. The volume of wear is therefore function of the mass, velocity and angle of impact of the erodent particles.

Erosive wear involves cutting (at grazing angle) or deformation (at normal angle) in ductile materials [128, 129], whereas it involves radial crack propagation from the points of impact in brittle materials [130].

Erosion may take part in the wear of recessed areas on magnetic heads, where flexible media cannot be in contact—in very much the same way as three-body abrasion introduced earlier. The erodent particles would be wear debris or contaminants trapped at the head-to-media interface.

Repetitive solid body impact is another source of wear. The most common form of impact wear in magnetic recording technology is caused by intermittent slider/disk impacts during steady state operation in hard disk drives [131].

1.3.5.5 Chemical wear

Singer [109] summarises as harmful chemical wear: H_2 or O_2 embrittlement that leads to fracture, enhanced diffusion that leads to stress gradients into a surface, and formation of surface films that enhance adhesive wear.

Chemical wear combines the effect of a reactive environment—forming a chemically reacted film on the exposed surface—and of the sliding action—wearing the film away, thereby exposing the surface to further corrosion. Reactive elements are mostly found in the atmosphere such as oxygen, forming an oxidized layer, water vapour producing pyrolysis and chain scission in polymers and forming hydroxides on metals, ceramics, etc. Water may also infiltrate porous materials and enhance crack propagation, a physical effect due to the non-compressibility of water well known in the pitting of metals [132].

1.3.6 Effect of wear and transfer on head performance

The requirement for high-density tape recording at acceptable read-back signal amplitude puts the highest demand on the physical spacing at the head-to-tape interface, which must typically be kept within a few 10s of nm. The separation loss term in the Wallace equations (6) and (7) is expressed as $S(\lambda) = \exp(-2\pi d/\lambda)$ or in decibels: $55\,d/\lambda$ dB [9]. An output loss of 6 dB is typically considered a failure [30, 133]: with a recording wave length of $\lambda \sim 0.5$ μm, 6 dB would correspond to a magnetic spacing of ~ 75 nm, including where it applies, the pole-tip recession (PTR), transfer film, lubricant, roughness, coating, magnetic-dead layer, and air cushioning.

The most common sources of spacing loss at the head-to-tape interface are:

i. PTR and staining on the head side.

ii. Protrusions, voids and heterogeneities on the tape side [134].

Aerodynamic effects may be in some cases another source.

1.3.6.1 *Pole-tip recession*

Materials with dissimilar wear resistances are used in recording head construction and pole-tip recession is one consequence of this heterogeneity. Several wear mechanisms are likely to operate at the head-tape contact. The dominant mechanism in terms of material removal is not necessarily the one responsible for pole-tip recession [22], thus simple screening experiments are not necessarily helpful in predicting composite wear of the head. Various factors such as hardness, elastic modulus, fracture toughness and scratch resistance, may come into play, although through different mechanisms.

Patton and Bhushan [135] describe the mechanism for differential wear as governed by two factors: the relative hardness and scratch resistance, and the relative recession from the tape-bearing surface (TBS) of the different head materials. Between two different materials at a same level, the one with the poorer mechanical properties is expected to wear at a higher rate until in less severe contact with the tape asperities and/or loose debris. At that stage, the material with superior mechanical properties will wear at a higher rate, until both materials reach the same level. The two preceding stages alternate until the recession attains a saturated value at a 'safe' distance from the tape asperities.

Bhushan and Patton [136], Patton and Bhushan [137] stipulate there is little contact between the tape and the recessed part of the head, hence assuming that differential wear results from loose wear debris particles trapped at the head-to-tape interface (three-body abrasion). Results from Scott and Bhushan [138] show that a combination of higher tape tension and more tape contamination lead to higher pole-tip recession, which also demonstrate that a three-body abrasion mechanism prevails.

Harrison *et al.* [139] further present experimental evidence for a three-body erosion mechanism in sandwich heads used in helical scan video tape recorders. The third bodies are assumed to be pulled-out ceramic particles transferred on to the track. The pullouts are therefore responsible for the track wear as this is out of contact with the tape.

Ceramics, chosen for their hardness, are generally used as air or tape bearing surface (ABS or TBS) material. Ceramics are brittle materials with low surface energy. The ionic or covalent bonding is directional, hence asperity contacts have low adhesive strength and adhesive wear is not a common mode of wear in ceramics. High hardness further makes abrasive wear an uncommon mode. Because of low fracture toughness, fatigue wear, *microfragmentation* (cleavage and fracture) are the most common modes of wear.

Al_2O_3-TiC ceramics are commonly used in tape and disk head construction, due to their exceptional hardness, toughness, chemical and thermal stability. TiC grains (~ 1 μm in size) are added to the alumina matrix to increase both hardness and toughness, and hinder crack propagation. The TiC particles bonded to the matrix, when intercepted by a crack exhibit extensive plastic stretching, contributing to the toughness by inhibiting the crack opening [117, 118]. However, Al_2O_3-TiC ceramics have been reported as being less wear resistant than single-phase ceramics such as Al_2O_3 and SiC [140, 141].

Many experimental results that illustrate the wear behaviour of Al_2O_3-TiC ceramics are discussed in the literature. Using a diamond tip, nano-friction [142], and resistance to nano-scratch and nano-wear have been measured as being higher on TiC phase [141]. In consequence, alumina was found to wear at higher rates than TiC during lapping, nano-wear / nano-scratch tests or sliding against CrO_2 tape [143] where abrasive wear is assumed to prevail. Considering material properties and surface roughness of the tape and head components, abrasive wear is not likely to be a dominant mode in conditions encountered in actual tape drives. Chandrasekar and Bhushan [144] state that the friction coefficient and wear of ceramics under limited load, in marginally lubricated sliding conditions is dominated by adhesion at the interface. In turn, adhesion is influenced by factors such as crystallographic, mechanical, thermal and electrical properties.

Gupta and Menon [145], sliding a diamond like carbon (DLC) coated hard disk against an Al_2O_3-TiC slider (at 25°C and 45% RH) found a high propensity to TiC intra-grain pull-out attributed to a difference in chemical composition, grain size and sintering conditions. Moreover, Clifton [146] testing tape heads in dry environment (30% RH) reports the recession of TiC with respect to the alumina. In such conditions, hardness is unlikely to control the ceramic wear behaviour.

Guo *et al.* [147] analysing the friction and wear behaviour of Al_2O_3-TiC and Al_2O_3-TiC-Co report microcutting and brittle fracture as the predominant wear mechanism, with pronounced plastic deformation. Debris is mainly powder-like and flake-like in shape, formed by inter-granular and/or transcrystalline fracture and/or by subsurface cracks expanding and interlinking in the plastic deformation zone. Eroded ceramics form radial, lateral and ring cracking, where properties such as microstructure or grain size effects are determinant. Commonly, the surface fracture energy is larger than the grain boundary energy; therefore, grain boundaries turn out to be the stress concentration area, and a potential crack nucleation zone.

How environment affects Al_2O_3-TiC wear is less well documented. Fischer and Mullins [148] report the higher wear of alumina in water than air, describing the wear mechanism as inter-granular fracture driven by chemisorption embrittlement: water attacks the bonds between neighbouring metal and oxygen ions at the crack tip, at which tensile stresses accelerate the reaction.

TiC was found to oxidise at temperatures above 450°C [149] usually exceeded by flash temperature [150]. However, TiC is embedded in Al_2O_3, a stable and very hard material, and contrary to SiC cannot form a wear plateau when oxidised in air upon sliding [151].

1.3.6.2 Stain

Another source of increased spacing at the head-to-tape interface comes from tape debris, generated by adhesive, abrasive or impact wear. Worn head and tape materials, together with foreign contaminants are introduced between the sliding surfaces resulting in three-body abrasion of tape and head surface (loose debris) or adhesion to drive components (*transfer* and *staining*) leading to polymer-polymer contact, increasing friction, head clogging and magnetic errors, and in the worst case scenario causing catastrophic failure [108].

The debris generation is generally reduced for uniformly distributed, non-agglomerated particle coatings and more flexible tapes. Environmental conditions (temperature and humidity) are also of prime importance when considering wear, friction and staining effects. Adsorption of atmospheric moisture relates to hygroscopic properties of material and a binder with increased water content may become softer and show higher friction [152].

The tape roughness is also a key parameter, since a tape having a high number of asperities (especially if new) is prone to generate debris. Exceptionally smooth tape provides a large real area of contact between the tape and drive components, which may cause the tape to shed.

The tape roughness usually decreases in the early cycles, due to removal of the higher asperities and asperity creep [143, 153, 154, 155 and 156]. The tape wear affects the friction at the head-to-tape interface by either increasing the real area of contact (decrease in roughness) if the contact is elastic, or reducing the adhesive strength due to the presence of debris and changes in the chemical nature of the tape surface. Surface chemical

changes may be due to liquids held by the porous binder (lubricant, cross-linker, dispersant, etc.) exuding to the tape during repeated asperity contacts, localised melting of the binder, oxidation and degradation of the polymer (coating) surface leading to decreasing its molecular weight [157].

The accumulation on the head of adherent deposits, forming either discrete spots or a continuous transfer film (of the order of 20 to 30 nm thick) is usually referred to as "stain" and is observed as brown, blue, white or transparent in colour [82, 158]. Unlike loose debris, these deposits cannot be easily removed with a cotton-tipped applicator and head cleaning solvent, but only by mechanical abrasion. The exact nature of these stains is the subject of much discussion.

Several chemical analyses of stains were reviewed by Bhushan and Hahn [158]: stains produced with γ-iron oxide tapes were reported of consisting in organic, iron (being more concentrated in brown stains) and oxygen constituents. It has also been noticed that staining forms preferentially in recessed areas or scratches on the head surface. The environmental conditions are also important for stain production, particularly humidity: Stain is reported to form more readily at very low humidity, generally below 35% RH [159], and is seldom encountered at high humidity (above 50% RH) [150]. Furthermore, increased surface temperature, due for example to bias current applied in MR heads, is likely to favour staining [40].

Gupta *et al.* [160] analysed the deposit formed on metal in gap (MIG) heads at 1.5 m/s, over up to 500 km at 22 ± 1°C and 45 ± 5% RH. Co-γFe_2O_3 tapes produced thick and patchy stains 30-150 nm thick, whereas metal particulate (MP) tapes produced a uniform film about 20 nm thick.

Ota *et al.* [150] analysed the brown stain appearing on VCR head surface as being a mixture of γ-Fe_2O_3 (magnetic powder in the tape) and non-conductive substance composed of the binder of the tape. Brown stain occurred at relative humidity (RH) below 40%, gradually decreasing to disappear above 45%. Debris of nanometre size was generally produced at low RH and debris of large size at high RH. The deposition on the head surface was associated to an increase in contact temperature between the head and tape reaching 200°C ~ 500°C in local and small contact regions. At these temperatures however, no crystallisation of iron was observed. The incidence of brown stain was inversely proportional to the tape tension and suppressed head wear.

Liew *et al.* [161] observed the formation of brown stain together with transparent materials. Although γ-Fe_2O_3 was the dominant oxide in the tape, they suggested that the deposits were mainly of Fe_3O_4. They further investigated the catalytic action on the stain formation of several metals located on the tape path. Cu was found to promote and Ni to inhibit the stain formation.

Stahle and Lee [162] tested helical scan heads 4h at 70°C/70% RH to clean and contour head, followed by 12h at 70°C/10% RH. They report the occurrence of two types of deposited film and brown stain. The film is visible on the glass and along the edges of the ferrite area, with a bluish-grey colour. It is mainly composed of ferrite head material and iron particles worn away from the head and tape, but free from organic binder material (*i.e.* Cl or N) from the tape. The brown stain is located on the metal region and may be made up of iron particles from the tape, pressed on the metal region. Neither the metal alloy nor the ferrite material were detected in the brown stain.

1.3.7 Wear protective layer—coating

Hard coatings are applied to magnetic heads and magnetic media—either hard disks (HDs) or metal evaporated (ME) tapes [163, 164]—, to protect the head-media interface against wear (hence pole-tip recession), corrosion, electrostatic discharge (ESD) damage and electrical shorts. Desirable properties are thus high hardness, good adhesion to the substrate, chemical inertness, high smoothness, high thermal conductivity, high resistivity and lack of magnetic response. For tape drives with a linear recording wavelength of ~ 0.5 μm, the coating thickness must be reduced below 10 nm to keep the signal loss to less than 1dB over the lifetime of the head (5000 hrs) [165]. As a comparison, coatings down to 10 Å thin are required for 100 GB/in^2 HD recording density [166].

Hard coating on softer substrate can decrease friction and wear by preventing ploughing on both a macro scale and a micro scale [167]. It typically exhibits residual compressive stresses, which can prevent the likelihood of tensile forces occurring. The hardness may be expected to be a major factor in promoting good wear resistance in coatings [168]. Most coatings are granular and their hardness will increase as the grains get smaller; the intergranular bond is also of great importance. A general trend observed for hard coatings is an increase in hardness with decreasing thickness. As an attempt to quantify this observation, it has been proposed to relate the composite hardness of the film + substrate combination to their respective hardnesses [169].

The most commonly applied coating is amorphous carbon (a-C) also known as diamond-like carbon (DLC): it has many attractive properties, such as hardness, inertness, resistivity and thermal conductivity, without the inconvenience of high roughness and high deposition temperature. a-C is a meta-stable amorphous material forming a random network of covalently bonded carbon in hybridised tetragonal (sp^3) and trigonal (sp^2) local coordination, with some of the bonds terminated by hydrogen [170]. These coatings usually reproduce the substrate topography and do not require post-polishing. Good adhesion is obtained for substrates that form carbides (*e.g.* Si, Fe, Ti...), whilst other substrates may require an interlayer of silicon [171].

Deposition methods typically used are, in sp^3/sp^2 (and hardness accordingly) decreasing order: cathodic arc deposition, pulsed laser vaporisation, direct ion beam (IB) deposition, plasma-enhanced chemical vapour deposition (PE-CVD), IB sputtering, and DC/RF sputtering. In the case of cathodic arc carbon coatings deposited on Al_2O_3-TiC substrates, a hardness of 38 GPa and an elastic modulus of 350 GPa were measured [172]. Most DLC coatings (with the exception of filtered cathodic arc deposition) contain hydrogen, which helps to stabilise sp^3 sites, to the detriment however of the coating hardness. DLC films have a high compressive stress that makes them stronger coatings than other tensile films, which have a tendency to crack [173].

Hard Disk recording commonly uses DLC coatings: the head is in intermittent contact with the disk. Tape recording poses the problem (besides the flexibility of tapes, usually restricting the coating to the head) that the tape is pressed against the head hence generates subsurface stresses resulting in fatigue wear. In such conditions, DLC might not to be a viable coating and other coatings should be considered.

Other used coatings include carbon nitride (CN), zirconia (Zr_2O_3), chromium nitride (CrN), chromium oxide (Cr_2O_3), and boron nitride (BN).

Sputtered zirconia films 20 to 50 nm thick have shown reasonably high hardness (~ 18 GPa), which were attributed to high compressive stresses (~ 8 GPa). However, wear resistance and adhesion to the substrate proved to be relatively poor.

Sputtered CrN films 50 nm thick may reach hardness above 20 GPa. These films can be produced with increasing amount of nitrogen although Cr/N ratio close to unity (slight excess in Cr) gives the best wear resistance. Polycrystalline films—by opposition to columnar-like films—show the best performance, hardness increasing with the film internal

stress. An electroplated chromium layer intercalated between columnar CrN coating and substrate was shown to induce a strong texturing effect on the CrN coating, thus presenting a more evident, straight and upward columnar structure [174].

c-BN films (bulk hardness of 30-40 GPa) are difficult to produce since, similarly to diamond films, softer intermediate layers ~ 50 nm thick are produced before a 'continuous' cubic phase starts to form.

The main wear mechanisms of plasma-sprayed Cr_2O_3 coatings applied to a piston ring have been reported to be plastic deformation, crack formation and spalling due to fatigue, brittle fracture and material transfer [175].

Cr_2O_3 coating, used since the 70s for gas-bearing application (> 0.5 μm thick) was introduced for tape-head coating as super-protective layer (SPL) in 1994 [176]. Although Cr_2O_3 has a bulk hardness of 9-11 GPa, films as thin as 20 nm have been deposited with hardness up to 30 GPa, which is attributed to a high compressive stress (3-4 GPa) [168, 165]. Again, lowest wear coefficients are achieved with polycrystalline films. To overcome adhesion problems, an interlayer of Cr has also been applied to the substrate before deposition.

Cr_2O_3 coatings, 50 to 200 nm thick (Cr interlayer ~ 10 nm), have been deposited using an optimised rf-diode sputtering process as polycrystalline samples having a grain size ~ 10 nm [133]. These films had hardness (15-30 GPa) and elastic modulus (110-210 GPa) comparable to cathodic arc deposited DLC films, the latter surpassing all other deposition techniques.

2 Chapter II - Experimental method

The experimental work reported here was performed in two stages: *wear test* and *analysis of the impact of wear on the tested samples*. The first stage consisted in fitting prototype ADR heads into ADR drives. The drives were placed in a climate chamber, and the heads put in sliding contact with a magnetic tape. The second stage consisted of analysing the surface of the heads and tapes—effectively the head-to-tape interface—subjected to the first stage, by means of a range of experimental techniques: optical microscopy (OM), atomic force microscopy (AFM), X-ray photoelectron spectroscopy (XPS) and Auger electron spectroscopy (AES).

A detailed description of the ADR heads and tapes, the experimental setup used during the wear test, i.e. drives, climatic chamber, procedure, etc. and of the different experimental techniques and routines specific to the analysis is provided in this chapter.

The last part of the chapter will be dedicated to the procedure implemented for measuring the temperature at the head-to-tape interface.

2.1 Material

2.1.1 Heads

2.1.1.1 Standard heads

ADR head technology was adapted from the digital compact cassette (DCC) head technology, with the major improvement of *sensor-first* design switched to *sensor-last* design.

In DCC heads, the magneto-resistive element (MRE) had to be deposited first on a perfect (freshly polished Al_2O_3) surface to reduce *Barkhausen noise* (BHN). A *barber pole* (BP) was located between the MRE and the *magnetic yoke*, making necessary the use of a high bias DC current to linearise the MR response, with the consequence of high power consumption. An *insulating oxide* layer was deposited between the BP and the yoke to avoid short circuits and electrostatic discharge, lowering the head efficiency.

The *sensor-last* design was made possible by using a planarisation technique, combining chemical and mechanical polishing (CMP), performed at several steps during the head production process. Use of high temperature for optimising the flux guide magnetic properties and the elimination of step coverage problems, with the benefit of lower short-

circuits, less stress is thus made possible. This technology further enables freedom in design to obtain low power consumption, higher efficiency (from 10.6% up to 18.6%), and the reduction of the smallest dimensions. The reduction in the separation-oxide thickness (0.6 μm to 0.3 μm) and in the distance from tape bearing surface to MRE (12 to 7 μm) are consequences of sharper steps, and the elimination of the barber pole (not necessary in purely digital application where some distortion may be accepted). As a result, the MRE resistance is increased by a factor of 2.6, and its thickness reduced from 35 to 30-nm, increasing the sensitivity with respect to the DCC head by a factor of 6 [19].

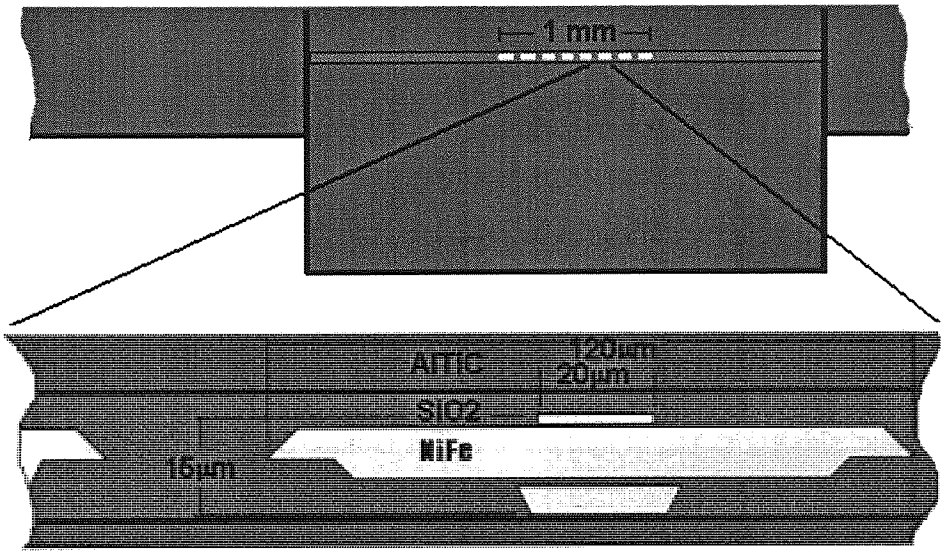

Figure 19. Top view of a multi-channel ADR head. Dimensions are only indicative.

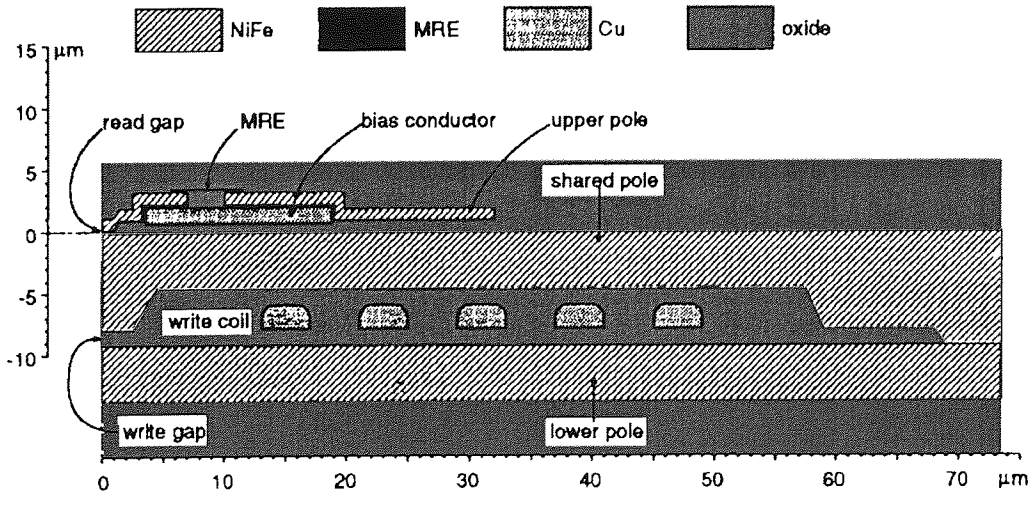

Figure 20. Cross-section of an ADR head.

For multi-track recording purpose, eight read/write channels are aligned over a length of about 1 mm perpendicular to the tape motion (Figure 19). The 8 channel data head consists of a combined write and read head. In Figure 20 the following layers can be distinguished (starting from bottom to top): the Bottom Flux Guide (BFG) or lower pole, write gap and Shared Flux Guide (SFG) or shared pole, the reader gap, and the Reader Flux Guide (RFG) or upper pole. The BFG and the RFG are 35.5 μm and 24 μm wide, respectively. All fluxguides or poles are made of standard Permalloy ($Ni_{80}Fe_{20}$), the write and reader gap of SiO_2. The write gap and read gap are 1.3 μm and 0.25 μm, respectively. On top of the RFG, SiO_2 is further deposited. An Al_2O_3–TiC substrate (bottom) and coverbar (top) encapsulate the whole thin film structure. Thus at the head surface NiFe, SiO_2 and Al_2O_3–TiC with respective hardnesses of 1.2 GPa, 8 GPa and 20 GPa (*c.f.* Table 4), are the materials susceptible to wear. The inductive write head consists of a 5-turn copper coil. The NiFe MRE of the read head is of the yoke type (see *e.g.* [177]). The Electric machining guides (EMG) are the two outermost structures at tape-bearing surface level in the thin film design (Figure 21): they are used to control the lapping process. These NiFe switches may be also used to monitor the head-to-tape interface temperature effects as will be shown later. The head contour radius is 1.3 mm to ensure a stable head to tape contact via a high-pressure profile regime.

Table 4. Physical properties of the materials involved in an ADR™ head construction. [31, 178,, 179, 180, 181, 182, 183 and 184]

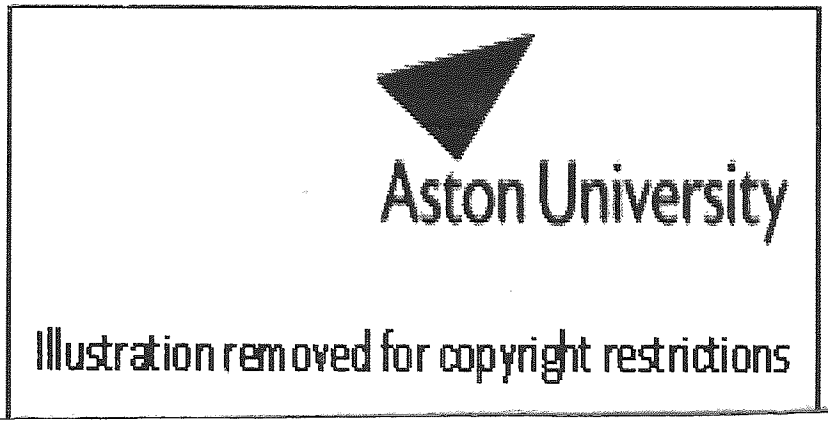

Figure 21. Thin film layout of the head design [185]. Both the left EMG and the line of the tape-bearing surface are indicated.

Two different manufacturers, HDL and Lafé, assembled the ADR heads used in this project. The most obvious difference in concept lays in the way the chips (Al_2O_3-TiC substrate bearing the thin film layout) are assembled to the cover bar. HDL heads have a 'U' structure: two side-blocks are glued to the chip, after what a cover bar is glued against the side-blocks/chip assembly. Lafé heads have an 'H' structure: a coverbar is glued to the chip (both of same width), the two end-blocks are added at both ends of the coverbar/chip assembly (*c.f.* Figure 22). A *sidebar shift*, that is a recession between the end-block and the chip/cover-bar assembly may occur at the Lafé tape-bearing surface. The difference in the two head layouts is expected to affect the wear behaviour. The chip edges (and consequently the EMG localised at each ends of the thin film) may be somewhat protected by the sidebar shift from severe tape contact, therefore wear and transfer.

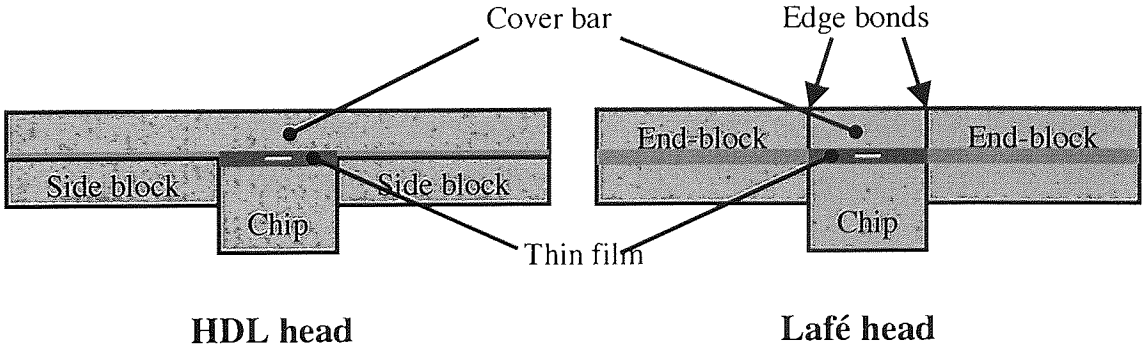

Figure 22. HDL versus Lafé head layouts.

2.1.1.2 Diamond-like carbon coated heads

Diamond-like carbon (DLC) coating was applied to the tape-bearing surface to improve wear resistance. DLC coating provided by four different suppliers, Commonwealth, Diamonex, Bekaert and Veeco have been tested.

DLC coatings were prepared both by Ion Beam Deposition (IBD) and Cathodic Arc (CA) [186,187]. All layers were 10-nm in thickness, but the hardness, elasticity and film stress varied. Hardness values ranged from 10 to 55 GPa, whereas the stress never exceeded 3 GPa except for the one layer with the highest hardness value, where a stress of 7.5 GPa was observed. Of all types of coating minimal four heads were put in wear test.

Commonwealth using ion beam deposition (IBD) provided 10, 15, 20, 25 and 30-nm thick DLC films (< 6% accuracy). Prior to deposition, a light pre-clean etch was performed to remove any atmospheric contamination and surface oxide (able to remove the equivalent of 2-nm of SiO_2).

Diamonex applied a so-called NILAD™ coating (hardness = 18 GPa, friction (incline plane) = 0.165) with a thickness of about 100 Å.

Bekaert applied a so-called DYLYN® coating (hardness = 10-32 GPa, friction = 0.05–0.15 / 100 Cr6 steel) with a thickness of about 100 Å.

Veeco deposition methods are referred as *cathodic arc* (CA - thickness = 90-100 Å, hardness = 45-55 GPa) and RF-IBD (thickness = 100 Å, hardness = 23 GPa).

2.1.1.3 SPL coated heads

In addition to carbon coatings, Cr/Cr_2O_3 coatings can also be applied. This coating, originally developed for the Digital Compact Cassette (DCC) [176, 188 and 189], had a nominal thickness of 55 nm (10 nm Cr and 45 nm Cr_2O_3).

The SPL coating is a reactive RF sputter-deposited layer using a chromium target in an argon/oxygen atmosphere [165]. A bias voltage of - 42 V was used for the heads tested here. Cr interlayer was found superfluous whilst increasing the head-to-tape interface spacing; therefore it had not been applied here. Under these conditions, the film internal stress was found to be either compressive (20 nm) or tensile (40 nm)—the absolute value was measured as ~ 2 GPa in both cases [185].

2.1.1.4 Dummy heads

Dummy heads were geometrically identical to the real heads. However, the whole head surface was constructed from a single material. Dummy heads were intended to isolate a selected material and provide a wide-enough homogeneous surface for XPS analysis, hence allow monitoring the chemical changes that occur at the head surface in sliding contact with a magnetic tape while still maintaining the contact geometry.

Experimental results on dummy heads made of three different ceramics are here reported. The first is Al_2O_3-TiC—the two-phase ceramic used as a base and cover bar in actual ADR™ heads; the second and the third are respectively TiO_2 and Al_2O_3 single-phase ceramics. The respective hardnesses of these ceramics are tabulated in Table 5.

Table 5. Vickers and Knoop hardness for three ceramics: titanium oxide, alumina and titanium carbide [190].

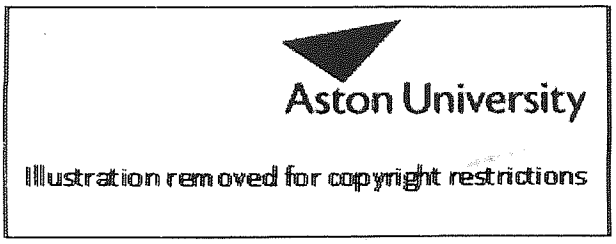

The purpose of testing Al_2O_3-TiC dummy heads was to identify the wear mechanisms and behaviour of the ceramic used in the actual head construction, isolated from other components of the head, and so to gain a better understanding of the physical and chemical changes occurring at its surface. Use of single-phase ceramics was intended to check the wear mechanisms specific to the two-phase nature of the Al_2O_3-TiC ceramic.

2.1.2 Tapes

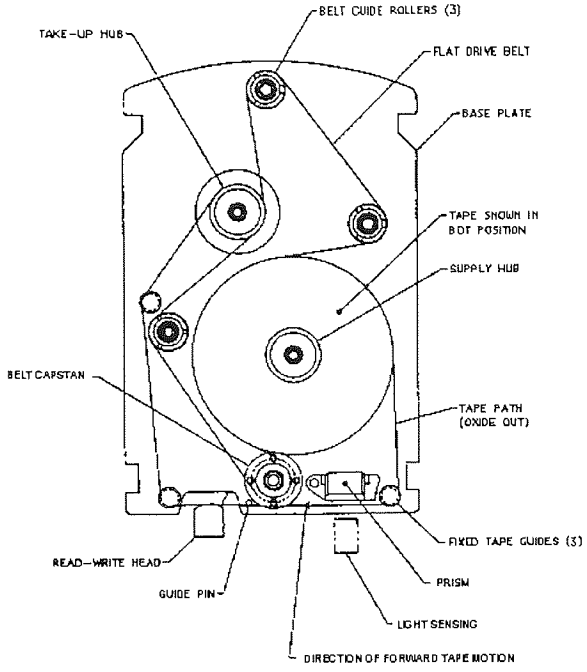

Figure 23. Diagram of a 15GB ADR quarter inch cartridge (QIC) uncovered, detailing its various parts.

The first generation ADR system uses a Co–γ–Fe_2O_3 tape of 8 mm in width and 1000 ft (304.8 m) in length. They were produced by Verbatim® in a quarter-inch cartridge (QIC) format depicted in Figure 23.

The magnetic coating, PET substrate and back-coat were respectively 1.1 μm, 6.0 μm and 0.9 μm thick. Al_2O_3 particles were used as a head-cleaning agent (HCA). In Figure 24 the hysteresis curves measured by Vibrating Sample Magnetometer (VSM) are shown both for the moving direction (MD) and transverse direction (TD). In Figure 24 the coercivity in the MD and TD is measured as 72 kA/m (900 Oe) and 50 kA/m (625 Oe), respectively. To calculate the saturation magnetisation (M_S) of the magnetic pigment, the magnetic packing density (p) has to be considered: a reasonable estimate, $p = 1/3$, results for the particles in an M_S around 360 kA/m. Furthermore the squareness ($S = M_R / M_S$) in MD and TD are $S_{MD} = 0.80$ and $S_{TD} = 0.36$, respectively. The switching field distribution (SFD) can also be derived from the hysteresis curve. It is defined here as

$$\mathrm{SFD} = \frac{M_R}{M_C}\left(\frac{\mathrm{d}M}{\mathrm{d}H}\right)^{-1}_{H_C} \qquad (35)$$

which in the MD equals 0.485. A crude estimation for the permeability (m) in the MD gives $m < M_R / H_C < 4$. For a comparison in recording characteristics and noise behaviour

with respect to other tapes such as a metal particulate (MP) or metal evaporated (ME), the reader is referred to [191].

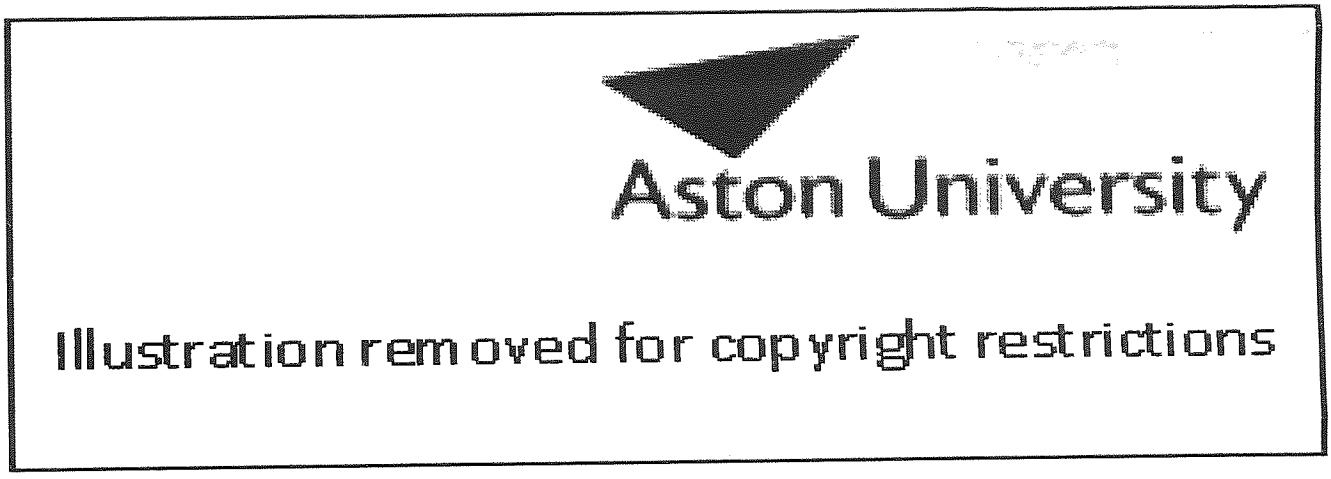

Figure 24. Hysteresis curves in MD and TD [185].

2.2 Wear tests in controlled environmental conditions

2.2.1 Drives

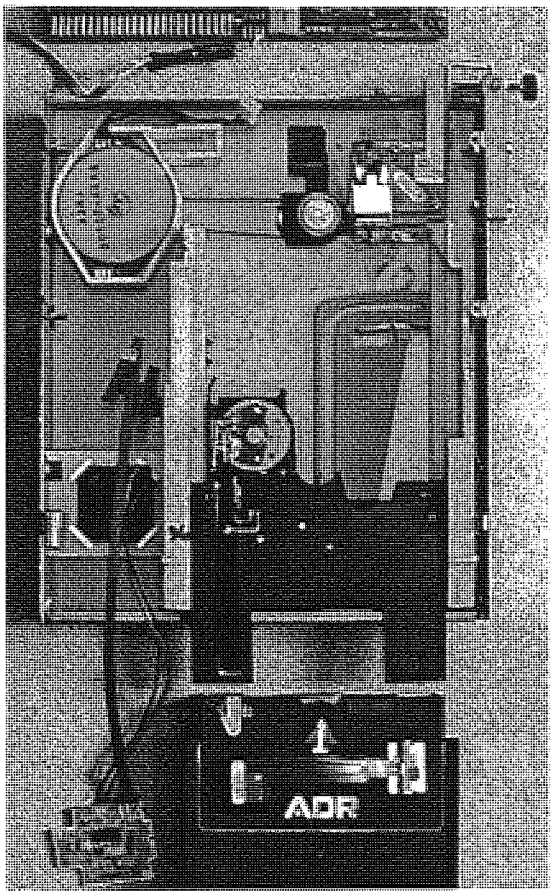

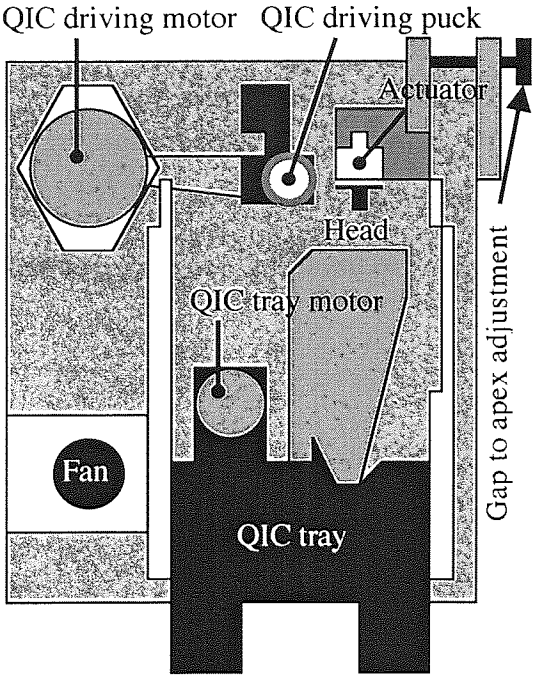

Figure 25. ADR drive mechanism.

Modified ADR drives, developed by OnStream to test the wear behaviour of prototype heads are described hereafter. A view of the drive inside mechanism is presented in Figure 25. The modifications with respect to commercial drives apply to the *end of tape* (EOT) *detection procedure*, the *firmware* (integrated software controlling the drive processes), and the *positioning of the head.*

The EOT detection relies in the original drives on the embossed servo signal. Here an infrared signal transmitted through holes perforated at the tape ends prompts the tape reversal.

The firmware has been modified in order to (i) shortcut the calibration procedure to allow mounting dummy heads, (ii) set different tape speeds, (iii) oscillate the actuator and (iv) step the head.

Additionally to the azimuth and zenith (or tilt) adjustments of the head already available (*c.f.* Figure 26), a lever was fitted to the drives for gap to apex adjustments.

The heads were oscillated at a frequency of 10 Hz and amplitude of 50 μm. At the beginning of test, the heads were set to their highest position. They moved laterally by one-track steps at each tape reversal, resulting in the utilisation of the whole tape width. The insertion depth, gap to apex, tilt and azimuth were respectively set to 1.6 ± 0.1 mm, 0° ± 30', 0° ± 5' and 0° (no quantitative verification).

ADR 15 GB QIC tapes supplied by Verbatim were usually tested at a speed of 1.1 m/s (44 ips).

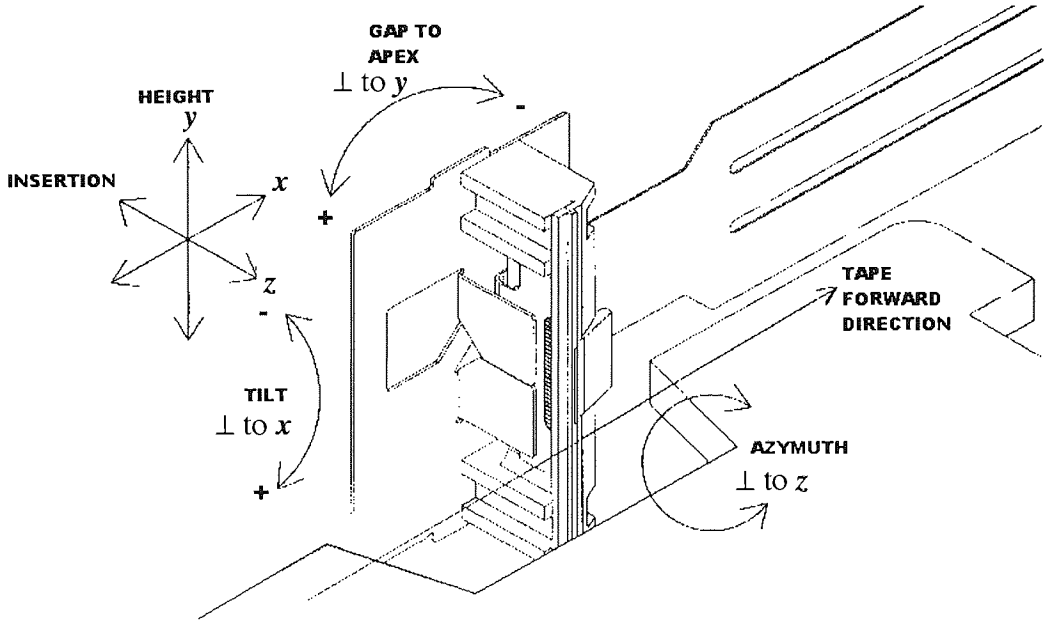

Figure 26. Head adjustments.

2.2.2 Environmental chamber

Controlled environmental condition was made possible via a commercial Heraeus Vötsch VLK 04/300 environmental chamber. Temperature and relative humidity (R.H.) in the range of 10°C~90°C and 10%~95%, respectively, could theoretically be chosen. However, in order to achieve simultaneously low temperature and low humidity, it was necessary to enclose the drives in a Perspex box within the chamber (Figure 27). A compressor coupled with a dryer unit was then used to blow dry air admitted within the chamber through coiled copper tubing; the copper tubing function was to cool the dry air before admission.

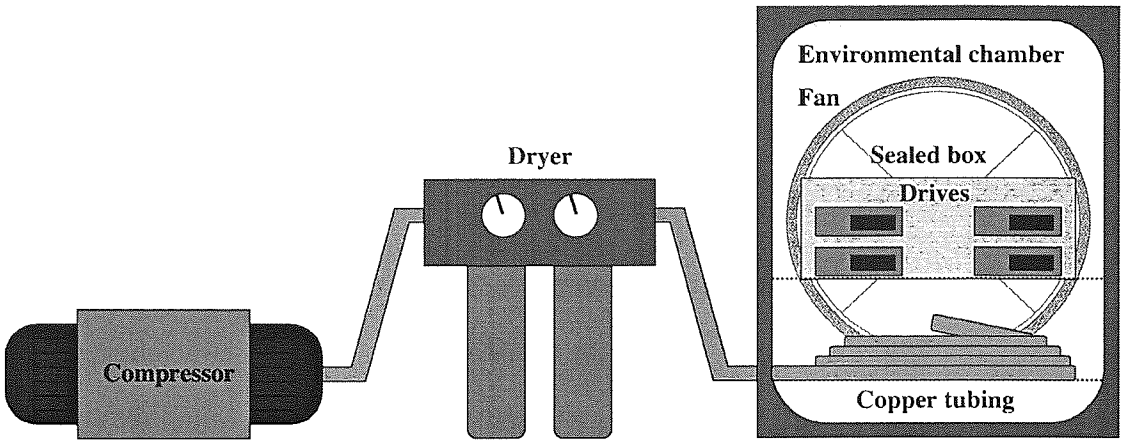

Figure 27. Environmental chamber setup for low temperature, low humidity.

An additional environmental chamber Vötsch VC 4034 was available, but only occasionally used.

2.2.3 Procedure

Up to 15 drives could be distributed between the two available climate chambers; the temperature and relative humidity (RH) experimental conditions for the experiment are summarised in Table 6. The first condition (25^0C/ 35%) is referred to as *pseudo-atmospheric* condition, whilst the remaining constitutes standard four corners of extreme climatic conditions—*hot and dry*: 40°C/10% RH; *hot and humid*: 40°C/80% RH; *cold and humid*: 10°C/80% RH; and *cold and dry*: 10°C/10% RH. The corresponding dew points are plotted in Figure 28. Dew point (DP) and vapour pressure (p_a) are usually physically more pertinent parameters; they are thus preferentially referred to as far as wear and staining are concerned. Both parameters are related *via*:

$$\begin{cases} DP = \dfrac{w \cdot 238.3}{17.294 - w} \\ w = \ln\left(\dfrac{p_a}{610.78}\right) \end{cases} \tag{36}$$

Knowing the saturation vapour pressure:

$$p_s = 610.78 \cdot \exp\left(\frac{t}{t + 238.3} \times 17.2694\right) \tag{37}$$

one can relate the vapour pressure p_a to the relative humidity $\%RH$:

$$p_a = p_s \cdot \frac{\%RH}{100} \tag{38}$$

Table 6. Choice of temperature-relative humidity combinations used for the wear tests.

Temperature	(°C)	10	40	10	25	40
Relative Humidity	(% R.H.)	10	10	80	35	80
Dew point	(°C)	-20	2.6	6.7	8.5	36
Vapour pressure	(Pa)	122	730	978	1100	5840

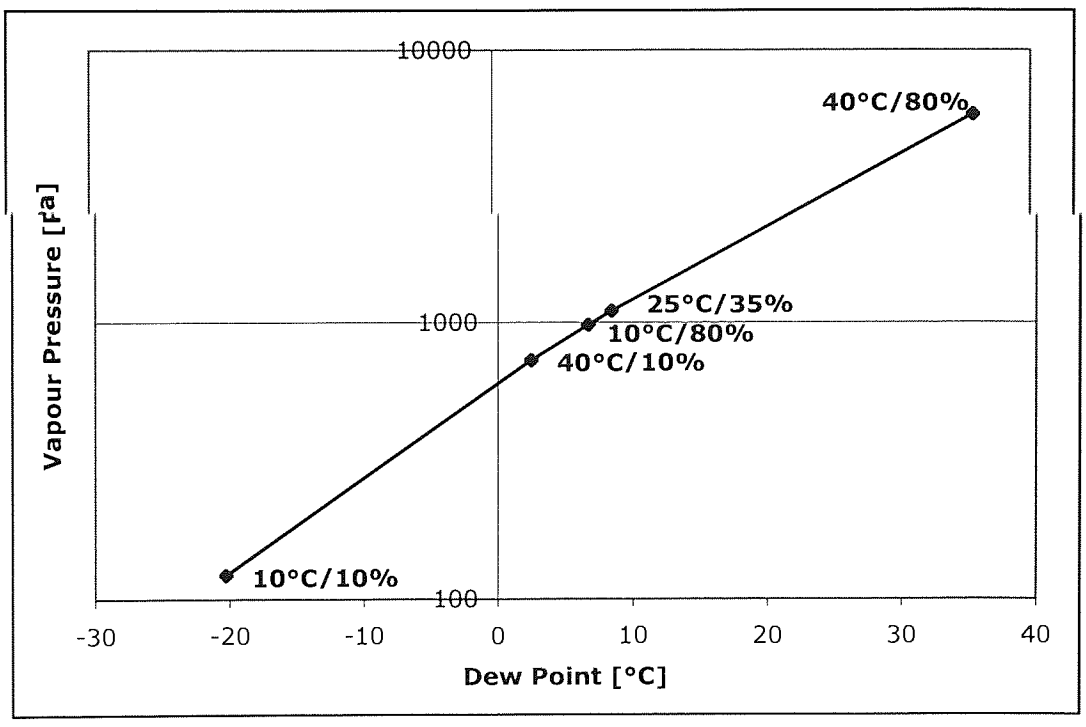

Figure 28. Dew point and vapour pressure at the five environmental conditions (couple temperature / relative humidity) considered.

The wear test consisted in sliding a Co-γFe_2O_3 tape against an ADR head, using the whole length of the tape at a constant speed of 1 m/s (44 ips) for up to 500 hours, which corresponds to 5500 passes, 2750 cycles or 1925 km. At the end of tape (EOT) the sliding direction was reversed, two successive tape reversals defining one cycle (two passes). At the end of each cycle, the head was shifted by one-track width so it could scan the whole

tape width during the test. Moreover, the head, mounted on an actuator, was oscillated at a frequency of 10 Hz and amplitude of 50 μm to simulate lateral track following in actual drives.

The most significant alterations at the head-to-tape interface were found to occur within the first few tens of hours. Therefore, for the first 100 hours, the test was interrupted every 20 hours. A further interruption occurred after 200 hours and the test ended after 500 hours.

The successive test sessions were therefore:

#	Hours	Passes	Cycles	km
1	20	220	110	77
2	40	440	220	154
3	60	660	330	231
4	80	880	440	308
5	100	1 100	550	385
6	200	2 200	1 100	770
7	500	5 500	2 750	1 925

The series of experiments generated large numbers of cycled tape and head samples allowing a detailed analysis to be performed.

The flowchart summarising the testing and analysis sequence is indicated below, Figure 29.

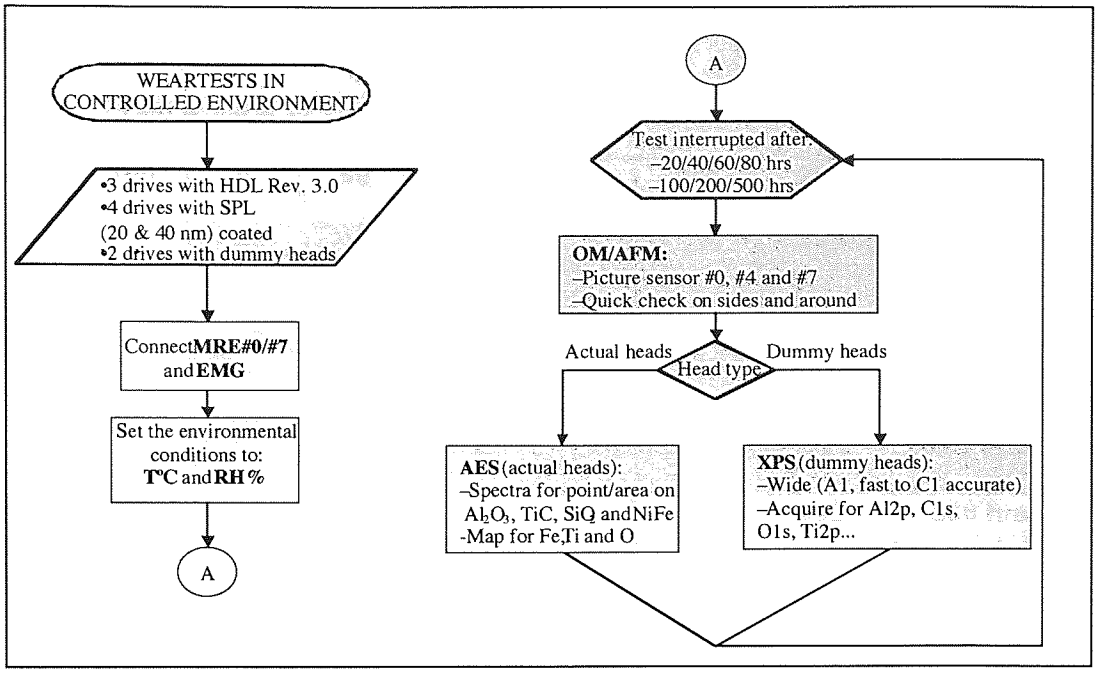

Figure 29. Flowchart outlining the test procedure for a combination of different heads.

Table 7 to Table 11 summarises the wear test procedure used in controlled environment for *standard non-coated*, *SPL coated* and *Al_2O_3-TiC dummy heads*. Typically, 3 to 4 non-coated, 4 SPL coated (2 of each thickness), and 2 Al_2O_3-TiC dummy heads were tested at a given condition, for reproducibility checks. The number of cycles run at each stage is recorded; the dash ("–") indicates whenever the test was continued without interruption. Exposure to (destructive) analytical tools such as AES or any incident that was likely to alter the sample is reported.

Table 7. Heads tested at 25°C and 35% RH.

Non coated		**20**	**40**	**60**	**80**	**100**	**200**	**500 hrs**	**Total**
323733		~110	~110	~110	~110	~110	~520/AES	foil cut	1070
322120		~110	~110	~110	~110	~110	~520	1670/AES	2740
326117		~110	~110	~110	~110	~110	~520	tape failure	1070
327620		–	–	–	–	517	~520	1670/AES	2740
SPL coated		**20**	**40**	**60**	**80**	**100**	**200**	**500 hrs**	**Total**
20 nm	310911	123	93	120	110	110	640	1670	2866
	326029	–	–	–	–	517	~520	1670	2707
40 nm	790317	109	118	100	114	110	640	1670	2861
	800424	–	–	–	–	517	–	~1220	1737
Al_2O_3-TiC Dummy		**20**	**40**	**60**	**80**	**100**	**200**	**500 hrs**	**Total**
873338(GL)		~110	~110	~110	~110	~110	~550		1100
873350(ST)		XPS					XPS		

Table 8. Heads tested at 40°C and 10% RH.

Non coated		**20**	**40**	**60**	**80**	**100**	**200**	**500 hrs**	**Total**
323330		~110	~110	~110	~110	~110	508+22	1624/ AES	2704
325322		~110	~110	~110	~110	~110	605	~1100/ AES	2255
325718		~110	~110	~110	~110	~110	605	1658	2813
327108		–	–	–	–	~550	~550	2195	3295
SPL coated		**20**	**40**	**60**	**80**	**100**	**200**	**500 hrs**	**Total**
20nm	322420	~110	~110	~110	~110	~110	605	1679/ AES	2834
	324214	–	–	–	–	~550	~550	2189	3289
40nm	796330	~110	~110	~110	~110	~110	43+534	1731	2860
Al_2O_3-TiC Dummy		**20**	**40**	**60**	**80**	**100**	**200**	**500 hrs**	**Total**
873339(GL)		~110 XPS	~110 XPS	129/XPS	121/XPS	120/XPS/AES	613/XPS		1203
873351(ST)				122/XPS	126/XPS	~110/XPS	608/XPS		1186

Table 9. Heads tested at 40°C and 80% RH.

Non coated		**20**	**40**	**60**	**80**	**100**	**200**	**500 hrs**	**Total**
326122		~110	~110	~110	118	134	528	~1650	2760
320714		–	–	–	–	~550 +100h static	527	1529	2606
326920		–	–	–	–	~550	~550	2018	3118
SPL coated		**20**	**40**	**60**	**80**	**100**	**200**	**500 hrs**	**Total**
20nm	327124	–	–	–	–	~550 +100h static	528	1538	2616
40nm	326115	–	–	–	–	~550 +100h static	Head damaged Massive pullout		550
	326130	~110	–	–	–	538	631	986	2265
Al_2O_3-TiC Dummy		**20**	**40**	**60**	**80**	**100**	**200**	**500 hrs**	**Total**
3818/3816(ST)		~110	~110	–	–	–	~1100	~1650	220/2750
3826/3822(GL)		~110	~110	–	–	–	1132	~1650	220/2782

Table 10. Heads tested at 10°C and 80% RH.

Non coated		**20**	**40**	**60**	**80**	**100**	**200**	**500 hrs**	**Total**
325919		~110	103	103	105	102	–	2255	2778
326119		–	–	–	380	–	749	1632	2761
326816		–	–	–	290	–	735		1025
SPL coated		**20**	**40**	**60**	**80**	**100**	**200**	**500 hrs**	**Total**
20nm	327621	–	–	–	380	–	739	1637	2756
	324034	–	–	–	380	–	731	1604	2715
40nm	321330	–	–	–	380	–	736	1632	2748
	322407	–	–	–	380	–	744	1646	2770
Al_2O_3-TiC Dummy		**20**	**40**	**60**	**80**	**100**	**200**	**500 hrs**	**Total**
3815/3820(ST)		~110	~110	–	–	344	1138	1723	220/2861
3824/3832(GL)		~110	~110	–	–	~330	1138	1706	220/2844

Table 11. Heads tested at 10°C and 10% RH.

Non coated		20	40	60	80	100	200	500 hrs	Total
327029		128	119	130	118	126	511	1665	2797
324335		–	–	–	–	–	1013	1681	2694
325524		–	–	–	–	569	619	1658	2846
SPL coated		**20**	**40**	**60**	**80**	**100**	**200**	**500 hrs**	**Total**
20nm/40nm	326128	–	–	–	–	574	586	1655	2815
	325017	–	–	–	–	581	513	1677	2771
	327017	–	–	–	–	583	602	1675	2860
Al_2O_3-TiC Dummy		**20**	**40**	**60**	**80**	**100**	**200**	**500 hrs**	**Total**
3819/3813		~110	~110	–	–	~550	~880		1100/550
3827/3827		~110	~110	–	–	~330	~1100		1100/550

2.3 Characterisation techniques

2.3.1 Atomic force microscopy

In this project, atomic force microscopy (AFM) was mainly used to map the head or tape topography, hence to directly assess the incidence of wear and staining on the head-to-tape interface spacing. Features such as *scratches*, *pole-tip recession* and *transfer film* over the head; *roughness*, *voids* and *asperities* over the tape were directly observable and measurable by means of AFM.

AFM uses a *force sensor* consisting of a *tip* mounted on a *cantilever* (Figure 30, left). A laser beam reflected by the cantilever hits a four-section photo-detector monitoring any vertical or lateral deflection. The deflection of the sensor is proportional to the force exerted by the surface according to *Hooke's law:* $F = -kx$. A feedback electronic (Figure 30, right) is combined with a probe/sensor and piezoelectric ceramics (Z PIEZO) to create the

positioning mechanism, maintaining the sensor at a constant distance from the surface. Two ceramics (X PIEZO and Y PIEZO) are added to scan the sensor in the X-Y plane.

Amongst the various imaging modes available [52], *contact* and *non-contact* modes were used here. In contact mode, the force exerted by the sample surface on the tip is repulsive. The movement of a soft cantilever in response to changes in the surface topography is detected by measuring the difference between the output on the upper and lower halves of the photodetector. Topographic data are thereby provided.

The torsion of the cantilever results in the lateral deflection of the laser beam. A measure of the friction force exerted by the scanned surface on the tip can therefore be derived from the difference between the output on the left and right halves of the photodetector. This characteristic is used in lateral force microscopy (LFM) to generate a friction coefficient map at the sample surface. Considering the typically very low value of the friction coefficient, the map usually shows very low contrast.

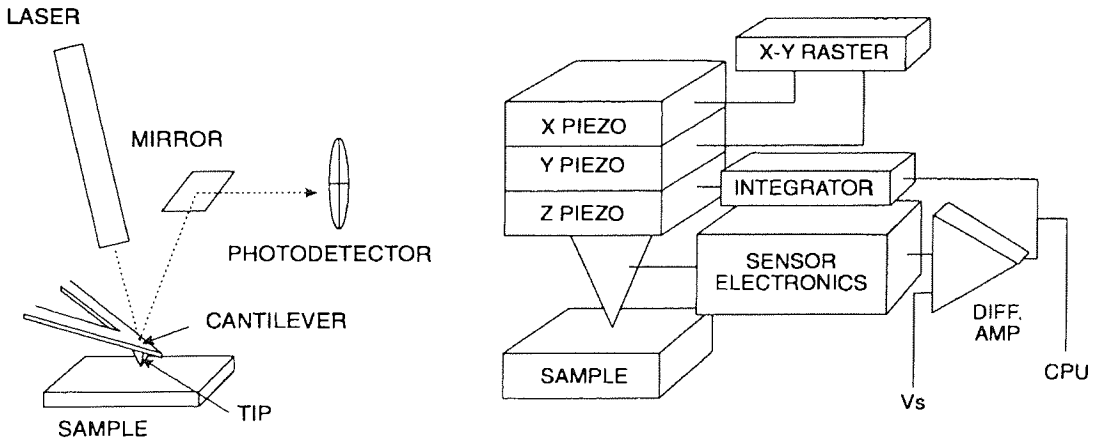

Figure 30. Force sensor (left); AFM system (right).

Non-contact mode can be advantageous for scanning soft or adhesive elements such as friction polymers transferred to the head surface. A stiff cantilever is oscillated above the sample surface at its resonant frequency. As the probe gets closer to the sample surface, the force gradients will change due to the attractive force between the tip and the sample thus changes in oscillation amplitude and phase can be detected and used in the feedback-control loop.

The topography of the head and tape surfaces were probed by means of a Topometrix™ Explorer SPM fitted with SPMLab V 3.06.06 software. For high resolution AFM scans a

ThermoMicroscopes™ Autoprobe M5 fitted with ThermoMicroscopes™ ProScan Software Version 2.1 was used. The sample analysed was fixed by means of a double-sided tape to a flat magnetized sample holder.

For head samples, image enhancement was restricted to the use of shading and/or first order levelling algorithms in order to resolve fine details at the head surface otherwise overwhelmed by its curvature. To account for the resulting distortion, and allow accurate quantitative interpretation, the central part of the scanned sensors were exported as a raw data file to a spreadsheet program and averaged to plot a mean cross-section across the sensor length.

Based on statistical analysis of magnetic tape surface measured by AFM, the tape roughness was shown to follow fractal geometry (for nearly five decades of length scales) and was expected to be resolution-dependant [192]. Therefore for tape samples, scan areas: 10 μm x 10 μm and 50 μm x 50 μm were selected, corresponding to resolutions of 20 nm and 100 nm respectively.

2.3.2 Surface chemical analysis

Surface chemical analysis was essential in this project to assess physical as well as chemical changes occurring at the head-to-tape interface. X-ray photoelectron spectroscopy (XPS) generally required wide homogeneous surfaces such as tapes or dummy heads. However, owing to its optimal energy resolution, XPS allowed identification of chemical state (*e.g.* oxidation, degradation, etc.) or environment occurring for elements present at the analysed surface.

Auger electron spectroscopy (AES) having its spatial resolution only limited by the electron beam spot size (~ 0.1 μm) was suitable for assessing the location, displacement, transfer, etc. of any element present at the sample surface. It was thus possible to trace any worn or transferred material, whilst identifying which specific areas they would target.

The basic concept of surface analysis consists in transferring energy to the surface region of interest by means of an incident beam of electrons, photons or ions, raise the atoms present in this region to excited states and collect the product of their relaxation either as electrons, photons, charged ions or neutral atoms of lower energy than of the incident beam. The surface sensitivity relies on the short inelastic mean free paths of the emitted

particles (a few atomic layers). The attenuation length including both the inelastic and elastic mean free paths being more easily measured, it is preferentially referred to [193]. A technique with good lateral resolution and providing information on the atomic composition, chemical state and structure is desirable [194].

2.3.2.1 *X-ray photoelectron spectroscopy*

XPS relies on the photoelectric effect: an X-ray photon (emitted from a Cu anode coated with Al or Mg, with characteristic energies of 1253.4 eV or 1485.6 eV respectively) ionises the target atom, which relaxes by emitting a photoelectron. The spectrum of the emitted photoelectrons conforms to the discrete binding energies of the electrons present in the target atoms providing a characteristic fingerprint.

The energy scale may refer to the binding energy (BE) of the level of origin or to the kinetic energy (KE) of the photoelectrons collected by the analyser. Kinetic and binding energies are related as follows [195, 194]:

$$\mathrm{KE} = h\nu - \phi - \mathrm{BE}. \tag{39}$$

$h\nu$ and ϕ are the incident X-ray photon energy and the work function, respectively.

The spectrum features series of peaks superimposed upon a background increasing in steps after each significant peak. An elastic photoemission process generates the significant peaks, which precise position is function, beside the intrinsic properties of the emitting element, of its environment and chemical state. The peak intensity depends on the atomic photoemission cross-section, as well as on the transmission characteristics of the analyser, itself function of the electron energy. The peak width, or full width at half-maximum (FWHM) ΔE, is the convolution of several contributions:

$$\Delta E = \sqrt{\left(\Delta E_n^2 + \Delta E_p^2 + \Delta E_a^2\right)}, \tag{40}$$

where ΔE_n, ΔE_p and ΔE_a state for the natural width related to the lifetime of the excited state, the photon source width and the analyser resolution, respectively.

The peaks are of three basic types: peaks due to photoemission from *core* levels (at high BEs) and *valence* levels (at low BEs) and peaks due to X-ray excited *Auger* photoemission. The photoemission cross section—therefore the peak intensity—is much smaller for valence than for core levels.

The dominant decay mechanism for core hole states created following photoemission results in electron emission, either from a Coster-Kronig transition, not normally detected, or an Auger transition, eventually giving rise to dominant peaks in the spectrum. Changing the X-ray source from Mg K_α to Al K_α will increase the photoelectron KE by 233 eV, leaving the Auger peaks unchanged (the converse is true for BE).

The step-like background is raised by an *inelastic* photoemission process: a portion of the photoelectrons contributing to the significant peaks are scattered and loose energy before they eventually leave the surface and make their way to the analyser.

XPS is a very powerful technique to analyse homogeneous surfaces, composed with elements in different chemical states and/or environments. By changing the angle of emission (the angle between the surface normal and the analyser axis), one can probe the sample subsurface at different depths. This technique is referred as angle-resolved XPS (ARXPS).

Due to its poor lateral resolution (except on modern instruments with resolutions up to 10 μm), XPS is not recommended for heterogeneous surfaces; other techniques such as AES are more adequate.

2.3.2.2 *Auger electron spectroscopy principle*

AES involves a more complex emission process than XPS (Figure 31). The target atom is ionised as an incident X-ray photon or electron dislodge a core electron. A second electron falling down from an upper level fills the hole left by the core (first) electron. The transition of the second electron releases an excess energy either in form of an X-ray photon (fluorescence) or as kinetic energy taken up by a third electron, which is ejected from the atom (Auger emission). The emitted Auger (third) electron is named by using three letters borrowed from the X-ray nomenclature. Each successive letter corresponds respectively to the first, second and third electron's level involved in the emission process (*e.g.* Figure 31 schematise the transition $KL_1L_{2,3}$). The resultant kinetic energy follows the relation:

$$E_{k\text{-ABC}} = E_A - E_B - E_C^* . \qquad (41)$$

where the three letters ABC describe the Auger transition; E_A, E_B and E_C^* are the energies of the first (A), second (B) and third (C) electron's level, respectively, the star reminding the ionised state of the emitting atom.

Figure 31. Diagram of the process of Auger emission ($KL_1L_{2,3}$) in a solid [196].

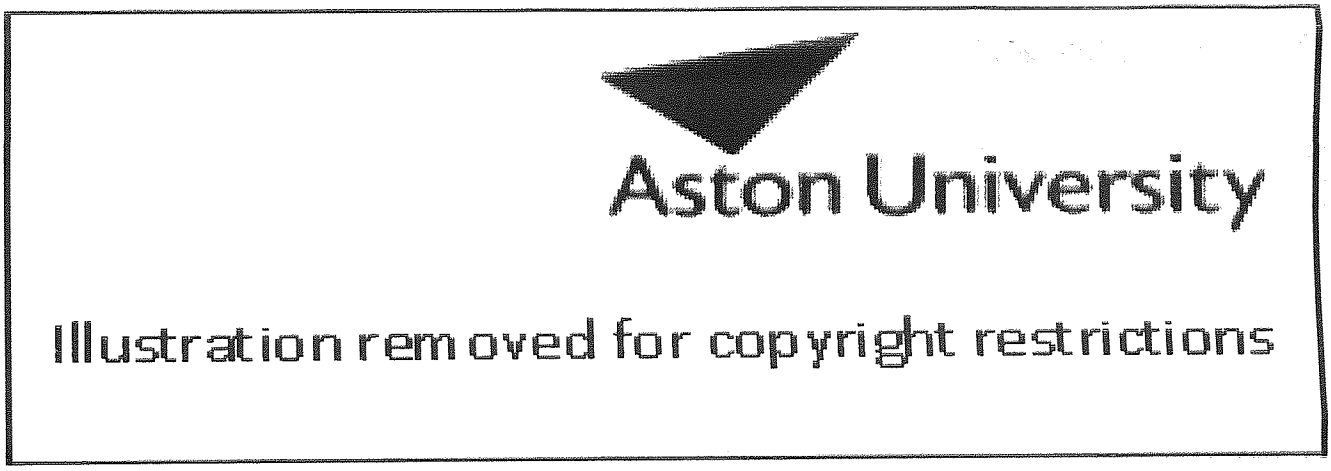

Figure 32. Various contributions to the peak and background intensities in AES [194].

Using equation (41) to calculate the energy and identify the corresponding transition on an Auger spectrum is complicated by the ionised (starred) energy term. The characteristic peaks discerned on the Auger spectrum are in fact routinely identified by means of standard databases.

A background is risen by backscattered (i) primary electrons, (ii) secondary electron and (iii) Auger electron (Figure 32). A Shirley background subtraction is generally used: Each electron is assumed to act as a source for scattered electrons at lower energy, hence the background at any energy is proportional to the total number of electrons collected at higher energy [197].

The beam (with a spot size of ~ 100 nm—5 to 10 nm with modern instruments) can then be either positioned on a particular point of the sample, or raster-scanned over a selected area. Secondary electrons are collected by means of a scintillator coupled with a photo multiplier to provide a scanning electron microscopy (SEM) image.

2.3.2.3 Sputter-depth profiling

Contamination of the surface by adsorbed components such as atmospheric hydrocarbons, water vapour, oxide layers or fingerprints... can be an obstacle when using surface-analysis techniques, only sensitive to a few atomic layers.

Ion sputtering may be used to remove surface layers with controlled thickness, allowing removal of adsorbed contaminant species and, by increasing the sputtering time, to obtain a depth-profile of the analysed surface. The depth resolution of this technique is a convolution of the sampling depth of the analysing technique (XPS and AES ~ 10 nm) and the extent to which the surface is disturbed (*via* collisional mixing, enhanced diffusion and segregation) by ion bombardment.

Sputtering ion beam (typically argon, 0.5 to 5 keV in energy) may be directed on to a limited surface area, which makes high resolution AES the most suitable technique to analyse the uncovered surface.

Time is the only scale directly accessible to the operator. Conversion to a depth scale requires knowledge of the sputter rate. However, the sputter rate may vary unpredictably, depending on numerous factors such as the target atom and projectile ion types, the energy and angle of incidence, the surface topography and crystallinity, the quality of the UHV, sample contamination... The best estimation may therefore be empirical, relying on compilation of experimental data or alternative experimental techniques such as surface profiling or optical interferometer to measure the depth of the crater formed after sputtering. TRIM or SUSPRE give a reasonable estimate of sputter rate.

2.3.2.4 *Electron analyser*

Photoelectrons (in XPS) or Auger electrons (in AES) emitted from the surface were collected and their energy measured in a concentric hemispherical analyser (CHA).

In CHA, an electrostatic field generated by two concentric hemispheres of radii r_1 and r_2 ($> r_1$) deflects the electrons entering the analyser at the input slit. Only the electrons travelling at the pass energy $E = e.V(r_0)$ will follow the mean radius r_0 ($= (r_1+r_2) / 2$) and exit the analyser by the output slit. $V(r_0)$ can be deduced from:

$$V(r_1) - V(r_2) = V(r_0)\left[\frac{r_2}{r_1} - \frac{r_1}{r_2}\right]. \qquad (42)$$

The energy resolution is expressed as:

$$\frac{\Delta E}{E} = \frac{w_1 - w_2}{4r_0} + \alpha^2, \qquad (43)$$

where w_1, w_2 and α are the input and output slits and the maximum angle of the entering electrons to the tangential direction.

An electron input lens is generally added between the sample and the CHA input (*c.f.* Figure 33), which allows to increase the space surrounding the sample for easier manipulation, whilst optimising the analysed area. Furthermore, the lens can be used as a retardation element, changing the electron kinetic energy as they enter the analyser. The analysers can thus be operated either at constant *absolute* (ΔE) or *relative* ($\Delta E/E$) energy resolution.

Figure 33. Cross-section of a CHA with standard input lens systems [198].

In XPS, spectral features closely spaced are to be resolved, to provide information on the chemical state of the analysed elements and this regardless of the energy implied. The analyser must therefore be used in constant *absolute* energy resolution and only limited by the natural width of the unmonochromatised X-ray source (0.70 eV and 0.85 eV for Mg Kαand Al Kα, respectively [198]) and the instrumental broadening. This requires an analyser absolute resolution of the order of 0.5 eV from 0 to 1500 eV. Since a relative energy resolution of 0.5 eV/1500 eV ~ 3×10^{-4} is difficult to achieve, photoelectrons are usually retarded to a constant or *pass* energy set between 5 and 200 eV, as they enter the analyser.

Electron retardation used for XPS causes the analysed surface area to vary with the kinetic energy, to the detriment of spatial resolution and is therefore not suitable for AES. Nevertheless, as due to the inherent Auger peak width and the deliberate degradation in energy resolution to maintain an acceptable signal-to-noise ratio and high-energy sensitivity, AES is usually operated at constant *relative* energy resolution (typically 2.5 x 10^{-3}).

2.3.2.5 *Experimental procedure*

Both XPS and AES were integrated in a Fisons Instrument VG ESCALAB 200-D multi-technique spectrometer operating at a base pressure lower than 1 x 10^{-9} mbar (ultra-high

vacuum (UHV)). The instrument was controlled *via* a personal computer running a VG ECLIPSE dedicated software package.

For XPS acquisition, Mg K_α X-radiation was used at a source excitation energy of 15 keV and emission current of 20 mA. A survey acquisition at 0° take-off angle (analyser normal to surface) was first conducted to identify the elements present in the near surface region. Next, acquisitions restricted to narrower binding energy regions corresponding to the identified elements could be conducted at five different take-off angles: 0°, 33°, 45°, 54° and 60° as suggested by Cumpson [199] for ARXPS. The CHA was operated with pass energy of 50 eV and 20 eV, for survey scans and single peak scans, respectively. Multiple scan allowed to increase the signal to noise ratio. The VG Eclipse instrumental data system uses Schofield cross-section to calculate the relative atomic concentrations from the X-ray photoelectron spectral peak intensities. The Cl peak was found to vanish with exposure to the X-ray beam, hence the Cl region spectra was always collected first.

Several apertures could be selected in XPS to admit electron into the analyser, amongst which the following were used here:

A1	B3	C1
2 mm × 3 mm large area	∅ 300 µm small area	∅ 150 µm small area

The tape-bearing surface has a width of 300-µm, therefore B3 and C1 are more suited to analyse dummy heads, avoiding collecting information from regions not directly affected by the sliding process. Nevertheless, widening the area is useful to collect information from the area surrounding the tape-bearing surface where tape debris is likely to accumulate. Moreover, widening the aperture increases the signal to noise ratio.

Chemical state of elements present over the sample were determined from the measured binding energies and comparing the experimental values of the chemical shift with standard databases [200, 201 and 202]. Correction was made for peak shifting due to build up of charge on the sample as a result of photoionisation; the C1s peak—BE: 284.6 eV—was usually used as a reference peak [200].

Once the peak had been identified, and the background subtracted, the peak area was calculated by integration, and normalised, dividing by the spectrometer *transmission function* (energy dependent) and the *sensitivity factor* [203] (varying according to the element and the Auger transition considered). The atomic percentage of a given element was fi-

nally computed as the ratio of the normalised area to the sum of all elements' normalised areas.

A peak fitting procedure was integrated to the VG ECLIPSE software package. The fitting method [204] used, iteratively minimizes the χ^2 calculated between the data points and the theoretical curve, the latter assumed to be a 30/70% mix of Gaussian/Lorentzian curves.

An electron gun fitted with a LaB_6 filament was used as the electron source for AES. The acceleration voltage could be set to up to 10 kV and the beam focused to a minimum spot size of the order of one tenth of a micron.

Scanning AES allowed mapping on a selected surface area the occurrence of a given element. After the selected area had been delimited *via* SEM imaging, a survey Auger spectrum was acquired, on which a well-defined peak was chosen for the element of interest. The electron beam was then raster-scanned over an array of points partitioning the selected area, measuring the Auger intensity simultaneously at the peak energy (P) and at the adjacent background (B). The result intensity (R) would be computed as the difference between the two energies divided by the background energy, *i.e.*

$$R = (P-B) / B. \qquad (44)$$

A compromise had to be found between on the one hand increasing the resolution (size of the partitioning array) and the dwell time of the scanning, and on the other hand decreasing the total experiment time, as a carbon contamination layer builds up during the sample exposition to the electron beam.

Two undesirable effects, namely charging and carbon contamination complicated AES. Charging is caused by the accumulation of electrons brought by the incident electron beam in insulating parts of the head. This charging results in a beam bending, which reflects on the collected spectra or element map, as energy shift, peak broadening and distortion; large charging could lead to a general instability, hence to spectral noise, or even make impossible to obtain any spectra at all. To avoid charging, the secondary electron emission and the primary beam had to be equalised. The acceleration voltage of the electron source was usually decreased under 4 kV, whilst the sample holder was tilted in such a way that the beam hit the sample surface at a grazing angle. This procedure had the side effect of lowering the signal.

During the exposition to the electron beam, a carbon contamination layer settled over the sample surface hindering the signal emitted from the overlaid species. To alleviate this phenomenon, ion etching was routinely performed with the risk of removing superficial species such as deposits and stains.

2.3.3 Optical microscopy

A Leitz (at OnStream MST, NL) and Olympus (Aston, UK) optical microscope were used to examine the head tape-bearing surface. By means of a digital camera (Leitz OM) or emulsion film camera (Olympus OM) fitted to the microscopes, images could be acquired numerically (Leitz OM) or developed and scanned *via* a film scanner (Olympus OM) and stored in a computer.

Sensors 0, 4 and 7, as well as features all over the tape-bearing surface susceptible to evolve throughout the test (*e.g.* defects, stains) were systematically inspected after 100 hrs, 200 hrs and 500 hrs of wear test; in the course of the project, the head-to-tape interface was found to undergo fast alteration, hence the first stage (0 to 100 hours) was further divided into 5 stages of 20 hours.

2.3.4 Optical phase shift interferometer

A 2D profile of some heads across the pole tip region was acquired by means of a WYKO TOPO 2D optical phase shift interferometer (OnStream MST, NL). The height was deduced from the phase difference of a travelling wave after impingement with the measured surface. A phase shift resulted from the difference in index between two distinct materials, which is interpreted as the equivalent difference in height [205]:

$$\Delta h = \frac{\lambda}{4\pi}\Delta\Phi = \frac{\lambda}{4\pi}\left[\arctan\left(\frac{2k_1}{1-k_1^2-n_1^2}\right) - \arctan\left(\frac{2k_2}{1-k_2^2-n_2^2}\right)\right] \qquad (45)$$

$\nu_i = n_i - i.k_i$ represents the complex index associated with a material i (= 1, 2) and λ, the light wavelength (*c.f.* Table 12).

Table 12. Complex index (n - i.k) for the different materials used in the head construction.

λ [nm]	n (NiFe)	k (NiFe)	n (SiO_2)	k (SiO_2)	n (Al_2O_3)	k (Al_2O_3)	n (AlTiC)	k (AlTiC)
400	1.45	2.5	1.55	0	1.63	0	2.23	0.55
450	1.59	2.78	1.54	0	1.63	0	2.25	0.50
500	1.73	3.05	1.54	0	1.63	0	2.26	0.46
550	1.87	3.33	1.53	0	1.63	0	2.24	0.43
600	1.96	3.52	1.53	0	1.63	0	2.22	0.42
633	2.01	3.62	1.53	0	1.63	0	2.19	0.42
650	2.03	3.67	1.53	0	1.63	0	2.18	0.43
700	2.09	3.79	1.53	0	1.63	0	2.15	0.45
750	2.13	3.89	1.53	0	1.63	0	2.13	0.49
800	2.16	3.96	1.53	0	1.63	0	2.12	0.54

2.3.5 Temperature measurement

2.3.5.1 Calibration

The temperature at the head-to-tape interface was deduced from the resistance measured across the MRE sensors poles and the electrical machining guide (EMG). The EMG is a NiFe magneto-resistive element flushed with the tape-bearing surface to control the lapping depth: as the tape-bearing surface level decreases, the EMG height *d* (*c.f.* Figure 34), hence the resistance increases up to a calibrated value at which the lapping is interrupted. The EMG being flush with the tape-bearing surface, it provided the closest measurement to the head-to-tape interface. MRE and EMG, both magneto-resistive strips are schematised in Figure 34.

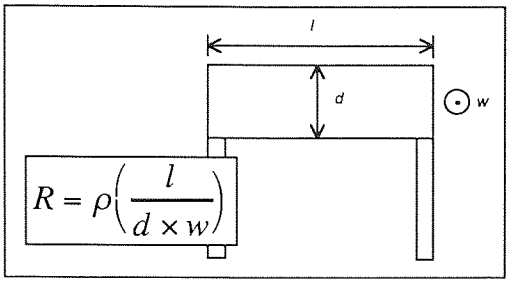

Figure 34. Magneto-resistive strip.

The changes in resistance are related to the changes in temperature *via*:

$$dT = \frac{dR}{\alpha R_0}, \tag{46}$$

where R_o is the initial resistance (including the connection to the resistive element) and α is the related temperature coefficient.

Integrating (46) over the range $\Delta R = R - R_0$ gives as a temperature change ΔT:

$$\Delta T = \frac{1}{\alpha} \ln\left(\frac{R}{R_0}\right). \tag{47}$$

(47) is usually approximated by [206,207,208 and 209]:

$$\Delta T = \frac{\Delta R}{\alpha R_0}, \tag{48}$$

α was determined as follows. The resistances of the MR sensor #7 (MRE7) and the two EMG (1 and 2) placed at the two ends of the sensor bearing chip, were measured for three different heads enclosed in a stove, which temperature varied from 10 to 80°C (Table 13). The slope of ΔR vs. ΔT divided by the resistance at 10°C gave $\alpha = (2.505 \pm 0.081) \times 10^{-3}$ 1/K. α has been measured elsewhere for Travan TR3/TR4 heads [206] as 2.7×10^{-3} 1/K and disk drive SAL-based MR heads as 2.39×10^{-3} 1/K [209].

Table 13. Resistance vs. temperature of MR sensor #7 and the two EMGs for three different heads.

T (°C)		10	20	30	40	50	60	70	80	α (10^{-3} K)
	HD1	64.4	65.9	67.4	69	70.6	72.2	73.9	75.6	2.508
MRE7 (Ω)	**HD2**	67.6	69.2	70.8	72.4	74.1	75.8	77.4	79.1	2.456
	HD3	68.3	69.8	71.4	73.2	74.8	76.4	78.2	80	2.471
<MRE7>		66.8	68.3	69.9	71.5	73.2	74.8	76.5	78.2	2.478
	HD1	560	571	588	603	617	632	647	663	2.654
EMG1 (Ω)	**HD2**	622	636	651	665	680	694	709	725	2.356
	HD3	584	598	612	626	641	656	671	686	2.502
	HD1	584	598	612	627	642	658	673	689	2.577
EMG2 (Ω)	**HD2**	536	549	562	575	589	603	616	630	2.513
	HD3	626	641	656	672	687	703	719	736	2.505
<EMG>		585	599	614	628	643	658	673	688	2.518

The temperature at the MRE and EMG is estimated from the measured resistances R using the relation:

$$T_R = T_{R_0} + \frac{R - R_0}{\alpha R_0} \tag{49}$$

where R_0 is a reference (initial) resistance, measured at the temperature T_{R0} and α is a constant previously determined as $\alpha = (2.505 \pm 0.081) \times 10^{-3}$ K^{-1} for any MREs and EMGs in ADR heads.

The EMG being flush with the insulator surface is likely to be worn off, causing d to decrease, hence R to increase. Using equation (49) to estimate the EMG temperature may thus lead to interpret the resistance increase as a rise in temperature. Inversely, transfer of conductive stains may decrease the EMG leading to underestimate the temperature rise. The reference resistance, R_0 should therefore be measured at each stage along the test.

2.3.5.2 *Transient regime*

Measurement of the temperature at the head-to-tape interface within the drives was conducted at ambient temperature and humidity (ranging typically from 20 to 30°C and 30 to 60% respectively). A thermo-probe fitted with 10 thermo-couples allowed to measure the temperature at 8 locations within the drive. The locations chosen are listed below.

Thermo-couple	**Head**	**Below HD**	**Above HD**	**Drive motor**	**God screw**	**QIC HD**	**QIC out**	**Air**
Location	Head's cover bar, right below	Deck, below the head	PCB metal pole right above the head	Driving motor, against the drum	PCB screw at ground	Cartridge base plate, near the head	Cartridge base plate, opposite to the head	Ambient tempera-true away from the drive

The resistances at the MRE and EMG were measured at the connection between the head foil and the PCB. An ohmmeter fitted within a Fluke™ multi-meter was used, in all cases for the EMG, only whenever the foil was disconnected from the PCB (no sense current) for the MRE. Whenever the foil was connected to the PCB (sense current), the voltage was measured *via* the Fluke™ meter at the MRE connections, and divided by the sense current (measured as I_S = 11.2 mA), to bear the MRE resistance. Since no significant difference was found between the resistance at sensors #0, #4 or #7, only the sensor #7 resistance was measured throughout the experiment.

The temperature was monitored whilst the drives went through the following sequence:

Phase I: the drive is connected to the power supply with no cartridge inserted.

Phase II: a cartridge is inserted; the tape is

put into contact with the head and

slid at a speed of 1.1 m/s.

Phase III: the cartridge is ejected; the drive remains powered.

Each phase lasts one-hour (3600 s), long enough for the system to reach a steady state. The temperature increase during the first two phases was fitted to the following equation

$$T = (T_S - T_0)\cdot\left(1 - e^{-t/\tau}\right) + T_0. \qquad (50)$$

T_0 and T_S stand for the initial and steady state temperature, respectively. τ is a time constant; the τ corresponding to the best fit is indicated in the chart legends.

2.3.5.3 Steady state regime

Temperature was monitored on a continuously running drive, fitted with a new head and loaded with a virgin tape, up to 115 hours. A first experiment was run in ambient temperature and relative humidity ranging from 17 to 26°C and ~ 30 to 60% RH, respectively (referred as non-controlled environment or NCE). In a second experiment, the drives were placed inside a climate chamber where the temperature and RH were set to 20°C and 30% for 65 hours then 35°C and 30% for 23 extra hours (referred as controlled environment or CE). A current (0.1 mA for NCE and 0.7685 mA for CE) was run across the EMGs whilst a sensor current (I_S = 11.2 mA) was run across the MRE. The resulting voltages (proportional to the sensor resistance) along with the temperature below the drive and the atmospheric temperature were recorded every hour using an automatic multi-channel voltmeter: Philips Multipoint Data Recorder PM8238 fitted with a set of thermocouples.

3 Chapter III—Results

Results of the prototype ADR heads described in the previous chapter, with particular attention to the wear behaviour and staining characteristics and their influence on the spacing at the head-to-tape interface are hereafter presented. The standard heads were analysed first: a preliminary characterisation of the head wear behaviour, head staining, and tape wear behaviour is here presented. A discussion on the head-to-tape interface dynamics and thermodynamics follows. Finally, a systematic testing in controlled environment is reported.

DLC and SPL coated head were analysed with respect to their wear resistance. The chapter concludes with a study of ceramic dummy heads: characterisation of the currently used tape bearing ceramic, Al_2O_3-TiC and two alternative single-phase ceramics, namely TiO_x and Al_2O_3 are further reported.

3.1 Standard heads

3.1.1 Head wear—preliminary results

Worn ADR heads formerly tested in non-controlled environment (25±5°C / 60±30%RH) at OnStream MST, Eindhoven, The Netherlands, were provided at the beginning of this project and allowed a preliminary characterisation of the head wear behaviour.

3.1.1.1 AFM analysis of ADR standard heads

An AFM scan of a virgin head (Figure 35) shows the insulator and ceramic surface (the latter referred as tape-bearing surface) at the same level and the pole surface in slight recession (~ 10 nm—Table 14). Scratches (a few hundred nm wide by up to 10 nm deep on the poles) covering the whole surface were attributed to the lapping process applied to the tape-bearing surface, perpendicular to the head width. The eight channels aligned along the head showed similar features.

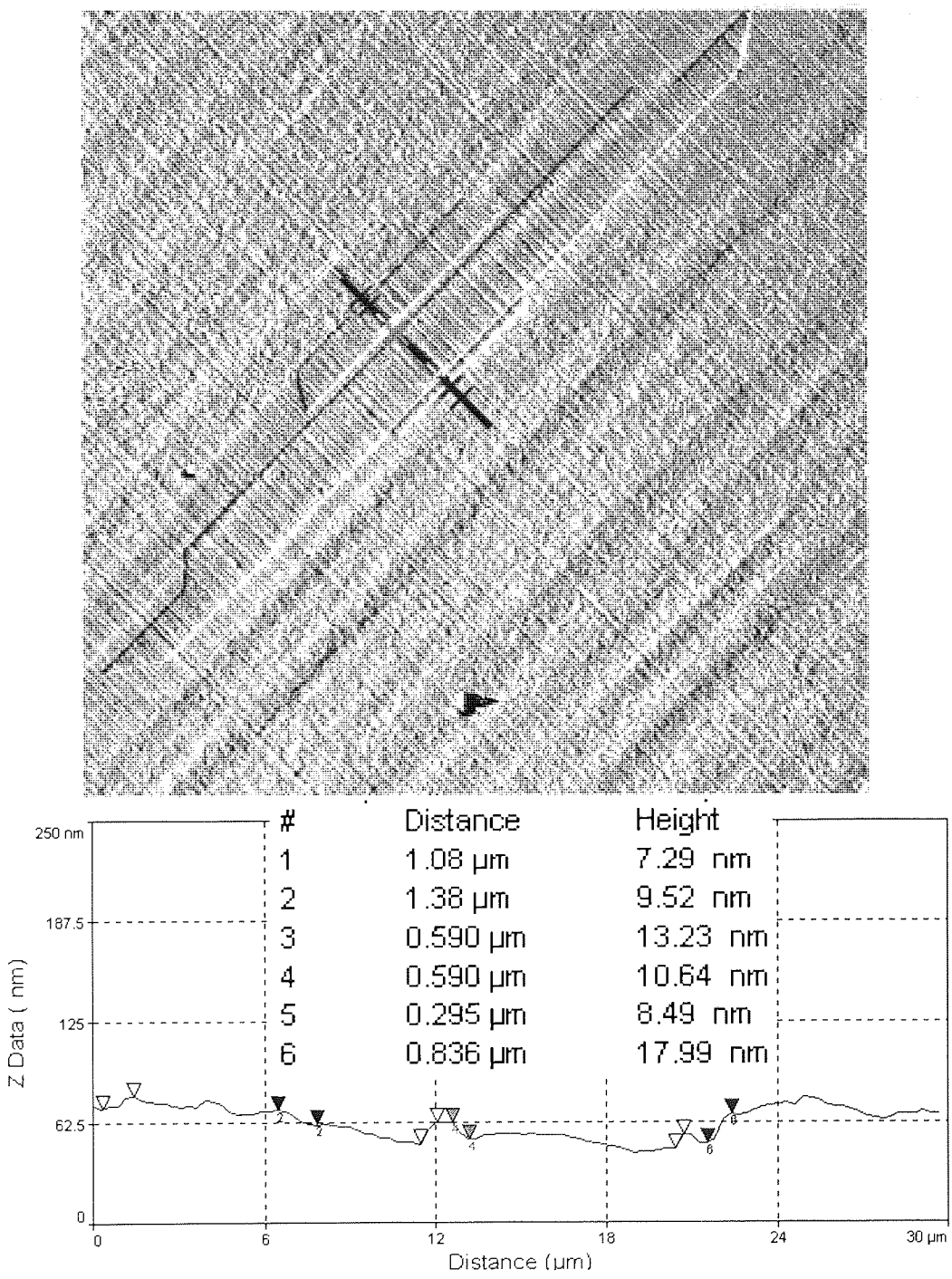

Figure 35. Levelled AFM map of a virgin head (channel #0): pole tip recession is of the order of 10 nm; scratches are few hundred nm wide by up to 10 nm deep.

Table 14. Roughness and recession (relative to the tape-bearing surface) measured by AFM for virgin and worn heads.

Area	RMS (nm)		Recession (nm)	
	Virgin head	Worn head	Virgin head	Worn head
Ceramic (base)	2.5	21.0	0	-
Top	-	5.1	-	0
Bottom	-	8.1	-	40 ± 20
Write pole	3.3	8.2	10	45 ± 10
Shared pole	3.5	7.1	10	45 ± 10
Insulator	5.3	7.2	0	30 ± 5
Ceramic (cover bar)	2.7	16.8	0	-
Top	-	3.6	-	0
Bottom	-	6.6	-	40 ± 20

Table 15. Knoop hardness (H_K in GPa) of the different head materials and tape magnetic particles.

Poles	Insulator	Ceramic		Tape coating
Permalloy:	Silica:	Alumina:	Titanium carbide:	Ferrite:
$Ni_{80}Fe_{20}$	SiO_2	Al_2O_3	TiC	Co-γFe_2O_3
1.18 GPa	5.4 ~ 7.4 GPa	20.6 GPa	27.5 GPa	11.8 GPa

The Permalloy pole material has Knoop hardness (Table 15) about one order of magnitude lower than the insulator and the ceramic. Such a difference might account for both the recession and the deeper scratches found on the pole surface (Figure 35). Root mean square (RMS) surface roughness is given for the different head components in Table 14.

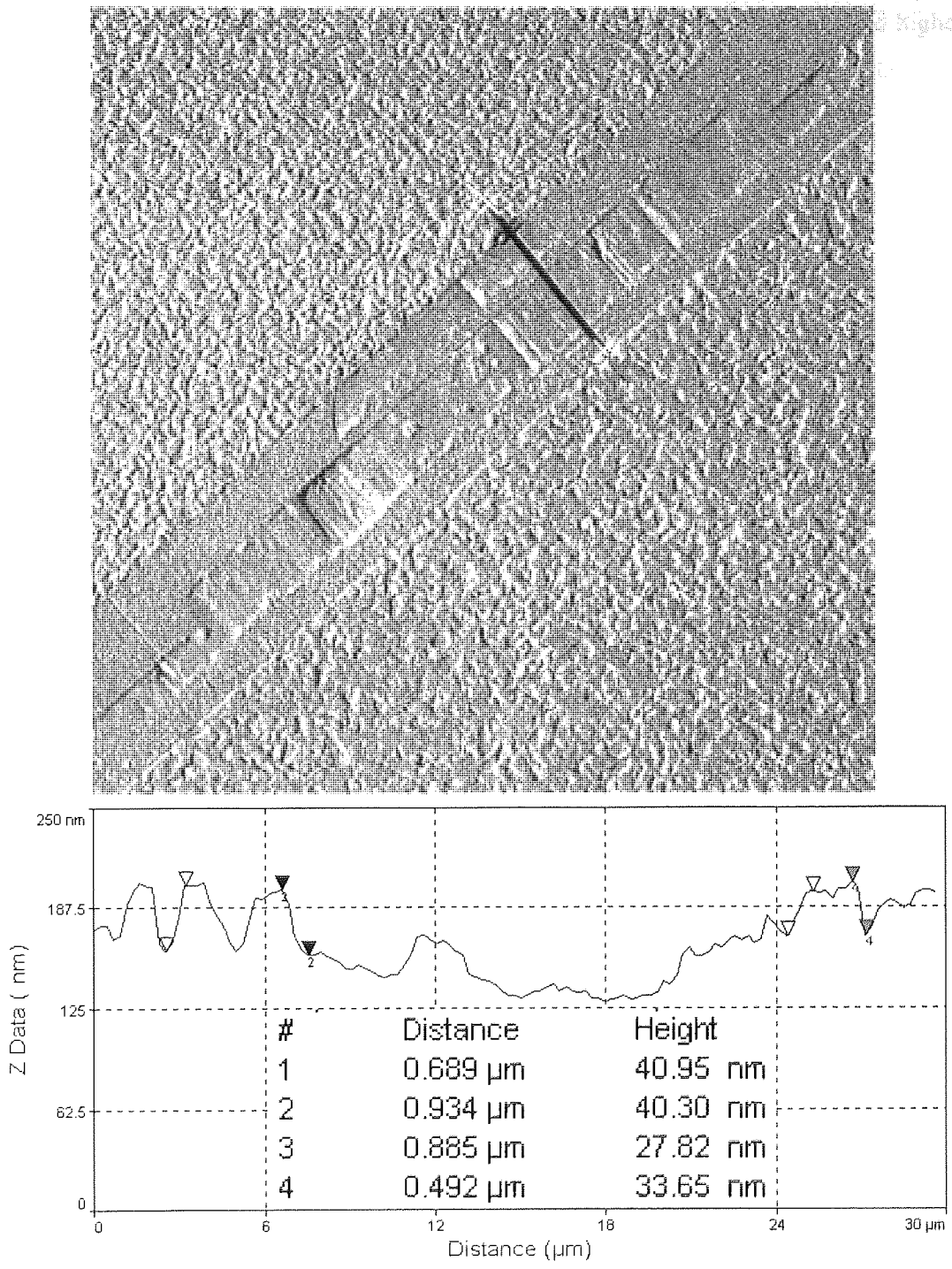

Figure 36. Levelled AFM map of a worn head (5000 passes at 1.5 m/s): the recession of the pole tip and insulator surfaces, and the depth of the ceramic pullouts are respectively 45 ± 10 nm, 30 ± 5 nm and 40 ± 20 nm (index 2, 3 and 1 respectively); groove depths are up to 150 nm; adhesive deposits are 1 to 10 µm wide by 30 to 60 nm high.

Fine scratches were still present on the pole and insulator after 10k passes (Figure 36), while they were hardly seen on the ceramic. Similar polishing has been reported on various tape path materials [141, 210] with hardness lower than the tape particles. The parti-

cles used here (Co-γFe_2O_3: H_K = 11.8 GPa and Al_2O_3 HCA: H_K = 20.6 GPa) had higher Knoop hardness than both SiO_2 and NiFe, and lower than the Al_2O_3-TiC ceramic.

Grooves (up to 150 nm deep and 10 μm wide—*c.f.* Figure 36) were also evident on the pole surface and more discreetly on the insulator surface.

Pitting (1 to 2 μm wide and 20 nm deep) occurred at the pole surface.

Debris were observed either as loose particles over the pole-tip, or adhesive deposits (1 to 10 μm wide by 30 to 60 nm high—*c.f.* Figure 36) most probably built up from mixtures of magnetic pigments, HCA, binder and lubricant transferred from the tape.

Preferential wear was clearly observed at the two-phase ceramic surface. By means of lateral force microscopy (LFM), the friction coefficient of the recessed part was measured as higher than that of the protruding part.

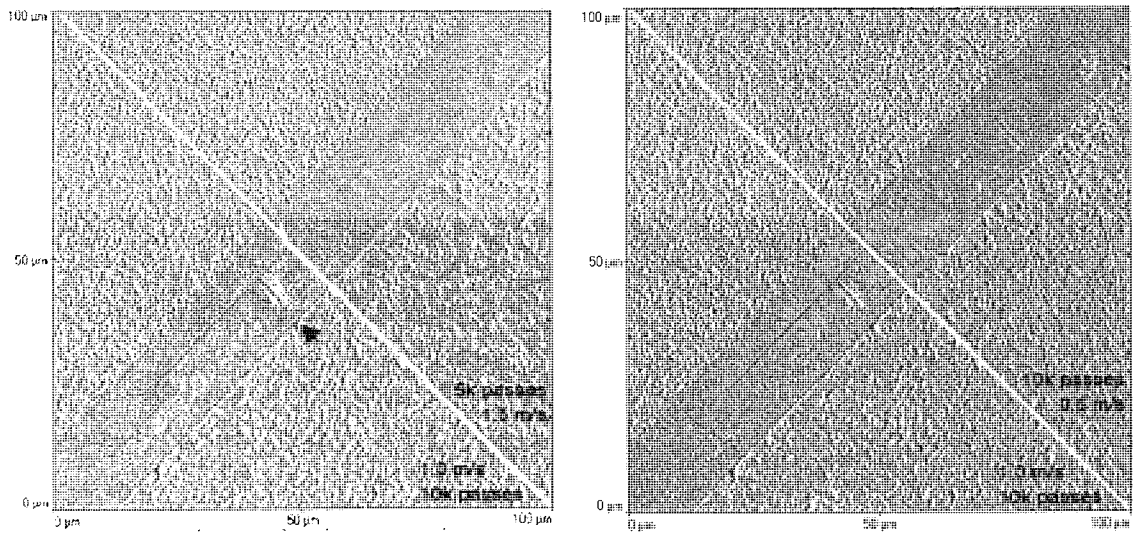

Figure 37. Worn head: 5k passes vs. 10k passes (left); 0.5 m/s vs. 1.0 m/s (right). The arrow indicates a detached fragment of the ceramic assumed responsible for the grooves on the pole tip.

A slit appeared at the glue joint between the ceramic cover bar and the insulator (Figure 37), for heads subjected to 10k passes at the highest sliding speed (1.0 m/s rather than 0.5 m/s). The slit edge vulnerability may favour ceramic pullout at the boundary: on Figure 37 the arrow shows the void left by a fragment detached from the ceramic edge and dragged across the poles. The fragment seems to have ploughed the deep grooves seen aligned on the pole tip (*c.f.* Figure 38).

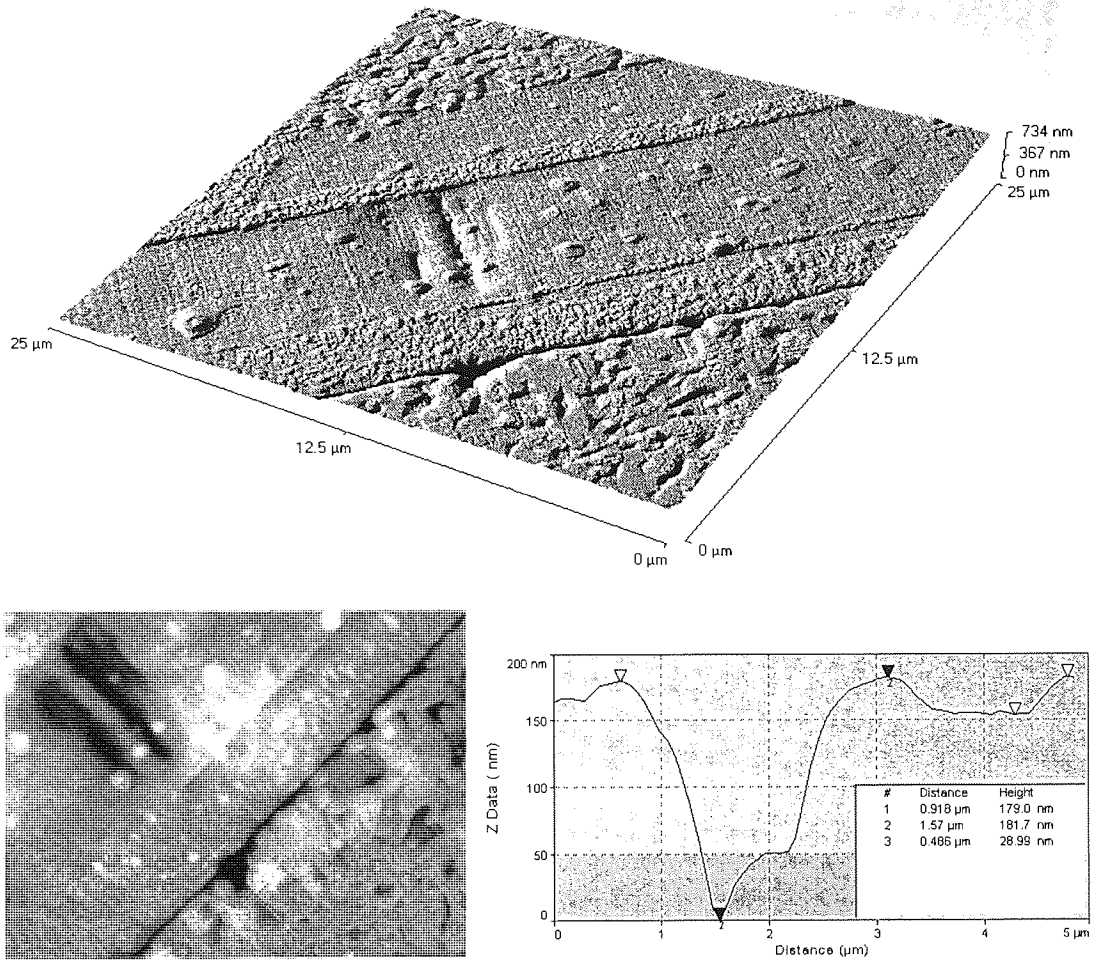

Figure 38. Atomic force micrograph of a worn ADR™ head (25°C/60% RH, 10K passes) showing a ceramic pullout at the glue line aligned with grooves on the pole region parallel to the sliding direction. The line scan shows the pullout at the glue line (#1 and #2) as about six time deeper than a typical pullout (#3).

3.1.1.2 AES analysis of ADR standard heads

The omnipresence of carbon found by Auger electron spectroscopy (Figure 39) is mainly due to the deposition of a carbon layer upon exposure to the electron beam. Sputter cleaning to limited depth - to preserve the superficial components such as stains and deposits—*via* argon bombarding is usually necessary to reduce C contamination.

Iron was present over the whole surface, the ratio Fe/Ni being around 4:1 on the pole area, as compared to 1:4 in bulk Permalloy. This spread in iron is attributed to the transfer of magnetic pigment from the tape to head surface and observed by AFM in form of adhesive deposits. Prolonged sputter cleaning decreased the Fe/Ni ratio, confirming the superficial nature of the transferred iron.

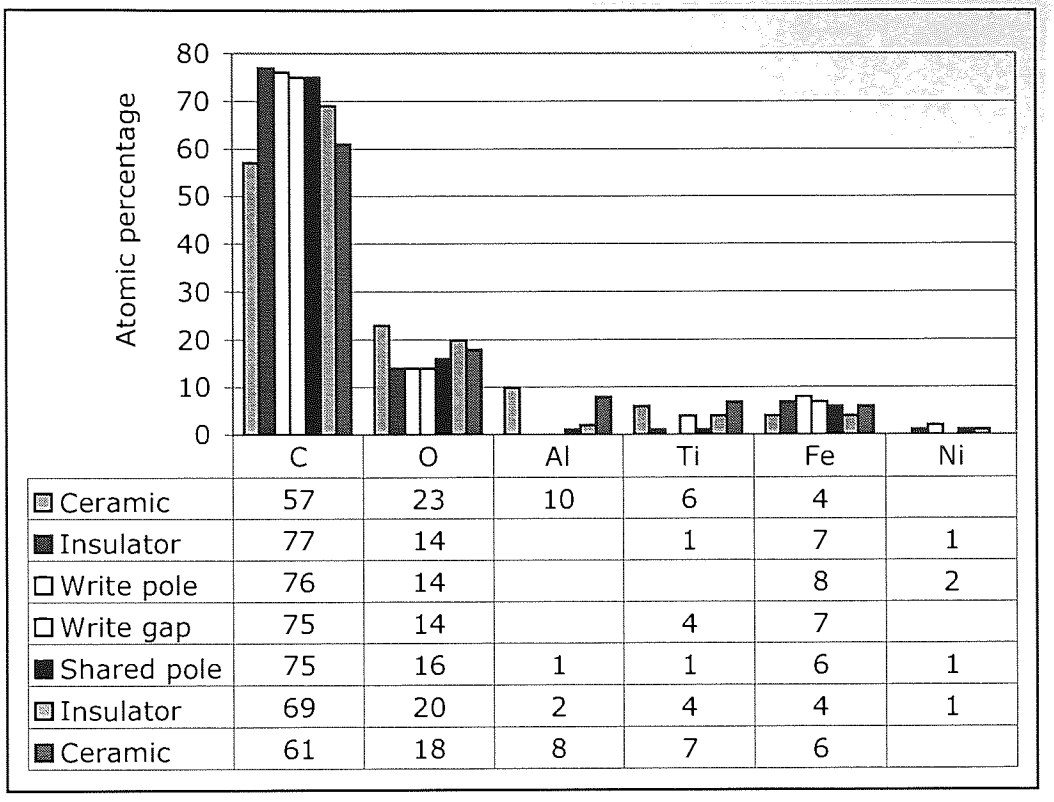

	C	O	Al	Ti	Fe	Ni
Ceramic	57	23	10	6	4	
Insulator	77	14		1	7	1
Write pole	76	14			8	2
Write gap	75	14		4	7	
Shared pole	75	16	1	1	6	1
Insulator	69	20	2	4	4	1
Ceramic	61	18	8	7	6	

Figure 39. Relative atomic concentration of elements on the different head regions measured by AES.

Titanium was present almost everywhere, including the pole-tip region. Ti comes most probably as loose debris pulled out from the ceramic and observed by AFM entrapped at the bottom of the deep grooves across the pole surface.

The presence of oxygen on the pole was assumed to originate either from the iron oxide and the binder transferred from the tape, or from the Permalloy oxidation.

Other contaminants were also present: *argon* from sputtering, and *chlorine* supposedly from handling. Chlorine is a constituent of the tape binder, but as such could not account for the measured concentration. A prolonged sputter cleaning eliminated the chlorine peak, confirming the chlorine superficial presence.

The correspondence on the SEM image in Figure 40 between the dark / light areas to the actual surface topography is not immediate. Properties such as the atomic number may affect the SEM contrast (on smooth Al_2O_3-TiC surfaces, brighter and darker regions correspond to high Ti and low Al atomic numbers respectively) [141].

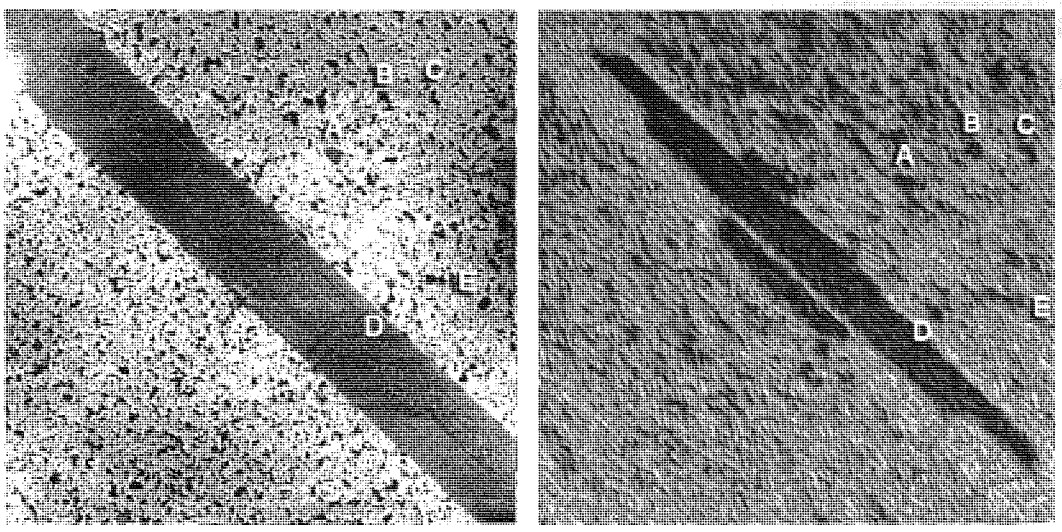

Figure 40. Comparison between AFM topography map (left) and AES map for O (right) of a worn head (after 5 k passes). The letters indicate an example of matching patterns.

Auger spectra (Figure 41) were acquired on two points located on dark and light regions of the scanning electron micrograph. Alumina (Al_2O_3) corresponded the dark region of the ceramic, the light region being mostly titanium carbide (TiC). Iron was found in higher concentration on the light areas.

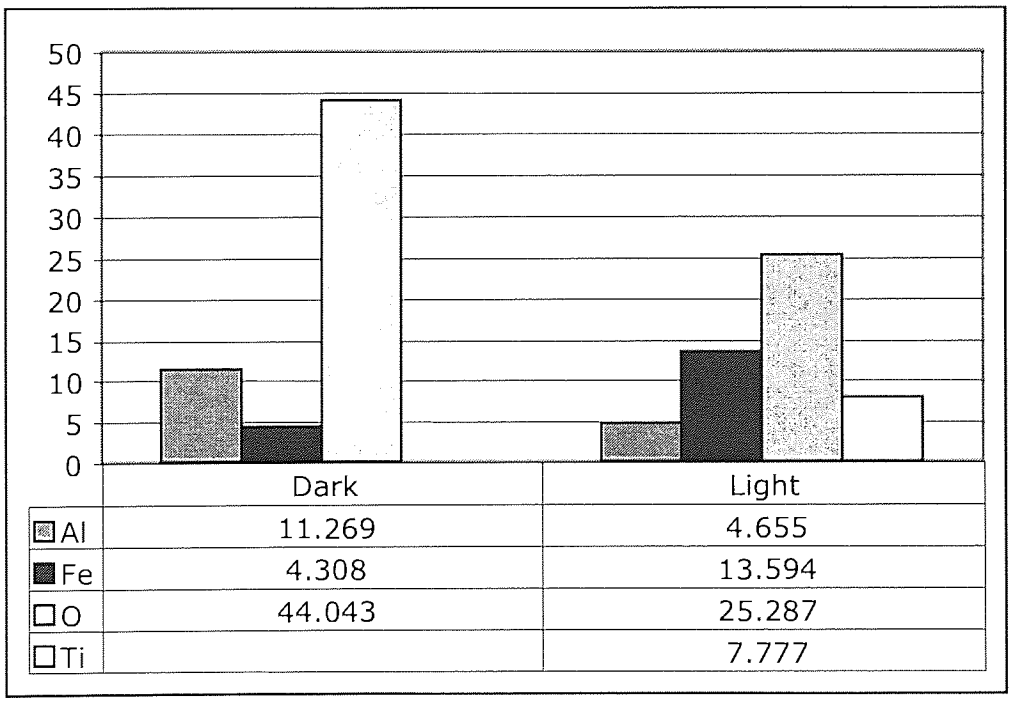

	Dark	Light
Al	11.269	4.655
Fe	4.308	13.594
O	44.043	25.287
Ti		7.777

Figure 41. Relative atomic concentration of elements on the light (back) and dark (front) parts of the ceramic measured by AES.

The AES pattern matches the AFM pattern, provided the geometric transformation operated on the AES image due to sample tilting and mirroring effect is taken into account. Thus, Figure 40 compares the topographic map and AES elemental map for oxygen, which has been inverted and distorted *via* an image processing software to mach the AFM pattern. The images show clearly O as a constituent of the protruding areas of the ceramic (bright on the AFM map). O occurred due to the presence of Al_2O_3, which constituted therefore the protruding areas of the ceramic, leaving to TiC the remaining recessed areas.

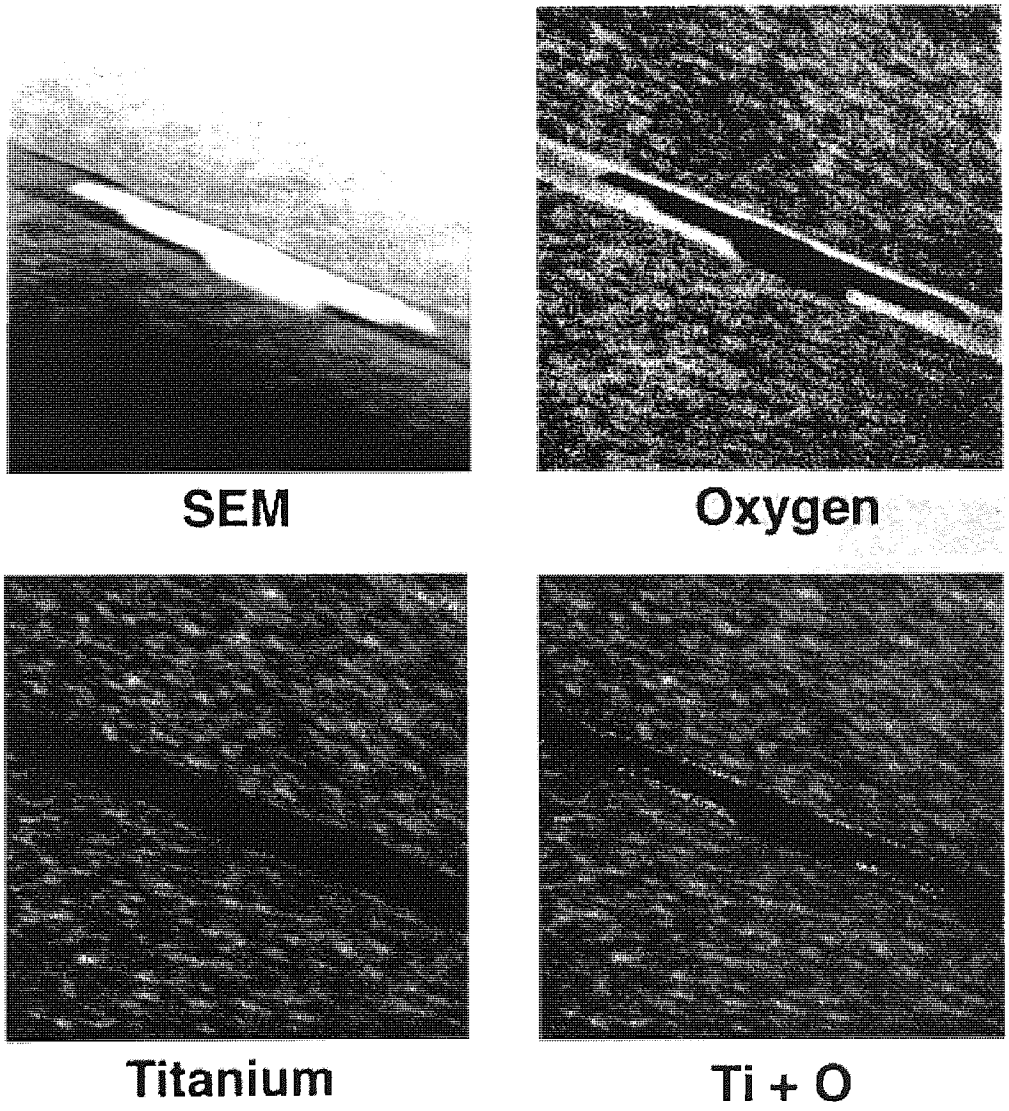

Figure 42. Auger micrograph of a virgin head: oxygen and titanium complete each other to span the ceramic region. Titanium is not discernible on the insulator/pole region and oxygen on the pole region.

Scanning Auger micrographs for Ti and O are presented Figure 42 (virgin head) and Figure 43 (worn head, etched) and Figure 44 (bitmap). Ti (from TiC component) and O (from Al_2O_3 component) patterns were clearly complementary over the ceramic area. The

presence of oxygen extended further to the insulator (SiO_2), sharply defining the pole area. Unlike O, Ti was found to spread over the insulator/pole area upon cycling.

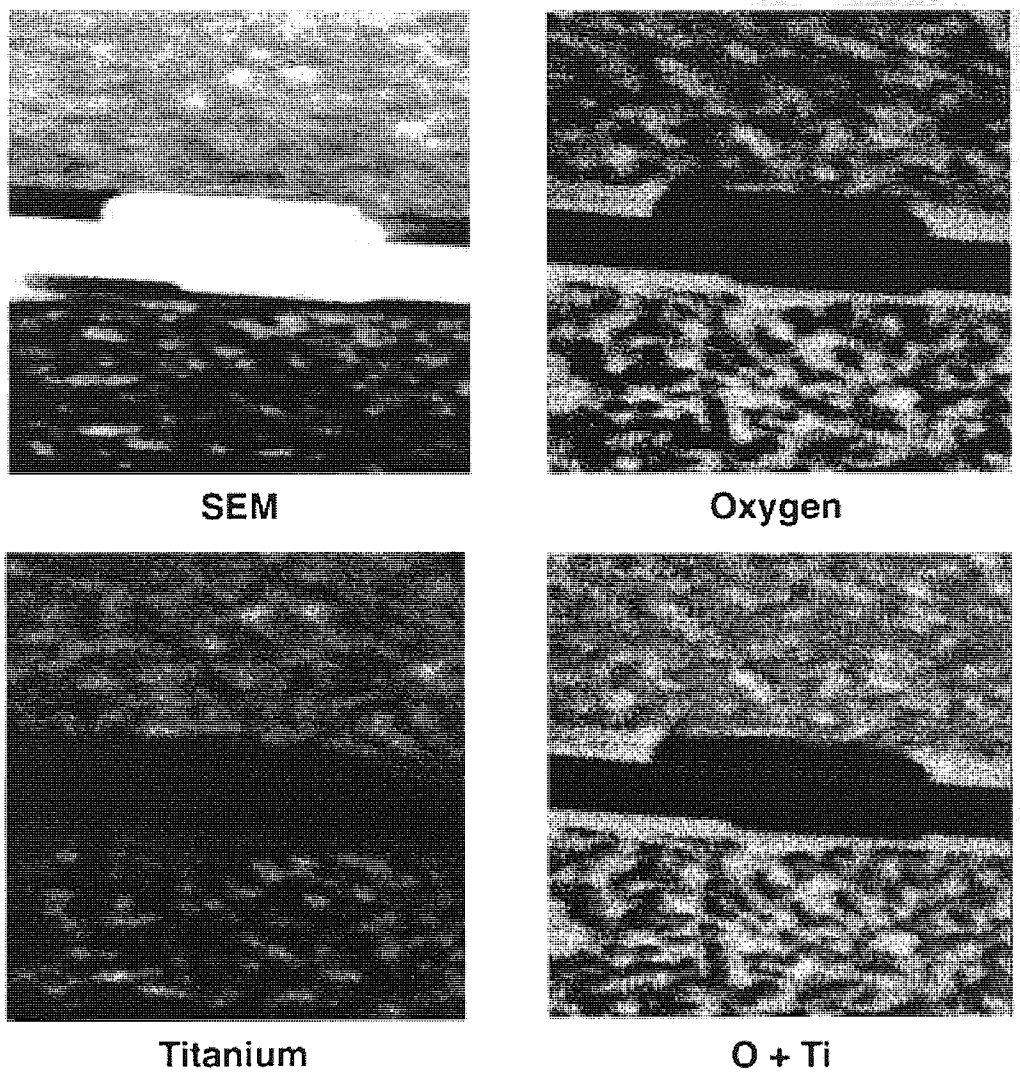

Figure 43. Auger micrograph of a worn head (etched by Ar sputtering), for oxygen and titanium. Oxygen is found on the recessed part of the ceramic, titanium on the prominent part. Titanium clearly spreads over the insulator/pole region.

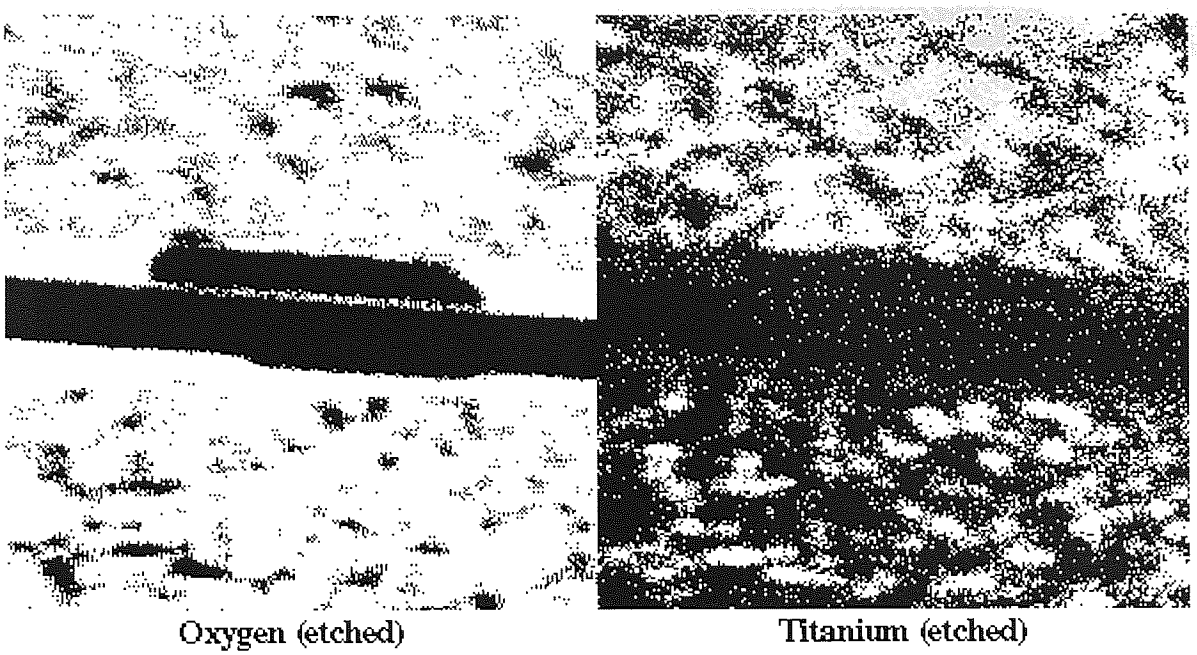

Figure 44. Scanning Auger electron micrograph of an ADR™ worn head (25°C/60% RH; 10K passes) showing the location of Ti and O on the head surface (white dots indicate the presence of the mapped element). Ti is found on the pole tip area.

Auger micrographs for oxygen and iron are presented Figure 45: the iron lies preferentially in the voids left on the oxygen map, hence on the TiC part of the ceramic. These results confirm once again the point AES (*c.f.* Figure 41): iron was transferred from the tape to the head ceramic surface preferentially on the recessed TiC.

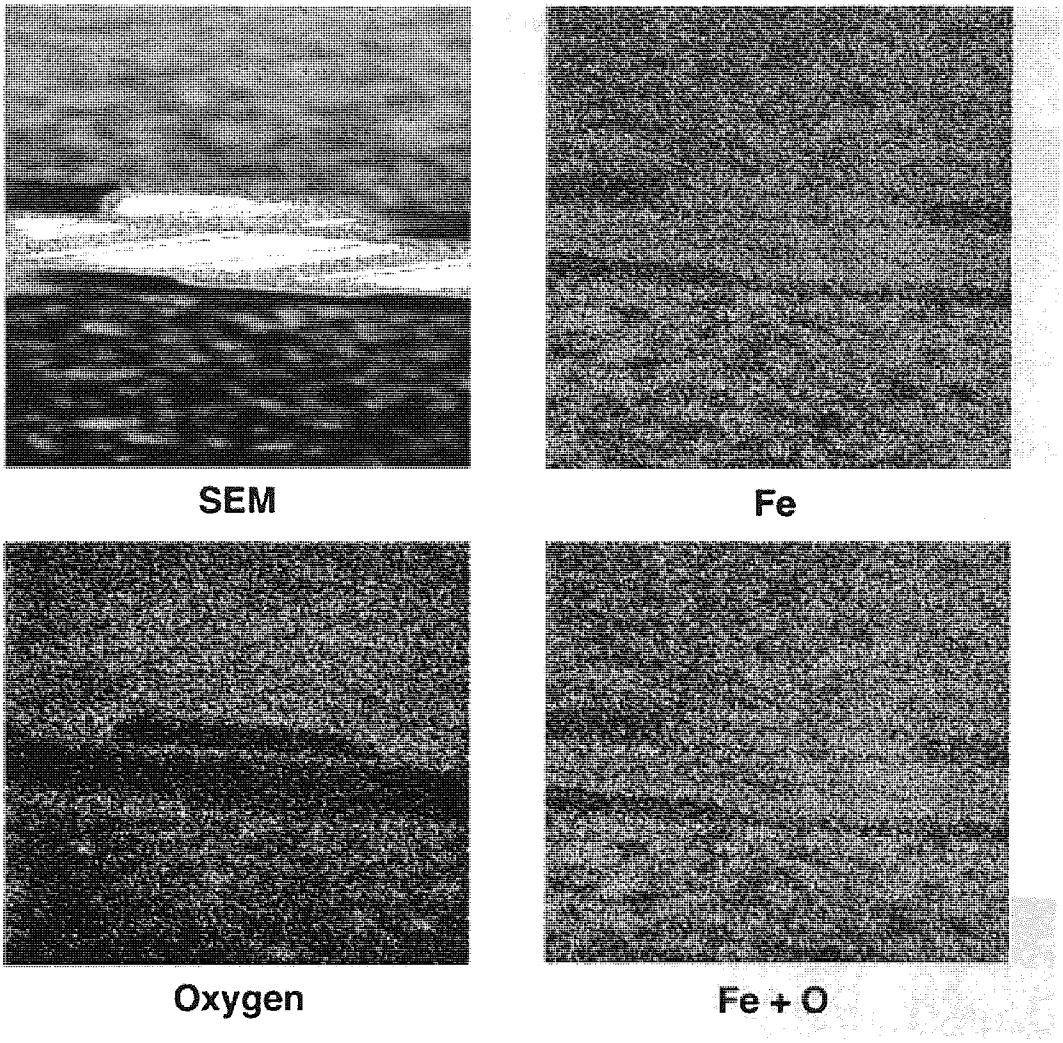

Figure 45. Auger micrograph of a worn head (no etching), for oxygen and iron. Iron and oxygen cover complementary regions of the ceramic, respectively prominent and recessed.

3.1.2 Head staining—preliminary results

An ADR head assembly cycled in non-controlled environment showing an exceptional accumulation of white debris visible with a naked eye, was selected for preliminary characterization of head staining.

3.1.2.1 AFM analysis of head staining

The contaminated head was imaged *via* AFM. Debris having dimensions of the order of 10 μm was thus observed over the tape-bearing surface (image not shown). In Figure 46, a transfer film (~ 15 nm high with respect to the insulator surface) was found to cover the pole surface, with the exception of the pole tip sharp end (upper left corner). The transfer film further drew a line on the insulator surface (upper left corner) above what is thought

to be the buried bias conductor sandwiched within the read yoke, *i.e.* between the upper (read) pole and the shared pole (*c.f.* Figure 20).

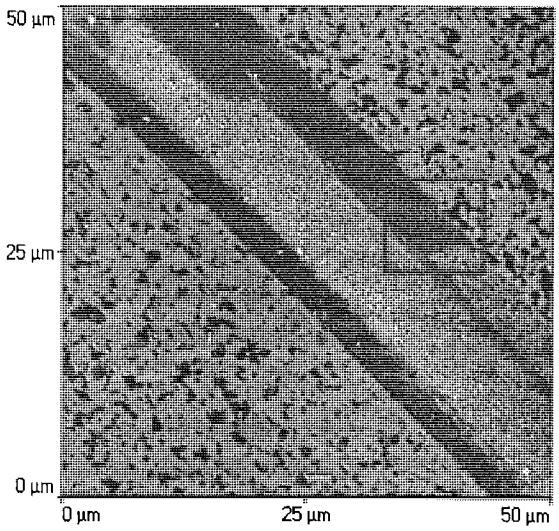

Figure 46. AFM image of a cycled ADR head: a transfer film (~15 nm thick) is clearly covering the pole tips.

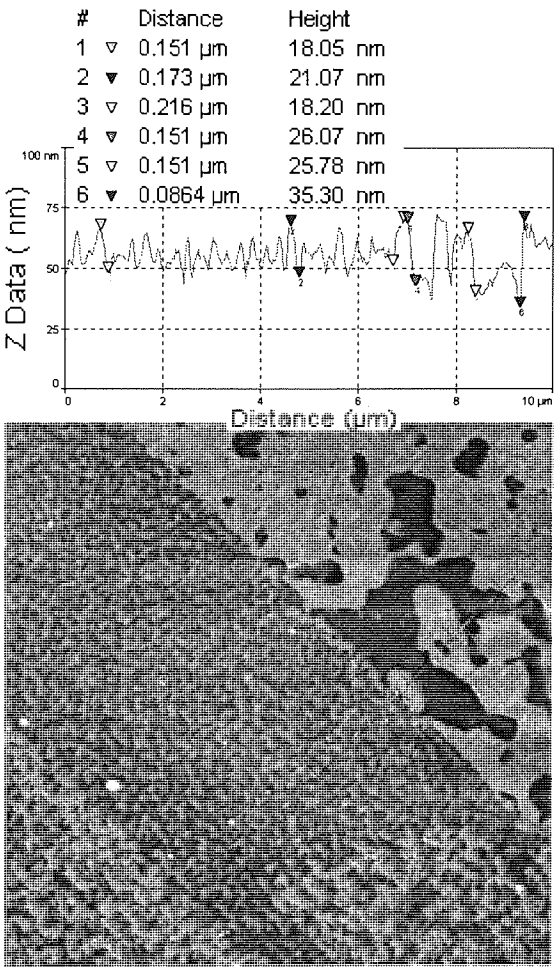

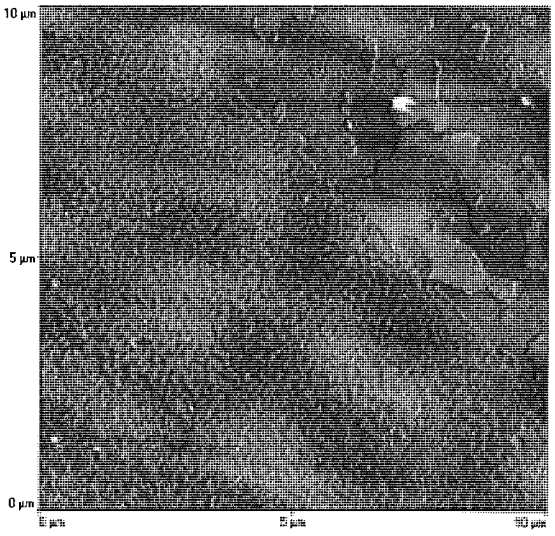

Figure 47. AFM image of cycled ADR head, in topography (left image) and lateral force (right image) mode.

A smoother transfer film was deposited over the shared pole narrow extremity (upper left corner). The remaining surface of the shared pole and the write pole (central area) was covered with a rougher film, with pits up to 20 nm deep (Figure 47). 20 nm should correspond roughly to both the stain thickness and the pole-tip recession, as stain was probably at tape-bearing surface level, only protected from the sliding tape by the pole-tip reces-

sion. For a virgin head and a worn head stained only with discrete deposits, the corresponding pole recessions were measured as 10 nm and 45 ± 10 nm respectively (*c.f.* Table 14): therefore staining seemed to protect the pole tip against wear.

A lateral force micrograph is presented in Figure 47, which corresponds to the region defined on the upper image. The recessed part of the ceramic appeared lighter than the protruding part, which indicates a higher nano-friction coefficient. The recessed part is attributed to the TiC phase of the ceramic, on which a thicker transfer film may result in a higher friction coefficient.

3.1.2.2 AES analysis of head staining

Figure 48 shows the location of O, Ti and Fe at the head surface. As previously (0), Ti and O were found on the SEM light and dark regions, respectively. However, slightly more Fe was found on the dark regions, therefore the Al_2O_3 phase. The difference was attributed to the substantial transfer observed here, which:

Forms a film covering the whole pole surface rather than a few discrete deposits (*c.f.* respective AFM scans) and

Is spread more homogeneously over the whole tape-bearing surface (*c.f.* respective Auger images); the apparent preferential staining over the Al_2O_3 phase may be due to a shadowing effect related to the recession of the TiC phase.

Staining first targeting the pole-tip area and TiC recessions as discrete deposits, would spread upon further sliding contact with the tape, in conditions favourable for transfer, over the whole pole tip and tape-bearing surface.

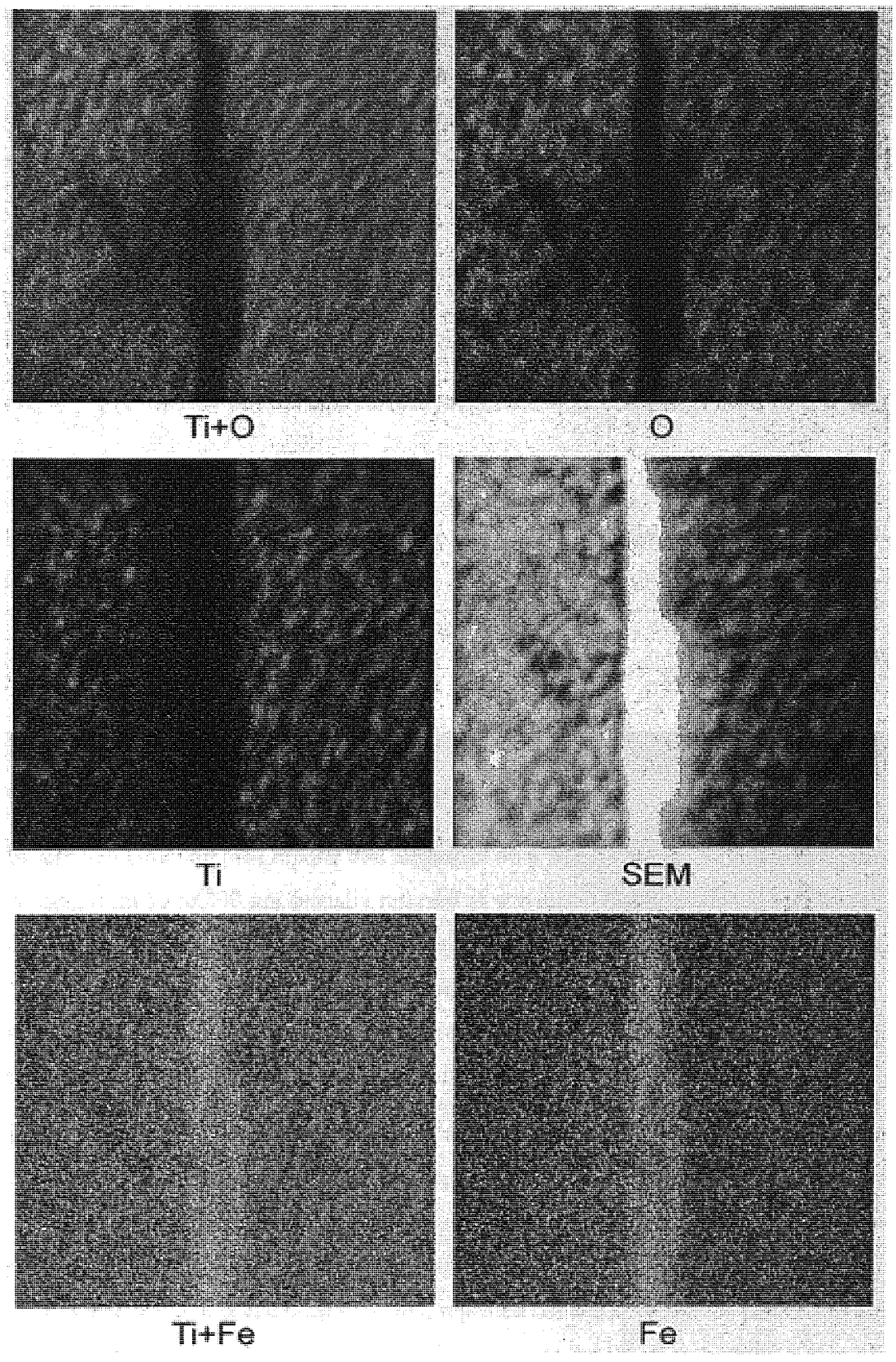

Figure 48. SEM and Auger imaging of a stained head. Bright spots indicate presence of the mapped element.

3.1.3 Tape Wear

The objective here was to characterise both a virgin tape and a worn tape, in an attempt to elucidate the physical and chemical changes occurring at the tape surface as a result of the sliding process.

3.1.3.1 AFM analysis of ADR tapes

Both the arithmetic average ($R_a = \frac{1}{L}\int_0^L |z - m| dx$) and the root mean square ($R_q = \frac{1}{L}\int_0^L (z - m)^2 dx$) of the tape surface roughness were calculated from 10 μm^2 and 50 μm^2 scans (Table 16).

Table 16. Roughness arithmetic average (R_a) and root mean square (R_q) calculated from AFM scans of 10 and 50 μm^2 tape surface areas.

	R_a (10 μm^2)	R_a (50 μm^2)	R_q (10 μm^2)	R_q (50 μm^2)
Virgin tape	13.28 nm	17.35 nm	16.93 nm	22.01 nm
Worn (centre)	13.92 nm	14.03 nm	17.07 nm	18.34 nm
Worn (edge)	18.80 nm	19.56 nm	23.85 nm	25.66 nm

Broese van Groenou [48] reports that asperities on a flexible media with wavelengths ranging from 50 to 200 μm (usually referred as waviness) can be flattened by plastic deformation, whereas the local stress is too low to affect smaller wavelengths (2~50 μm). The roughness reported here was scale dependent only for the virgin tape. The longer wavelength asperities (waviness) were therefore flattened in the sliding process, leaving only the smaller scale roughness measurable at both the resolutions used.

The smaller scale roughness seems unaffected by the sliding process at the tape centre, whilst it increased at the edge. Magnetic tapes are in principle calendered by an intermediate manufacturing process: the tape is passed between a steel and a highly compressed paper roller under high pressure (~ 60 to 100 MPa) and high temperature (50 to 80°C) [153]. Once the tape is enclosed in a QIC, repeated contact between the centre and the driving belt seemed at first consideration to perpetuate the initial smoothing action of the calendering process. On the other hand, roughness appeared to increase at the tape edge, not in contact with the driving belt.

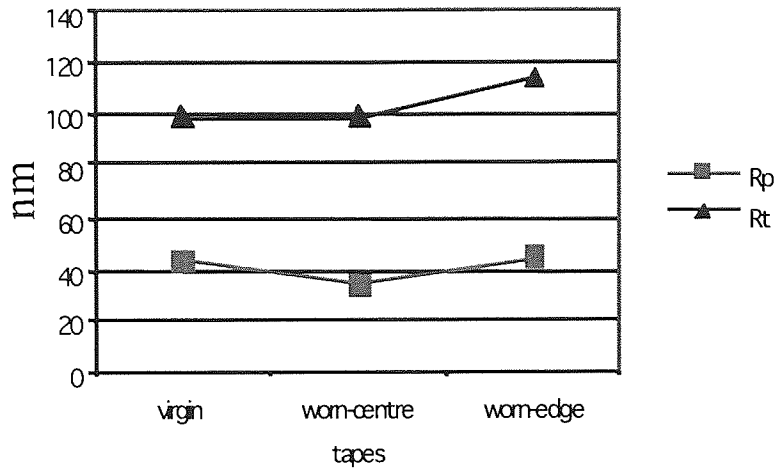

Figure 49. Peak to valley (R_t) and peak to mean (R_p) measured from a 10 μm² scan.

The peak to valley (R_t) and peak to mean (R_p) parameters were also measured and are presented (Figure 49) for a 10 μm² area scan. The R_t parameter followed the same trend as the R_q parameter, constant at the tape centre whilst increasing at the edge. However, the R_p parameter was found to decrease at the tape centre, being constant at the edge. From these observations, it appeared that cycling hollowed out the valleys over the whole tape surface, whereas it flattened the highest asperities only at the centre, which was in contact with both the driving belt and the head poles (*c.f.* above).

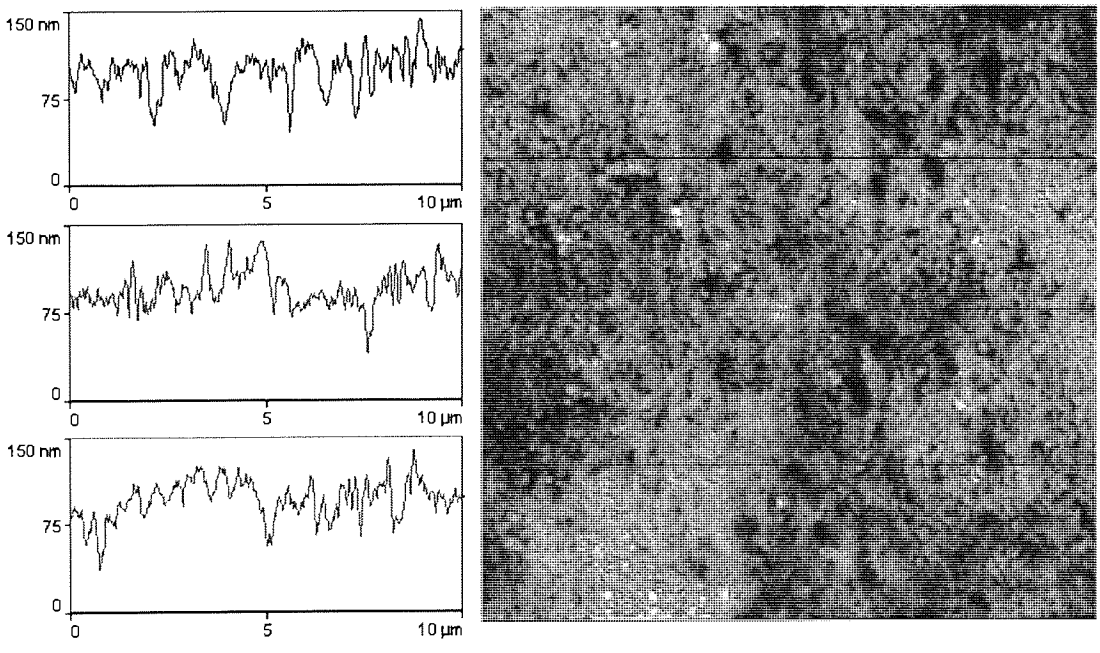

Figure 50. 10 μm² area AFM scan of a virgin tape.

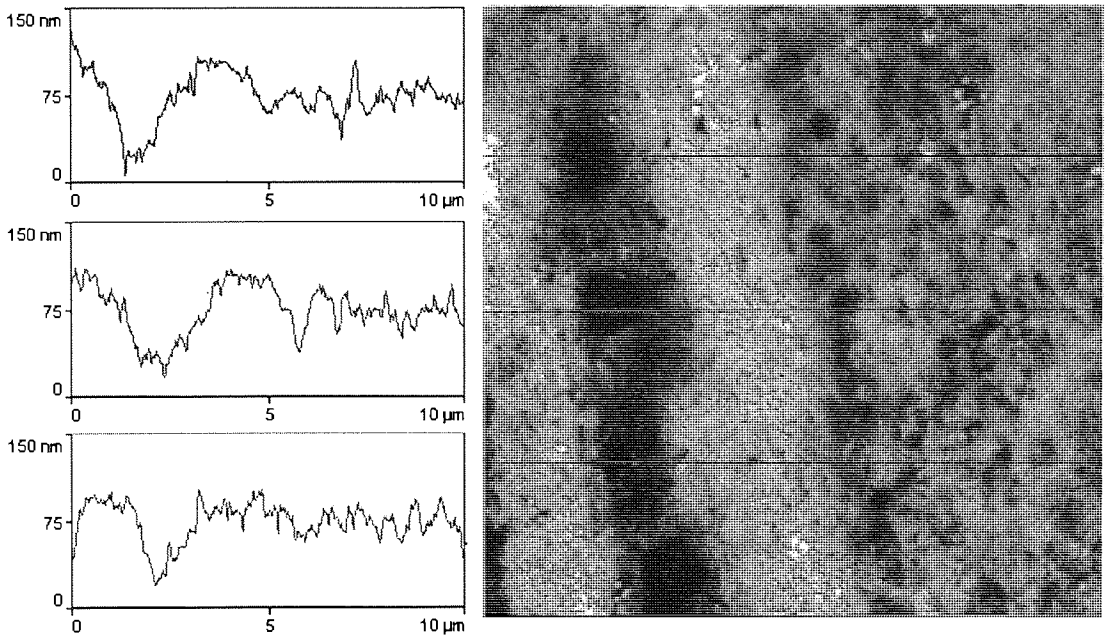

Figure 51. 10 µm² area AFM scan of a worn tape (centre).

The AFM images confirm the previous statement: the valley maximum depth, from ~ 0.5 µm wide × 60 nm on the virgin tape (Figure 50), increased to 1~2 µm wide × 70~100 nm deep on the worn tape (Figure 51 and Figure 52). The maximum peak height was roughly constant at the tape edge (~ 60 nm) whereas it decreased at the centre (~ 30 nm).

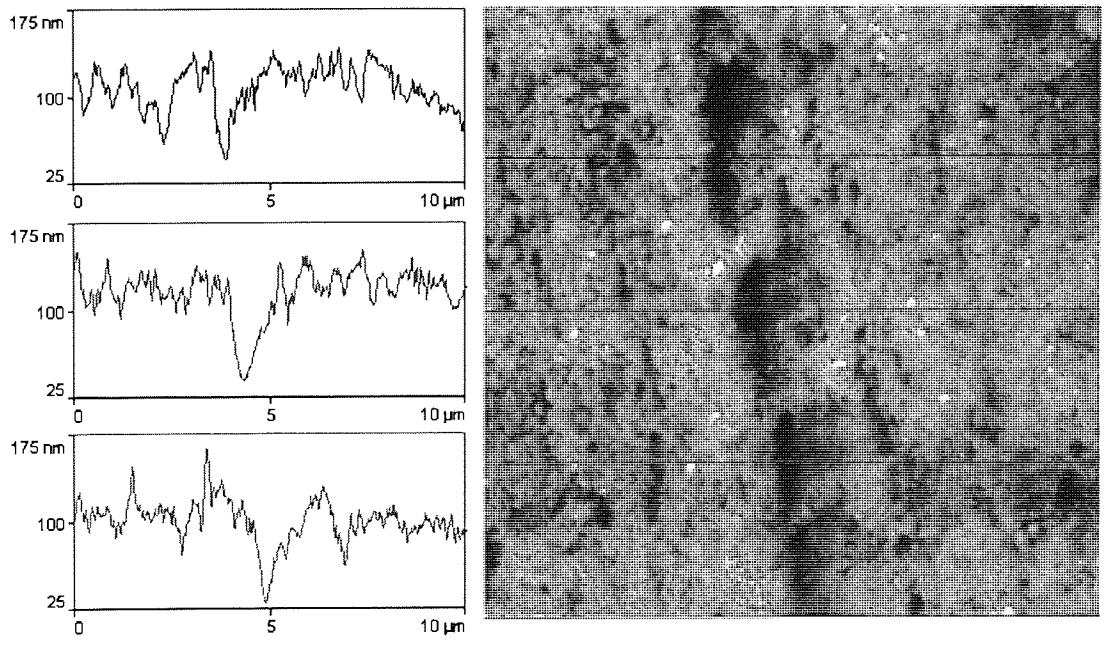

Figure 52. 10 µm² area AFM scan of a worn tape (edge).

The increased valley maximum depth on the tape surface (up to 100 nm deep) may involve ploughing by laminate particles worn from the ceramic, which larger dimension is of the order of one micron, or adhesive wear as will be discussed later.

3.1.3.2 XPS analysis of ADR tapes

Five elements were identified from the XPS spectra: carbon (C), oxygen (O), iron (Fe), nitrogen (N) and chlorine (Cl).

C was found in the *binder*, the *lubricant* (fatty acid ester, *e.g.* $C_{13}H_{27}$-O-C(=O)-$C_{18}H_{37}$) and in a *contaminating hydrocarbon layer* that usually forms on the sample surface upon exposition to the X-ray beam.

O was found in the *binder*, in the *lubricant*, in the *dispersant* and in the metal oxides (*magnetic pigment*: Co modified γFe_2O_3 and *HCA*: Al_2O_3).

Fe was a constituent of the *magnetic pigments*.

N and Cl were only present in the *binder* (urethane: H_2N-NH-C(=O)-O-C_2H_5 or vinyl chlorine: H_2C=CHCl).

Synthesis of the C peak revealed five different chemical states for carbon corresponding to the following bonds:

C-C/C-H was present in the *lubricant* and the surface *contaminant* (hydrocarbon chains), and possibly in the *binder*.

C(=O)-O was present in the *binder* and the *lubricant*.

C-N, C-Cl and C-O were typical of the *binder* resin.

3.1.3.3 XPS depth profile of ADR tapes

At a given take-off angle θ, only the photoelectrons emitted from atoms within a depth of $d(\theta) \sim 3\lambda \cos\theta$ (where $\lambda \sim 3$ nm is the attenuation length [194]) would manage to escape the sample surface and be eventually collected by the analyser. Hence, collecting photoelectrons at various take-off angles permits to probe the sample within varying "skin" depths (*c.f.* Table 17).

Table 17. Depth probed by the photoelectrons (attenuation length, λ ~ 3 nm) at take-off angle θ.

Take-off angle θ	0°	33°	45°	54°	60°
Depth $d(\theta) \sim 3\lambda \cos\theta$	9 nm	7.5 nm	6.4 nm	5.3 nm	4.5 nm

Several methods have been proposed for extracting depth profile from angle resolved XPS [211, 212]. However, none of these methods is simple and gives accurate results.

A very simple calculation based on a naive model is thereafter proposed. The idea is to transform an intensive parameter—the relative atomic concentration within a certain layer—into an extensive parameter—the atomic population—therefore proportional to the layer volume. The atomic population $n(\theta)$ is calculated by dividing the layer volume $V(\theta)$ by the sum of the atomic concentrations $C_i(\theta)$ weighted by the atomic volumes attributed to each identified element i, *i.e.*:

$$n(\theta) = \frac{V(\theta)}{\sum_i C_i \times V_i(\theta)}, \qquad (51)$$

where $V_i(\theta)$ [cm^3] = atomic weight [g/mol] / density [g/cm^3] / Avogadro number [1/mol].

The choice of a density is critical: here the density of the element as given by most periodic tables is chosen, rather than the density of the compound which it is part of. In this way it is overestimated by a factor of ~ 2 to ~ 3 for organic compounds and underestimate it by a factor of ~ 2 for inorganic compounds. The intention, however, is to obtain a semi-'quantitative' rather than an absolute depth profile.

The population of element i within the layer probed at a take-off angle θ, is then:

$$n_i(\theta) = n(\theta) \times C_i(\theta), \qquad (52)$$

hence the population of element i in the layer sandwiched between $d(\theta)$ and $d(\theta+\Delta\theta)$ is simply: $\Delta n_i(\theta) = n_i(\theta+\Delta\theta) - n_i(\theta)$, *i.e.* when expressed as a concentration:

$$\Delta C_i(\theta) = \frac{\Delta n_i(\theta)}{\sum_i \Delta n_i(\theta)}. \qquad (53)$$

The concentration depth profile obtained using the above calculation is presented in Figure 53.

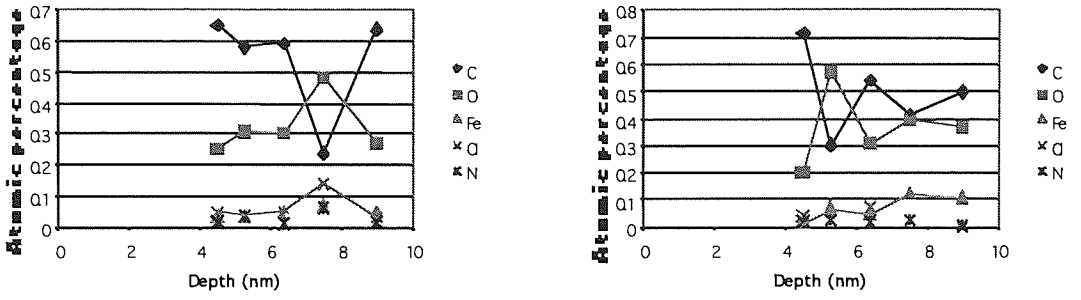

Figure 53. Depth profile for virgin tape (left) and worn tape (right).

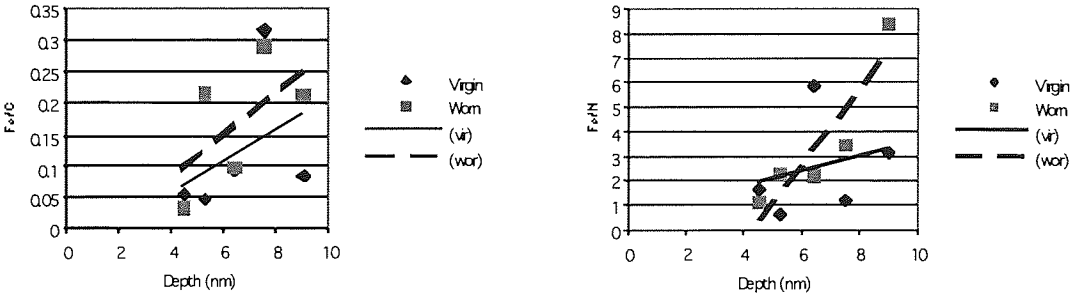

Figure 54. Atomic concentration ratios: iron over carbon (left) and nitrogen (right).

As suggested by different authors [126, 157] an interpretation based on the ratio of element concentrations rather than the concentrations is more meaningful. The ratio of Fe/C and Fe/N are therefore plotted in Figure 54: both were increasing along with the depth, as would be expected from the location of iron deeper than both the lubricant (C) and the binder (C and N) [213]. As the tape was cycled, Fe/C and Fe/N appeared fairly unaffected at shallow depth whereas they increased deep below the surface, Fe/N even more markedly. This behaviour was likely to result from a binder depletion (increase in Fe/N) partly taken over by the lubricant exuding from the porous coating. Similar results on MP tapes have been reported by Hempstock *et al.* [157].

3.1.4 Temperature and Friction at the Head-Tape Interface

The proposed task was to analyse the correlation between friction and temperature in ADR drives. Both these parameters were monitored in actual running conditions in the hope of gaining from a better knowledge of the dynamics and thermodynamics at the head-to-tape interface, a better understanding of the wear behaviour.

3.1.4.1 *Dynamics of the head / tape Interface—problem definition*

ADR 30GB drives use ADR 15 GB quarter inch cartridge (QIC) manufactured by Verbatim (*c.f.* Figure 55). The original QIC design has been modified (*e.g.* addition of a third guide roller and third tape guide) as to hold a greater tape length for larger storage capacity.

The tape tension at the QIC head window calculated for the original design [214] and needed to be revised for the ADR 15 GB QIC design. Additionally, the tape elasticity not included in the referred calculation had to be considered as due to a longer and thinner tape.

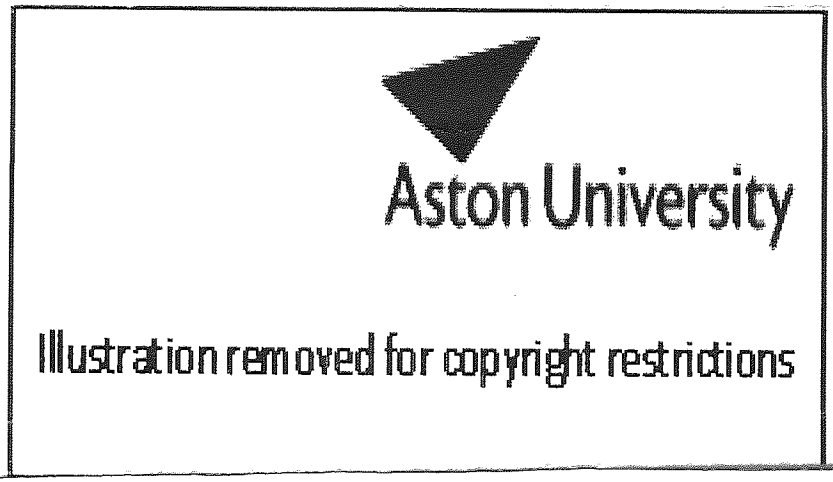

Figure 55. ADR 15 GB QIC; different parts (left) and dynamics (right).

Let S_1 and S_2 be the peripheral speeds of respectively the take-up and supply reel, the speed differential may be expressed as (*c.f.* Figure 55) [214].

$$\frac{S_1 - S_2}{S_1} = \frac{T_3 - T_1}{E_b \sigma_b} + \frac{t_b}{D_2} - \frac{t_b}{D_1}, \qquad (54)$$

where E_b, σ_b and t_b are the belt elastic modulus, cross section and thickness respectively. Similarly:

$$\frac{S_1 - S_2}{S_1} = \frac{\tau' - \tau}{E_t \sigma_t} + \frac{t_t}{D_2} - \frac{t_t}{D_1} \tag{55}$$

where E_t, σ_t and t_t are the tape elastic modulus, cross section and thickness respectively.

Using the following relations

$$\begin{cases} \tau' = \tau_h . \exp(\mu\theta_1) \\ \tau_h = \tau . \exp(\mu\theta_2), \\ \tau + T_2 = T_1 + T_S \end{cases} \tag{56}$$

the tape tension force τ_h in the head window can be expressed as

$$\tau_h = \frac{(T_3 - T_2 + T_S) + E_b \sigma_b (t_b - t_t)\left(\frac{1}{D_2} - \frac{1}{D_1}\right)}{\frac{E_b \sigma_b}{E_t \sigma_t}\left[\exp\left(\mu(\theta_1 + \theta_2)\right) - 1\right] + 1} . \exp(\mu\theta_2), \tag{57}$$

with:

T_3–T_2 = equivalent friction of two belt idler rollers;

T_S = equivalent friction of the supply reel bearing;

E_b = belt elastic modulus = 267 MPa;

t_b = belt thickness = 70 μm;

w_b = belt width = 3.8 mm;

E_t = tape (PET) modulus = 7.39 GPa;

t_t = tape thickness = 6.0 μm;

w_t = tape width = 8.0 mm;

D_1 = diameter of the take up reel;

D_2 = diameter of the supply reel; = 15.24 mm to 53.85 mm;

μ = coefficient of friction of the belt around the guide post;

θ_1 = 0.75 radian + arcsine [$^1/_2 D_1$/(37 mm)]; wrap angles of the tape

θ_2 = 0.94 radian + arcsine [$^1/_2 D_2$/(49 mm)]; around the guide posts

The 15 GB QIC cartridge has full and empty reel circumferences of respectively 169.17 mm and 47.87 mm [215], which corresponds to respective diameters of D_f = 53.85 mm and D_e = 15.24 mm. The tape length wound on a reel between time 0 and t, is

$$L(t) = \frac{\pi}{4} \cdot \frac{\left| D(t)^2 - D(0)^2 \right|}{t_t}. \tag{58}$$

$D(t)$ and t_t refer to the reel diameter at time t and to the tape effective thickness, respectively.

The maximum tape length is specified as L_{max} = 347.5 m, hence:

$$t_t = \frac{\pi}{4} \cdot \frac{\left(D_f^2 - D_e^2 \right)}{L_{max}} = 6.0 \mu m. \tag{59}$$

From (58), it follows that:

$$D_1(t) = \sqrt{\left(D_f^2 - \frac{4}{\pi} \cdot L(t) \cdot t_t \right)} \quad \text{and} \quad D_2(t) = \sqrt{\left(\frac{4}{\pi} \cdot L(t) \cdot t_t + D_e^2 \right)} \tag{60}$$

The tapes have been tested by the manufacturer at 20 ± 4°C temperature and 50 ± 10% relative humidity [215]: in these conditions the instantaneous tape tension force has been measured in the limits of 0.21 N to 1.05 N between BOT and EOT. τ_h is found to fall into these limits, provided that:

$$(T_3\text{-}T_2)+T_S \sim 0.4 \text{ N and } \mu \sim 0.7. \tag{61}$$

The normal force applied by the tape on the head surface (*c.f.* Figure 56) is estimated using the relation [216]:

$$F_n = \tau_h \sin\left(\frac{\Theta}{2} \right) \times \left[1 + \exp(f.\Theta) \right], \tag{62}$$

with:

$$\Theta = 2\arcsin\left(\frac{h}{\sqrt{L^2 + h^2}} \right). \tag{63}$$

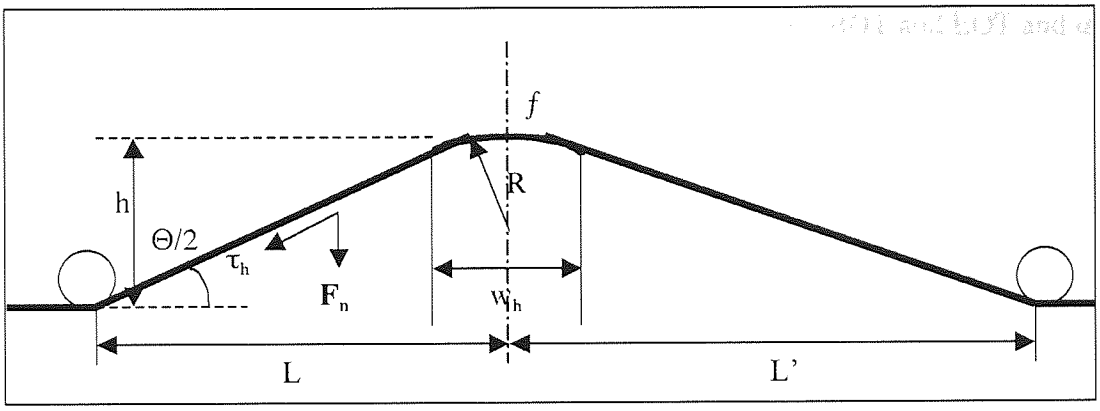

Figure 56. Schematic cross-section of the head-to-tape interface region. L = 10.06 mm, L' = 11.59 mm, R = 1.3 mm and w_h = 0.3 mm. h, Θ and f are the tape protrusion depth, wrap angle and friction coefficient against the head, respectively.

3.1.4.2 Application: normal contact force between the tape and the head

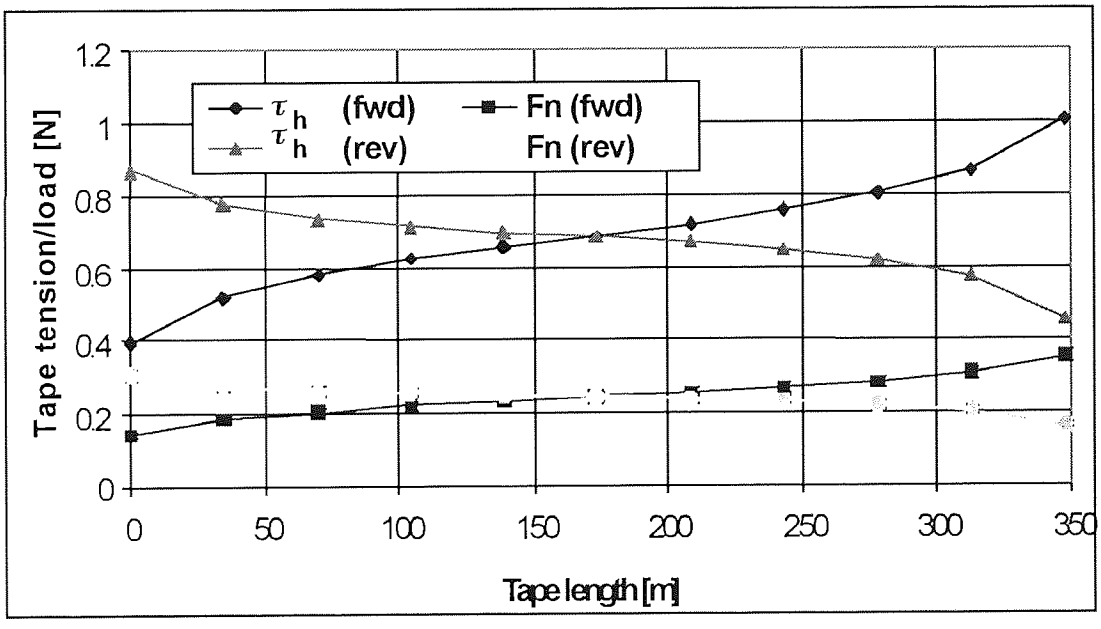

Figure 57. Tape tension force τ_h in the head window and normal force F_n at the head/tape interface as a function of the tape length L *around the take-up reel.*

The tape tension has been measured [217] for a set of ten ADR 15GB QIC at 23°C (30-60% RH). The average (filtered) tape tension ranged from ~ 0.40 ± 0.03 N to 1.00 ± 0.09 N, an interval covered by the tension calculated using (57) provided that:

$$(T_3 - T_2)+T_S \sim 0.56 \text{ N and } \mu \sim 0.26. \qquad (64)$$

The resulting F_n was calculated for $h = 1.7$ mm and $f = 0.3$ from BOT and EOT and is also presented Figure 57.

The 'S' shape displayed on Figure 57 is typical of tape tension measurements, the skew inherent to the cartridge asymmetry (*c.f.* Figure 55).

The head-to-tape interface friction coefficient $f = 0.3$ was estimated after the temperature measurements discussed in the following sections. The tolerance on this parameter is wide: error bars indicating Figure 57 the change in F_n from $f = 0.0$ to $f = 1.0$, are barely noticeable.

3.1.4.3 Temperature at the head-to-tape interface

Using a transducer to monitor the tape tension force within the drive in running conditions has been under consideration. However, since introducing a foreign body into the QIC head window may affect the running conditions, a model correlating the temperature - monitored *via* thermo-sensitive resistances embodied in any head - to the friction behaviour at the head-to-tape interface will here be considered for a more practical estimation.

Tape asperities, much softer than head asperities, are expected to deform readily during initial contact. The typical magnetic head-to-tape interface falls therefore in the rough (head)-smooth (tape) interface category (*c.f.* 1.3.4). The contact is furthermore assumed to be elastic. The calculation of the Peclet number (Table 18) states the ADR specific case as intermediate between the low (i) and high-speed (ii) cases. The solutions are therefore presented for both cases, giving a range where the actual solution should be found. Finally, the rough-rough case is also considered as it corresponds to the possible contact between the head and magnetic particles not coated by the tape binder.

Table 18. Parameter used in Bhushan's model.

PARAMETER		VALUE	UNIT	*N.B.*
$q = f \cdot p_a \cdot U \cdot \left(\frac{A_a}{A_r}\right)$		1.08×10^{7}	W/m^2	frictional heat - elastic contact
		3.75×10^{7}	W/m^2	- plastic contact
$Q = f.U.F_n$		7.29×10^{-2}	W	frictional power heat
$q' = f.U.p_a$		3.04×10^{4}	W/m^2	per A_a
f		0.30		head/tape friction
U		1	m/s	tape sliding speed
	Head	Tape		
E	4.50×10^{11}	7.39×10^{9}	Pa	elastic modulus
ν	0.24	0.33		Poisson ratio
H	2.26×10^{10}	2.50×10^{8}	Pa	Knoop hardness
$E_c = \frac{1}{\frac{1-\nu_h^2}{E_h} + \frac{1-\nu_t^2}{E_t}}$		8.17×10^{9}	Pa	composite modulus
s_p		2.00×10^{-8}	m	composite standard deviation of summit-height distribution, estimated after AFM
R_p		1.00×10^{-4}	m	composite mean radius of the curvature of asperity summit distribution, typical value
$\frac{A_r}{A_a} = \frac{3.2p_a}{E_c\sqrt{\sigma_p/R_p}}$		2.81×10^{-3}		elastic contact [61]
$\frac{A_r}{A_a} = \frac{2p_a}{H}$		8.10×10^{-4}		plastic contact [218, 219]
$w_t = b$		8.00×10^{-3}	m	tape width = slider width
$w_h = l$		3.00×10^{-4}	m	head width = slider length
$A_a = w_t.w_h$		2.40×10^{-6}	m^2	apparent area of contact
$A_r = A_a.\ (A_r/A_a)$		6.73×10^{-9}	m^2	real area of contact

Table 18 continued.

PARAMETER	VALUE	UNIT	*N.B.*
d_{max}	1.00×10^{-5}	m	typical value
$\bar{d} = \frac{3}{4} d_{max}$	7.50×10^{-6}	m	mean diameter of contact
$\bar{l}_i = \bar{d}\sqrt{\frac{A_a}{A_r}}$	1.42×10^{-4}	m	mean distance between contacts
$\bar{A} = 0.64\left[\left(\frac{b}{l}\right)\sinh^{-1}\left(\frac{l}{b}\right) + \sinh^{-1}\left(\frac{b}{l}\right) + \frac{1}{3}\left(\frac{b}{l}\right)^2 + \frac{1}{3}\left(\frac{l}{b}\right) - \frac{1}{3}\left(\frac{b}{l} + \frac{l}{b}\right)\cdot\left(\sqrt{1+\left(\frac{b}{l}\right)^2}\right)\right]$	2.88		area factors [220]
$A_m = 0.64\left[\left(\frac{b}{l}\right)\sinh^{-1}\left(\frac{l}{b}\right) + \sinh^{-1}\left(\frac{b}{l}\right)\right]$	3.19		
F_n	0.24	N	equation (62)
$p_a = F_n/A_a$	1.01×10^{5}	Pa	
$p_r = F_n/A_r$	3.61×10^{7}	Pa	
PECLET NUMBER			
$L = \frac{U\bar{d}}{2\kappa_{head}}$	0.63		
$L = \frac{Ul}{\kappa_{tape}}$	1250.00		
$L = \frac{3Ud_{max}}{16\kappa_{head}}$	0.31		

	AlTiC	SiO_2	Tape coating		
k	6.0×10^{-6}	7.4×10^{-7}	2.4×10^{-7}	m^2/s	thermal diffusivity
r	4220	2650	1810	kg/m^3	density
Cp	700	703	900	J/(kg×K)	specific heat
k	16	1.38	0.38	W/(m×K)	thermal conductivity

Table 19. Average and maximum temperature increase due to friction at the head-to-tape interface, according to Bhushan's model.

PARAMETER	VALUE	UNIT	*N.B.*
(i) ROUGH-SMOOTH/HIGH-SPEED: $L = \frac{U\bar{d}}{2\kappa_{head}} > 10$			
$r_l = \frac{1}{1 + \frac{k_t}{\bar{A}k_h}\sqrt{\frac{2\kappa_h}{U\bar{d}}}}$	0.99		Partition parameter
$\bar{\theta} = r_l\left(\frac{f.p_a.U}{\rho_h C p_h}\right)\cdot\left[\frac{A_a}{A_r}\sqrt{\frac{U\bar{d}}{2\kappa_h}} + \sqrt{\frac{Ul}{\kappa_h}}\right]$	2.94	°C	Average temperature
$r_{lm} = \frac{1}{1 + \frac{k_t}{0.67A_m k_h}\sqrt{\frac{2\kappa_h}{U\bar{d}}}}$	0.99		
$\theta_m = r_{lm}\left(\frac{3}{2}\frac{f.p_a.U}{\rho_h C p_h}\right)\cdot\left[\frac{A_a}{A_r}\sqrt{\frac{U\bar{d}}{2\kappa_h}} + \sqrt{\frac{Ul}{\kappa_h}}\right]$	4.40	°C	Maximum temperature
(ii) ROUGH-SMOOTH/LOW-SPEED: $L = \frac{Ul}{\kappa_{tape}} < 0.5$			
$r_l = \frac{1}{1 + \frac{k_t}{k_h}}$	0.98		Partition parameter
$\bar{\theta} = \frac{f.p_a.U}{k_t + k_h}\cdot\left[\frac{\bar{A}}{2}\frac{A_a}{A_r}\bar{d} + \bar{A}l\right]$	8.73	°C	Average temperature
$\theta_m = \frac{f.p_a.U}{k_t + k_h}\cdot\left[\frac{A_m}{2}\frac{A_a}{A_r}\bar{d} + A_m l\right]$	9.67	°C	Maximum temperature

Table 19 continued.

PARAMETER	VALUE	UNIT	*N.B.*
(iii) ROUGH-ROUGH/HIGH-SPEED: $L = \frac{3Ud_{max}}{16\kappa_{head}} > 10$			
$r_1 = \frac{1}{1+\sqrt{\frac{k_t\rho_t Cp_t}{k_h\rho_h Cp_h}}}$	0.90		Partition parameter
$\bar{\theta} = r_1\left(\frac{f.p_a}{\rho_h Cp_h}\right)\cdot\left[0.65\frac{A_a}{A_r}\sqrt{\frac{Ud_{max}}{\kappa_h}}+\sqrt{\frac{Ul}{\kappa_h}}\right]$	2.83	°C	Average temperature
$\theta_m = r_{1m}\left(\frac{f.p_a}{\rho_h Cp_h}\right)\cdot\left[0.95\frac{A_a}{A_r}\sqrt{\frac{Ud_{max}}{\kappa_h}}+1.5\sqrt{\frac{Ul}{\kappa_h}}\right]$	4.13	°C	Maximum temperature
(iv) ROUGH-ROUGH/LOW-SPEED: $L = \frac{3Ud_{max}}{16\kappa_{head}} < 0.5$			
$r_1 = \frac{1}{1+\frac{k_t}{k_h}}$	0.98		Partition parameter
$\bar{\theta} = \frac{f.p_a.U}{k_t+k_h}\cdot\left[0.28\frac{A_a}{A_r}d_{max}+\bar{A}l\right]$	3.45	°C	Average temperature
$\theta_m = \frac{f.p_a.U}{k_t+k_h}\cdot\left[0.33\frac{A_a}{A_r}d_{max}+A_m l\right]$	3.96	°C	Maximum temperature

The temperature within the drive was expected to be consistently higher than room temperature and strongly dependent on the position where it was measured. Heat can be generated within the drives, either mechanically (*e.g.* driving motor, cartridge loader motor, actuator, tape friction), electrically due to Joule effect (*e.g.* PCB, MRE) or magnetically (MRE, flux guides, actuator).

Accurate temperature monitoring is essential if one aims to correlate it to (and hence estimate) the friction at the head-to-tape interface from the previously discussed model.

3.1.4.4 Transient Regime

– Phase I –

As the drive was connected to the power supply heat was generated (Joule effect) in the drive electronic components. The corresponding τ (no sense current) layed between 10 to 15 min (~ 600 to 900 s) depending on the location within the drive (Table 21).

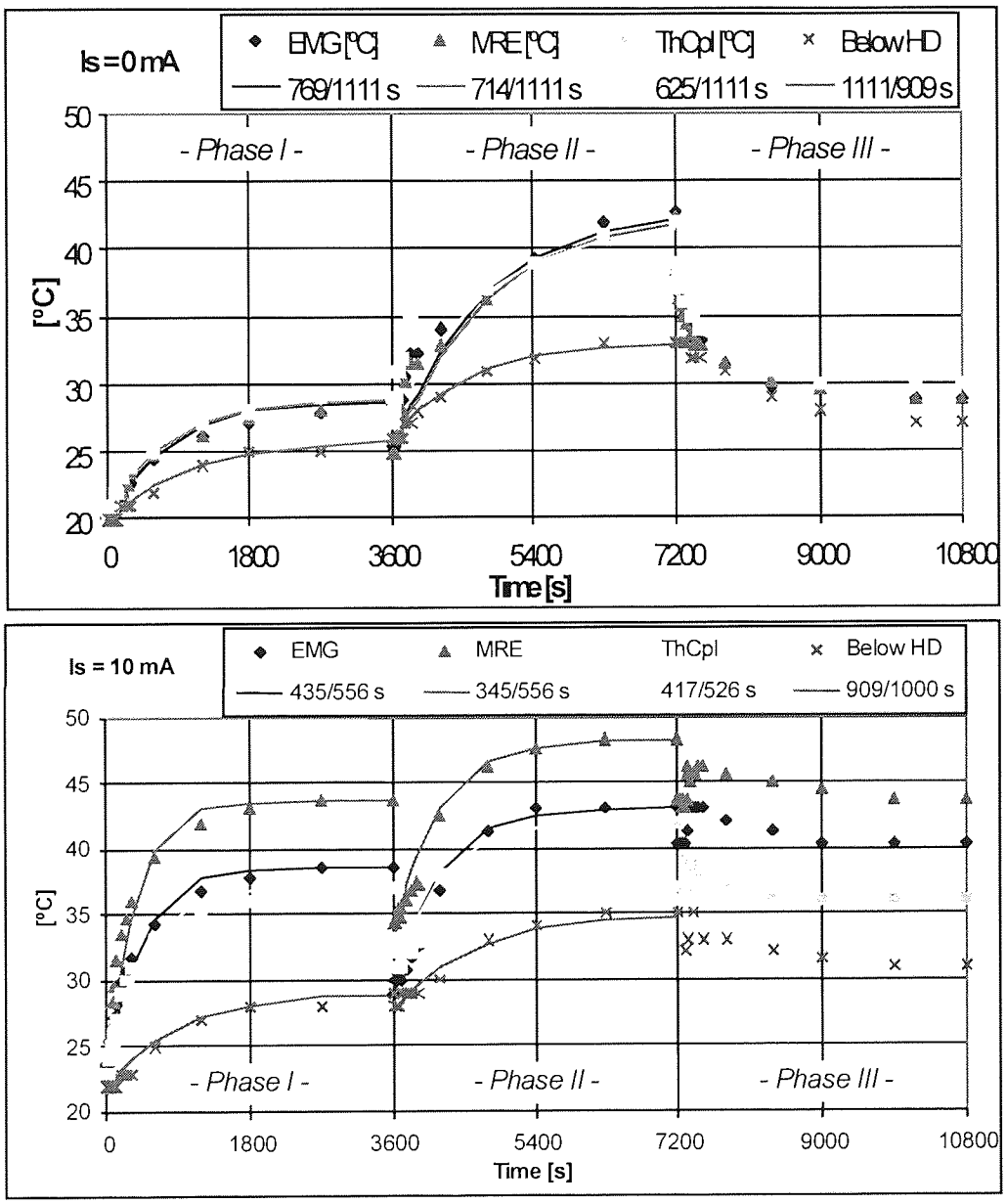

Figure 58. Temperature at the head-to-tape interface - with and without sense current - as measured via the EMG, MRE and thermo-couple fitted against the head. The thermo-couple placed below the head gives a measure of the ambient temperature. τ is indicated in seconds for phase I/phase II.

When a sense current ran through the MRE (measured here as I_S = 11.2 mA), an additional Joule effect ($\propto RI_S^2$) had to be considered. The source being the MRE, the temperature increase measured (Figure 58) *via* MRE (τ ~ 5 min) was therefore faster.

The power generated by the 8 MR elements ($R \sim 60\ \Omega$) is $8RI_S^2 \sim 48$ mW. The model described above calculated the rise in temperature at the head-to-tape interface due to the frictional power heat Q. The electrical power heat generated by the 8 MR elements has also its source at the head-to-tape interface, therefore can be substituted to the frictional power heat in the above model. The temperature increase due to the 8MR elements is calculated in Table 20. On Figure 58, at steady state, the temperature due to the MRE was measured as $\Delta T = T_{MRE} - T_{EMG} \sim 5°C$, which is in good agreement with the temperature calculated in Table 20.

Table 20. Temperature increase at the head-to-tape interface due to frictional power heat and electrical power heat, using the model described previously.

Heat source	Average increase in temperature ($\overline{\theta}$)	Maximum increase in temperature (θ_m)
Q = **72.9 mW** (Friction)	8.7°C	9.7°C
$8RI_s^2$ = **48 mW** (MRE)	5.8°C	6.4°C

Table 21. Temperature increase and time constant measured after Figure 58, phase I. TC stands for thermocouple and HD for head.

	I_s = 0 mA		I_s = 11.2 mA			
	Head	Below HD	MRE	EMG	TC HD	Below HD
ΔT [°C]	9	6	22	17	15	6
τ [minute]	10-13	18	5	7	7	15

– Phase II –

1) As a cartridge was inserted, a steep drop in temperature was observed ($\Delta T \sim 5°C$ in Figure 58). The drop occurred only when a tape came into contact with the head (Figure 59) and hence was barely related to the intrusion of the whole QIC body. Further evidence is that the temperature at locations remote from the head-tape contact (*e.g.* at motor or ground screw) was little affected.

The tape coming to contact with the head, heat *convection* to air ($\propto h.A.(T_{EMG}-T_{Below})$) was taken up by *conduction* to the tape ($\propto k_{tape}.A.(T_{EMG}-T_{QIC})/\Delta x$). Using h = 10 W/(m^2.K), k_{tape} = 0.38 W/(m.K), A ~ tape width × head width ~ 2.4 mm^2, $T_{EMG}-T_{Below}$ ~ 12°C, $T_{EMG}-T_{QIC}$ ~ 20°C, one finds: convection ~ 290 μW vs. conduction ~ 3.0 W. The loss by convection to air could not compete with the loss by conduction to the inserted tape, even considering the estimation uncertainty. The four-order of magnitude difference is indeed believed to prompt the immediate temperature drop at the head-to-tape interface. As the tape temperature increased inside the drive, the losses would decrease probably by one order of magnitude (as ΔT changed from 20 to ~ 2°C, the loss changed from 3.0 to 0.3 W).

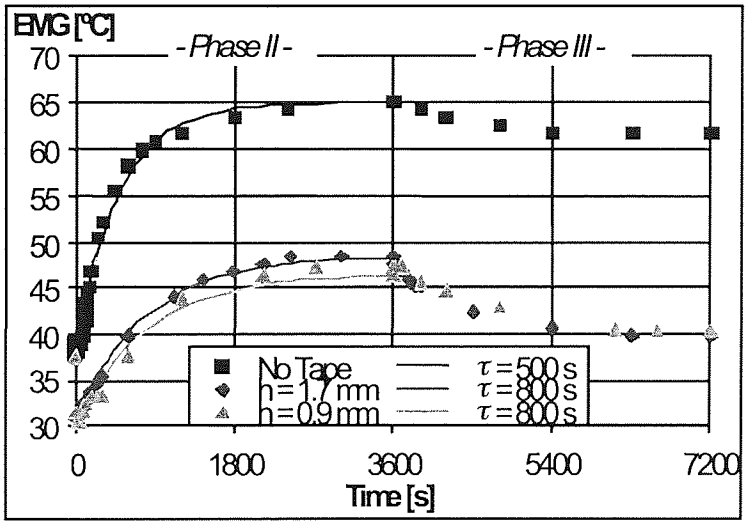

Figure 59. Temperature measured at the head-to-tape interface via the EMG for different protrusion depth. 'No tape' indicates the insertion of a QIC where the whole tape had been rolled around one reel, therefore not present in the head window. The initial temperature is in all cases 37 °C.

2) As the tape started to slide against the head at a speed of 1 m/s, friction produced heat. A bump is observed in Figure 58 for I_S = 0 mA at beginning of phase II. The EMG bump fits equation (50) with τ ~ 100 s (not shown), which is slightly shorter than the sensor current heating time constant: the source is now located right at the head-to-tape interface, with which the EMG is flush.

The contribution of the frictional heat to the temperature increase at the head-to-tape interface is cumbersome to isolate from the other contributions. However, it seems reasonable to assume it as being proportional to the temperature difference between the EMG and the thermo-couple below the head in steady state. That temperature difference was

found to be the most stable over several experiments (here ~ 9.4 ± 1.1°C), and was not affected whether or not a sense current caused the MRE to heat up. This temperature difference is comparable to Bhushan's model prediction (temperature increase due to friction: $\overline{\theta} = 8.7°C$ and $\theta_{max} = 9.7°C$) provided that the protrusion depth $h = 1.7$ mm and the friction coefficient $f = 0.3$. $f = 0.2$ and $f = 0.4$ correspond to $\overline{\theta} = 5.8°C$ and $\overline{\theta} = 11.7°C$, respectively.

The *protrusion depth* did not affect the temperature drop at head to tape contact (*c.f.* Figure 59). However, decreasing the protrusion depth from $h = 1.7$ mm to $h = 0.9$ mm was found to decrease the steady state temperature by up to 1°C. Using Bhushan's model, one finds a corresponding decrease

(i) *power heat* $Q = f.F_n.U$ from 73 to 38 mW,

(ii) *average temperature* from ~ 8.7 to 8.0°C and

(iii) *maximum temperature* from ~ 9.7 to 8.8°C.

An increase of the time constant for reaching the steady state from $\tau \sim 8$ min (no tape) to $\tau \sim 13$ min (tape in contact with the head) is noticeable, a retard attributed to the tape cooling effect.

Table 22. Temperature increase and time constant measured after Figure 58, phase II. TC stands for thermocouple and HD for head.

	$I_s = 0$ mA		$I_s = 11.2$ mA			
	Head	Below HD	MRE	EMG	TC HD	Below HD
ΔT [°C]	17	7	14	14	11	7
τ [minute]	18	15	9	9	9	17

– Phase III –

The motor stops while the power is still on. The drive gradually recovers the steady state it had in phase I.

3.1.4.5 *Steady State Regime*

The friction coefficient was calculated using

$$f \sim \frac{\bar{\theta}}{r_1\left(\frac{p_a}{\rho_h C p_h}\right)\cdot\left[0.65\frac{A_a}{A_r}\sqrt{\frac{\overline{Ud_{max}}}{\kappa_h}}+\sqrt{\frac{\overline{Ul}}{\kappa_h}}\right]}, \qquad (65)$$

derived from Bhushan's model (Table 19; rough-smooth, low speed case (i)) - the contribution of f to the apparent pressure p_a was neglected. $\bar{\theta}$ was taken as the temperature difference between the EMG and below the head, which as discussed above (transient regime), is mainly attributed to the frictional heat at the head-to-tape interface (provided the reference resistance R_o in (48) stays constant throughout the experiment—*c.f.* 2.3.5.1).

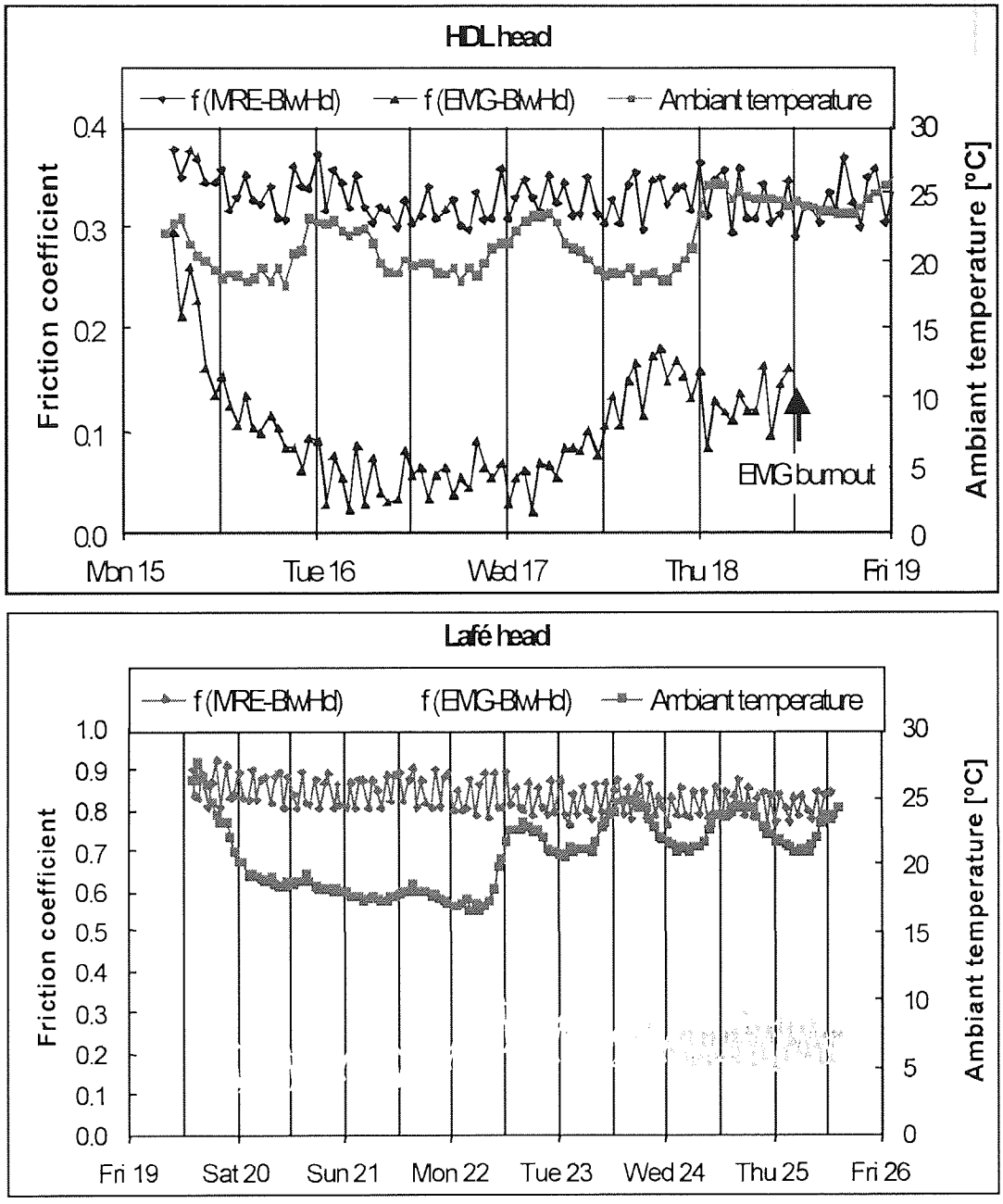

Figure 60. Continuous wear test for a HDL (upper chart) and Lafé (lower chart) heads in non-controlled environment. The friction coefficient is calculated using (65) where $\overline{\theta}$ *is taken as the temperature at the EMG minus the temperature below the head.*

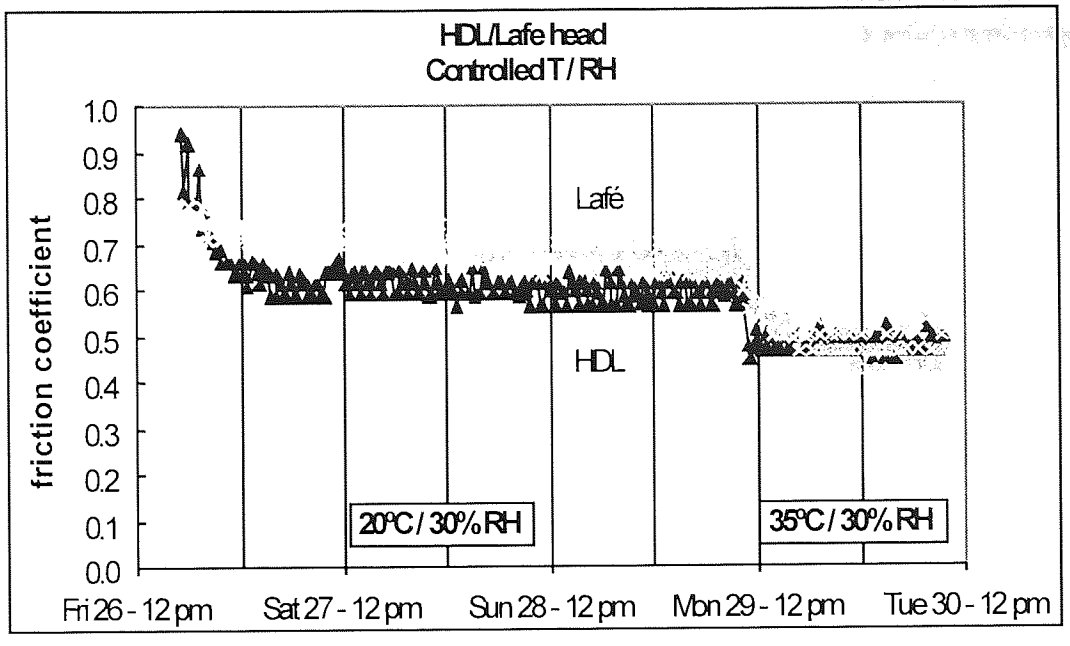

Figure 61. Continuous wear test for a HDL and Lafé heads in controlled environment.

The result of (65) is plotted Figure 60 for non-controlled environment (range: 20—40°C and 30—60% RH) and Figure 61 for controlled environment (20°C / 30% RH then 35°C / 30% RH). HDL and Lafé refer to two different head manufacturers (*c.f.* Figure 22). The accuracy of the measurement can be estimated from the fluctuation in temperature as ±2°C. Most of this fluctuation is attributed to changes in the cartridge configuration, the tape being wound around reels at different distance to the head.

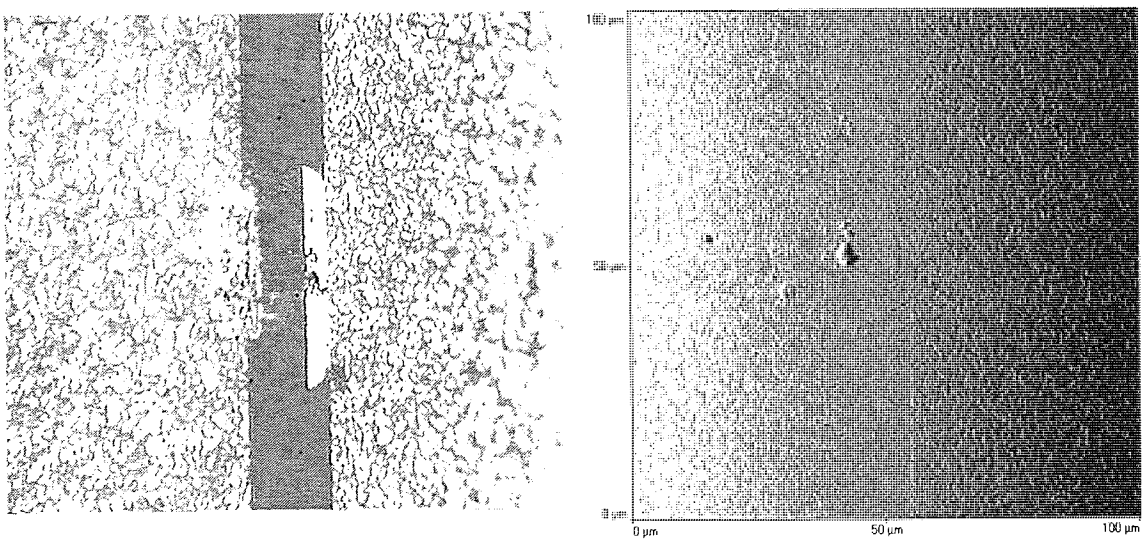

Figure 62. EMG burnout observed with an optical microscope (left) and AFM (right—image not levelled).

An instant drop was observed for HDL heads in all cases, down to a relative minimum after 24 hrs ($f \sim 0.05$) in non-controlled environment (Figure 60) and 12 hrs ($f \sim 0.6$) in controlled environment (Figure 61), supposedly in relation with deposition of stain at the head-to-tape interface. In non-controlled environment, the friction increased after 48 hours up to a maximum ($f \sim 0.15$) corresponding to a minimum in ambient temperature. As the ambient temperature increased again, the friction slightly decreased. This may pertain to the thermodynamic property of stain, mainly of polymeric nature. After 78 hours of testing, the EMG resistance burned out (Figure 62). The EMG is a particularly sensitive thin magneto resistive stripe, and the drive deck, the PCB and the multi-channel voltmeter must be carefully grounded all together to minimize the chances of EMG burn-out. It is located opposite to the bright D-shaped tip embodied in the insulator layer (Figure 62, left).

In controlled environment, for HDL heads the friction was found almost constant ($f \sim 0.6$) after the initial drop, as long as the ambient temperature stayed constant. As the ambient temperature increased form 20 to 35°C, the friction abruptly decreased ($f \sim 0.5$) and re-mained constant. No initial drop was observed for Lafé heads, whose friction was found to strongly fluctuate around a stable average value.

Friction fluctuation is related to the presence of a transfer film on the head surface (slid-ing of two polymers - tape coating / head staining - against each other): staining was clearly observed on the head tested for 100 hours. A decrease in friction with increasing temperature was obvious in controlled environment: HDL transition was abrupt whilst Lafé transition was more progressive.

A sidebar shift, that is a recession between the end-block and the ship-coverbar assembly may occur at the Lafé tape-bearing surface (Figure 22) resulting in less severe contact between head and tape, hence reducing the effect of wear and transfer on the head-to-tape interface dynamics.

3.1.5 Wear tests in controlled environmental conditions

3.1.5.1 AFM analysis of ADR heads tested in five controlled environmental conditions

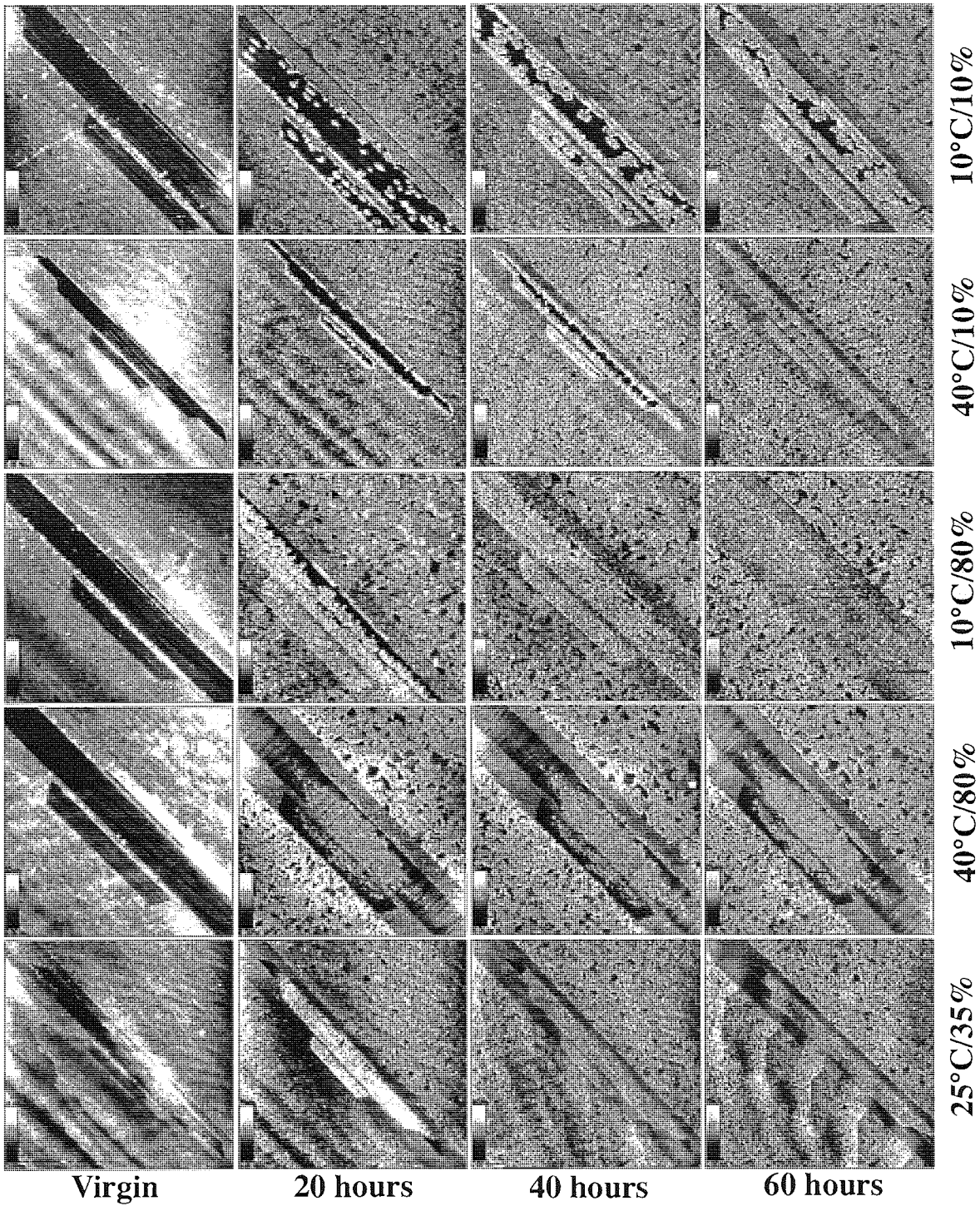

Figure 63. AFM map of the pole tip region in the five environmental conditions, from 0 to 60 hours.

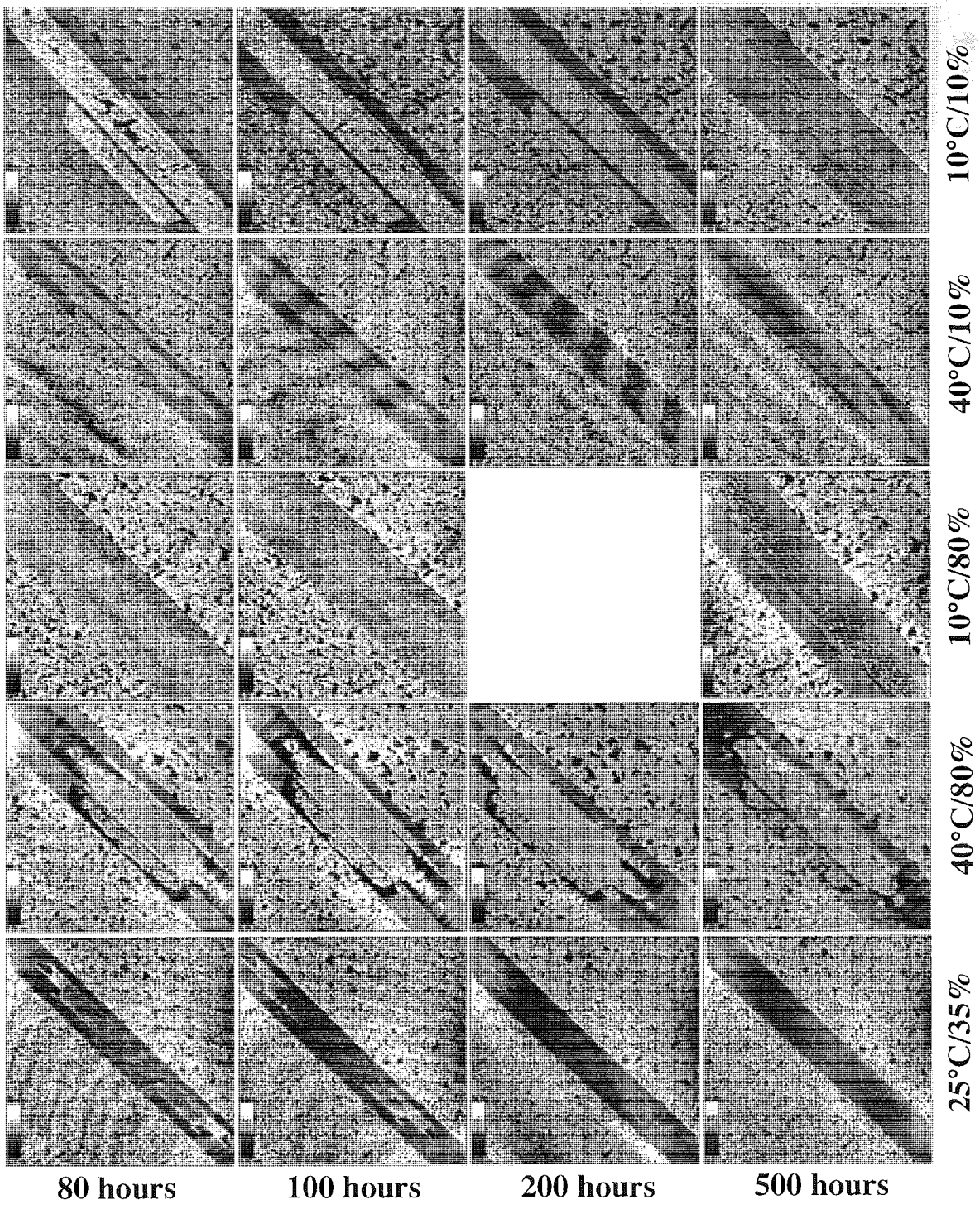

Figure 64. AFM map of the pole tip region in the five environmental conditions, from 80 to 500 hours.

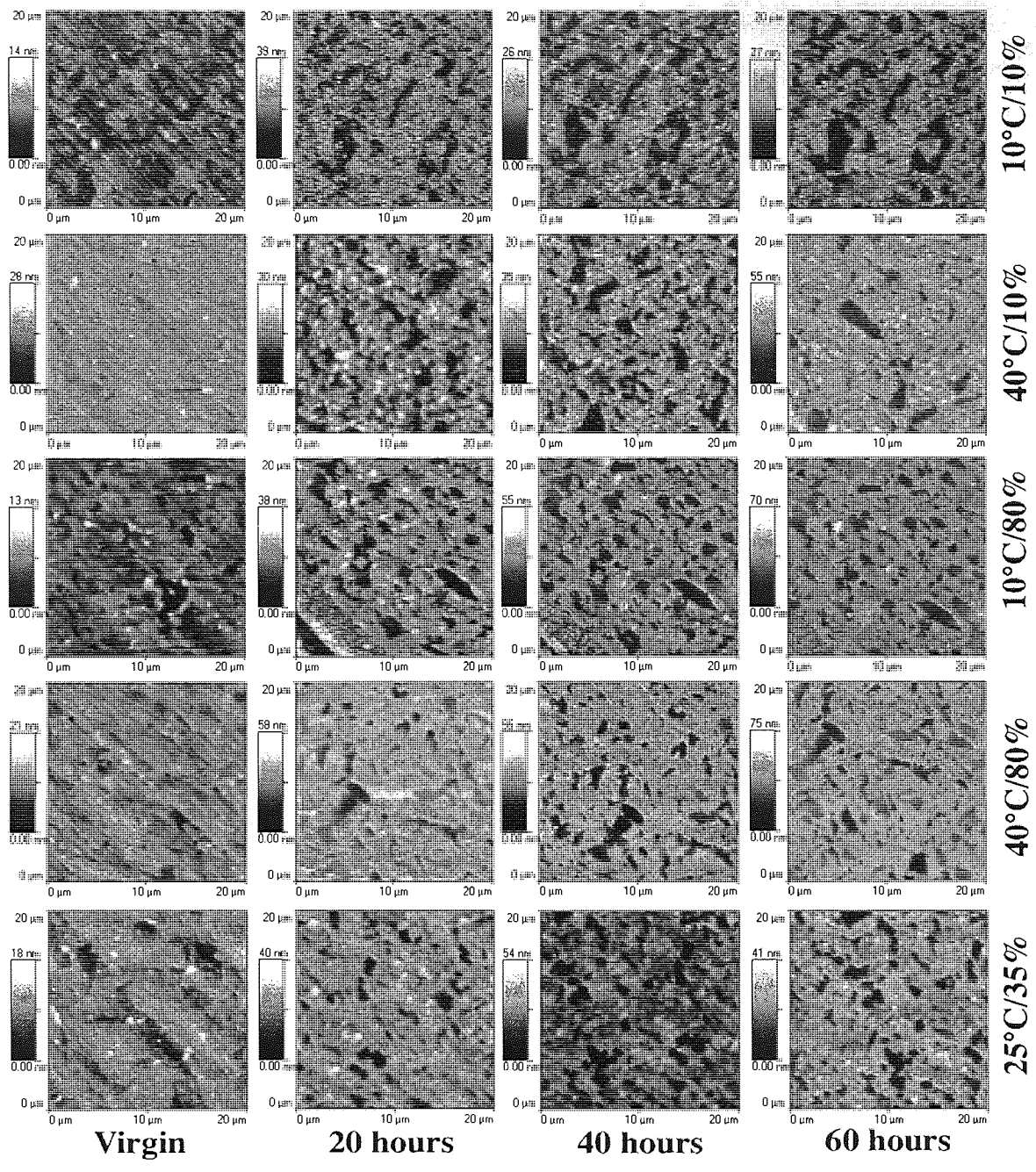

Figure 65. AFM map of the tape-bearing surface in the five environmental conditions, from 0 to 60 hours.

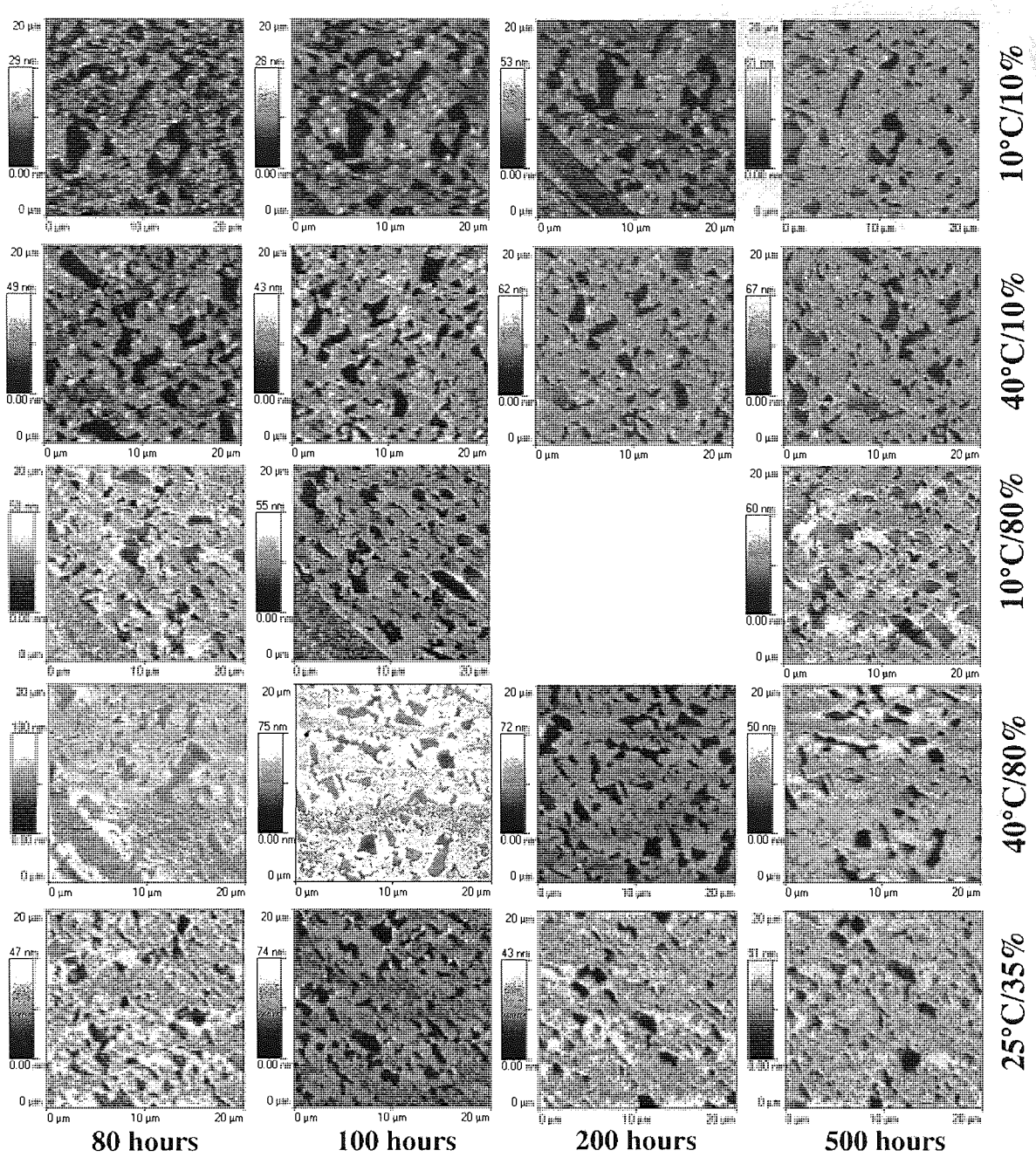

Figure 66. AFM map of the tape-bearing surface in the five environmental conditions, from 80 to 500 hours.

AFM topography maps of the pole region of heads tested in the five environmental conditions, for up to 500 hours are shown in Figure 63 and Figure 64. Figure 65 and Figure 66 show an enlarged image of the read side ceramic area (upper right). The scanning direction was chosen to be at 45° with respect to the sliding direction, to distinguish scratches parallel to the sliding from scanning line artefacts.

Within the first 20 hours of test, a pattern formed at the tape-bearing surface in relation to the appearance of a series of pullouts (darker area, *i.e.* recessed area). These pullouts have been clearly identified as targeting the TiC.

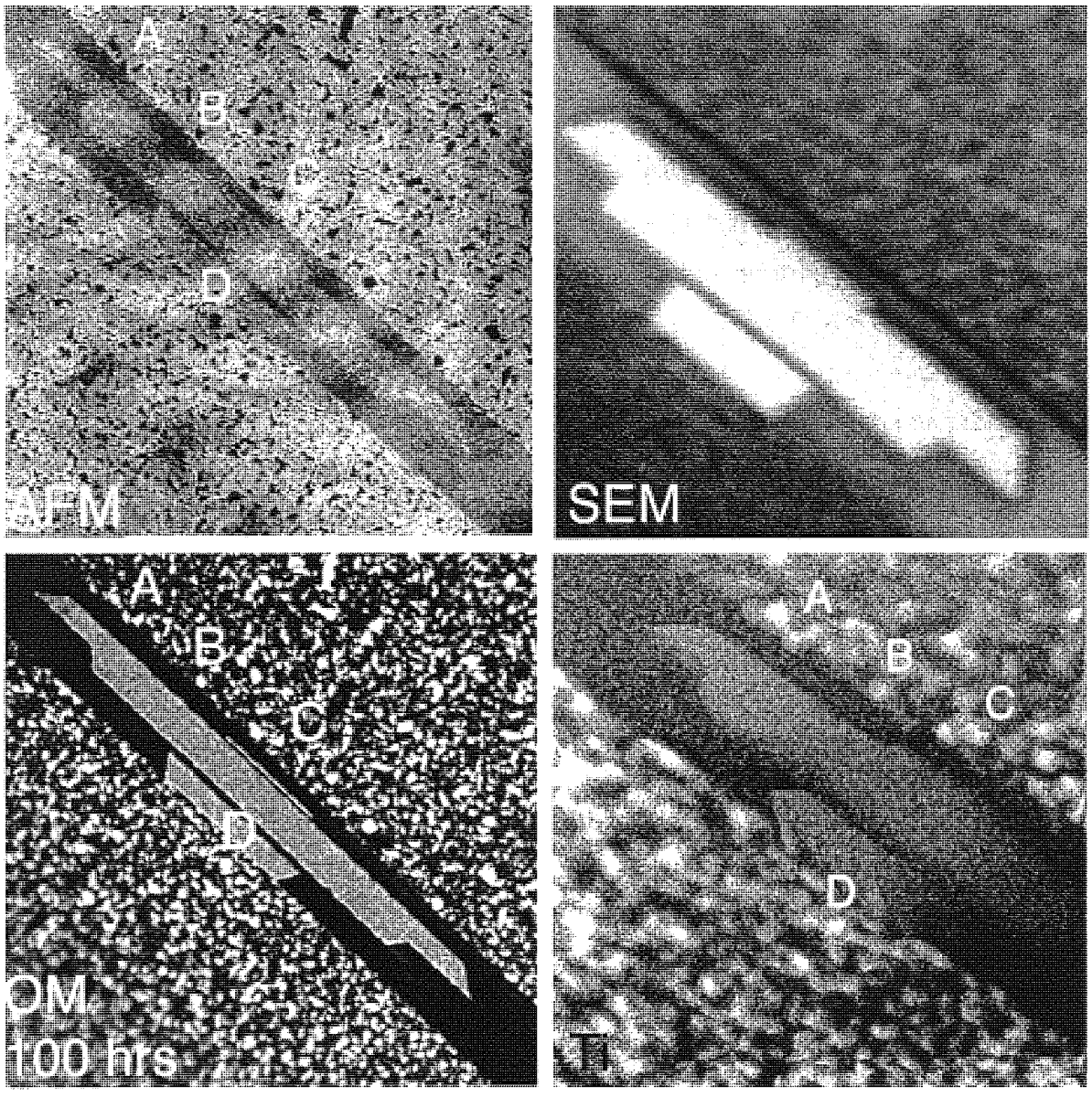

Figure 67. Atomic force micrograph (upper left), optical micrograph (lower left), scanning electron micrograph (upper right) and Auger electron map for oxygen (lower right) of a head tested at 40°C/10% RH for 500 hours.

Figure 67 shows views of an ADR head (one selected channel out of eight) obtained using four different imaging techniques: atomic force microscopy (AFM), scanning electron microscopy (SEM), optical microscopy (OM) and Auger electron spectroscopy (AES). The TiC appears as bright spots on the Ti AES map. These spots correspond exactly to the ones appearing on the OM image where (as on the SEM image) both the pole and the

TiC region, metal-like materials, are expected to appear clear. Moreover, the patterns seen on the ceramic surface are similar in all respects on the OM and AFM image, and thus clearly indicate that the recessed region (*i.e.* dark on the AFM topographic map) corresponds to the TiC grains.

The left side of Figure 68 illustrates the surface topography profile measured by AFM, *i.e.* $z(x)$; the recessions correspond to the TiC intra-grain pullout (or delamination). The right side of Figure 68 corresponds to the bearing ratio BR(z), *i.e.* the percentage of data points which height is above z. The BR ratio curve typically features three plateaux delimited by two transitions—the intermediate plateau relates to the steep pullout sides and dwells between 70~80%, which corresponds to the ratio Al_2O_3 to TiC. d is chosen as a measure of the pullout depth, the height difference between these two transitions (measured at the inflexion points); this measure was fairly invariable between different profiles.

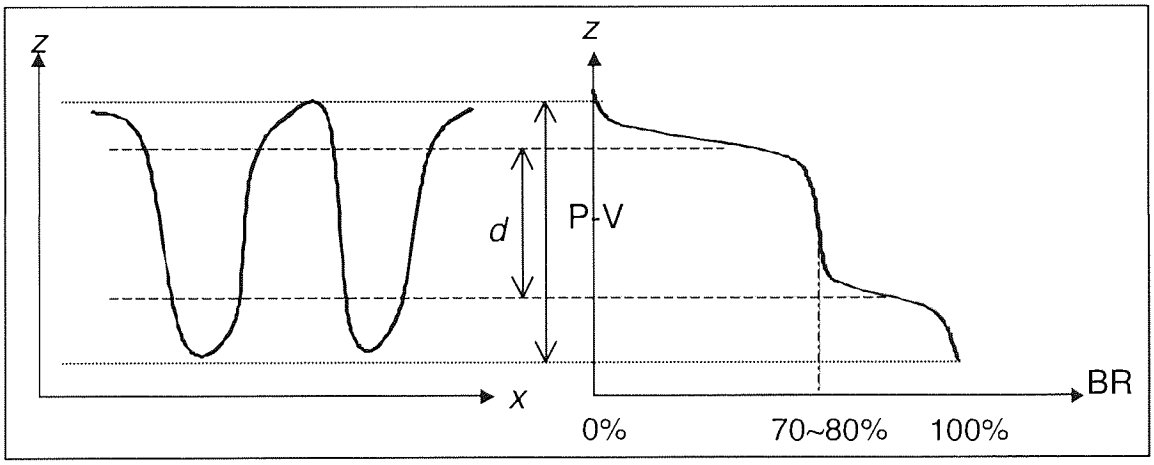

Figure 68. AFM profile (right) and corresponding bearing ratio (BR) measurement (left) for a worn Al_2O_3-TiC ceramic; the TiC phase corresponds to the recessed part on the AFM profile.

The pullout depth was fit to the following equation:

$$d = (d_S - d_o) \cdot \left(1 - e^{-t/\tau}\right) + d_o \qquad (66)$$

where d, d_o and d_s are the pullout depth respectively at time t, beginning of test and end of test, and the time constant τ indicates how fast d converges towards d_s.

The pullout depth is plotted in Figure 69. Accuracy was estimated by comparing successive measurements, on the same bearing ratio curve and on different curves measured

over the same head surface. The error Δz was thus never exceeding 5 nm. This is valid for all pullout measured after the bearing ratio, reported in this thesis.

After 500 hours of test the pullout depth is, to a good approximation, independent of the environmental condition (20 ~ 23 nm). At an earlier stage, high relative humidity (80%) resulted in the deepest pullouts (~ 24 nm and ~ 18 nm, at 40°C and 10°C respectively after 200 hours). Given a relative humidity, pullout depth increased with temperature. These variations in pullout depth at an early stage of the test were likely to relate to a preferential transfer of tape material within the pullout, promoted at low humidity: stains accumulated within the recession decreasing the measured pullout depth. As the test proceed the stains eventually decreased in thickness.

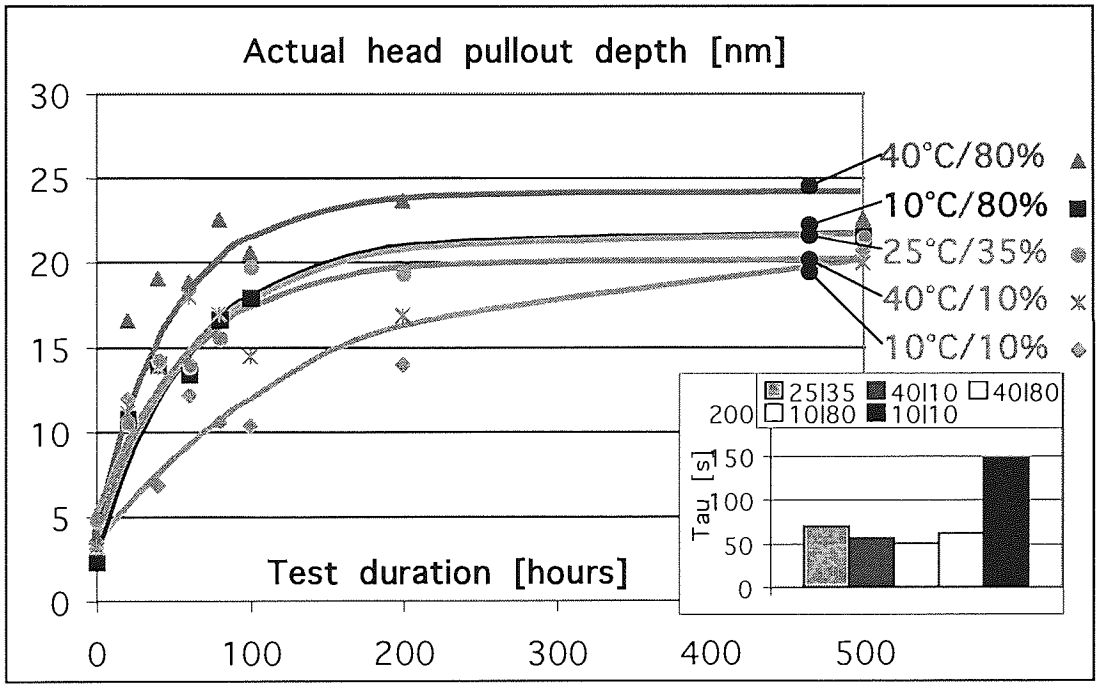

Figure 69. TiC intra-grain pullout depth measured at the tape-bearing surface of ADR heads. The lines are power trend interpolated to the scatter data using equation (66). The deeper pullouts are measured at high humidity. At a given RH, high temperatures correspond to deeper pullouts. After 500 hours the depth at any conditions falls into a narrow range between 20 and 23 nm.

In all conditions other than the *hot and humid* condition, a transfer film was deposited over the whole pole tip area (*c.f.* Figure 63, Figure 64 and Figure 70). A maximum thickness of about 40 nm was reached after ~ 20 hours, after whitch the film tended to level with the surrounding insulator filling the pole-tip recession. The film was then ~ 20 nm thick which corresponds roughly to the magnetic particle thickness. At low humidity, the

film formed at the pole edges and along the pole scratches then spread towards the centre. At higher humidity, the film formed at the centre of the pole.

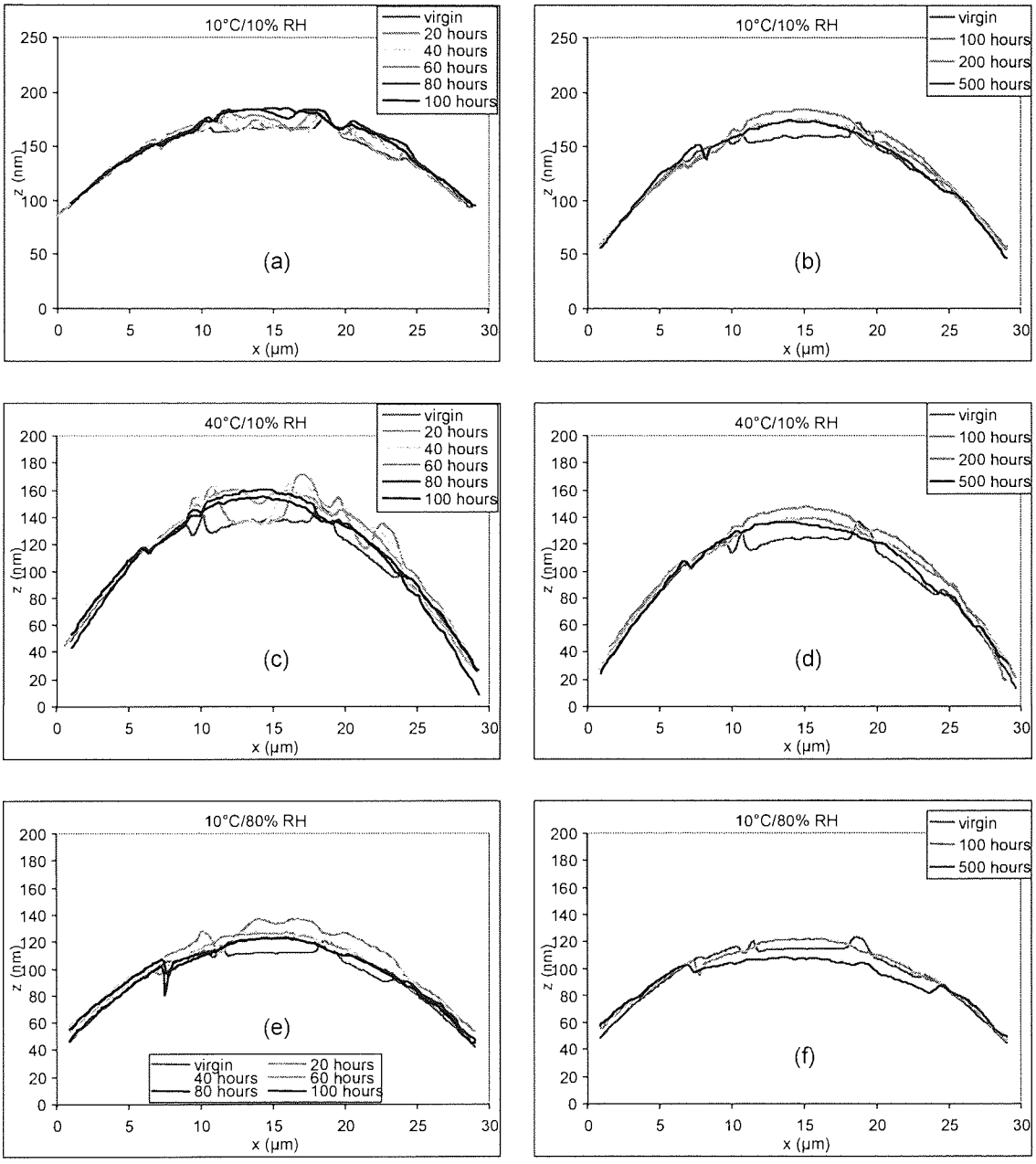

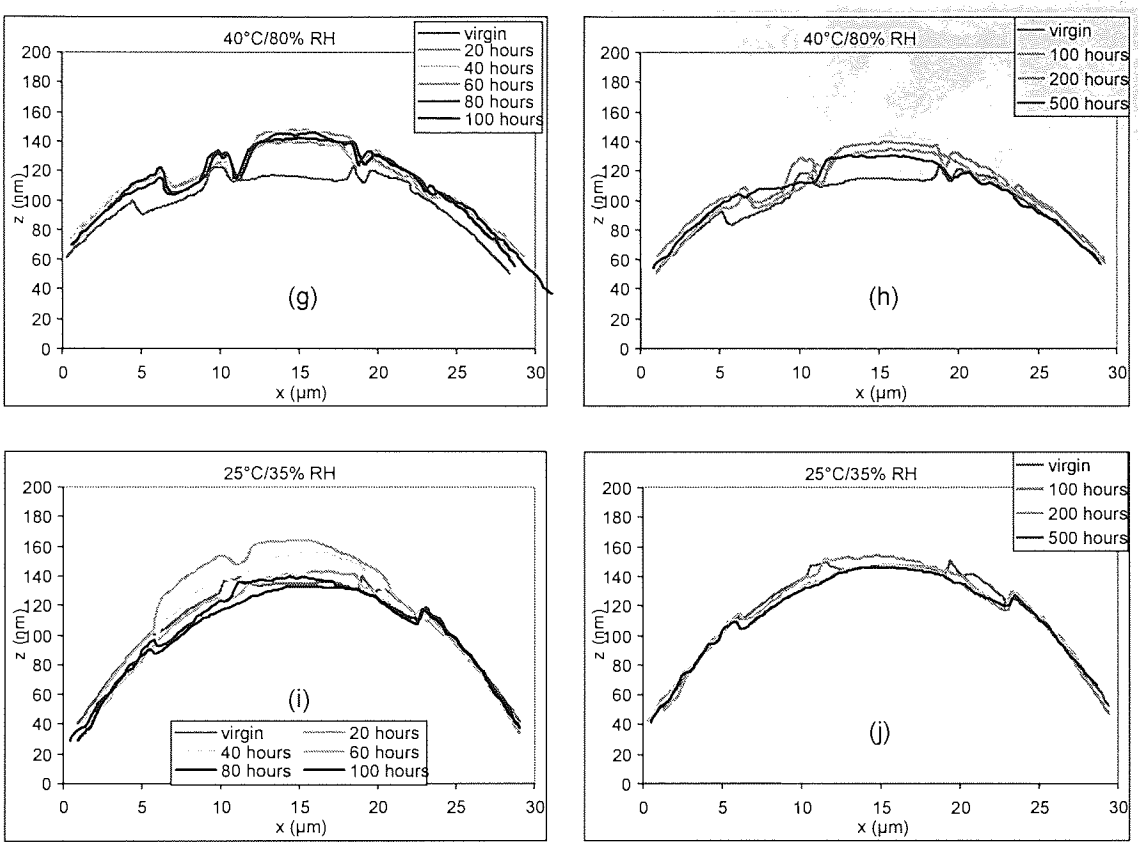

Figure 70. Averaged cross section of ADR heads (central pole-tip area) as measured by AFM at different stages along the wear test in five environmental conditions.

3.1.5.2 *High resolution AFM analysis of ADR heads tested in five controlled environmental conditions*

Figure 71 shows high-resolution AFM (HR-AFM) in non-contact mode of the Al_2O_3-TiC tape-bearing surface, virgin (top-left) and after 500 hours of test (remaining). In all conditions except 40°C/80%, scratches can be seen at the bottom of the TiC intra-grain pullouts, flecks on and ripples across the protruding surface, indicative of the presence of stain. The scratches reveal the presence of a soft material (transfer film) at the bottom of the TiC intra-grain pullouts, whereas ripples were presumably caused by a slip-stick mechanism occurring at the head-to-tape interface upon sliding.

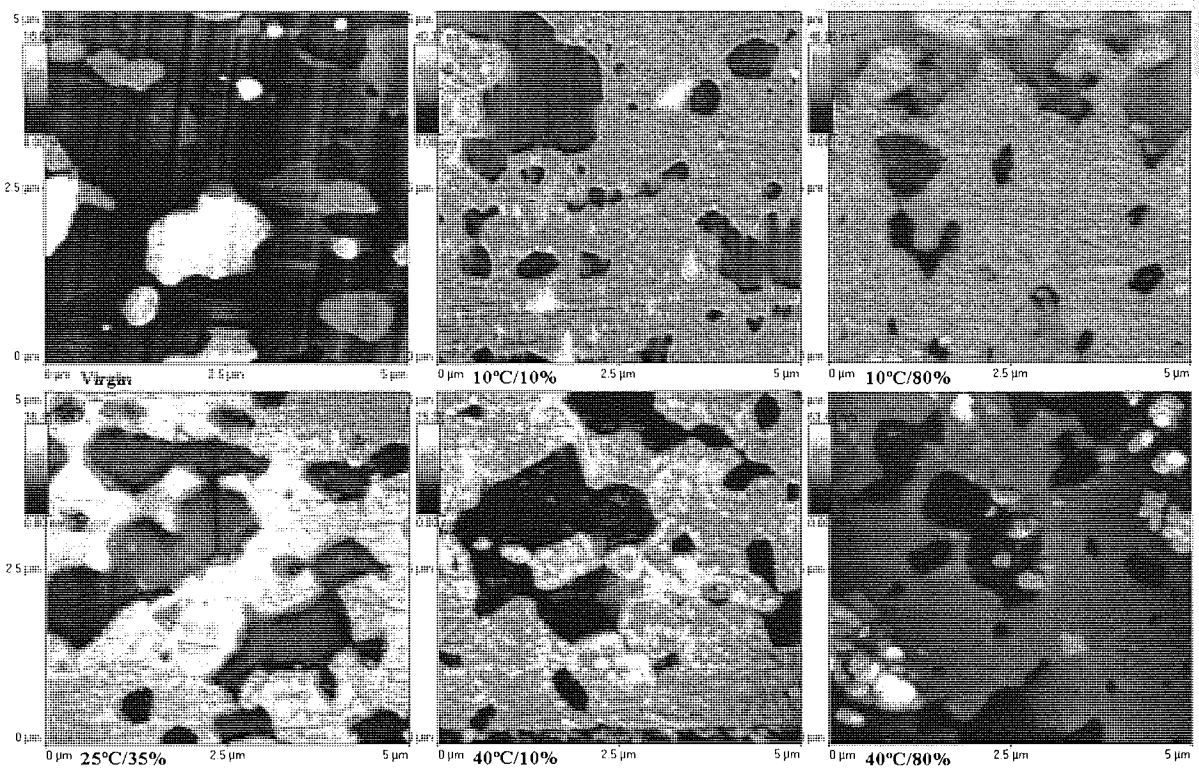

Figure 71. High resolution non-contact AFM of the ceramic tape-bearing surface. A virgin head is shown at the top left; the remaining has been tested for 500 hours. The direction of sliding is the vertical direction.

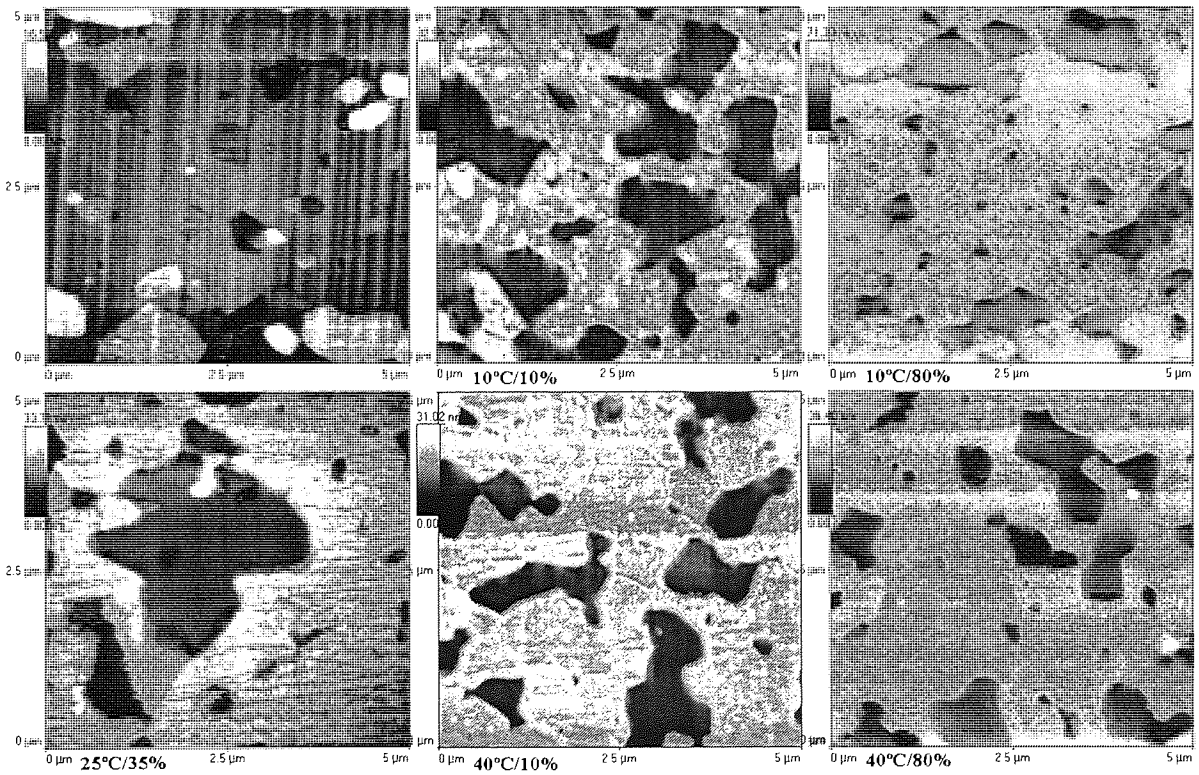

Figure 72. High resolution contact AFM of the ceramic tape-bearing surface. A virgin head is shown at the top-left; the remaining has been tested for 500 hours. The direction of sliding is the vertical direction.

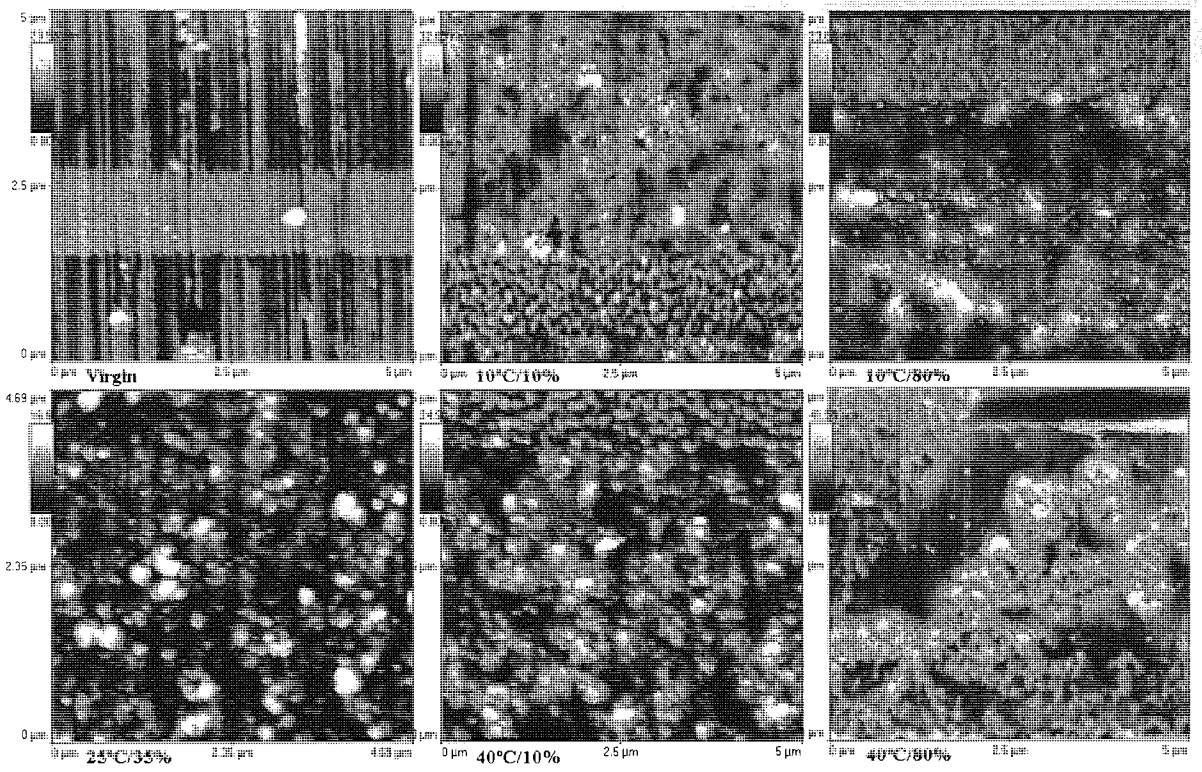

Figure 73. High resolution non-contact AFM of the pole tip area. A virgin pole tip is shown at the top left; the remaining has been tested for 500 hours. The direction of sliding is the vertical direction.

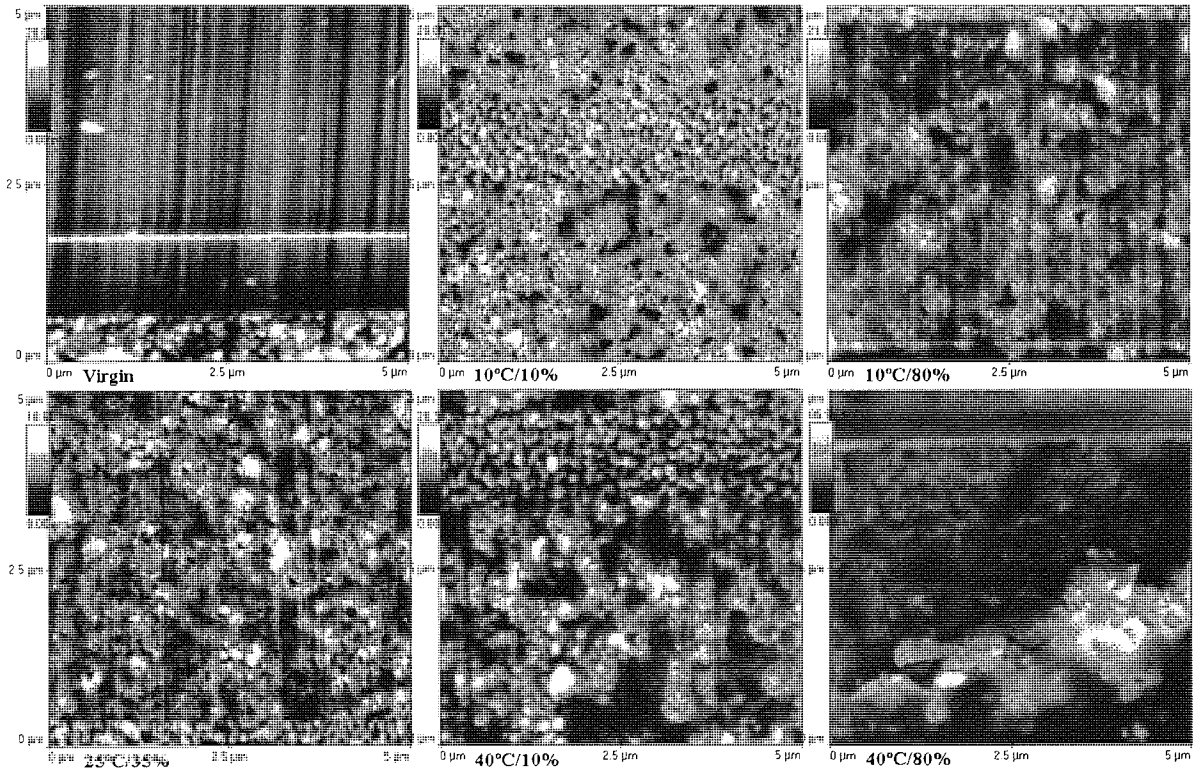

Figure 74. High resolution contact AFM of the pole tip area. A virgin pole tip is shown at the top left; the remaining has been tested for 500 hours.

The hot and humid condition (40°C/80%) result in a generally clean surface stained with discrete scattered lumps.

The contact mode (Figure 72) shows the same general features as the non-contact mode. The only difference seems to be the removal of some deposits/flecks away from the surface by the tip.

Two sorts of stain can be seen on the high-resolution image of the pole tip area (Figure 73 and Figure 74): (i) a transfer film—conglomerate of deposits bound together upon sliding—prominent at low temperature and humidity (10°C/10%) and (ii) lumpy deposit, prominent at 40°C/80%.

Lower temperature resulted, in smoother stain, compared to the lumps forming at higher temperature. The thinner stain was found at 10°C/80%. Evidence of needle-like magnetic particles could not be found at that resolution. Other than the resolution, the binder may envelop hence screen the particles.

3.1.5.3 OM analysis of ADR heads tested in five controlled environmental conditions

The optical micrograph presented in Figure 75 allows assessing the colour of stain, ranging from clear to dark brown (the latter at low humidity and for tenacious stain at 40°C/80%). The brown colour is typical of stain containing magnetic pigment and produced by γ–Fe_2O_3 tapes. Similarly, blue stain usually occurs when using MP tapes [158, 82]. The stain hue (interference colours) gives an indication of the stain thickness, which therefore increases in the order: 10°C/80%, 25°C/35%, 40°C/10%, 10°C/10% and 40°C/80% (only at pole centre).

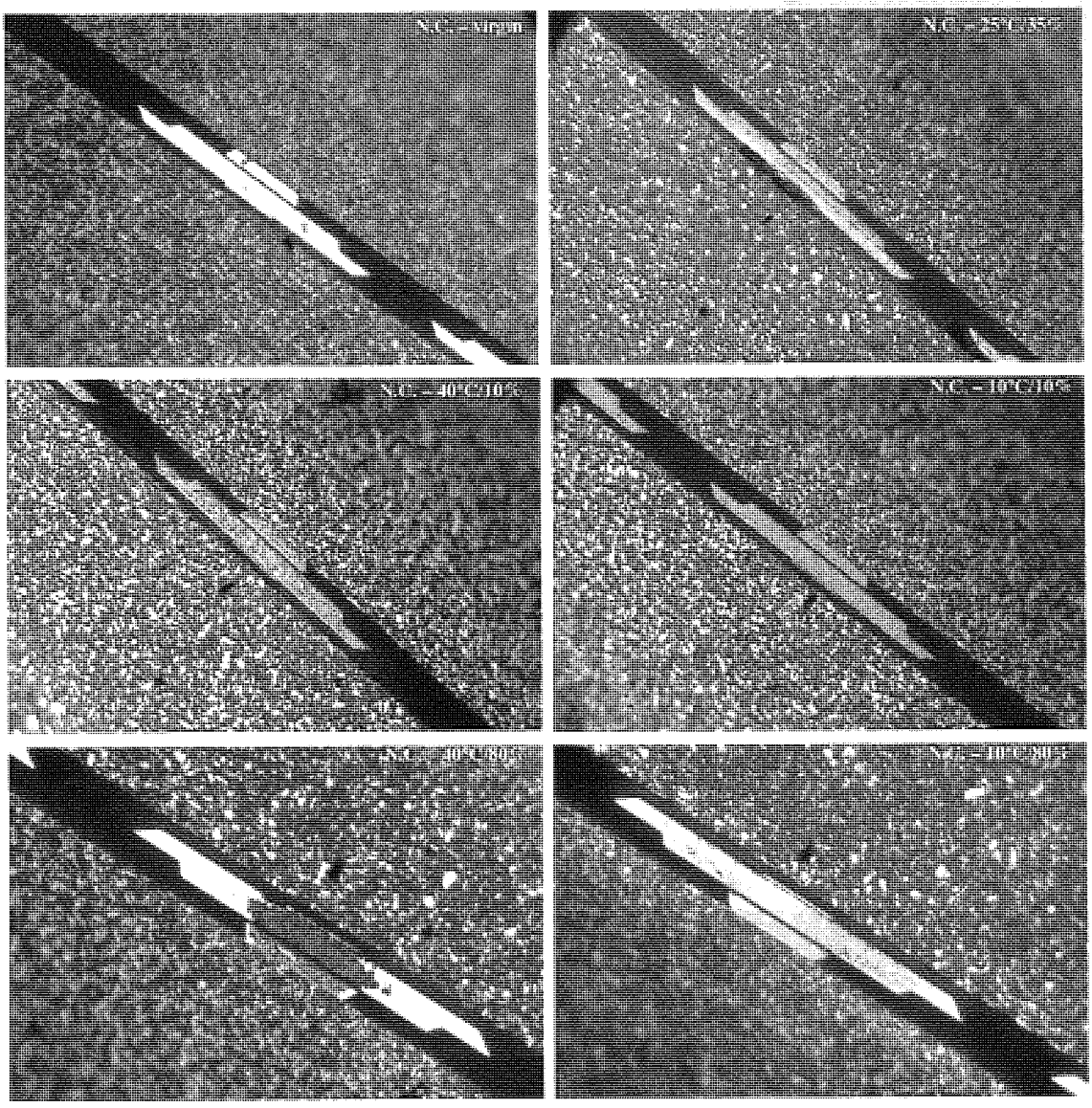

Figure 75. Optical micrograph of the pole tip region in the five environmental conditions, after 500 hours of test.

3.1.5.4 AES analysis of ADR heads tested in five controlled environmental conditions

AES for Al, Ni, Fe, Ti, O and C are presented in Figure 76. Fe was found in its highest concentration over the pole tip area with the exception of the 40°C/80% condition; in hot and humid condition organic friction polymer is more likely to transfer onto the head surface, therefore differing from the ferrite-rich stain transferred in other conditions.

In *hot and humid* condition, a lozenge was clearly identifiable, which delimitated a carbon rich area. The lozenge (clearly visible on the C map) corresponds to a previously ex-

posed area contaminated with carbon. C was also found in high concentration in discrete spots all over the head surface attributed to debris mostly composed of organic material (friction polymer) transferred from the tape binder.

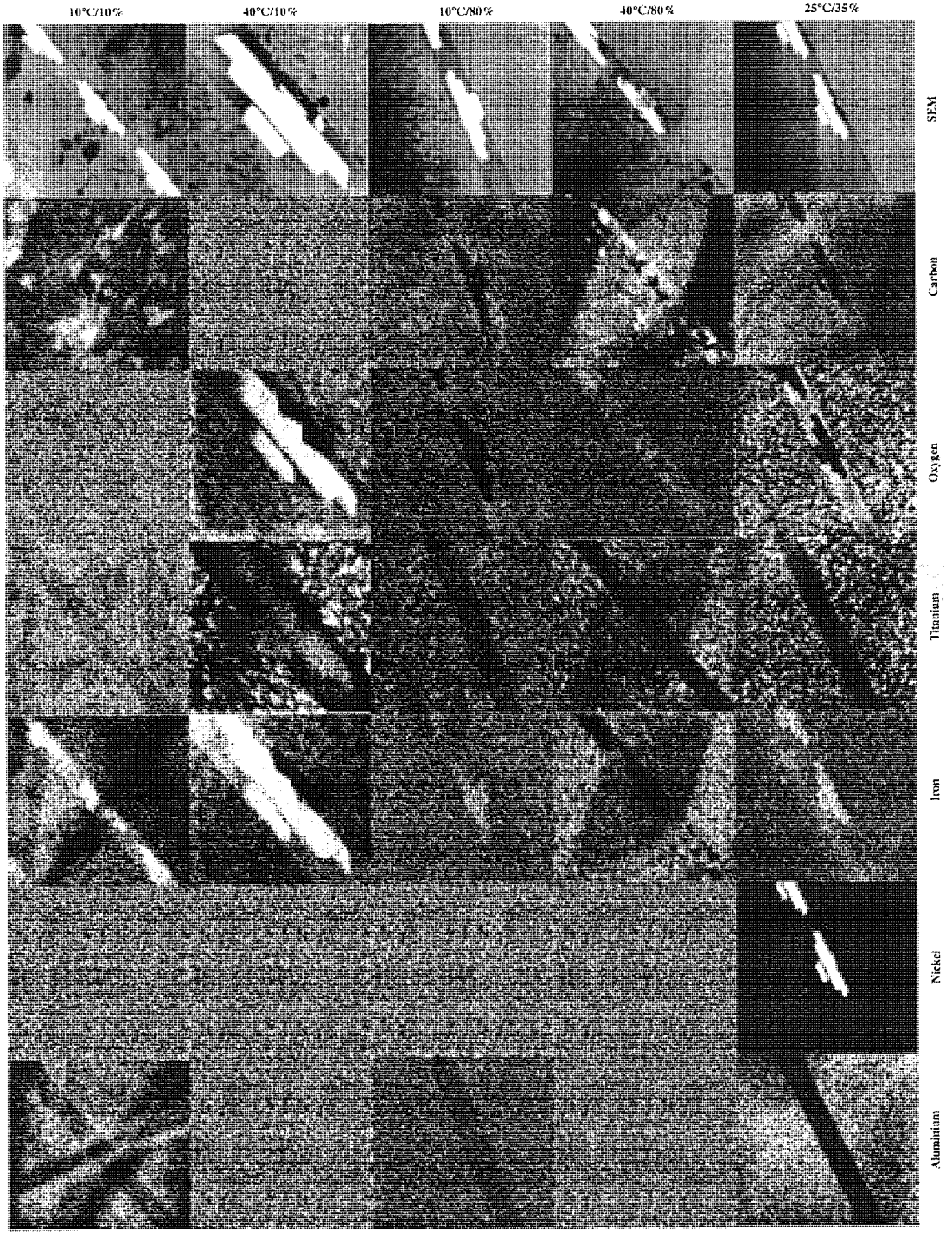

Figure 76. AES map for Al, Ni, Fe, Ti, O, C and secondary electron (SEM), in four environmental conditions, after 500 hours of test.

3.2 Coated heads

3.2.1 SPL coated heads—wear tests in controlled environmental conditions

3.2.1.1 AFM analysis of SPL coated heads

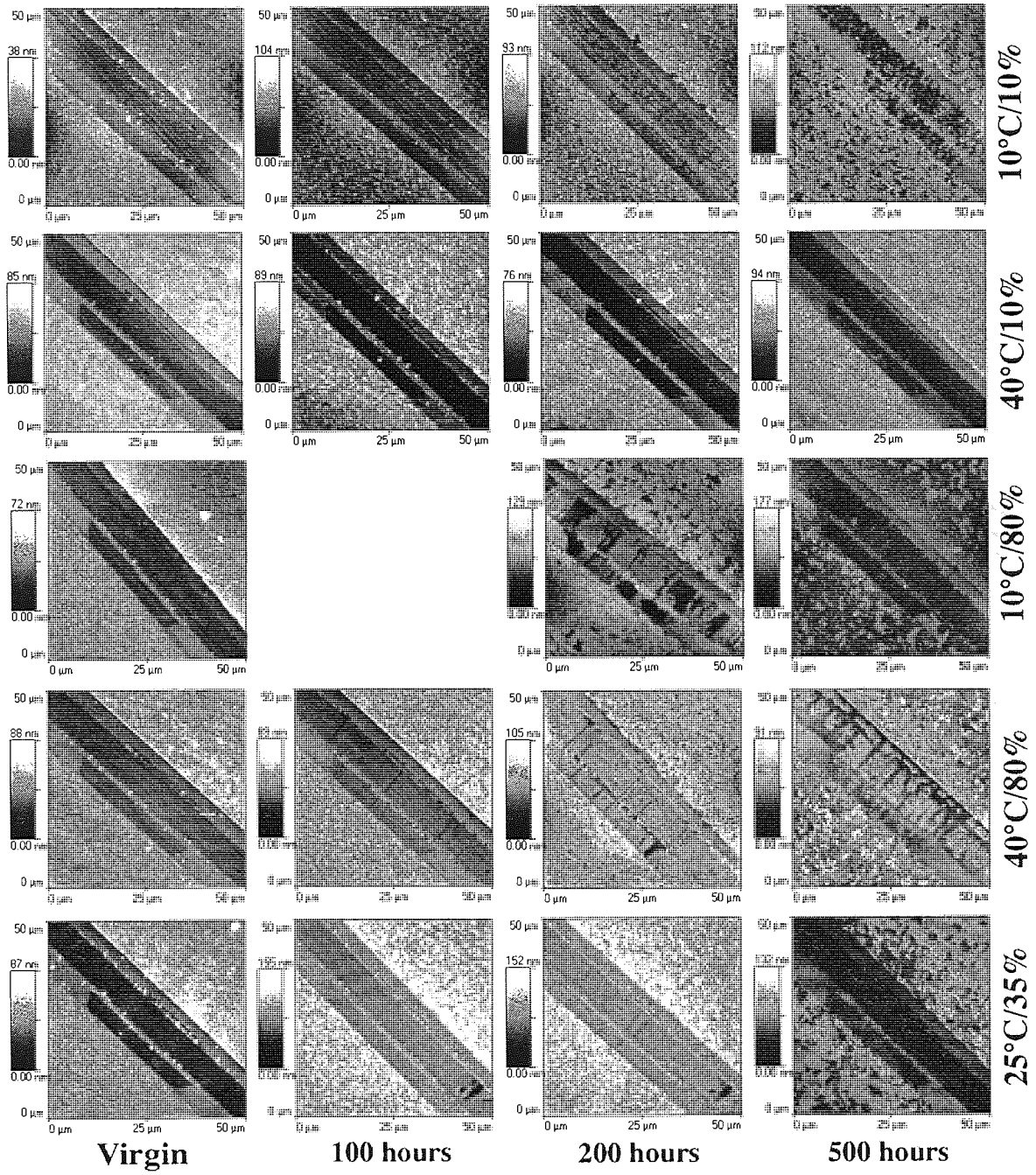

Figure 77. AFM map of the pole tip region of 20 nm SPL coated heads in the five environmental conditions, from 0 to 500 hours.

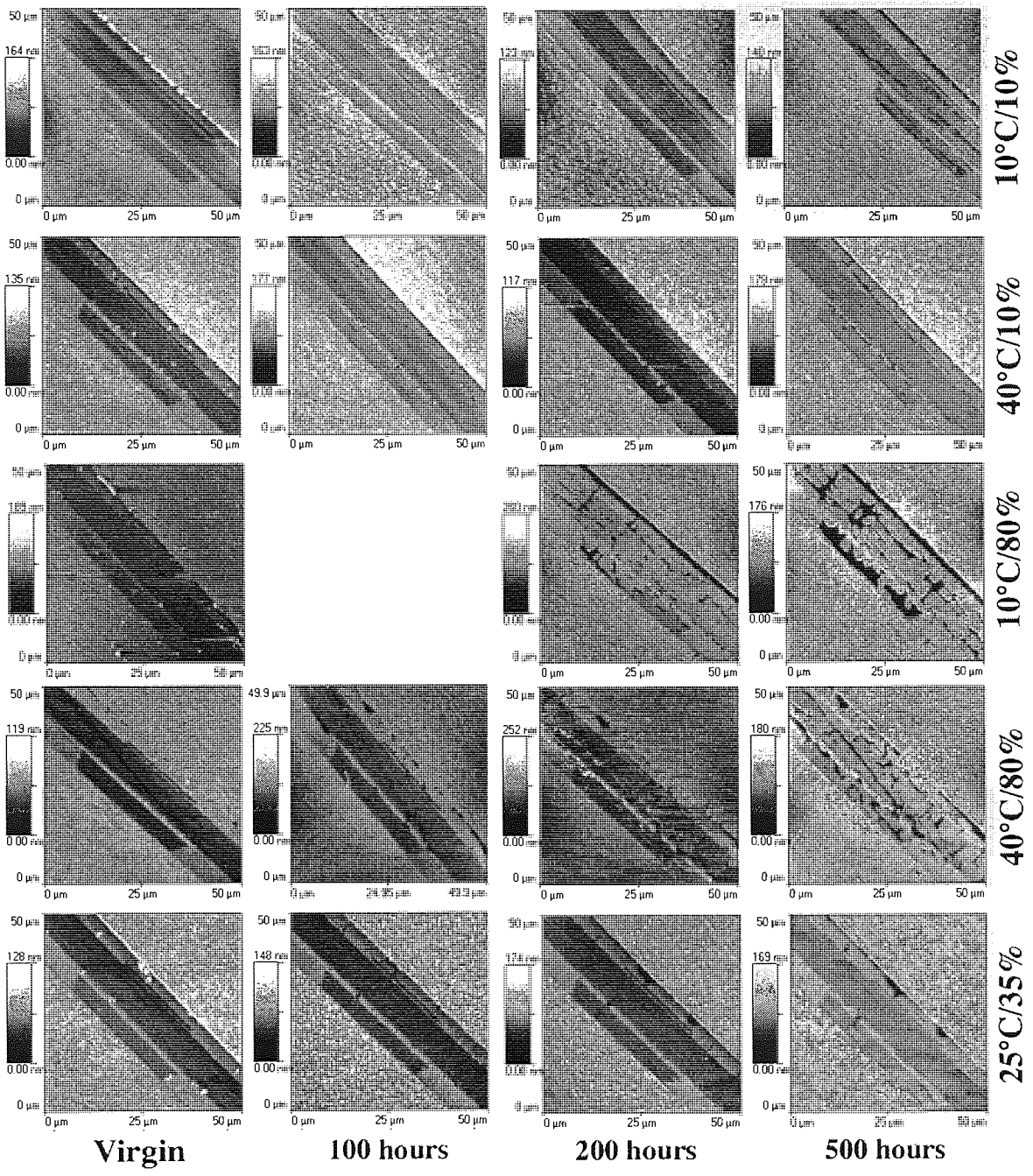

Figure 78. AFM map of the pole tip region of 40 nm SPL coated heads in the five environmental conditions, from 0 to 500 hours.

The AFM topographical maps of the pole-tip region for the 20 nm and 40 nm SPL coated heads tested in five environments are presented in Figure 77 and Figure 78. The wear behaviour depended critically on the environmental condition. The most severe damage occurred at high humidity (80% R.H.) and given a relative humidity, was more pronounced at low temperature (10°C).

Wear produced either fragments delaminated from the tape-bearing surface (designated as pullouts) or scratches on the pole tip. Pullouts first damaged the coating then the exposed substrate surface (only for 20 nm SPL). Scratches were of different nature according to the coating thickness: aligned with the sliding direction in the case of 20 nm thick coatings or replicating the scratches formed during the grinding/lapping process in the case of 40 nm coatings. Grinding and lapping are used on the virgin heads to shape the head contour, whilst trying to keep the pole-tip recession within a range of ten nanometres.

3.2.1.2 OM analysis of SPL coated heads

SPL:	Poles	TiC	Ins/ Al_2O_3	Stain:
Yes	Dark gold	Brown	Light grey	Yes
No	Bright gold	Bright gold	Dark grey	No

Figure 79. Optical micrograph of the pole tip region of 20 nm SPL coated heads in the five environmental conditions, after 500 hours of test.

Table 23.SPL coating (20 nm) remaining on the respective head surface area according to the environmental condition.

SPL 20	25°C/35%	40°C/80%	10°C/80%	40°C/10%	10°C/10%
TiC	50%	0%	0%	100%	50%
Al_2O_3/SiO_2	100%	50%	50%	100%	100%
NiFe	100%	50%	0%	100%	0%

Figure 79 shows an optical micrograph of 20 nm SPL coated heads after 500 hours of wear test in the five environmental conditions. Alteration by the coating of the head materials' colour made the coated and uncoated areas (from where coating has been pulled-out) easy to discern. The percentage of remaining coating on the different head parts could thus be estimated according to the colour changes (Table 23).

The 20 nm SPL coating wear over the pole was found to depend on the temperature (the coating was entirely removed at 10°C), whereas wear over the tape-bearing surface was found to depend on the humidity (higher at high humidity). Moreover, the coating was less prone to wear when located on the Al_2O_3 than the TiC phase: pullouts were found mainly over the TiC phase, which at high RH remained completely uncovered, whilst coating was removed (partially) only at high humidity above the Al_2O_3 and SiO_2 areas. It may be noticed here a parallel with non-coated heads and the preferential wear of the TiC with respect to the Al_2O_3 phase.

In Figure 80, the 40 nm coating was found to wear mainly on the poles, then to a lesser extent, above the insulator (*c.f.* Table 24). Similarly to what was observed on the AFM topographical maps, the coating wore above the pole tip surface replicating the lines drawn on the uncovered pole tip surface during the grinding/lapping process. These lines eventually linked at high humidity resulting in increased wear, leaving the pole tip extensively uncovered. Low temperature was an aggravating condition. Wear on the insulator was also observable at high humidity, although favoured in that case at high temperature.

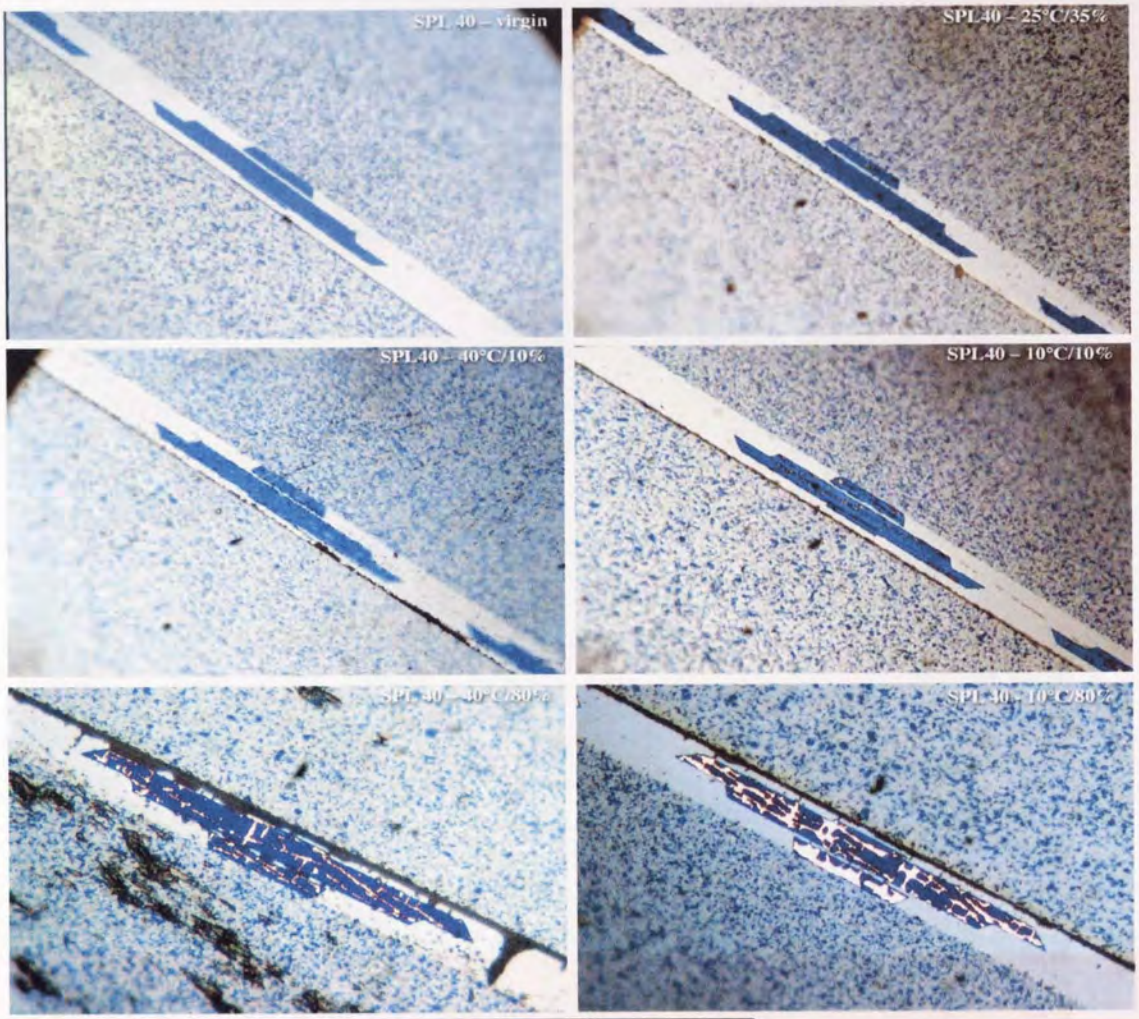

SPL:	Pole	TiC	Ins/ Al_2O_3
Yes	Dark blue	Blue	Light Grey
No	Bright	Bright blue	Dark grey

Figure 80. Optical micrograph of the pole tip region of 20 nm SPL coated heads in the five environmental conditions, after 500 hours of test.

Table 24. SPL coating (40 nm) remaining on the respective head surface area according to the environmental condition.

SPL 40	25°C/35%	40°C/80%	10°C/80%	40°C/10%	10°C/10%
TiC	100%	100%	100%	100%	100%
Al_2O_3	100%	100%	100%	100%	100%
SiO_2	100%	80%	90%	100%	100%
NiFe	90%	60%	40%	90%	60%

3.2.1.3 AES analysis of SPL coated heads

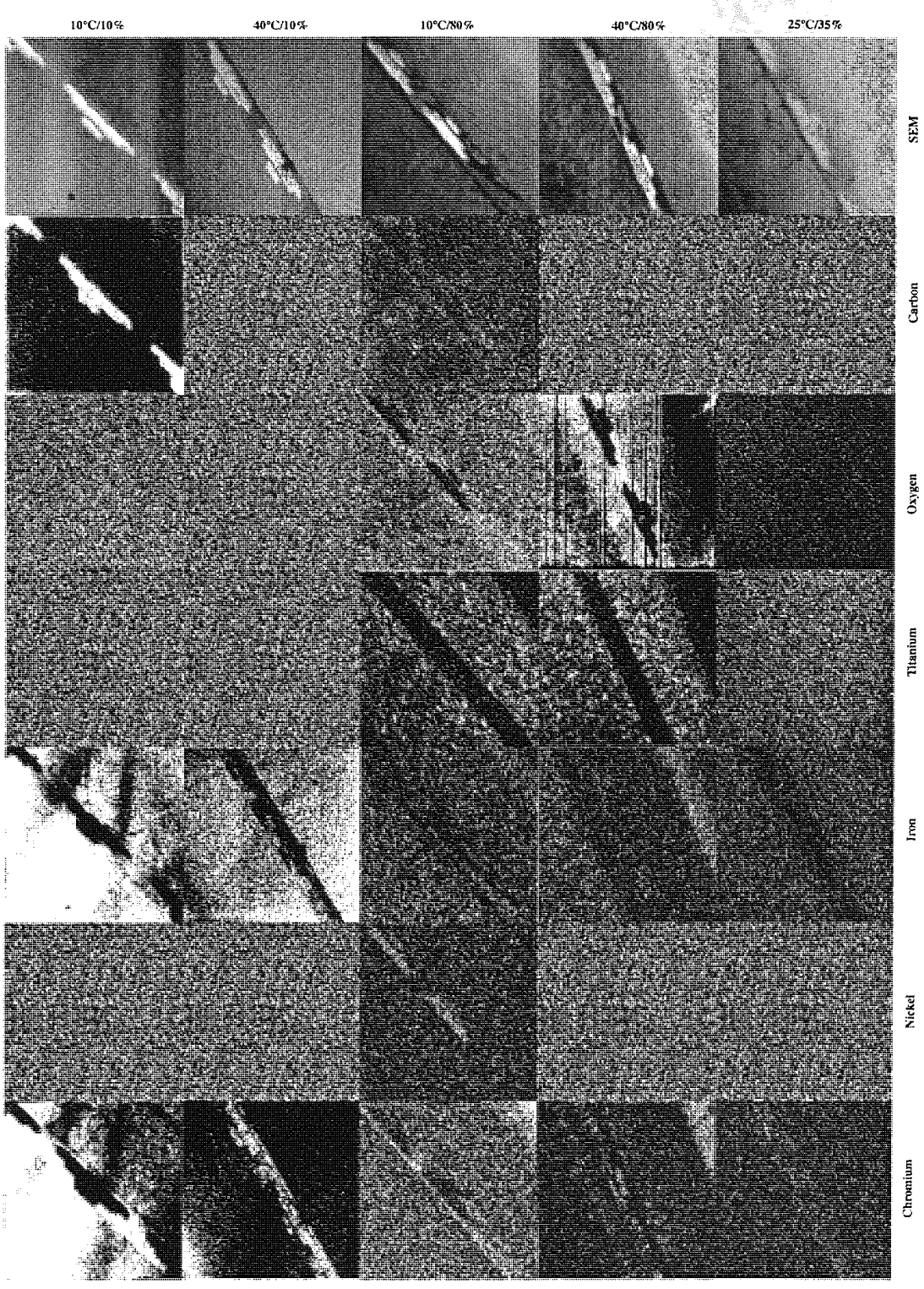

Figure 81. SPL 20: AES map for Cr, Ni, Fe, Ti, O, C and secondary electron (SEM), in four environmental conditions, after 500 hours of test.

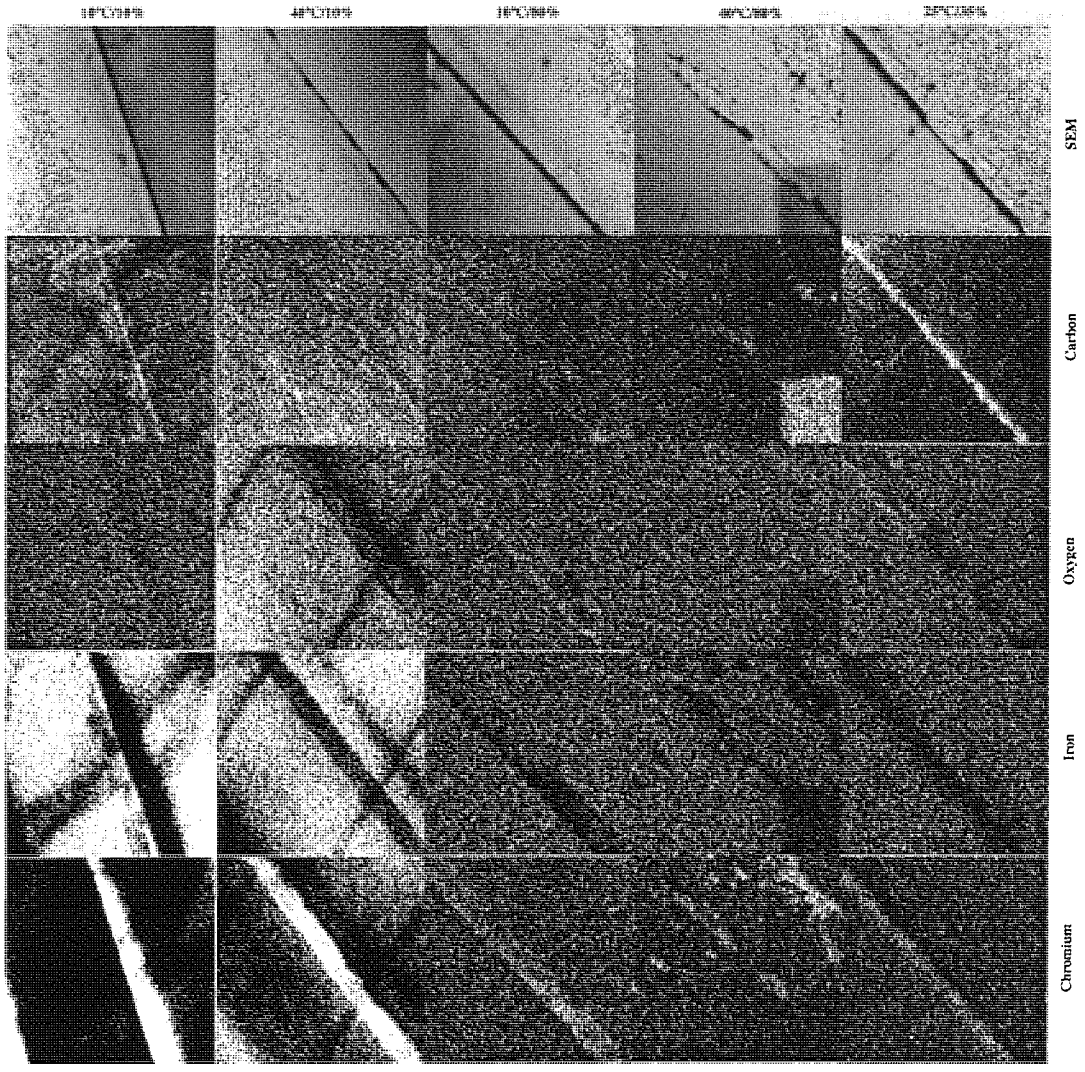

Figure 82. SPL 40: AES map for Cr, Ni, Fe, Ti, O, C and secondary electron (SEM), in four environmental conditions, after 500 hours of test.

Figure 81 and Figure 82 shows AES maps of the head surfaces coated with 20 nm and 40 nm SPL, respectively, after being tested for 500 hours in the five environmental conditions.

Ti and O were clearly identified on the head surface at high humidity, as well as Ni at low temperature (20 nm coating), which indicated the extensive removal of the SPL coating. Iron was clearly identified at low humidity, over the tape-bearing surface and insulator regions. Iron is found in the magnetic pigments transferred as stains from the tape coating. The stain seemed thus to provide some protection and inhibits the coating wear. The Fe concentration also increased at tape take-off where the transfer film is thicker (very

marked at 40°C/80% RH). The head-to-tape contact pressure has been calculated to be ~ 3 times higher at the contact edge (tape take-off) than in the middle [165].

Cr (from the coating) was more persistent on the poles at high temperature, then at low RH. It was found in higher concentration no matter what condition, beyond the contact between the tape-bearing surface and the tape.

The surface areas not covered with iron rich stain (usually recessions, steps or outside the head-to-tape interface) leaved Cr (from the SPL coating) in high concentration. At high humidity, the SPL coating is likely to be worn on the most protruding area (tape-bearing surface), which would account for the higher concentration of Cr on the pole tip region.

3.2.2 Diamond like carbon (DLC) coated heads

3.2.2.1 OM and WYKO interferometer analysis of ADR heads coated with diamond like carbon

All DLC coatings were found to have disappeared after 100 hours as evidenced by:

i. A significant decrease in pole-tip recession: the presence of DLC coating introduces an additional phase shift hence increases the pole-tip recession measured *via* WYKO interferometer.

ii. Occurrence of staining on the pole tips observed on visual inspection with an optical microscope.

iii. Changes in surface aspect at the vicinity of the sidebar shift (Figure 83) or towards the edges of the tape-head contact area.

The first point (i) can be quantified: the pole-tip recession measured *via* WYKO decreased over the first 100 hours from 69 to 48 nm (Commonwealth), 55 to 40 nm (Diamonex), 74 to 51 nm (Bekaert) and 46 to 38 nm (Veeco).

Table 25. Pole-tip recession measured via *WYKO for heads coated by four different manufacturers, virgin and tested for 100 hours.*

	0 hours nm	100 hours nm	0 hr-100 hrs nm
Commonwealth	69	48	21

Diamonex	55	40	15
Bekaert	74	51	23
Veeco	46	38	8
Average	61 (12.8)	44.3 (6.2)	16.8 (6.8)

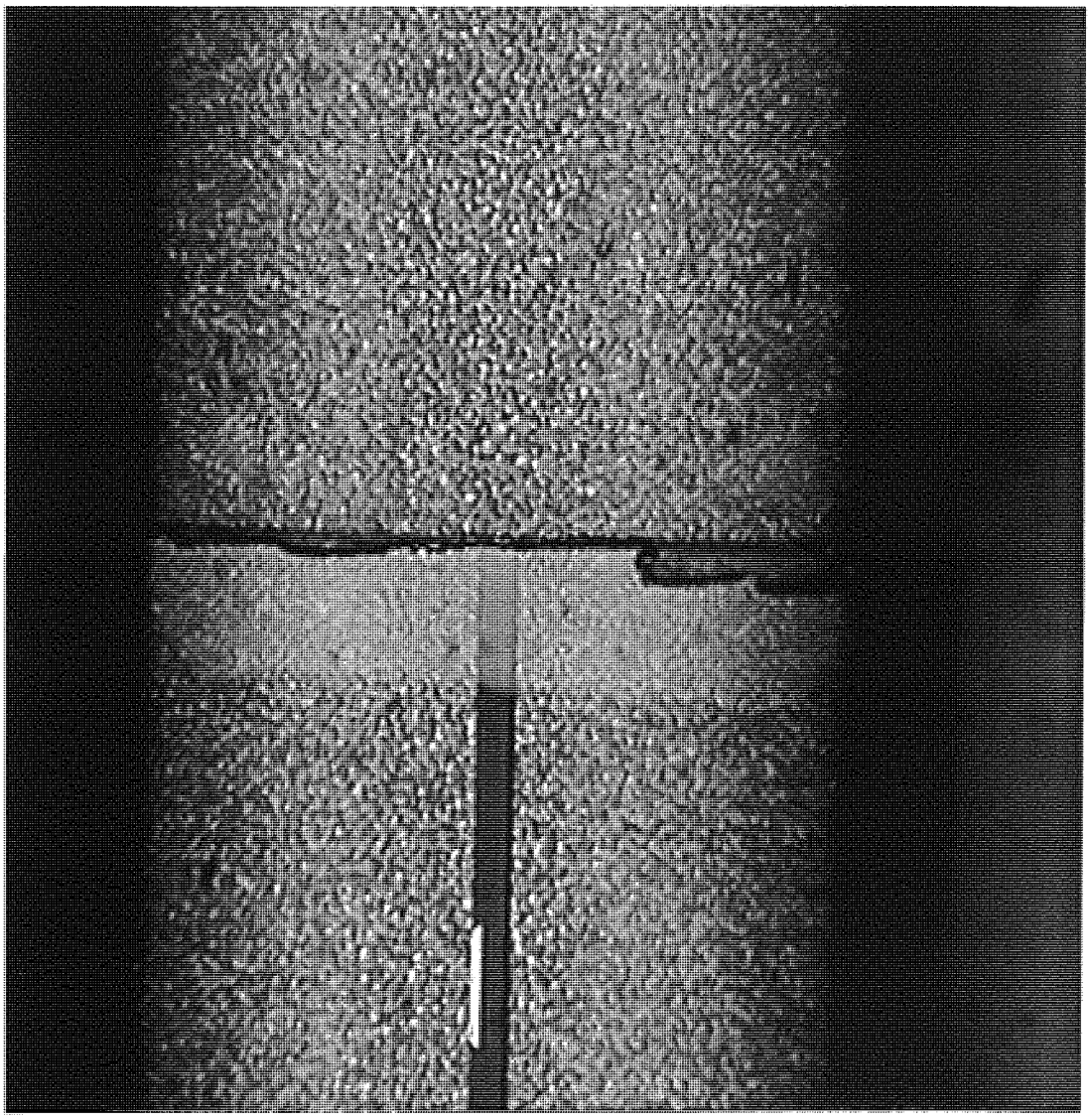

Figure 83. DLC coating is removed after 100 hours test, except in the recession caused by the sidebar shift.

A Bekaert head was tested for 48 hours. The pole-tip recession was measured by means of a WYKO interferometer as 60 nm at the beginning of the test (0 hr), 55 nm after 24 hrs and 51 nm at the end of test (48 hrs). The progressive decrease supports the thesis of an

abrasive rather than delaminative wear as the dominant wear mechanism [185]. Similar results were reported by Scott *et al.* [221].

Delamination may however be involved to some extent, and consequently extremely hard DLC laminar particles may be responsible for the presence of grooves across the tape-bearing surface (Figure 84).

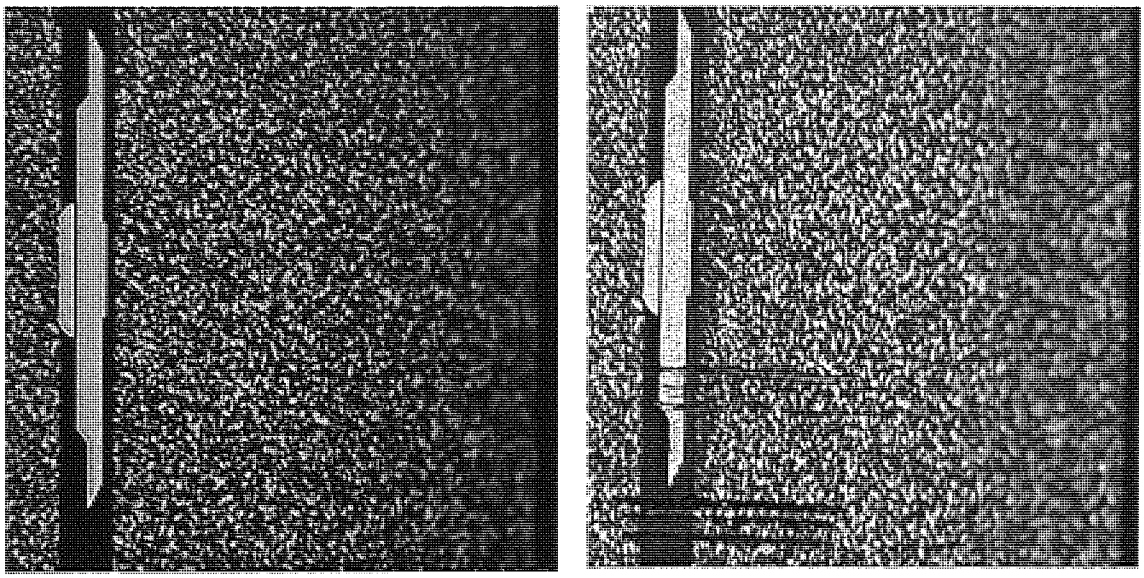

Figure 84. DLC coated head (Bekaert), at beginning of test (left) and after 48 hrs (right). Scars and delimitation of the tape-bearing surface tape contact region (line on right) are visible on the tested head attesting that the coating is being worn off.

3.2.2.2 AFM analysis of ADR heads coated with diamond like carbon

As shown in Figure 85 the pole-tip recession had not changed after 100 hours of wear test (~ 55 nm). The decrease in pole-tip recession measured by the WYKO interferometer was therefore exclusively related to a change in optical properties at the tape-bearing surface as DLC was worn away. After 100 hours, patches and stripes were observed across the pole tip: it was unclear whether this would correspond to staining or rests of DLC coating; in this latter case, delaminative wear would be involved above the pole tips.

The sidebar shift region is shown for two different heads: Figure 86 for a virgin head and Figure 87 for a head tested for 100 hrs. On the virgin head, the coating is homogeneously textured with slight TiC protrusions replicated by the DLC coating on either side of the glue line. The sidebar shift was measured here as ~ 350 nm (indexes #1–#2 on the 2D profile). After 100 hours of testing, the ceramic had clearly been protected within the sidebar shift recession (~ 340 nm) where the surface is similar in every respect to the vir-

gin one. As one gets further from the glue line, the ceramic surface becomes polish-smooth, in transition from the virgin to the worn ceramic surface seen on the opposite protruding side. Pullouts are ~ 10 nm deep x 1 μm wide. The pullout depth corresponding to the DLC thickness, chipping of the DLC coating is more likely than of the uncoated ceramic surface. Two different mechanisms could be operative: abrasive wear, responsible for the surface polishing, and delaminative wear, responsible for chipping.

The grooves seen optically on Figure 84 are shown Figure 88 as observed by AFM. Their deepness (~ 200 nm) is far beyond the DLC coating thickness and reveals a severe, catastrophic plastic deformation.

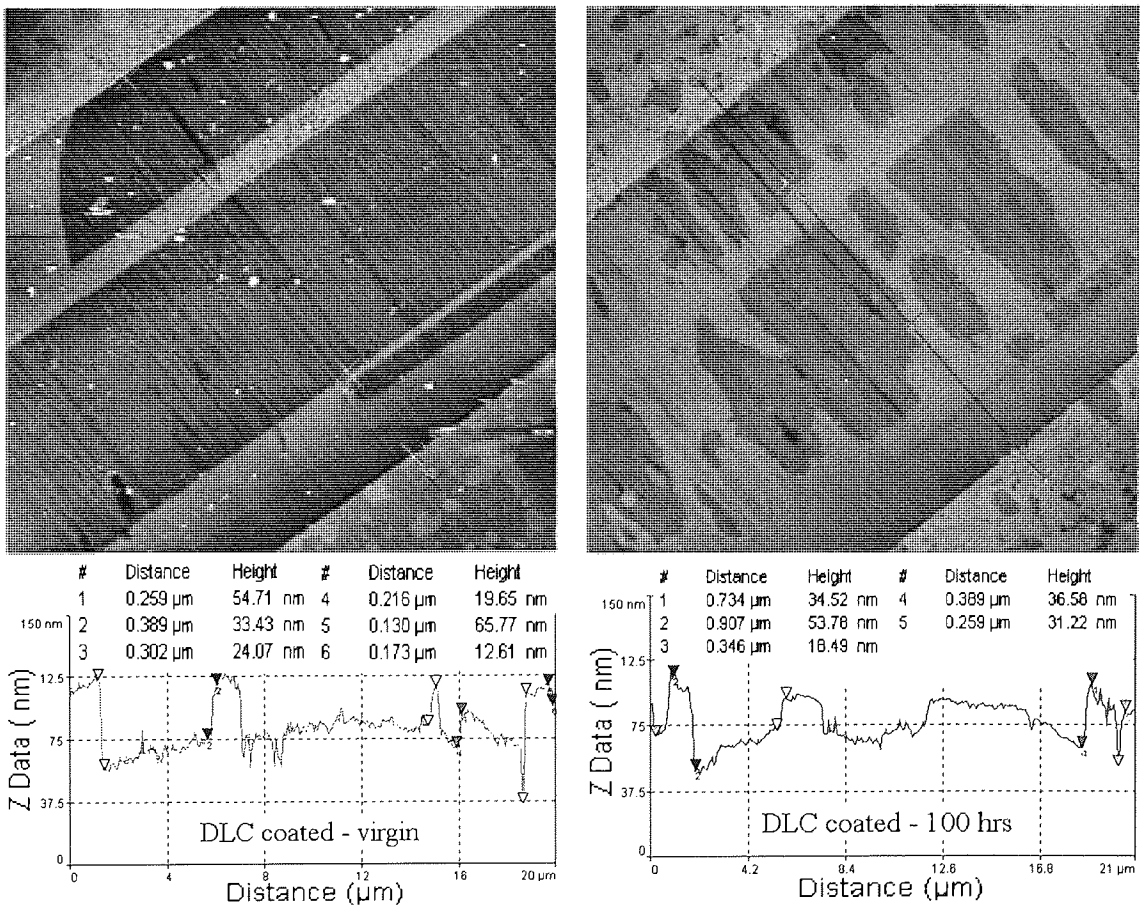

Figure 85. AFM image showing the topography of the DLC coated head before and after a wear test.

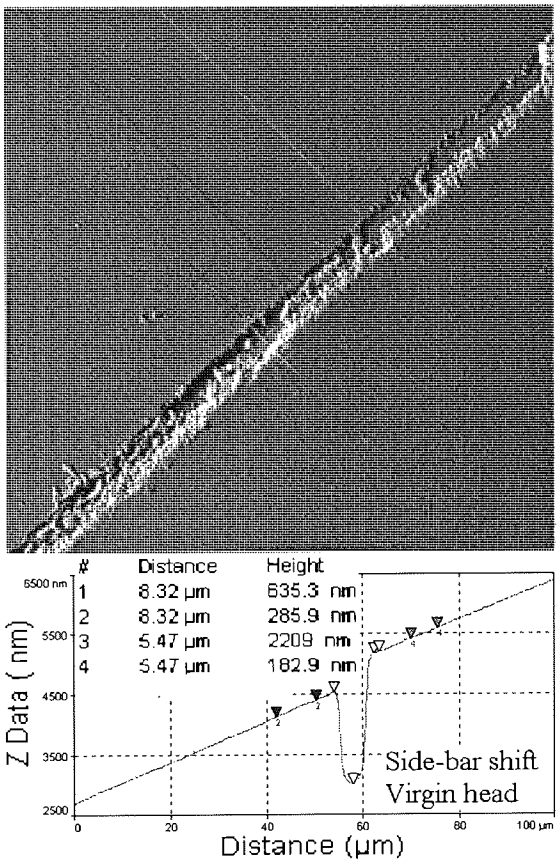

Figure 86. Side-bar shift at the glue line of a virgin DLC coated head.

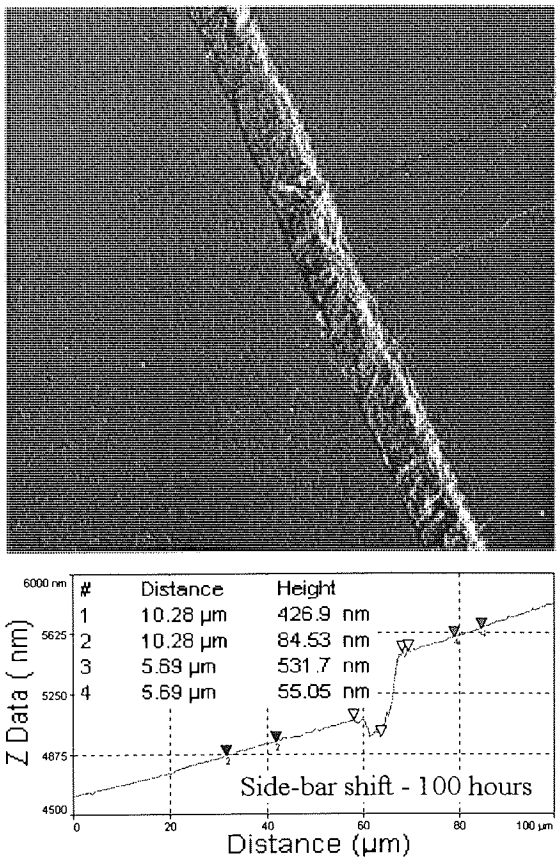

Figure 87. Side-bar shift at the glue line of a DLC coated head tested for 100 hours.

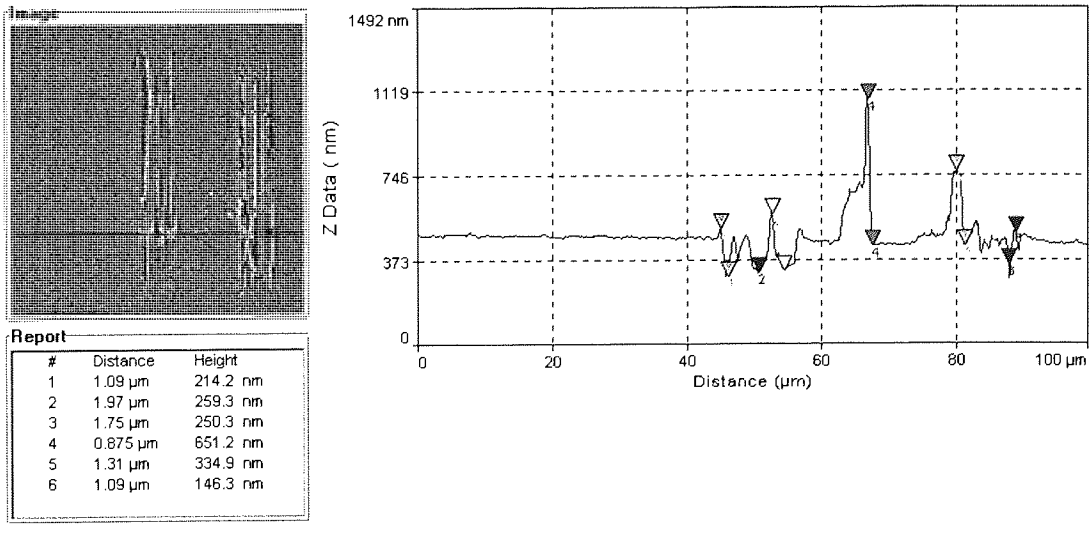

Figure 88. Scars observed on a DLC coated head (sensor #4) tested for 48 hours.

3.3 Ceramic full-contour dummy heads

3.3.1 Al_2O_3-TiC dummy heads

3.3.1.1 AFM analysis of Al_2O_3-TiC dummy heads

As was observed on the standard heads, the TiC phase recession appeared within 20 hours of the test (*c.f.* Figure 89 to Figure 92). Moreover, flecks of stain were visible, concentrated at 10% RH and scattered at 35% RH on the alumina plateau and bottom of TiC intra-grain pullouts, whereas none was visible at 80% RH. Greenleaf (GL) and Sumitomo (ST)—recognizable at their different TiC grain-size (larger on GL)—showed similar wear and staining characteristics.

The pullout depth measured from the AFM scans is presented in Figure 93. The time constant τ (*c.f.* 3.1.5.1) at which the pullout depth converges to its maximum value is plotted below: with a notable exception at 10°C/10% R.H., all conditions showed equilibrium depth had been reached around 100 hours. Besides, the pullout depth at the end of test, d_s ranged between 20 to 25 nm. Sumitomo showed the most dispersed pullout depths. The main difference with Greenleaf ceramics, *i.e.* the smaller grain size, seems to result in the greater spread between the different conditions.

At 10°C/10% R.H., the pullout depth remained particularly low, due presumably to a massive stain transfer within the recession.

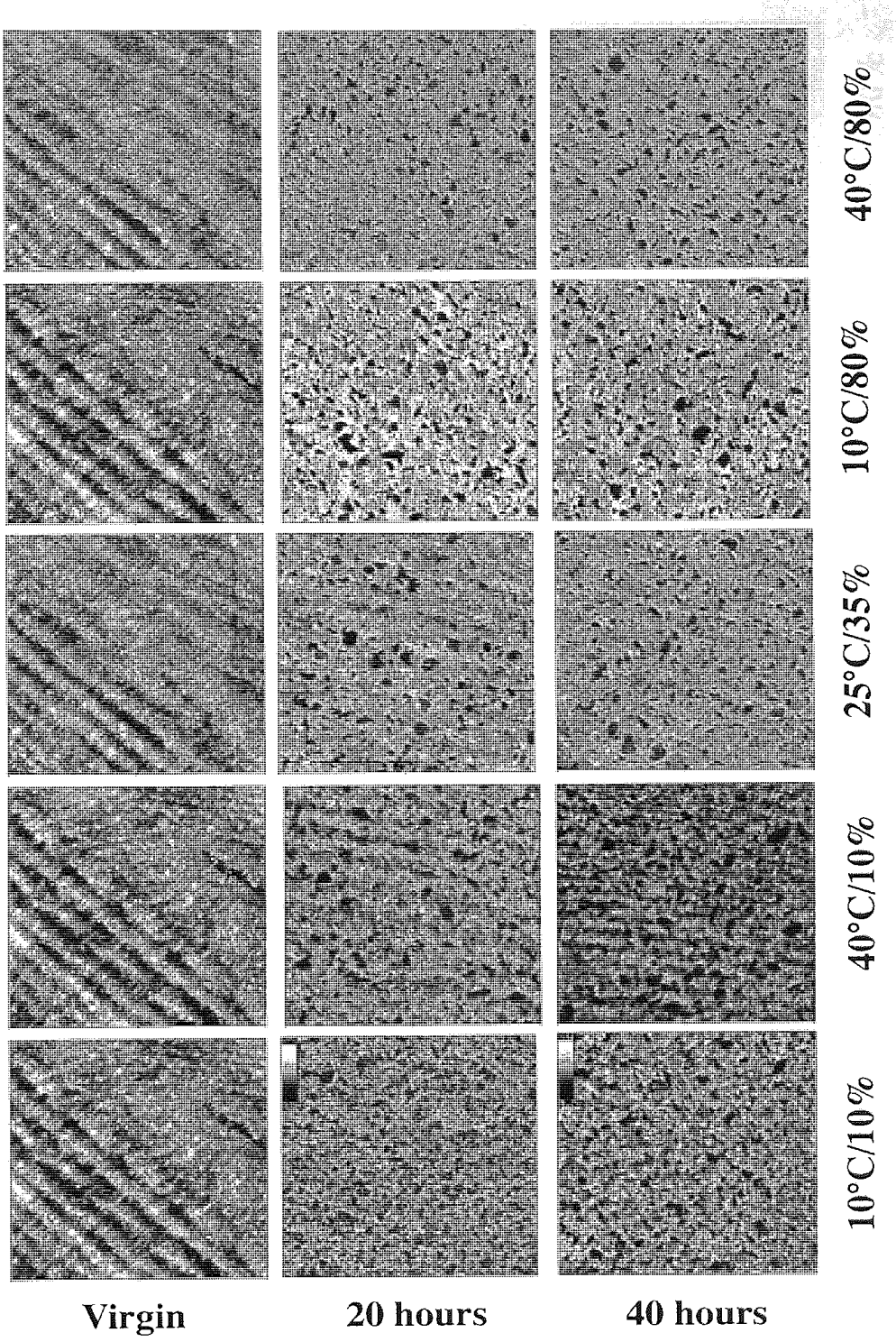

Figure 89. AFM scan of Greenleaf Al_2O_3-TiC dummy head, virgin, after 20 and 40 hours of test in five different environmental conditions. Dark areas and white flecks (low R.H.) correspond to the recessed TiC phase and transferred material (stains), respectively. Striations are supposedly artefacts inherent to the AFM.

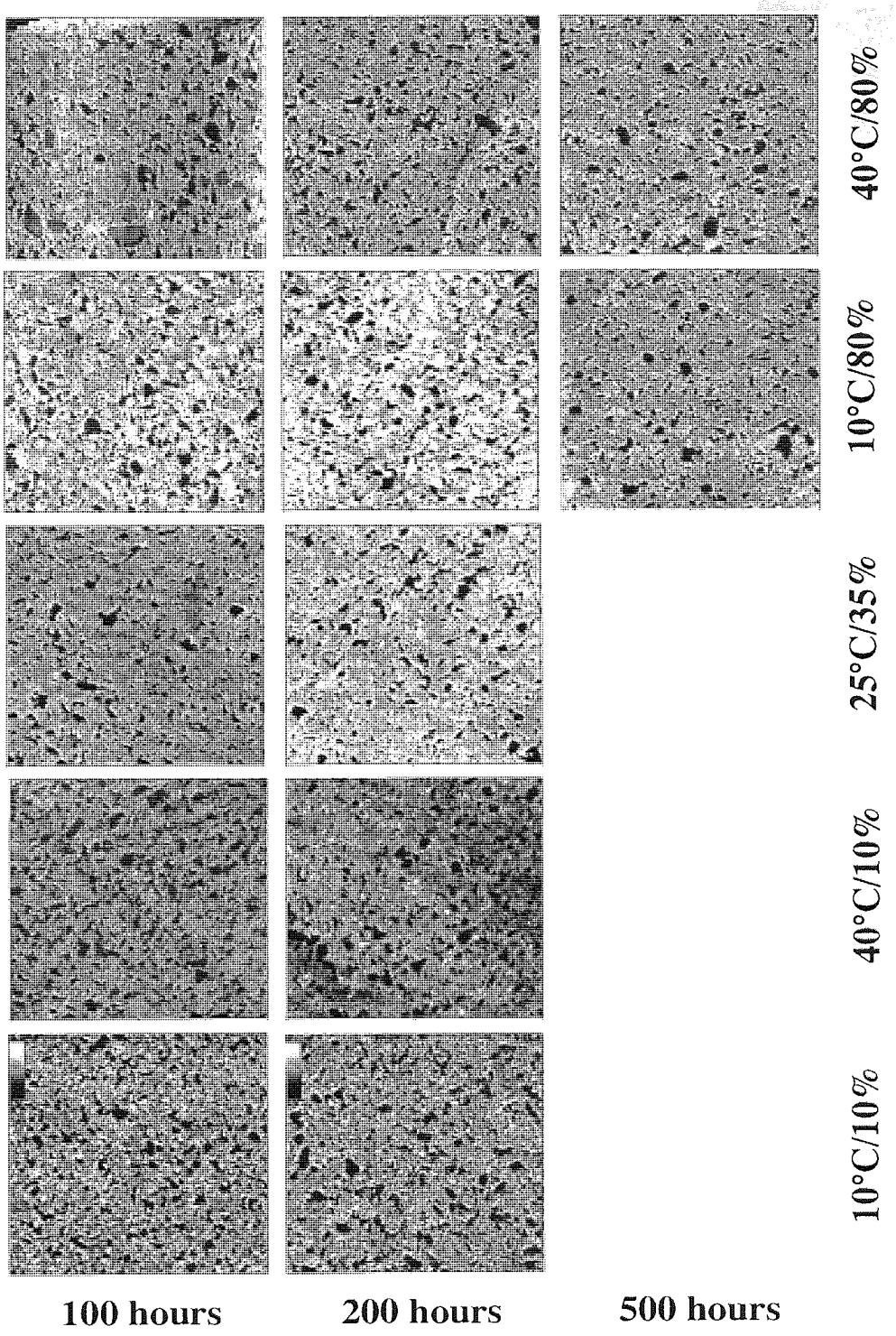

Figure 90. AFM scan of Greenleaf Al_2O_3-TiC dummy head, after 100, 200 and 500 hours of test in five different environmental conditions. Dark areas and white flecks (low R.H.) correspond to the recessed TiC phase and transferred material (stains), respectively.

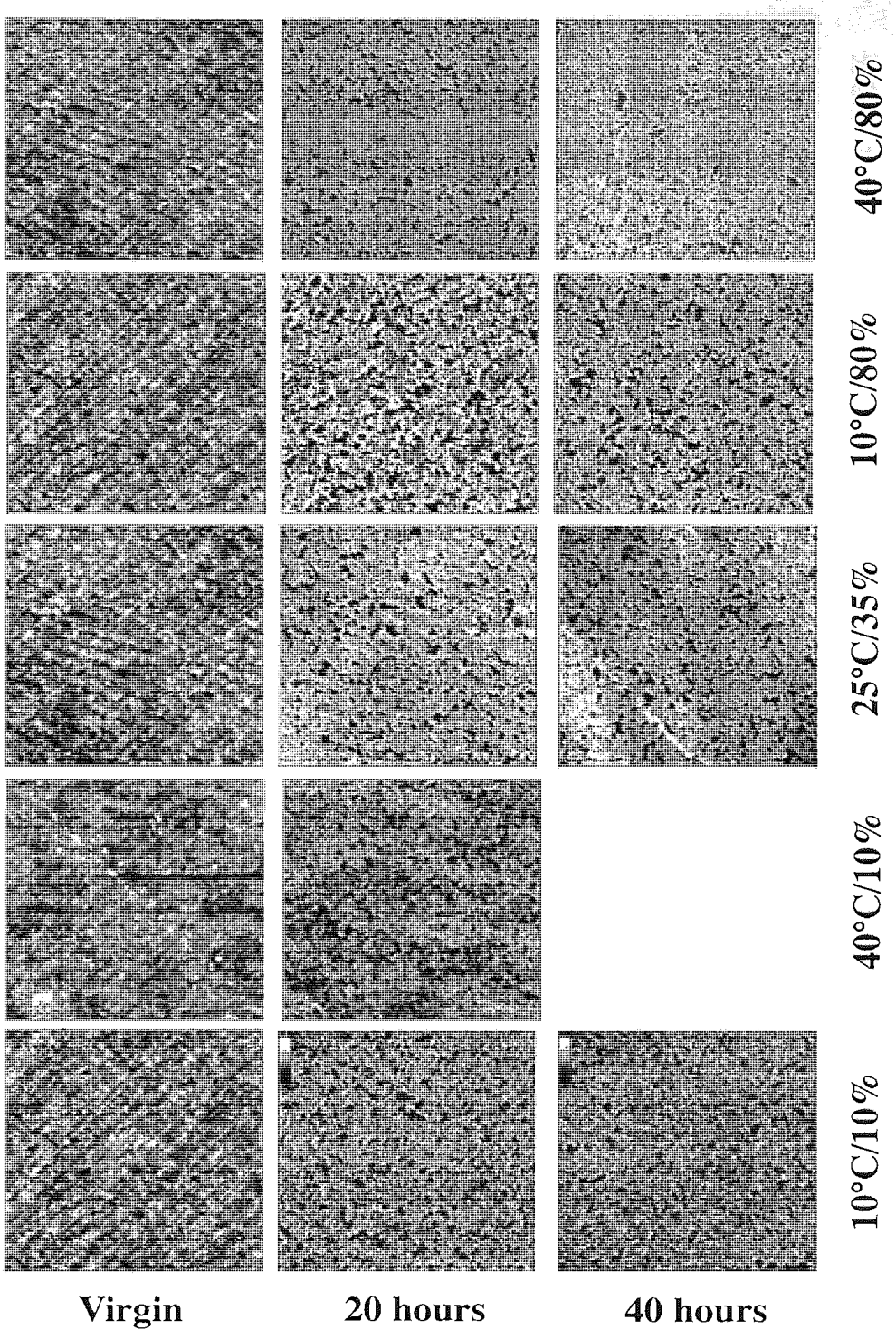

Figure 91. AFM scan of Sumitomo Al2O3-TiC dummy head, virgin, after 20 and 40 hours of test in five different environmental conditions. Dark areas and white flecks (low R.H.) correspond to the recessed TiC phase and transferred material (stains), respectively.

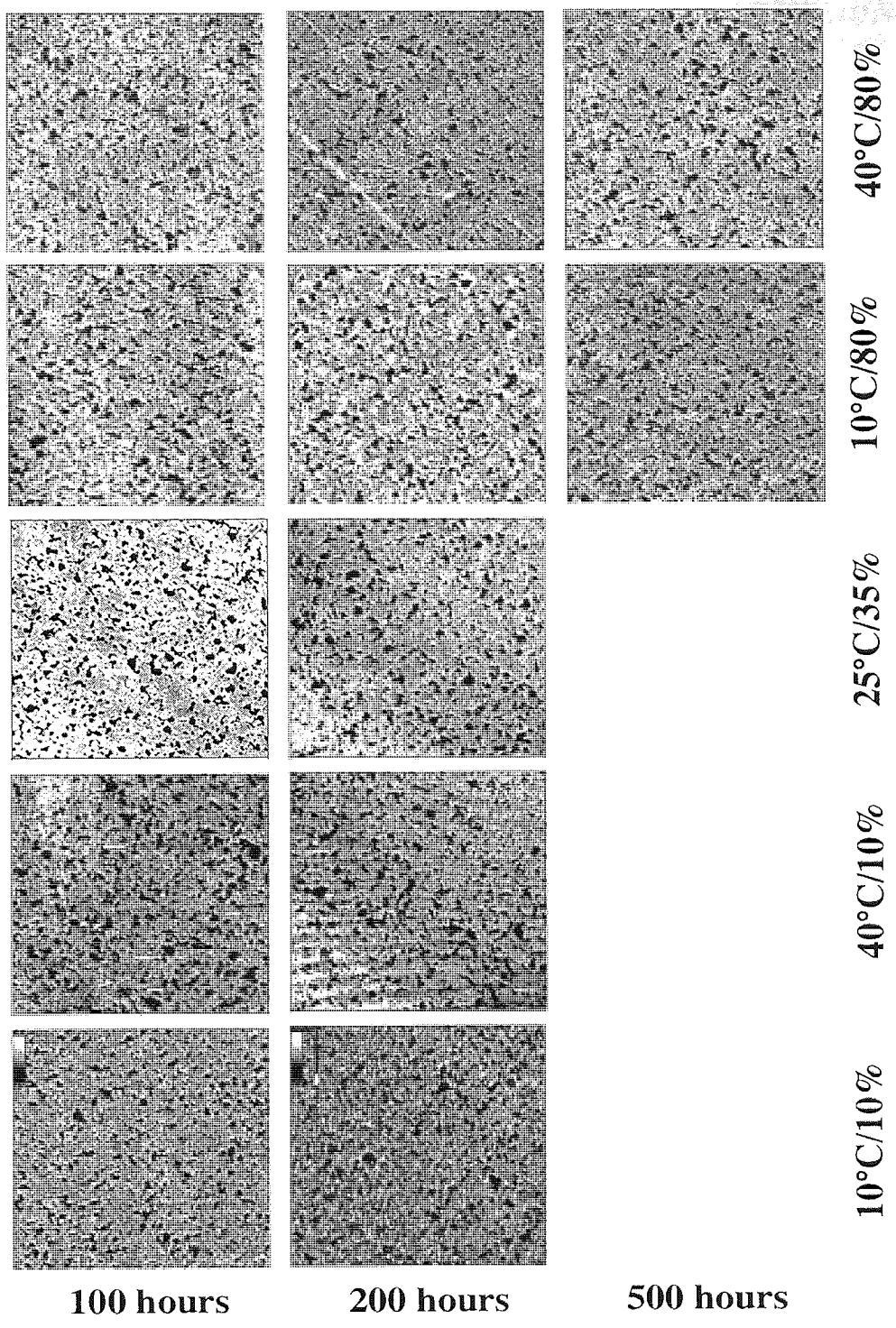

Figure 92. AFM scan of Sumitomo Al2O3-TiC dummy head, after 100, 200 and 500 hours of test in five different environmental conditions. Dark areas and white flecks (low R.H.) correspond to the recessed TiC phase and transferred material (stains), respectively.

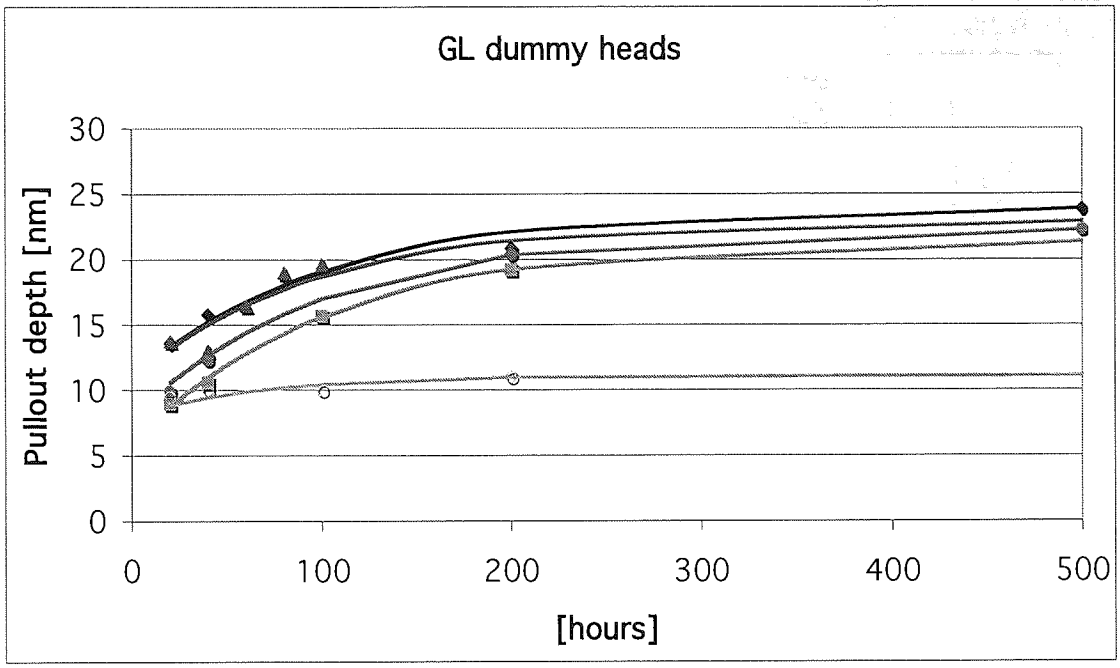

10°C/80% 40°C/10% 25°C/35% 40°C/80% 10°C/10%

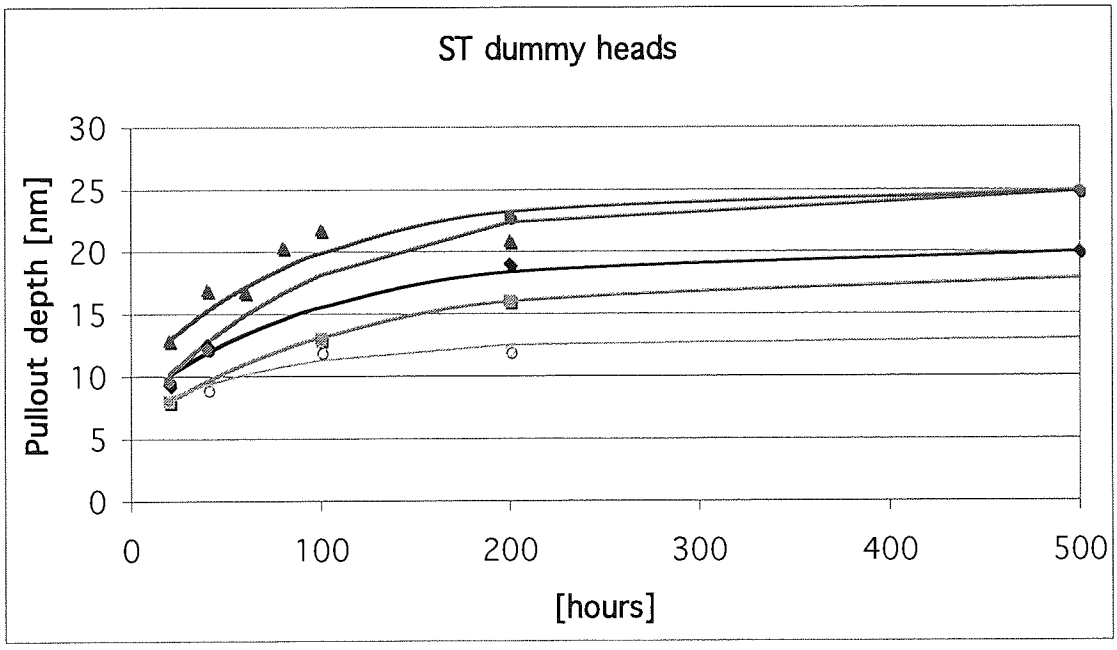

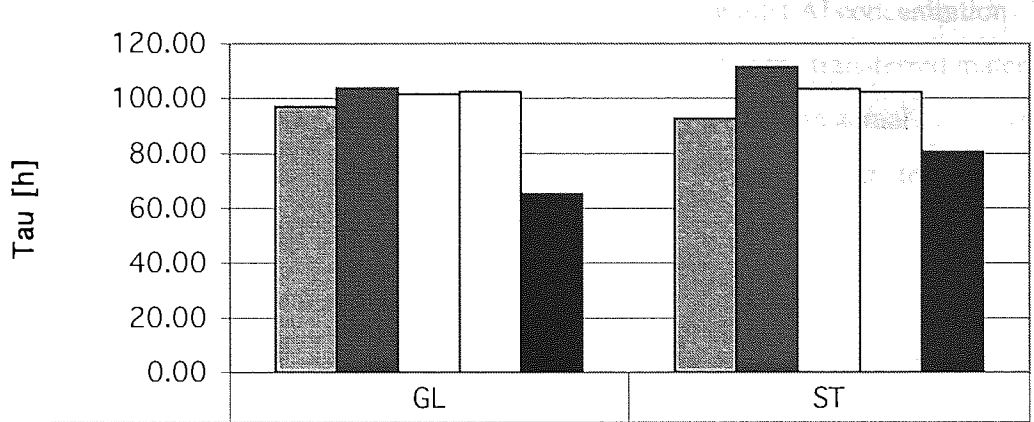

	GL	ST
25°C/35%	97.14	92.88
40°C/10%	103.93	111.67
40°C/80%	101.58	103.58
10°C/80%	102.53	102.42
10°C/10%	65.57	80.77

Figure 93. Upper charts: pullout depth measured from AFM scans of Greenleaf (top) and Sumitomo (middle) dummy heads (Figure 89~Figure 92). Lower chart: time constant related to the pullout depth increase (see text).

3.3.1.2 XPS analysis of Al_2O_3-TiC dummy heads

Quantification of the XPS spectra measured on Al_2O_3-TiC dummy heads tested in different environmental conditions is presented in Figure 94. Errors in XPS quantification are cumbersome to evaluate, as they are dependant on many factors such as the element considered, its proportion, its environment, etc. A fair estimation was deduced from the fluctuation observed between successive quantifications of identical XPS peaks. The elemental concentration derived from the quantification was thus estimated accurate at ±0.5% (absolute error). This estimation holds for all XPS quantification presented in this thesis.

Fe was clearly transferred in higher quantity at lower humidity (10% and 35% R.H.); moreover, the transfer rate increased with the temperature. A plateau was reached after 100 hours at the highest temperature (40°C). The plateau may relate to the fact that at high temperature/low humidity, the early flecks tended to disperse, forming a transfer film (see AFM scans above), which thickness eventually reached a steady state. Temperature seemed therefore to influences the transfer rate and overall aspect.

The Ti concentration decreased markedly at low humidity, whilst Al concentration seemed not as much affected, it may therefore be assumed that the transferred material preferentially deposited on the TiC phase (as observed previously in actual head analysis). At higher humidity, Al and Ti were found to have similar trends: the transferred material is likely to either differ in nature, or show no preferential staining.

The N—which comes from the tape binder transferred onto the head surface—appeared at conditions unfavourable to Fe, *i.e.* at high humidity or at low temperature. N may then be overwhelmed by highly concentrated Fe. In low transfer conditions only the most superficial tape material (low Fe vs. high binder/lubricant content) is expected to stain the head.

Si was found in high concentration on worn heads, likely to originate mostly from lubricants found in various parts of the QIC or drive.

GREENLEAF **SUMIMOTO**

10°C/10%

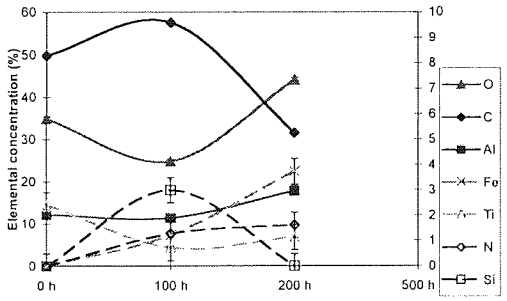

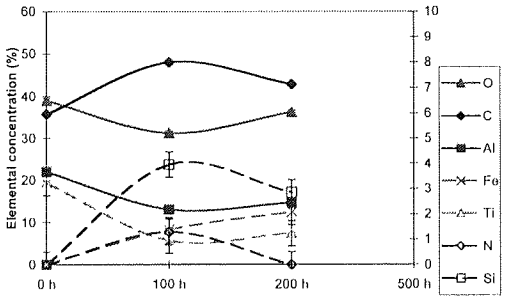

40°C/10%

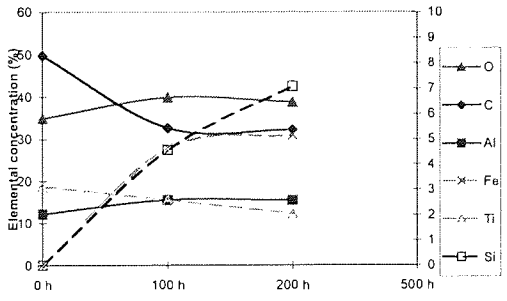

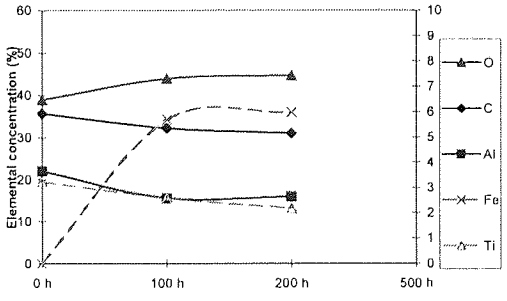

25°C/35%

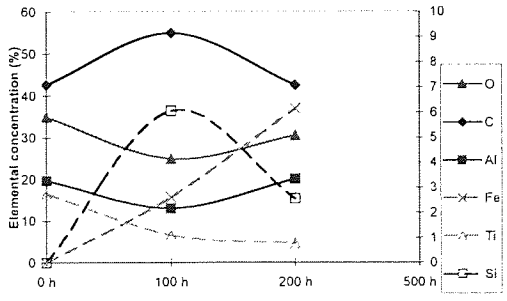

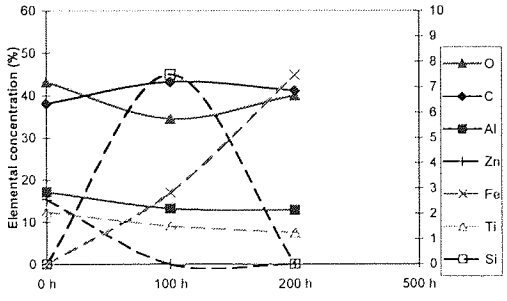

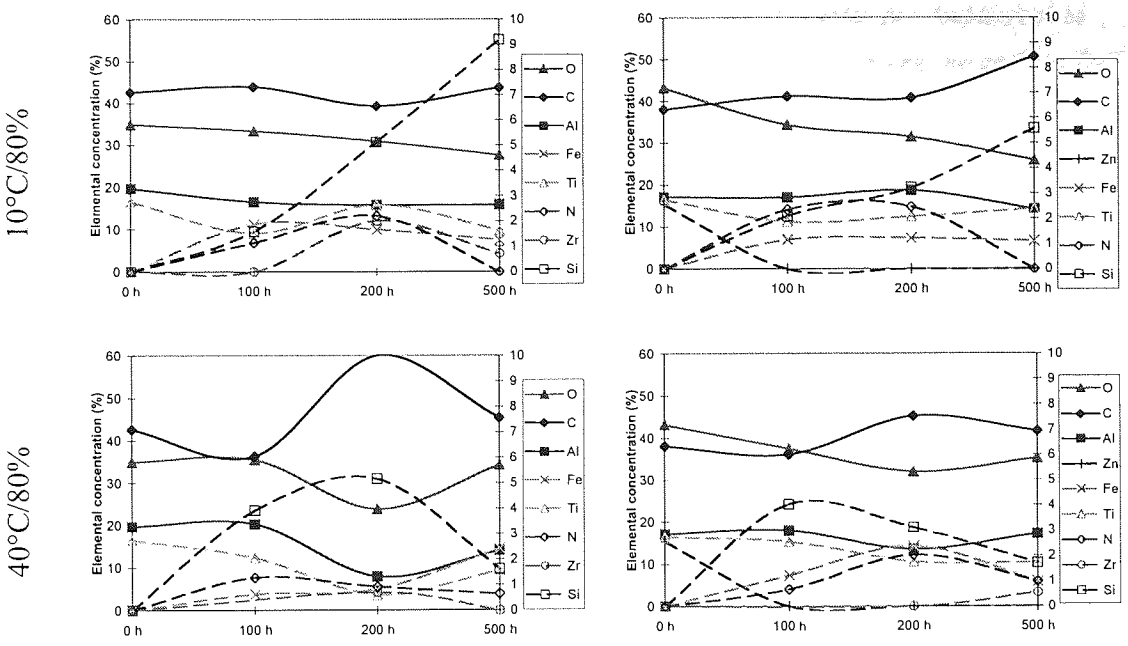

Figure 94. Elemental concentration of the different constituents found at the dummy head surface, deduced from the quantification of the respective XPS spectra. The dashed lines refer to the secondary (right-hand) axis. The quantification is estimated accurate at ± 0.5% (representative error bars are indicated at 10°C/10%).

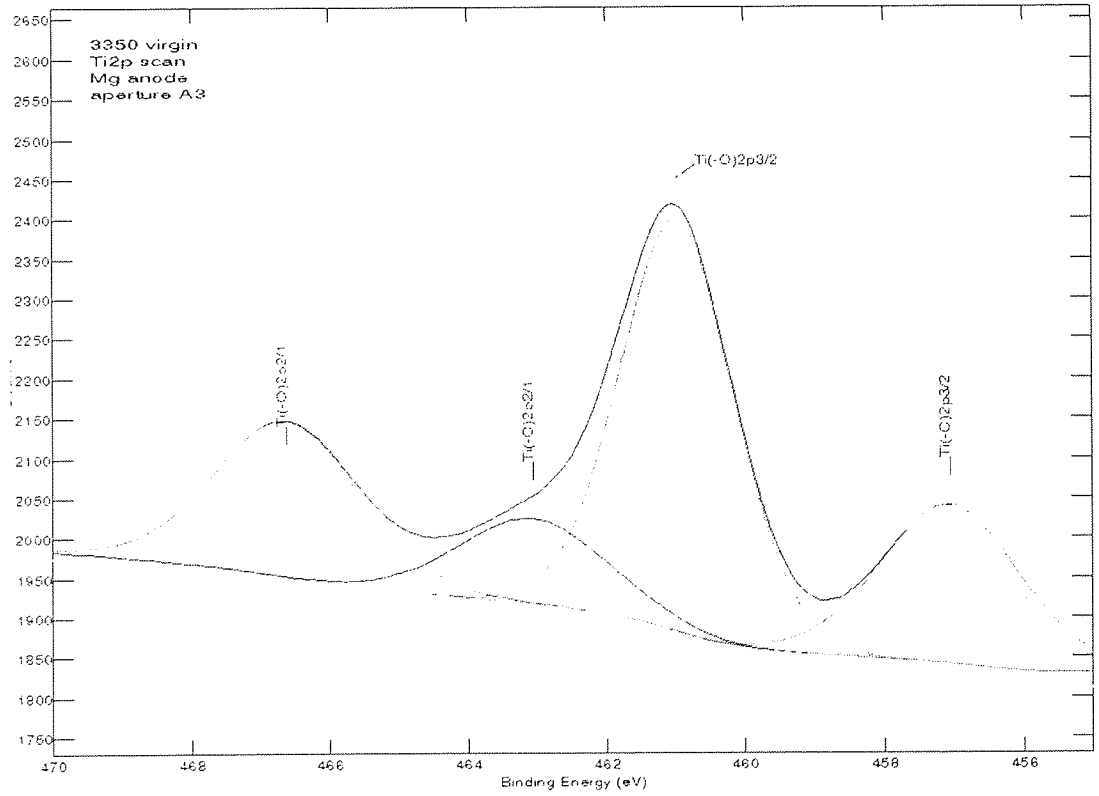

Figure 95. XPS spectrum of Al_2O_3-TiC full-contour head zoomed on the Ti doublet: two doublets can be noticed, corresponding at higher bonding energy to the Ti-O bond and at lower bonding energy to the Ti-C bond.

Figure 95 shows the Ti 2p peak from the XPS spectra acquired for a virgin Al_2O_3-TiC dummy head: it can be fitted to a convolution of two doublets corresponding to the TiC (Ti-C) and TiO_x (Ti-O) compounds, respectively. The area ratio between the two doublets gives an estimation of the proportion of oxidized Ti vs. TiC.

The general trend for the concentration ratio of C to O bonded Ti (Ti(-C)/Ti(-O)—*c.f.* Figure 96) was to increase over the first 100 hours of test probably due to the depletion of superficial TiO_x, then eventually decrease as the freshly exposed TiC surface becomes oxidized again, once the interface has reached a steady state.

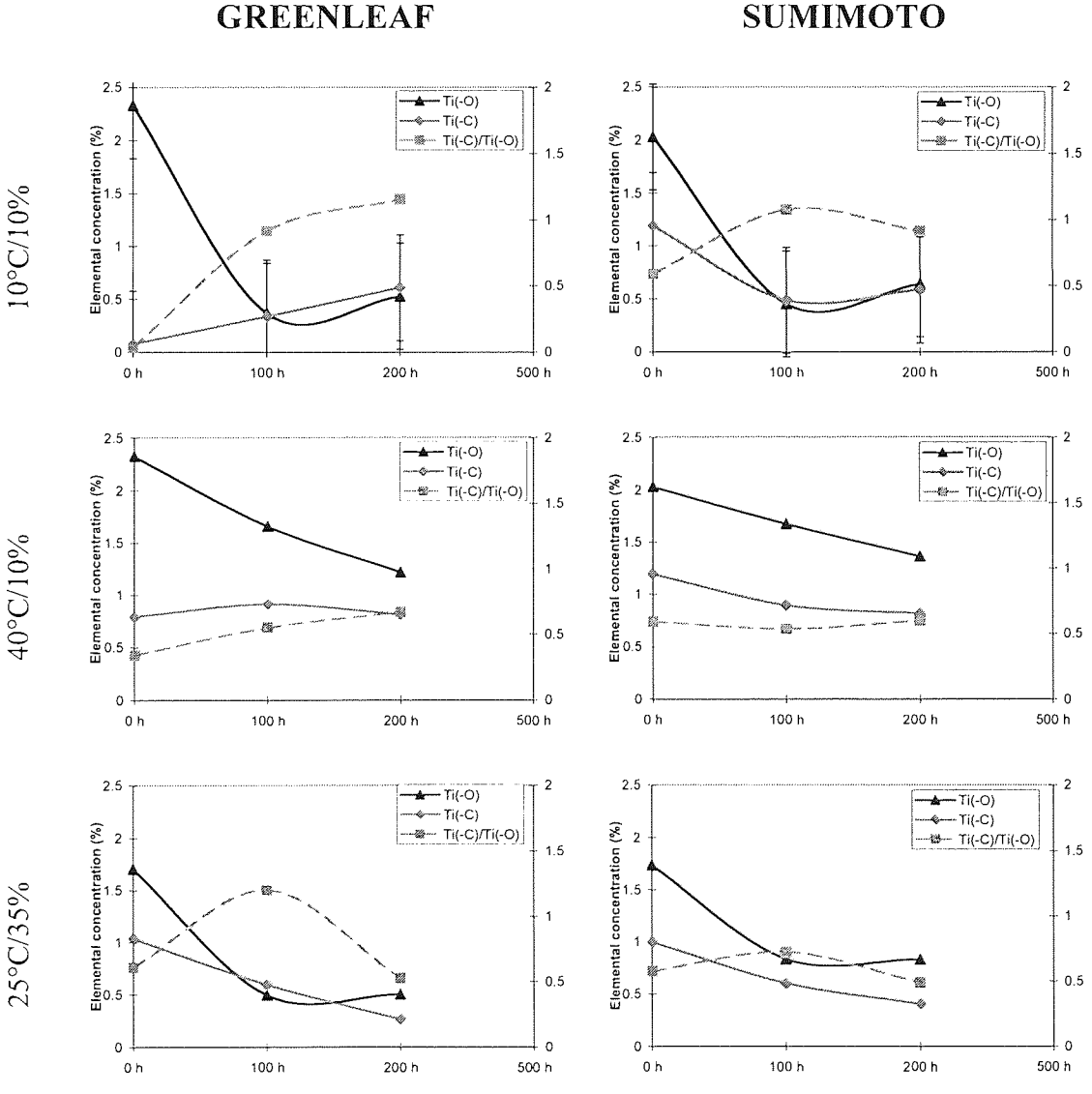

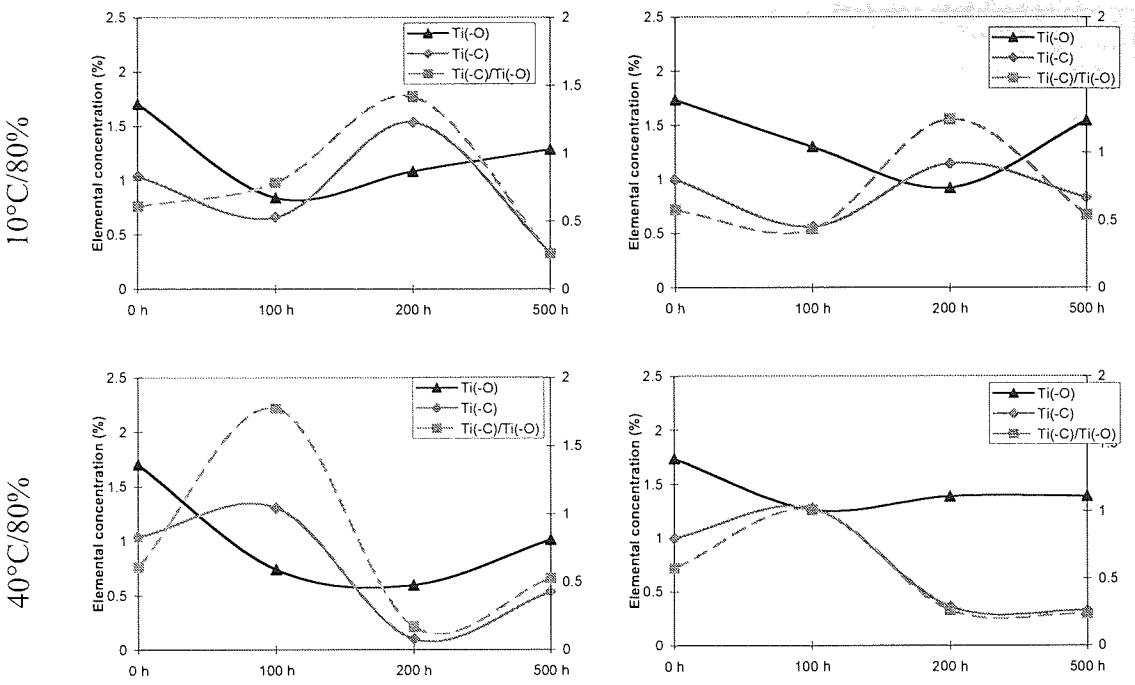

Figure 96. Decomposition of the Ti concentration (Figure 94) in O and C bonded Ti contributions. The dashed lines refer to the secondary (right-hand) axis. The quantification is estimated accurate at ± 0.5% (representative error bars are indicated at 10°C/10%).

3.3.1.3 XPS depth profile of a virgin Al_2O_3-TiC dummy head

A depth profile of a virgin GL Al_2O_3-TiC full-contour head is presented Figure 97. Each successive point on the X-axis corresponds to an additional 12 minutes etching, which is assumed to remove a depth of roughly 12 x 60 s x 0.01 nm/s ~ 7 nm at the sample surface. The approximate depth corresponding to each successive etch is therefore estimated as follows:

Sputter time	0 min	12 min	24 min	36 min	48 min	60 min
Depth	0 nm	7 nm	14 nm	21 nm	28 nm	35 nm

The titanium concentration reached its highest point around 7 nm below the surface as the C contamination layer was sputtered away. The ratio Ti-O/Ti-C decreased from 2% to about 0.5% for sputtered depth beyond 7 nm. The accuracy of the measurement was no better than 0.5%, hence it can be assumed that practically, the oxidized titanium layer was no thicker than 7 nm.

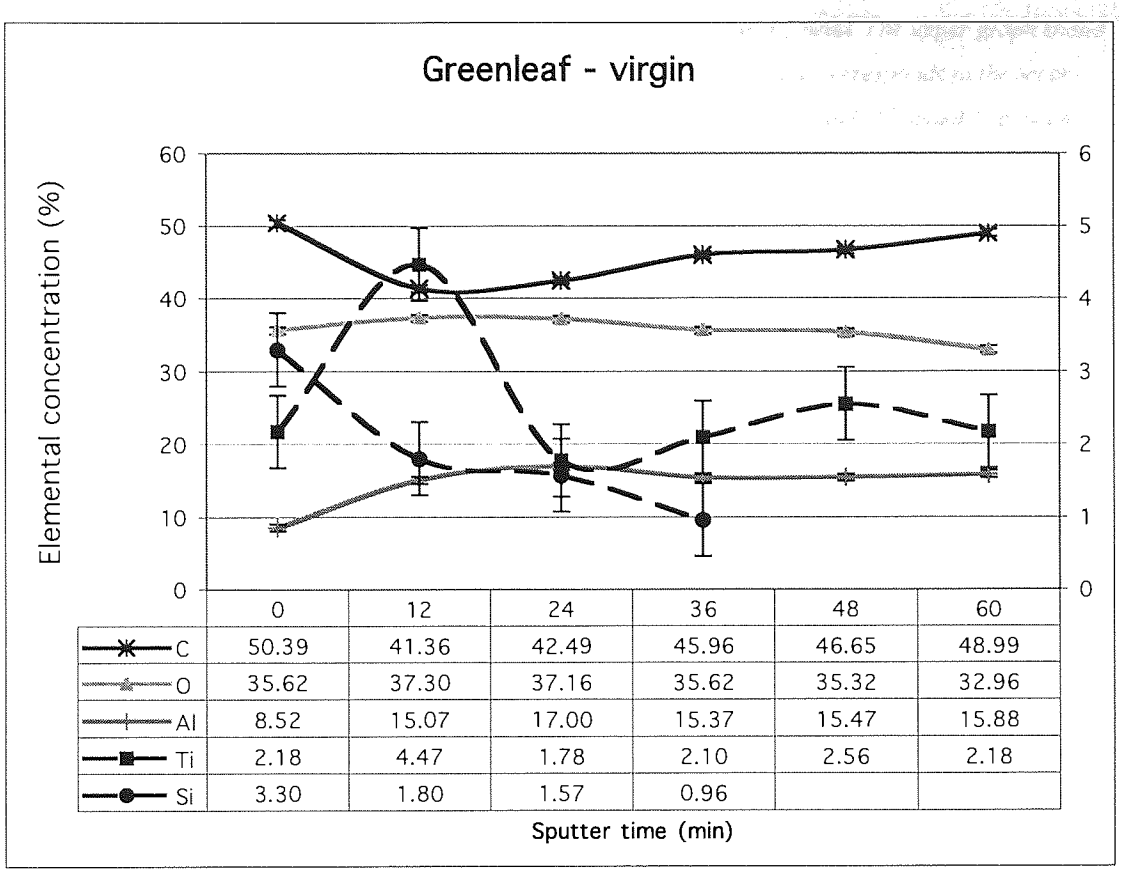

	0	12	24	36	48	60
C	50.39	41.36	42.49	45.96	46.65	48.99
O	35.62	37.30	37.16	35.62	35.32	32.96
Al	8.52	15.07	17.00	15.37	15.47	15.88
Ti	2.18	4.47	1.78	2.10	2.56	2.18
Si	3.30	1.80	1.57	0.96		

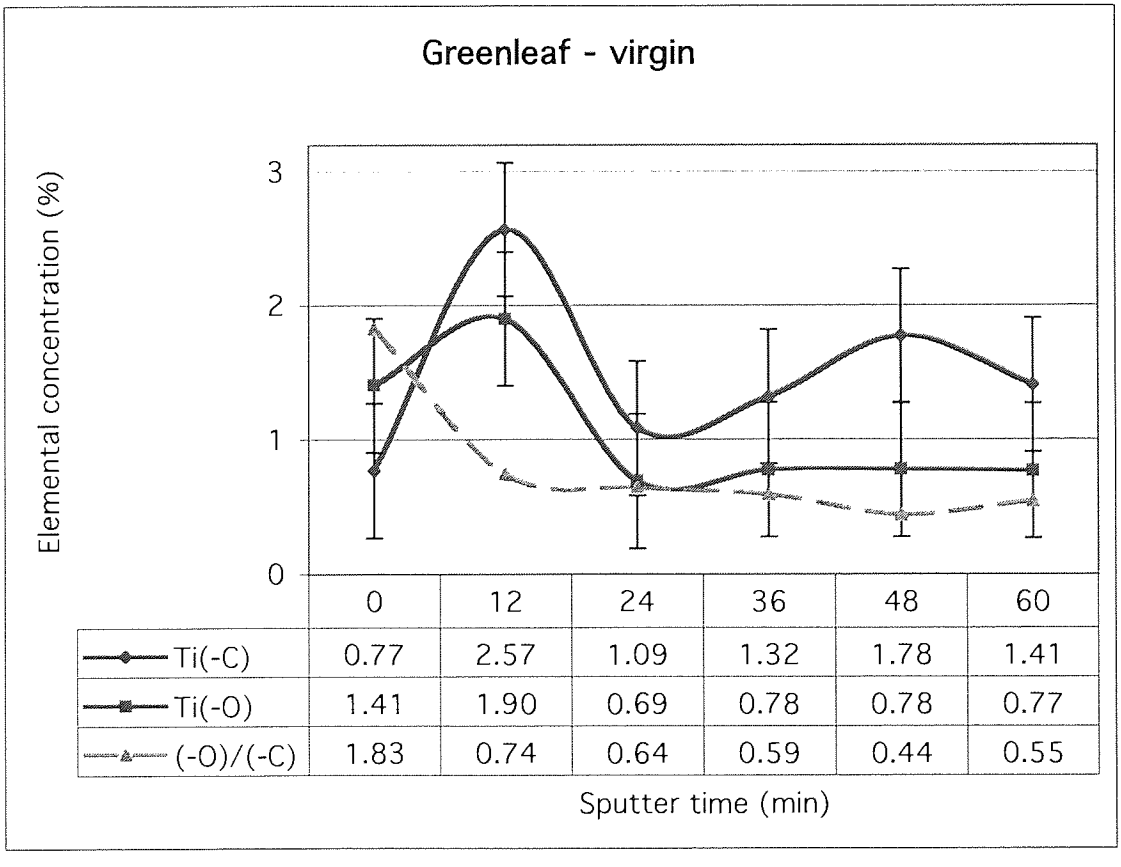

	0	12	24	36	48	60
Ti(-C)	0.77	2.57	1.09	1.32	1.78	1.41
Ti(-O)	1.41	1.90	0.69	0.78	0.78	0.77
(-O)/(-C)	1.83	0.74	0.64	0.59	0.44	0.55

Figure 97. XPS depth profile of a GL Al_2O_3-TiC full-contoured virgin dummy head. The upper graph shows the relative concentrations of all the elements identified (the discontinuous line corresponds to the secondary left axe). The lower graph further decomposes the Ti concentration into C and O bonded Ti concentrations, corresponding to the titanium carbide and titanium oxide, respectively; the discontinuous line indicates the oxide to carbide ratio.

3.3.2 TiO_x dummy heads

3.3.2.1 AFM analysis of TiO_x dummy heads

AFM scans of the TiO_x dummy heads are presented in perspective in Figure 98 and as a levelled orthogonal projection in Figure 99 (virgin) and Figure 100 (worn). Virgin heads showed mainly scratches (~ 10 nm) likely to be formed during the lapping process. On a close look one may distinguish the grain boundary.

As the test proceeded, scattered pullouts appeared (up to 40 ~ 80 nm deep) within 20 hours. These pullouts are attributed to shallow grains, bonded over a restricted surface, and therefore easily removed upon sliding contact with the tape. They can conveniently serve as indentation helping to assess the extent of wear, all along the test.

At 10°C/10%, the scratches tended to smooth out as they were gradually covered with stain transferred from the tape. The transfer material first patchy and rough, tended to spread out, becoming smoother and homogeneous as the test proceeded.

At 25°C/35%, the same process as at 10°C/10% occurs, although the scratches seem to disappear at an increased rate. After 200 hours, the contrast rough / smooth is more marked, eventually corresponding to film-like / very patchy stain respectively.

At 40°C/80%, pullouts also formed, but scratches hardly disappear. The occurrence of a rough/smooth contrast during the test was not observed in this condition; however, hot and humid condition is known to hinder stain transfer. The persistence of scratches indicates a fair wear resistance of the material.

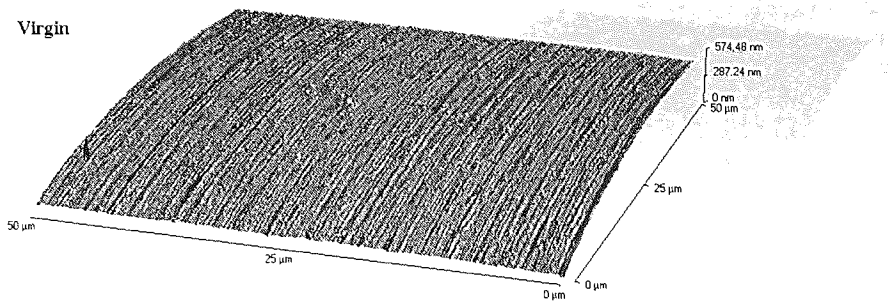

virgin

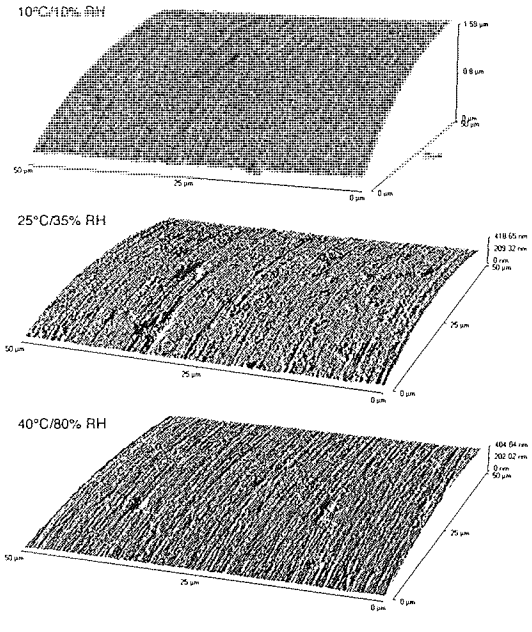

20 hours

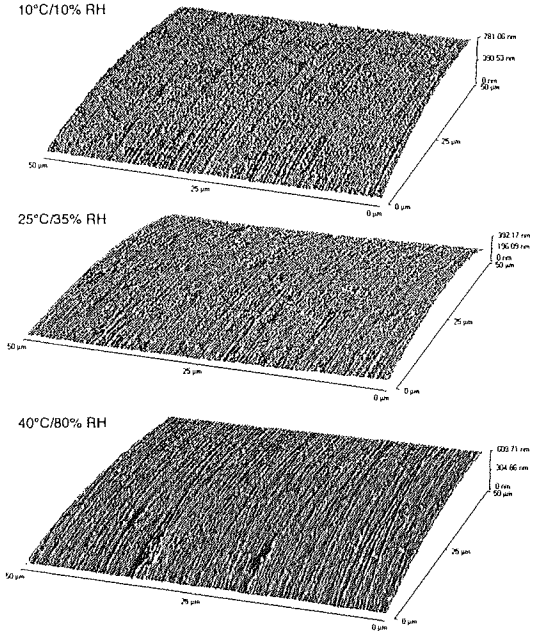

40 hours

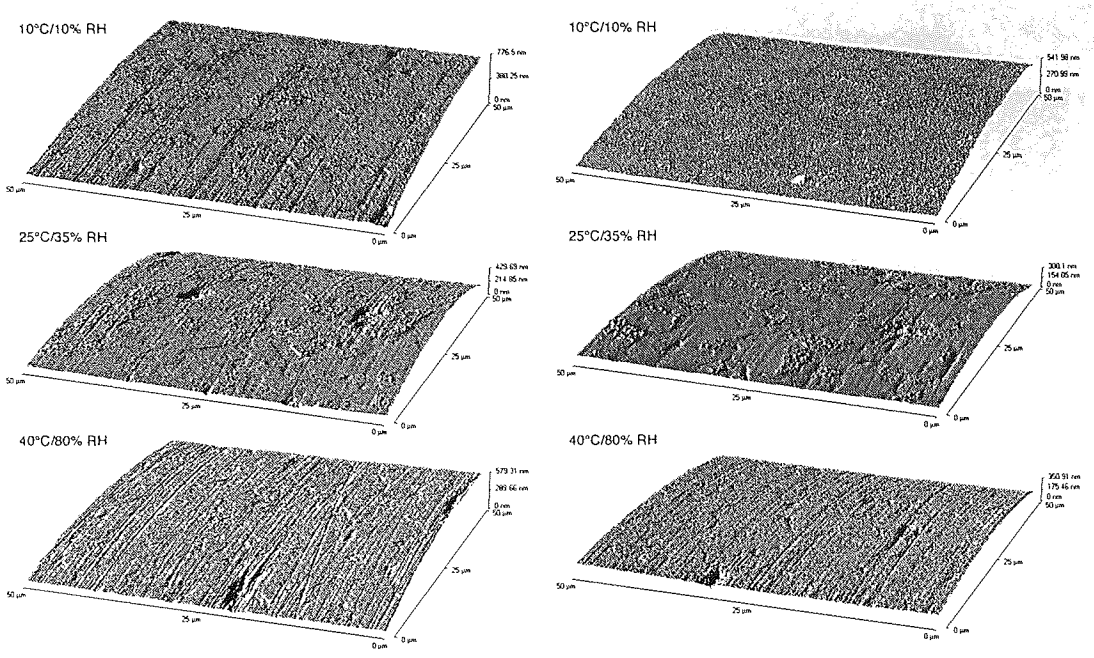

Figure 98. 3D perspective AFM scans of TiO_x dummy heads showing the actual surface curvature. Heads were tested for 20, 40, 100 and 200 hours, in three different environmental conditions. The main features are the presence of pullouts from 20 hours on and transfer of stain in dry/cold (uniform film after 200 hours) and pseudo-atmospheric (patchy deposits) conditions.

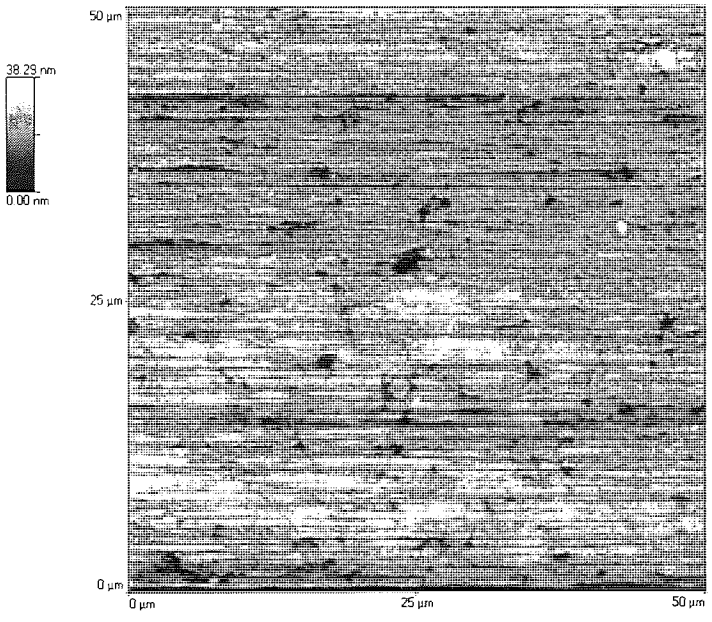

Figure 99. Levelled AFM scan of a virgin TiO_x head.

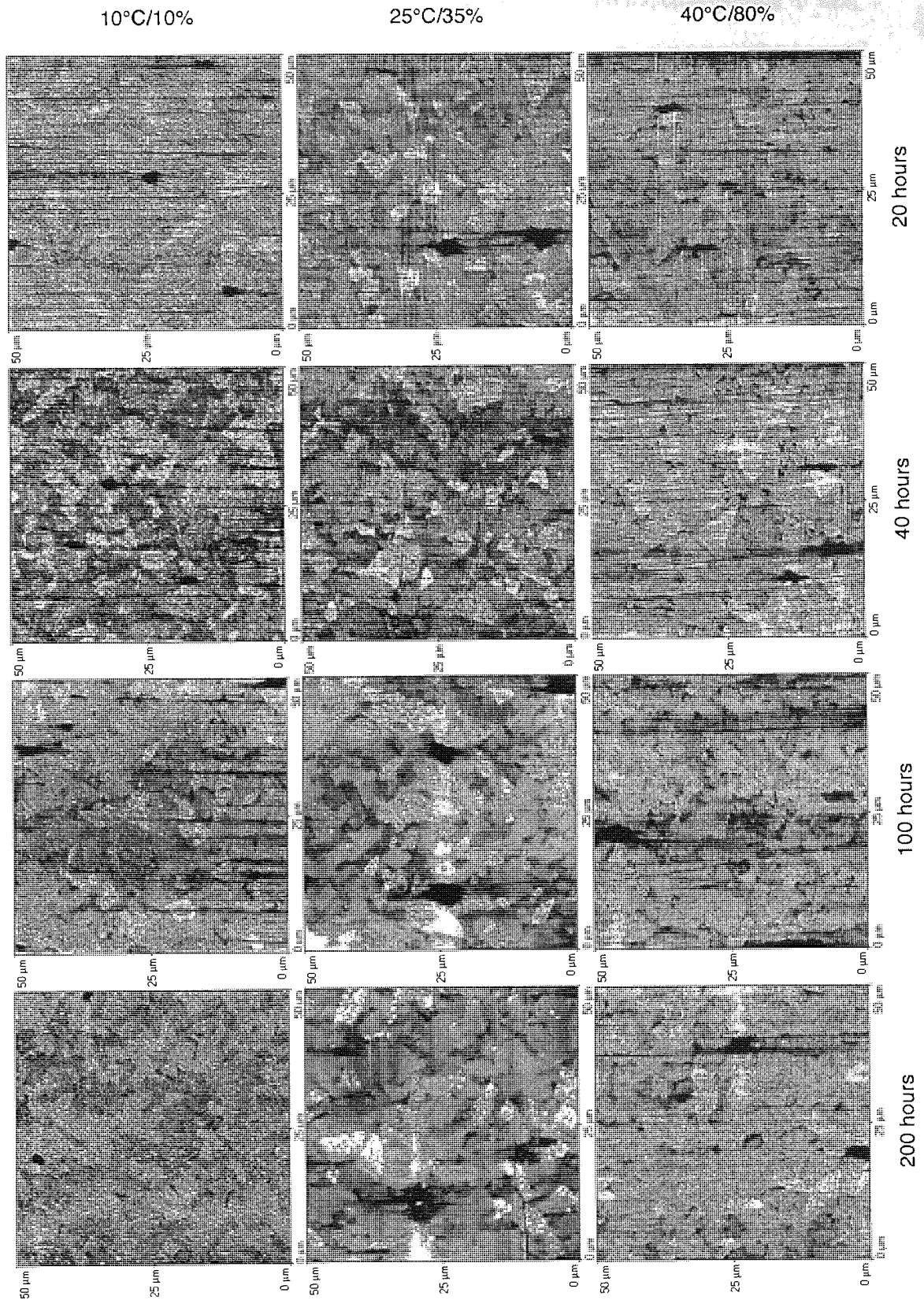

Figure 100. Levelled AFM scan of TiO_x heads, tested for up to 200 hours in three different environmental conditions.

In all three conditions, the shallow pullout formed within 20 hours, change little in size, indicating limited wear.

3.4 XPS analysis of TiO_x dummy heads

Ti was detected at high concentration: the Ti peak corresponds to the oxidized form whilst the O peak can be fitted to a convolution of two peaks (Figure 101): the most intense peak corresponds to oxygen bound to Ti (530.6 eV); the smaller one is typical of structures containing hydroxyl (O–H) groups (532.5 eV) [222].

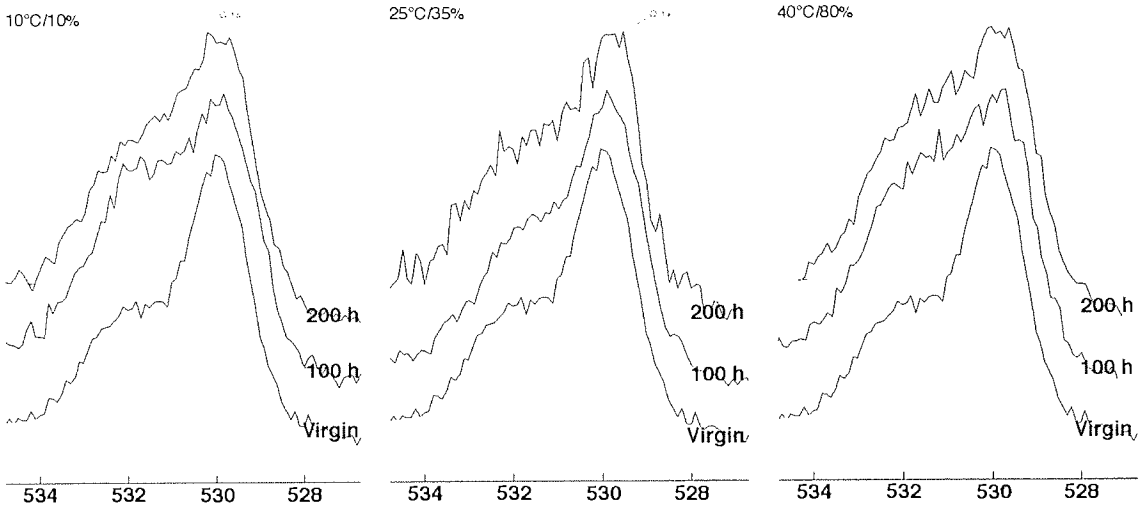

Figure 101. XPS spectrum of TiO_x dummy head zoomed on the O peak. The peak can be fit to the convolution of two peaks corresponding to the O-H bond and Ti-O bond.

As the test proceeded, the apparent Ti concentration decreased from above 30% to below 10% (Figure 102). No such decrease affected the O concentration whilst the O peak shape evolved, the O–H to TiO_x ratio increasing, particularly at high humidity. Simultaneously, the Fe concentration rose, indicating a stain transfer from the tape. The lower Fe concentration after 200 hours conjugated with the delayed disappearing of scratches at 10°C/10% RH as compared to 25°C/35% RH is attributed to the slower transfer rates at lower temperature.

Si was already present over Al_2O_3-TiC heads and is likely to come from the tape or drive lubricants. N is present in tape binder transferred onto the head surface.

Overall no drastic differences were observed between the three conditions.

TiO_x

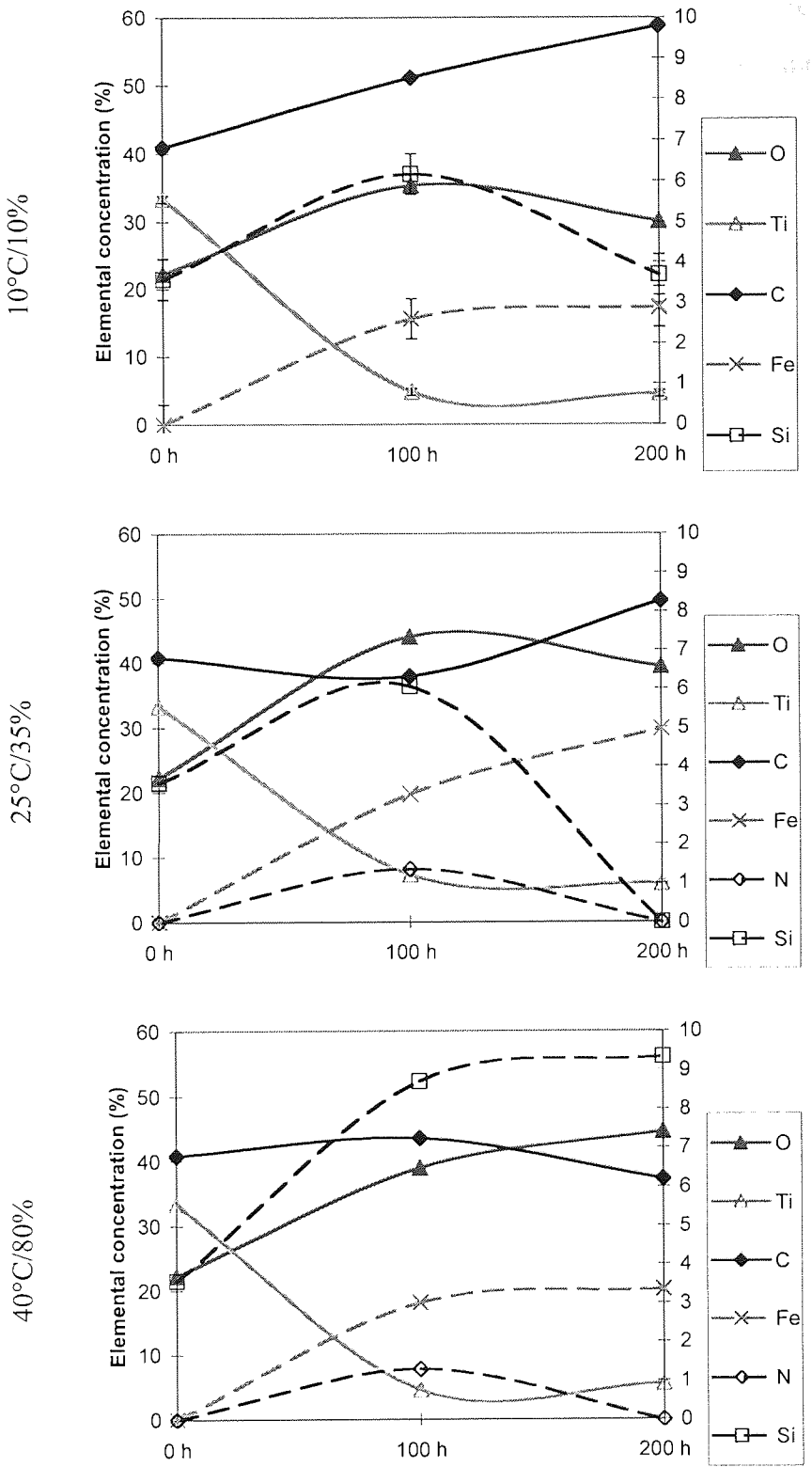

Figure 102. Elemental concentration of the different constituents found at the dummy head surface, deduced from the quantification of the respective XPS spectra. The dashed lines refer to the secondary (right-hand) axis.

3.4.1 Al_2O_3 dummy heads

TiO_2 has a substantially lower hardness than Al_2O_3 or TiC (*c.f.* Table 5). To investigate the effect of a high hardness on the single-phase ceramic wear resistance, Al_2O_3 ceramic wear behaviour was further examined.

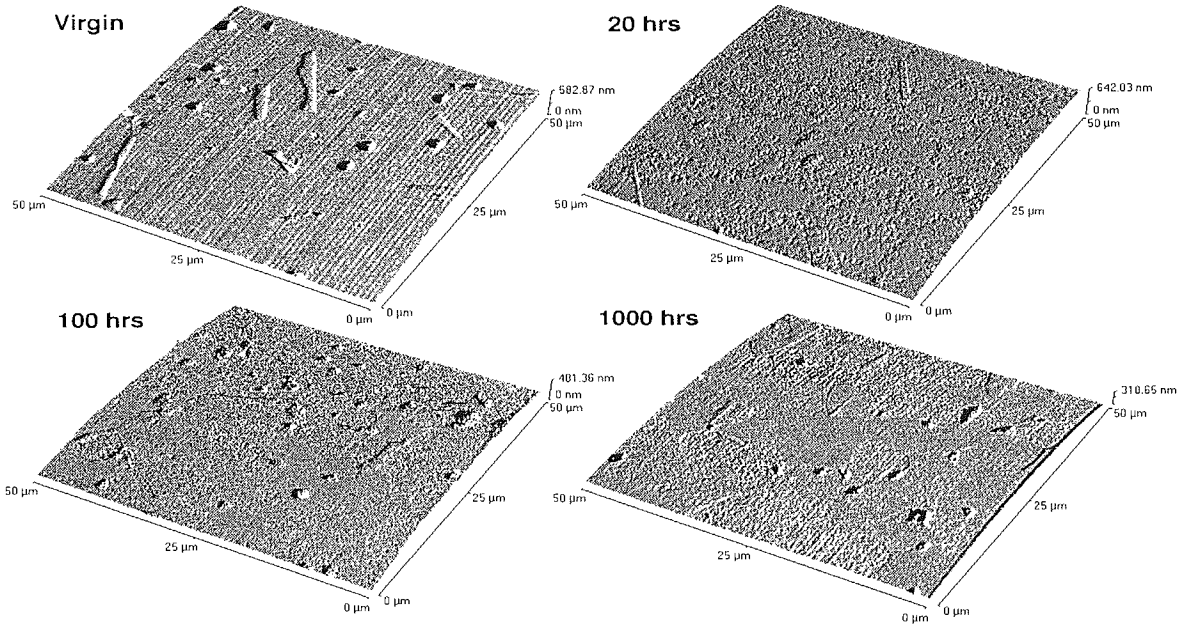

Figure 103. Shadowed perspective AFM scans of Al_2O_3 dummy heads showing the actual surface curvature. Heads have been tested for 0, 20, 100 and 1000 hours, in pseudo-normal condition (25°C/35% RH). Pits ~ 200 nm deep are present all along the test.

Al_2O_3 heads were tested in *pseudo*-atmospheric condition (25°C/35% RH), for up to 1000 hours (11 000 passes = 5 500 cycles = 3 850 km), with interruption after 20 and 100 hours. Pits about 200 nm deep found all over the virgin head surface remained all through the test, only slightly filled with deposits after 20 hours. Scratches (formed during the head lapping process) present on the virgin head disappeared after 20 hours. Deposits, visible over the head surface after 20 hours, tended to spread upon further testing, whilst the grain contour became apparent. Even after 1000 hours of test, the step between recessed grains and protruding grains seldom exceeded 10 nm. Although Al_2O_3 (Knoop hardness: 25.5 GPa) is much harder than TiO_x (Knoop hardness: 7.0 GPa), the wear behaviour appeared to be essentially identical. Unlike Al_2O_3-TiC double-phase ceramic, both tested single-phase ceramics showed no evidence of preferential wear and globally only very superficial wear.

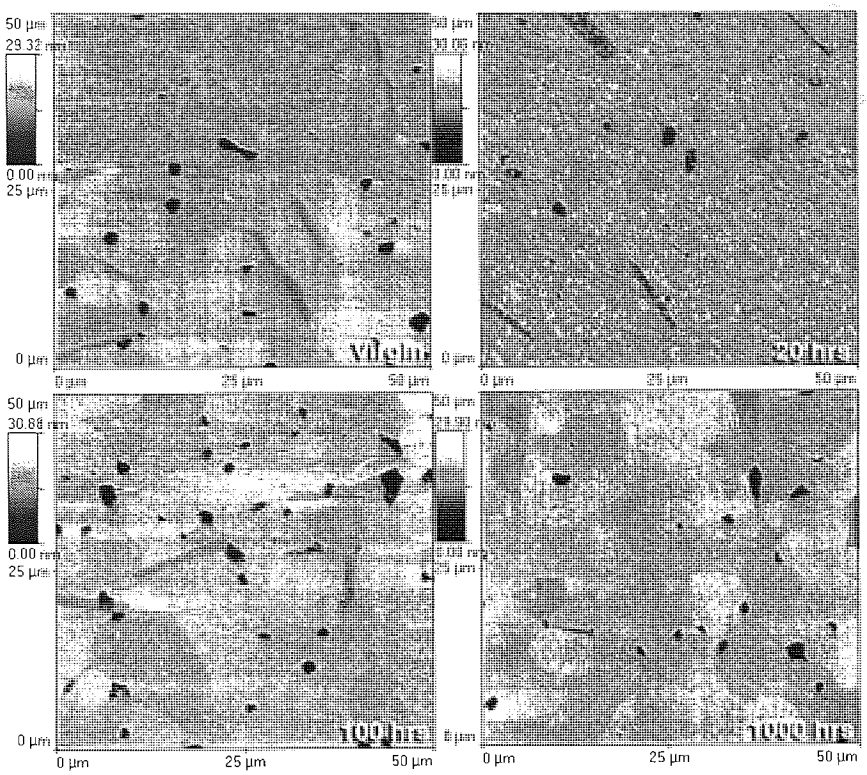

Figure 104. Levelled AFM scan of Al_2O_3 heads, tested for up to 1000 hours in three different environmental conditions.

4 Chapter IV—Numerical modelling of the head subsurface stress due to the contact with a rough tape

4.1 Principles and method

Any magnetic recording head relies on very hard materials (ceramics), either as air- or tape-bearing surface (ABS and TBS), or as wear/corrosion protective coatings. These materials may fail by fracture (as the tensile stress in the elastic solid exceeds the fracture strength) after very limited plastic deformation, a process known as *brittle fracture*. Cracks may thereby propagate from pre-existing cracks or internal cracks, and eventually link together to form wear particles. To understand the above process, it is essential to assess the stress distribution within the solid considered.

Contact between two rough bodies occurs over many asperity contacts. The contact modelling may therefore involve two steps. First, a single pair of asperities constituting a single asperity contact must be considered (*c.f.* 1.3.2.2). Second, the effect of coupling a large number of asperity contacts must be taken into account.

Amongst the numerous available methods, two methods are reported and implemented here: a matrix inversion method applied to two dimensional profiles [73, 74] and a conjugated gradient method, applied to 3D profiles, potentially accelerated with use of multi-level multi-summation (MLMS) technique [75].

4.1.1 Two dimension modelling—matrix inversion method

First the frictionless two-dimensional contact of two elastic bodies is considered, depicted in Figure 16 for a single asperity pair, with the following assumptions.

Inside the contact:

$$\delta(x) = \delta_1(x) + \delta_2(x) \text{ and } p(x) > 0 \qquad (67)$$

Outside the contact:

$$\delta(x) > \delta_1(x) + \delta_2(x) \text{ and } p(x) = 0 \qquad (68)$$

In frictionless contact, where horizontal displacement are ignored:

$$\delta_1(x)\cdot\frac{E_1}{\left(1-\nu_1^{\,2}\right)}=\delta_2(x)\cdot\frac{E_2}{\left(1-\nu_2^{\,2}\right)} \tag{69}$$

The classical plane strain solution for the vertical displacements due to any applied pressure distribution is [73]:

$$\delta(x)=\frac{2\left(1-\nu^2\right)}{\pi E}\int_A P(x')\cdot\ln\left|\frac{d}{x'}\right|\cdot dx'-\frac{(1+\nu)}{\pi E}\int_A P(x')dx' \tag{70}$$

where d stands for the distance at which zero vertical displacement is assumed and A stands for the contact area.

In the case of multiple contact, (70) may be formulated as:

$$\delta(x)=\frac{2\left(1-\nu^2\right)}{\pi E}\sum_{L=1}^{N}\int_{A_L} P(x')\cdot\ln\left|\frac{d}{x'}\right|\cdot dx'-\frac{(1+\nu)}{\pi E}\sum_{L=1}^{N}\int_{A_L} P(x')dx' \tag{71}$$

where N is the number of contact spots and A_L the corresponding contact areas.

In order to solve (71) numerically, the equation is discretised by dividing the contact boundary into elements, over which the pressure is assumed to be uniform. In practice the height values are digitised real surface data, measured at discrete points ΔL apart, ΔL being the sampling interval. The expression for the incremental displacements ΔW_{ij} due to incremental pressures ΔP_j becomes:

$$\Delta W_{ij}=\frac{2\cdot\Delta P_j\cdot(1-\nu^2)\cdot\Delta L}{\pi E}\left[K+\left(n-\frac{1}{2}\right)\cdot\ln\left(n-\frac{1}{2}\right)-\left(n+\frac{1}{2}\right)\cdot\ln\left(n+\frac{1}{2}\right)\right] \tag{72}$$

when $i\neq j$,

$$\Delta W_{ij}=\frac{2\cdot\Delta P_j\cdot(1-\nu^2)\cdot\Delta L}{\pi E}\left[K+\ln\left(\frac{1}{2}\right)\right] \tag{73}$$

when $i=j$, with

$$K=\ln\left(\frac{d}{\Delta L}\right)+\frac{1}{2}\cdot\frac{1-2\nu}{1-\nu} \tag{74}$$

and $n=x'/\Delta L$. d is taken as 20000 ΔL. the total displacement due to all the elemental pressures ΔP_j is thus:

$$\Delta W_i = \sum_{j=1}^{M} \Delta W_{ij} \tag{75}$$

where M is the total number of contacting elements.

(75) can be formulated in the following matrix form:

$$\Delta W_i = \sum_{j=1}^{M} C_{ij} \Delta P_j \tag{76}$$

The matrix of influence coefficients $[C_{ij}]$ is square and symmetric, the off-diagonal terms being derived from (72) and the diagonal terms from (73).

To solve the above problem with a computer, one inputs the digitised height values from a profiling instrument such as an AFM, the Young's modulus for each body, the total normal load, and a rigid body displacement step, δ_R. The two opposed bodies being approached until initial contact, the initial values ΔW_i are calculated using the penetration distance δ_i and equation (69). Non-zero δ_i define the contacting points, hence the values of n used to calculate C_{ij}. The incremental pressure ΔP_j is determined using the inverse of (76), which requires the inverse of C_{ij} to be calculated. Terms corresponding to negative (tensile) pressures are then removed and a reduced set of simultaneous equations is set-up. The set of contact points, hence the influence coefficients are updated and a new set of ΔP_j is calculated. The previous procedure is repeated until all pressures are positive (compressive).

Once the ΔP_j are calculated, vertical displacements outside the contact regions are determined by means of (76), and then the coordinates of the two bodies is updated. The incremental pressures ΔP_j are added to the total elemental pressure P_j; as long as $\Delta L \cdot \sum_{j=1}^{M} P_j$ is lower than the total load per unit width, the upper body is given a further vertical displacement and the above process is repeated.

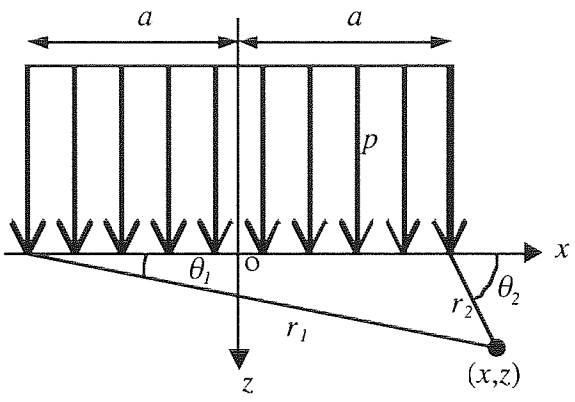

Figure 105. Uniform distribution of pressure showing notation used to evaluate subsurface stresses.

The subsurface stress components, due to a normal pressure $p(x)$ and a tangential traction $q(x)$ uniform over the strip schematised in Figure 105, can be evaluated at any point in the body of the solid [69, 74]:

$$\sigma_{xx} = -\frac{p}{2\pi}\{2(\theta_1 - \theta_2) + (\sin 2\theta_1 - \sin 2\theta_2)\} - \frac{q}{2\pi}\left\{4\ln\left(\frac{r_1}{r_2}\right) - (\cos 2\theta_1 - \cos 2\theta_2)\right\} \quad (77)$$

$$\sigma_{zz} = -\frac{p}{2\pi}\{2(\theta_1 - \theta_2) - (\sin 2\theta_1 - \sin 2\theta_2)\} - \frac{q}{2\pi}(\cos 2\theta_1 - \cos 2\theta_2) \quad (78)$$

$$\sigma_{xz} = -\frac{p}{2\pi}(\cos 2\theta_1 - \cos 2\theta_2) - \frac{q}{2\pi}\{2(\theta_1 - \theta_2) + (\sin 2\theta_1 - \sin 2\theta_2)\} \quad (79)$$

where $\tan\theta_{1,2} = z / (x \pm a)$, $q = \mu.p$ and $r_{1,2} = \{(x \pm a)^2 + z^2\}^{1/2}$.

Therefore, given the surface pressure distribution calculated above, the principle of superposition can be used to yield the complete subsurface stress field.

4.1.2 *Three dimensional modelling—conjugated gradient*

A multi-level multi-summation (MLMS) technique combined with conjugated gradient (CG) method providing a fast numerical solution of rough contact problems has been proposed by Polansky and Keer [75].

The overall problem is formulated as follows. Contacting rough surfaces are described by two sets of height data, corresponding to a surface grid, obtained by 3D surface imaging device (*e.g.* AFM) or generated by a computer. The set of all grid nodes is denoted by:

$$I_g = \{(i,j): 0 \le i < M_x, 0 \le j < M_y\} \tag{80}$$

where $M_{x,,y}$ refers to the grid dimension. The plane $z = 0$ coincides with the plane of contact. The composite surface height h_{ij} is defines as the sum of the heights of the two surfaces at node (i, j). The composite surface deflection $u(x, y)$ is defined as the sum of the elastic deflections of the two contacting surfaces at (x, y):

$$u(x,y) = -\iint_{S_g} K(x-x', y-y')\, p(x',y')dx'dy', \tag{81}$$

where S_g is divided into $N = M_xM_y$ rectangular surface elements S_{ij} centred at the grid nodes. The contact pressure distribution $p(x, y)$ is approximated by a piece-wise constant function, uniform and equal to p_{ij} within each surface element.

For a pair of homogeneous elastic solids in contact, the kernel $K(x, y)$ is given by the Boussinesq formula [69]:

$$K(x,y) = \left(\frac{1-\nu_1^2}{\pi E_1} + \frac{1-\nu_2^2}{\pi E_2}\right)\frac{1}{\sqrt{x^2+y^2}}, \tag{82}$$

where $E_{1,2}$ and $\nu_{1,2}$ are the Young modulii and Poisson ratios of the two contacting solids 1 and 2.

$u(x, y)$ may be discretised as:

$$u_{ij} = -\sum_{(k,l)\in I_g} K_{i-k,\,j-l}\, p_{kl}, \quad (i,j) \in I_g, \tag{83}$$

with

$$K_{ij} = \iint_{S_g} K(x_i - x', y_j - y')dx'dy', \quad (i,j) \in I_g. \tag{84}$$

K_{ij} has been calculated for a rectangular patch load of dimensions $2a$ x $2b$ acting on elastic half-space [223]:

$$K_{ij}=\frac{1}{\pi E^{*}}\left\{\begin{aligned}&(x_i+a)\ln\left[\frac{(y_j+b)+\sqrt{(y_j+b)^2+(x_i+a)^2}}{(y_j-b)+\sqrt{(y_j-b)^2+(x_i+a)^2}}\right]\\&+(y_j+b)\ln\left[\frac{(x_i+a)+\sqrt{(y_j+b)^2+(x_i+a)^2}}{(x_i-a)+\sqrt{(y_j+b)^2+(x_i-a)^2}}\right]\\&+(x_i-a)\ln\left[\frac{(y_j-b)+\sqrt{(y_j-b)^2+(x_i-a)^2}}{(y_j+b)+\sqrt{(y_j+b)^2+(x_i-a)^2}}\right]\\&+(y_j-b)\ln\left[\frac{(x_i-a)+\sqrt{(y_j-b)^2+(x_i-a)^2}}{(x_i+a)+\sqrt{(y_j-b)^2+(x_i+a)^2}}\right]\end{aligned}\right\}. \tag{85}$$

The elastic contact problem can be summarised by the following system of equations and inequalities:

$$\sum_{(k,l)\in I_g} K_{i-k,j-l}p_{kl}=h_{ij}+\alpha,\quad (i,j)\in I_c\ ; \tag{86}$$

$$p_{ij}>0,\quad (i,j)\in I_c\ ; \tag{87}$$

$$\sum_{(k,l)\in I_g} K_{i-k,j-l}p_{kl}\geq h_{ij}+\alpha,\quad (i,j)\notin I_c\ ; \tag{88}$$

$$p_{ij}=0,\quad (i,j)\notin I_c\ ; \tag{89}$$

$$a_x a_y \sum_{(i,j)\in I_g} p_{ij}=P_0 \tag{90}$$

where α is the unknown 'rigid body' approach of the two solids, P_0 is the total normal load supported by the contact, a_x and a_y are the grid spacing in x- and y-directions, and I_c is the set of all grid nodes that are in contact, which is the discrete analogue of the real area of contact.

After the elemental contact pressures p_{ij} have been determined for all of the grid nodes, the corresponding subsurface stresses at any given depth $z > 0$ can be computed using expressions available in the literature [223, 224, 225].

Thus, the subsurface stress field caused by a uniform patch of length $2a$ and $2b$, in the x- and y- directions, respectively, on the surface of a semi-infinite space is

$$\sigma_{kl} = \sum_{i,j \in I_g} \frac{p_{kl}}{2\pi} \left\{ \begin{bmatrix} A_{ij}(x_i + a, y_j + b, z) + A_{ij}(x_i - a, y_j - b, z) \\ -A_{ij}(x_i - a, y_j + b, z) - A_{ij}(x_i + a, y_j - b, z) \end{bmatrix} + \mu \begin{bmatrix} B_{ij}(x_i + a, y_j + b, z) + B_{ij}(x_i - a, y_j - b, z) \\ -B_{ij}(x_i - a, y_j + b, z) - B_{ij}(x_i + a, y_j - b, z) \end{bmatrix} \right\}, \quad (91)$$

with

$A_{xx}(x,y,z) = 2\nu\left[\tan^{-1}\left(\frac{xz}{yR}\right) - \tan^{-1}\left(\frac{x}{y}\right)\right] - \tan^{-1}\left(\frac{y}{x}\right) + \tan^{-1}\left(\frac{yz}{xR}\right) + \frac{xyz}{R(x^2+z^2)}$	$B_{xx}(x,y,z) = 2\ln(R+y) + \frac{x^2 y}{R(x^2+z^2)} + (1-2\nu)\frac{y}{R+z}$
$A_{yy}(x,y,z) = 2\nu\left[\tan^{-1}\left(\frac{yz}{xR}\right) - \tan^{-1}\left(\frac{y}{x}\right)\right] - \tan^{-1}\left(\frac{x}{y}\right) + \tan^{-1}\left(\frac{xz}{yR}\right) + \frac{xyz}{R(y^2+z^2)}$	$B_{yy}(x,y,z) = 2\ln(R+y) - \frac{y}{R} + (1-2\nu)\frac{y}{R+z}$
$A_{zz}(x,y,z) = -\tan^{-1}\left(\frac{y}{x}\right) - \tan^{-1}\left(\frac{x}{y}\right) + \tan^{-1}\left(\frac{yz}{xR}\right) + \tan^{-1}\left(\frac{xz}{yR}\right) - \frac{xyz}{R(x^2+z^2)} - \frac{xyz}{R(y^2+z^2)}$	$B_{zz}(x,y,z) = \frac{z^2 y}{R(x^2+z^2)}$
$A_{xy}(x,y,z) = -(1-2\nu)\ln(R+z) - \frac{z}{R}$	$B_{xy}(x,y,z) = 2\ln(R+x) - \frac{x}{R} + (1-2\nu)\frac{x}{R+z}$
$A_{xz}(x,y,z) = \frac{z^2 y}{R(x^2+z^2)}$	$B_{xz}(x,y,z) = -\tan^{-1}\left(\frac{xy}{Rz}\right) + \frac{xyz}{R(x^2+z^2)}$
$A_{yz}(x,y,z) = \frac{z^2 x}{R(y^2+z^2)}$	$B_{yy}(x,y,z) = -\frac{z}{R}$

where $R = \sqrt{(x^2 + y^2 + z^2)}$ and μ is the friction coefficient.

The CG method was originally developed for unconstrained optimisation, but has been extended to quadratic optimisation problems with linear inequality constraints, such as the contact problem (86)–(90). Compared with other iteration methods [76, 77, 78 and 79], CG required less levels of iteration, has a relatively high rate of convergence and

being a simultaneous iteration method, is compatible with techniques such as MLMS to decrease the computation time. The detail of the algorithm can be found in Polansky and Keer [75].

The CG-method algorithm was implemented in C. The program takes the topography of the head and the tape measured by AFM and converted to a text file as an input, and gives as an output the pressure distribution in form of a text file, which can be plotted subsequently using software such as Mathematica or Matlab.

4.2 Application to ADR head to tape contact

4.2.1 Two dimension modelling—matrix inversion method

The ADR head and tape AFM profiles are shown before (Figure 106) and after (Figure 107) the iterative approach used to calculate the pressure distribution, described previously. The result is plotted in Figure 108 along with the value of the resultant total load per unit length at each successive iteration step, up to the target load. The target load per unit length in this example was taken as equal to (referred to as actual load) and 1000 times (referred to as high load) the load calculated at the head-to-tape interface (~ 0.25 N; *c.f.* Figure 57), divided by the head-to-tape interface apparent area of contact (A_a = 0.3 mm × 8 mm) and multiplied by the profile length ($\Delta L \times N$ = 0.100 μm × 200 = 20 μm). The target loads per unit length were therefore 2.1 N/m and 2.1 kN/m, respectively. A factor of 1000, by which the actual load was multiplied, was justified by the minute real area of contact occurring at the actual head-to-tape interface, resulting, for such short sample-length in one single pressure peak. The result of this 2D modelling is only indicative; a more accurate analysis will be proposed in the more realistic 3D case discussed later.

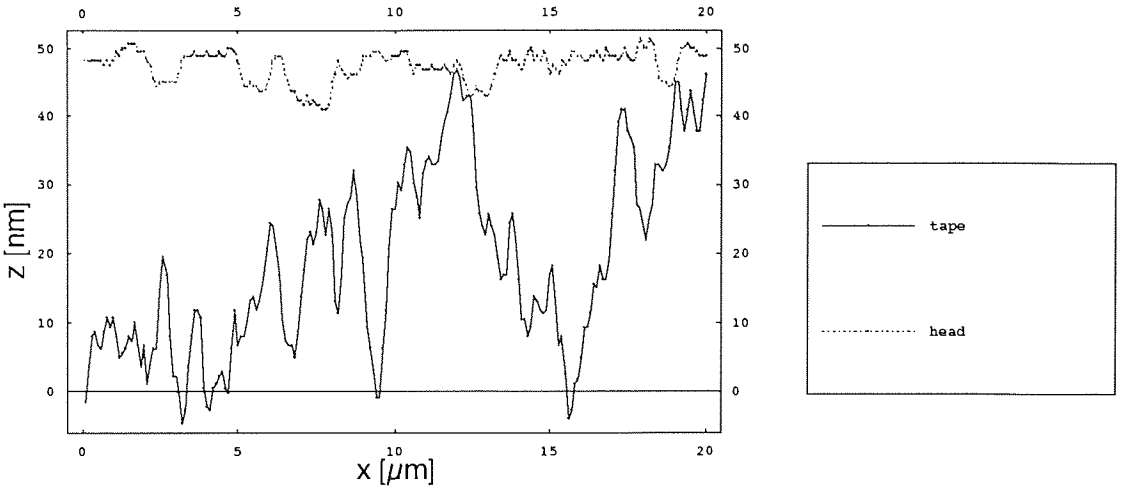

Figure 106. 2D AFM profile of the head (dashed line) and tape (continuous line), in initial unloaded contact.

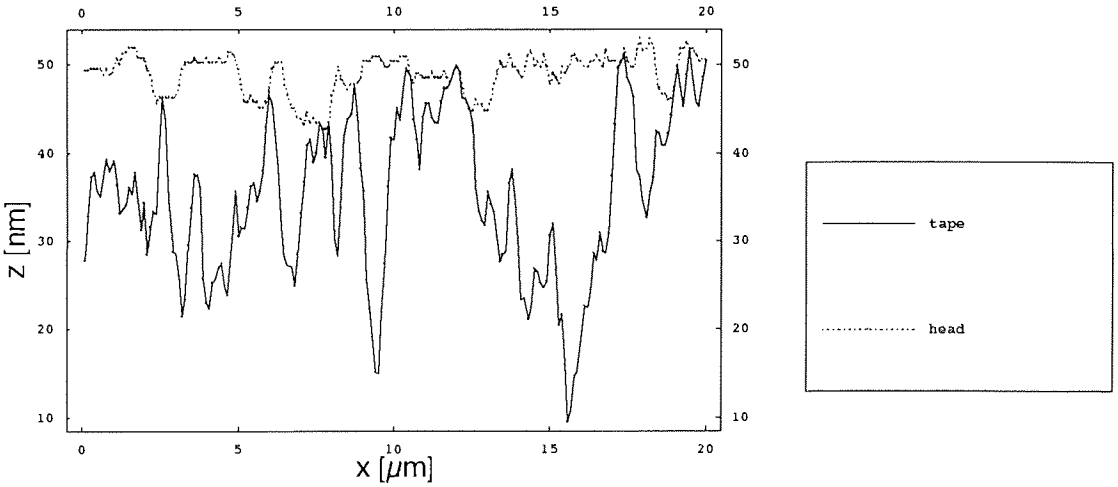

Figure 107. 2D AFM profile of the head (dashed line) and tape (continuous line), in loaded contact (high load) after an iterative approach.

The pressure distribution (Figure 108) peaks slightly above 15 MPa and 300 MPa, for actual and high loads, respectively. The yield strength of a typical binder is $Y \sim 10$ GPa [61] and for a hard material—polymer interface, plastic flow is expected to occur when the pressure exceeds $p_{max} = 1.852\ Y \sim 20$ GPa. For high load as for actual load, it is therefore justified to assume the contact as purely elastic.

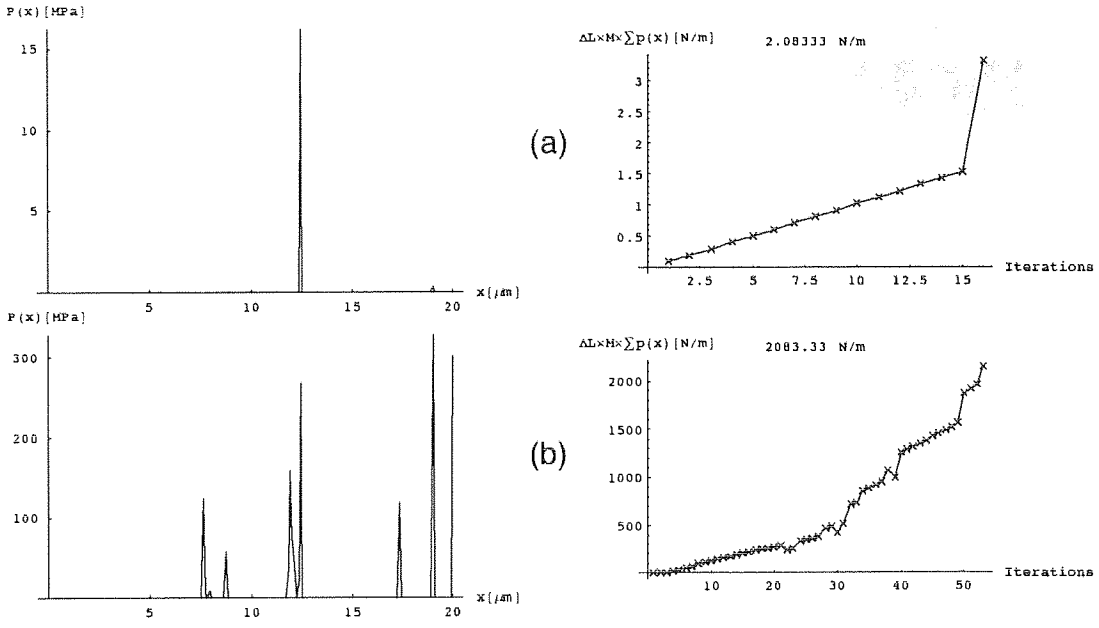

Figure 108. Calculated pressure distribution corresponding to the surface in loaded contact (Figure 107) and total load evolution during the successive iterations (the target load is indicated on top).

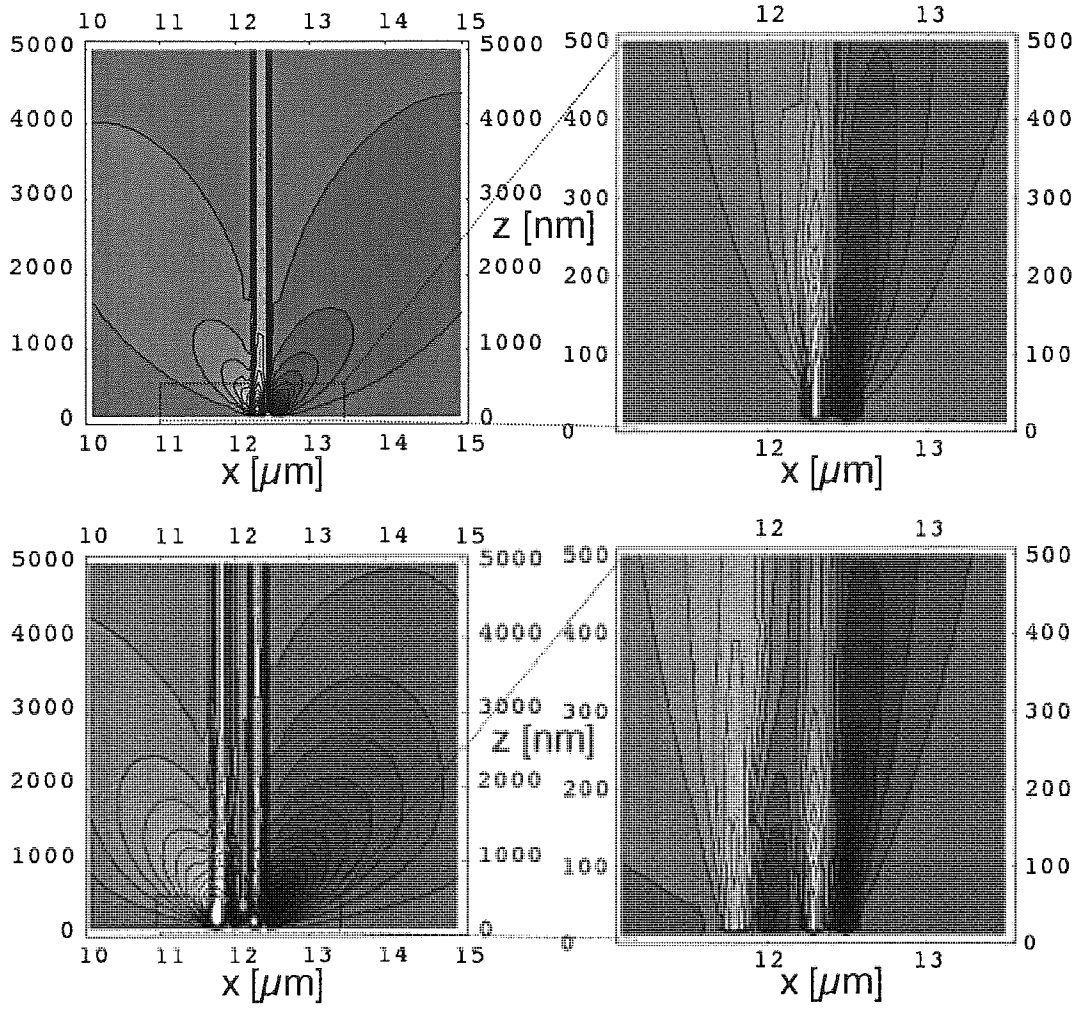

Figure 109. Distribution of subsurface orthogonal shear stress σ_{xz} in frictional contact (μ = 0.1).

The contour plots of the subsurface orthogonal shear stress σ_{xz} and principal shear stress τ_1 are presented in Figure 109 and Figure 110, respectively. First, the maximum stress changed in magnitude (*c.f.* Figure 111), but remained at a constant depth, between the actual and high load. The maximum depth was estimated here above 100 nm, or three times deeper than the typically measured TiC intra-grain pullout depth. The above remark on the lack of reliability of the method for quantitative interpretation should however be kept in mind.

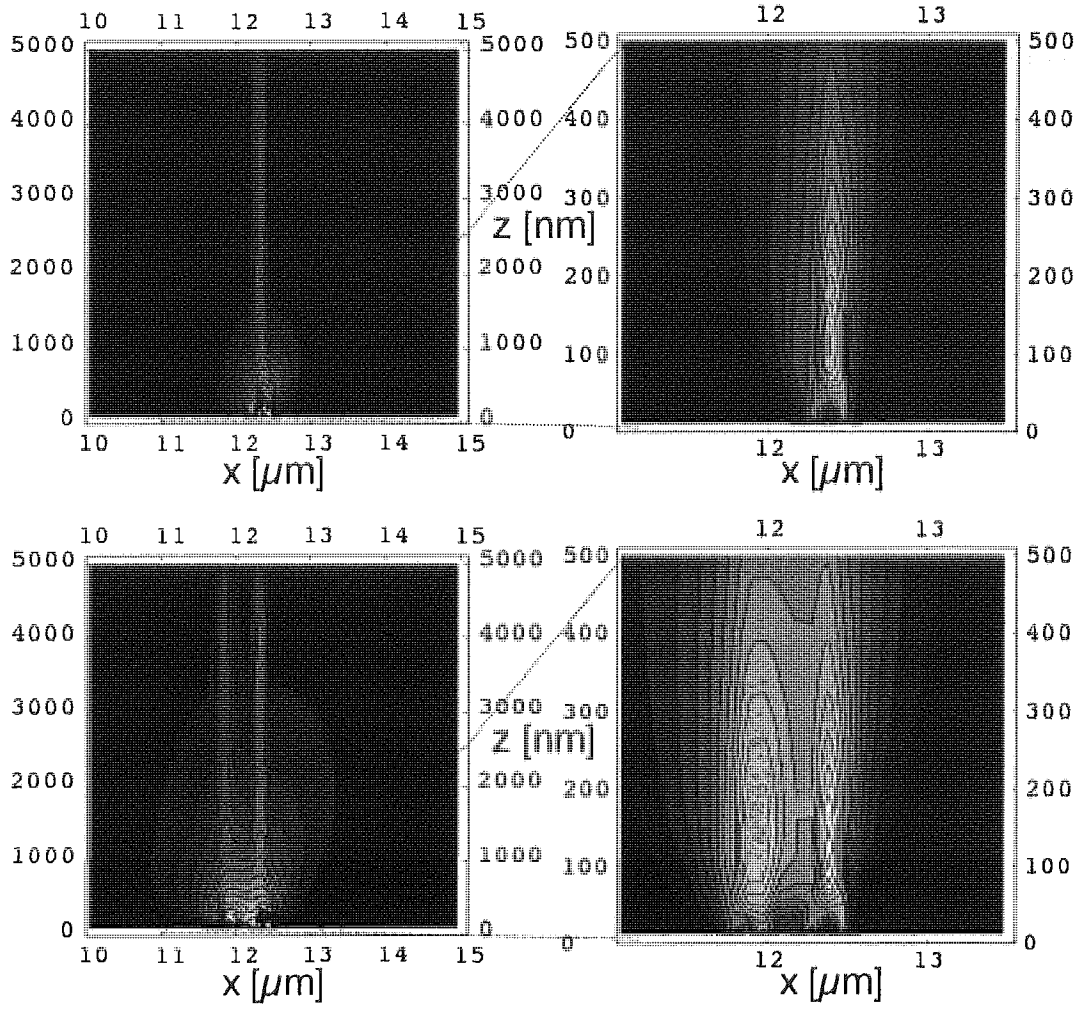

Figure 110. Contour-plot representing the distribution of subsurface maximum shear stress τ_1 in frictional contact ($\mu = 0.1$).

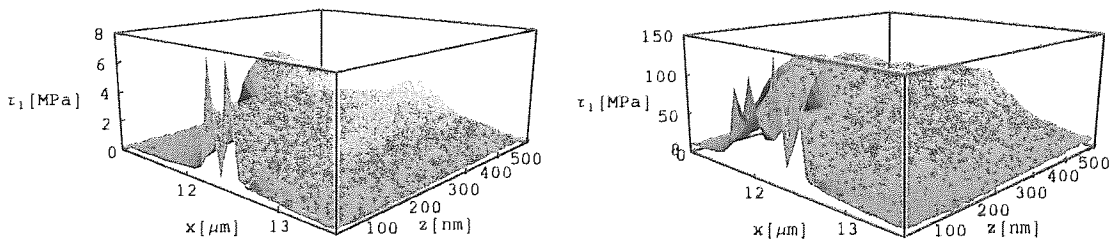

Figure 111. 3D surface-plot representing the distribution of subsurface maximum shear stress in frictional contact ($\mu = 0.1$).

4.2.2 Three dimensional modelling—conjugated gradient

Figure 112 represents the surfaces of the ADR head and tape, imported from an AFM scan, used in the 3D modelling. The normal load used in the calculation was the average normal load calculated at the actual head-to-tape interface ($F_n \sim 0.25$ N—*c.f.* above). The apparent pressure was therefore: $p_a = F_n / A_a = 0.25$ N / 2.4 mm^2 = 104 kPa.

The calculated real pressure distribution is shown Figure 113. The pressure was zero except at two adjacent nodes, hence the ratio of the real to apparent area of contact can be calculated as: $A_r / A_a = 2 / 2500 = 8\times10^{-4}$, which must be compared with $2.8\times10^{-3} / 8\times10^{-4}$ for an *elastic / plastic* deformation, calculated previously using a formal (non numerical) model (*c.f.* Table 18). The pressure peaks above 100 MPa, or far below the plastic yield criterion calculated above, *i.e.* $p_{max} = 1.852\ Y \sim 20$ GPa.

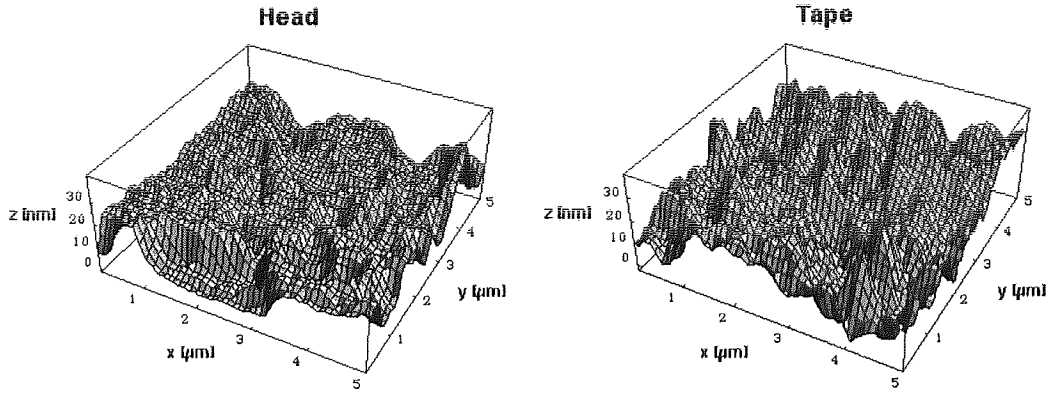

Figure 112. 3D AFM topography mappings used in the contact stress numerical modelling.

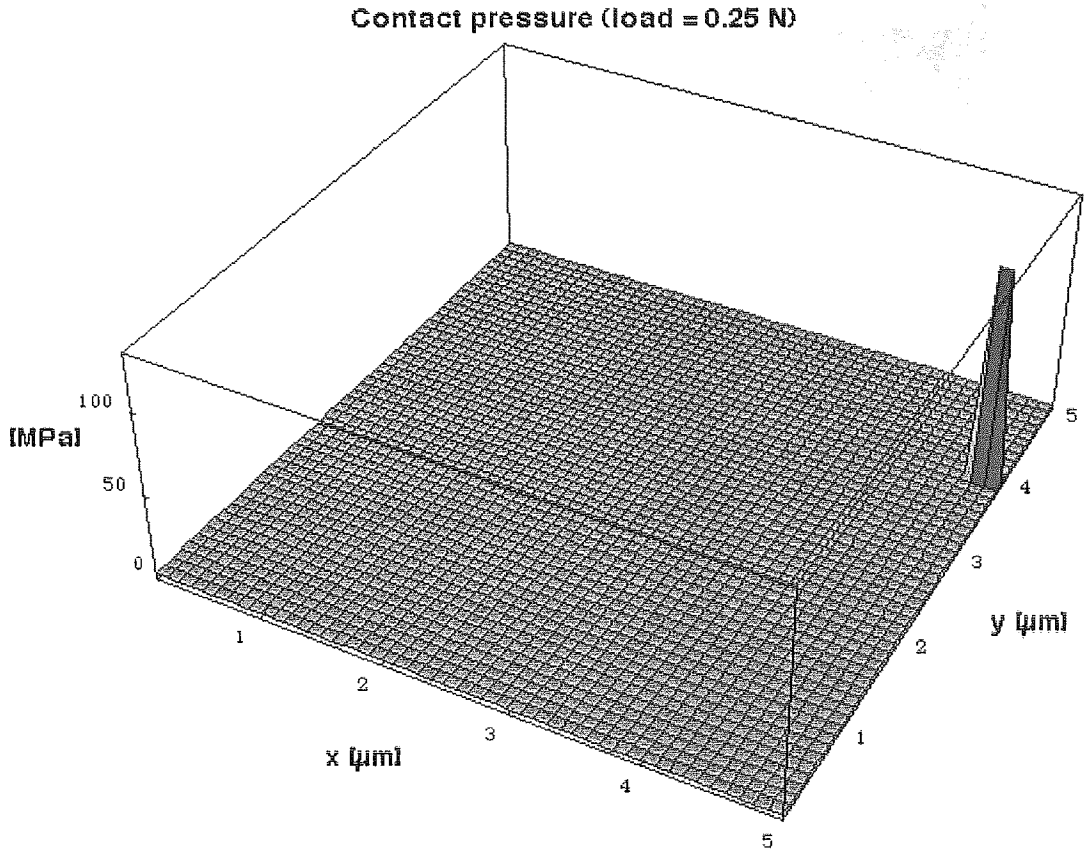

Figure 113. Real pressure distribution calculated using the CG method.

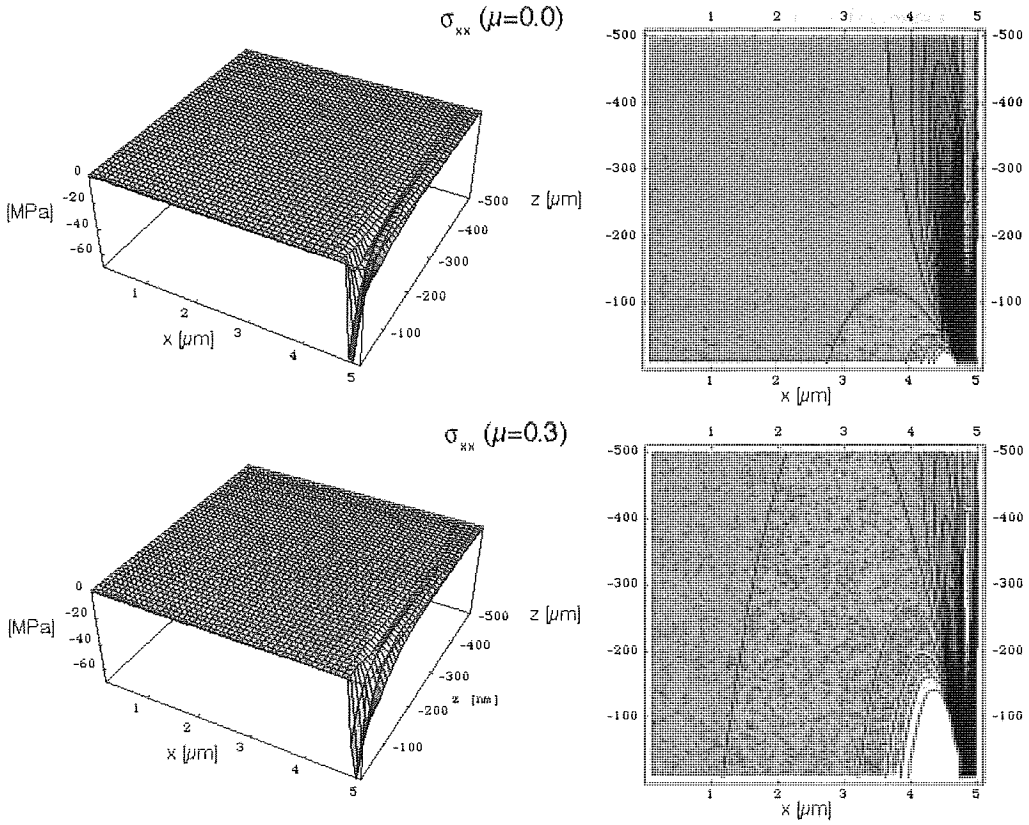

Figure 114. Head subsurface stress σ_{xx} for frictionless (μ=0) and frictional (μ=0.3) contact.

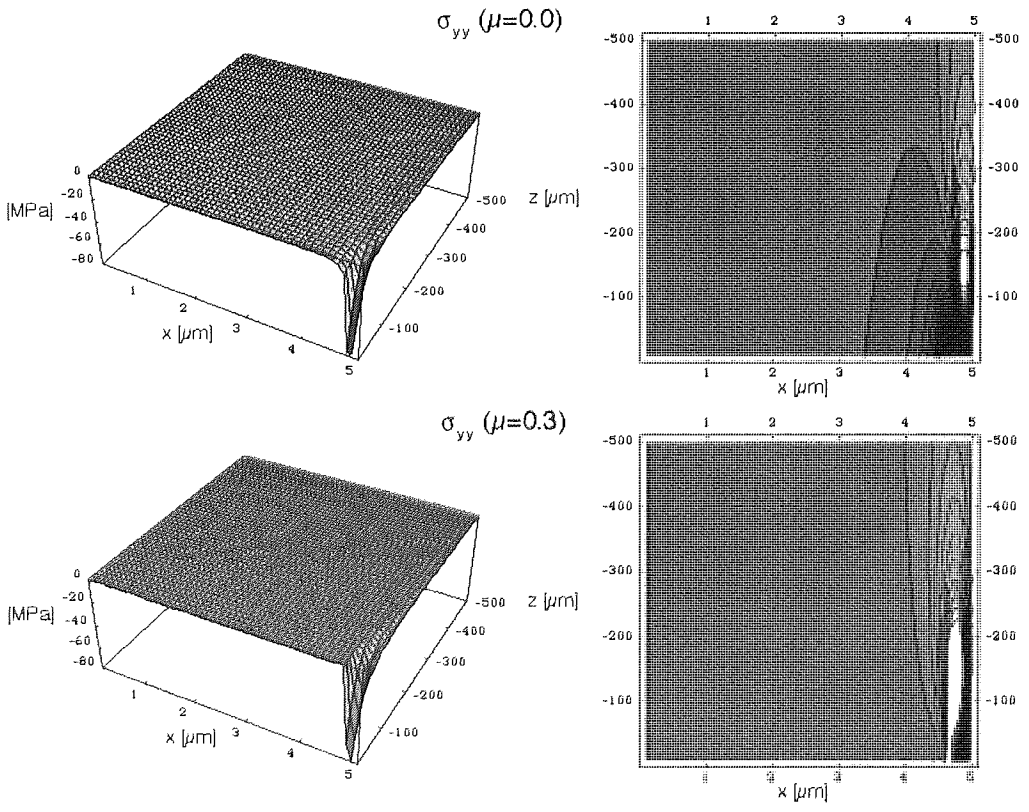

Figure 115. Head subsurface stress σ_{yy} for frictionless (μ=0) and frictional (μ=0.3) contact.

The subsurface stresses σ_{xx} and σ_{yy} are plotted Figure 114 and Figure 115, respectively. The stresses were mainly compressive, with a maximum at the head surface ($z = 0$). However, σ_{xx} was tensile at the trailing edge of the contact—increasing with increasing friction—and below the contact, with a maximum at z ~ - 300 nm. σ_{yy} also became tensile with a maximum at z ~ - 150 nm, which as friction was applied, moved opposite to the friction force and towards the surface. σ_{zz}—plotted in Figure 116—was only compressive, with its maximum at $z = 0$.

The head subsurface shear stress σ_{xz} is presented Figure 117. In frictionless contact, the maximum/minimum was found at ~ - 60 nm; as one applies a friction force, both the maximum amplitude and minimum amplitude decreased, whilst the latter moved towards the surface. The von Mises stress $\sqrt{J_2}$ is displayed Figure 118: its maximum was located ~ 30 nm below the surface.

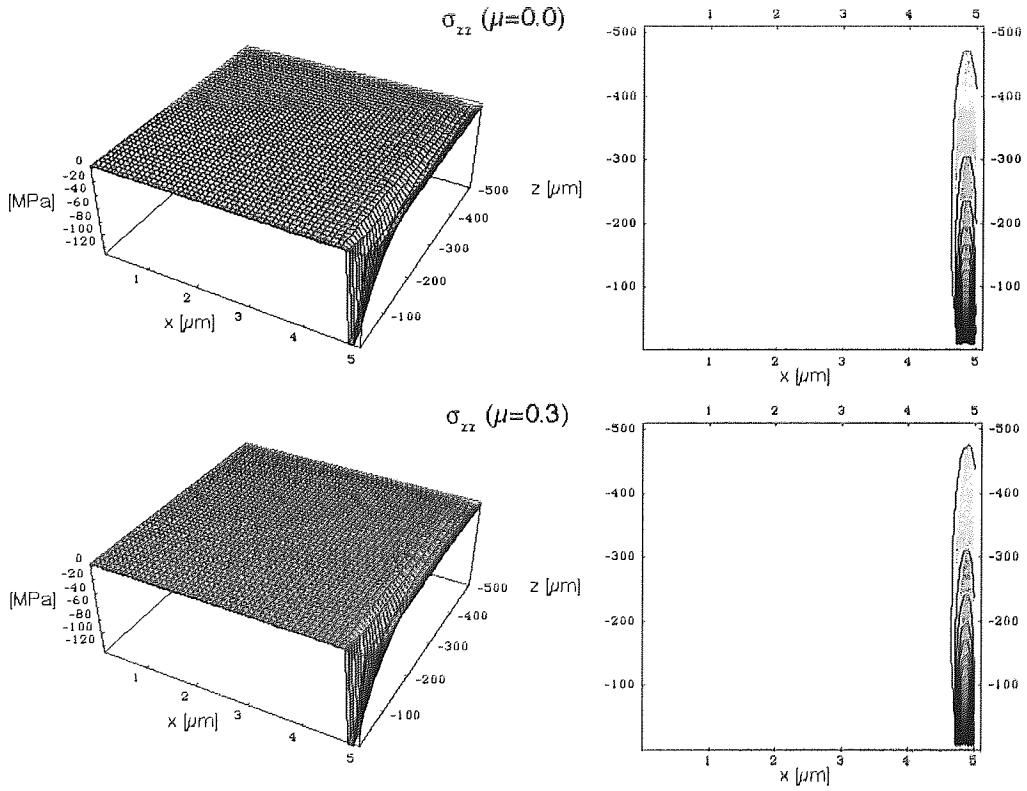

Figure 116. Head subsurface stress σ_{zz} for frictionless (μ=0) and frictional (μ=0.3) contact.

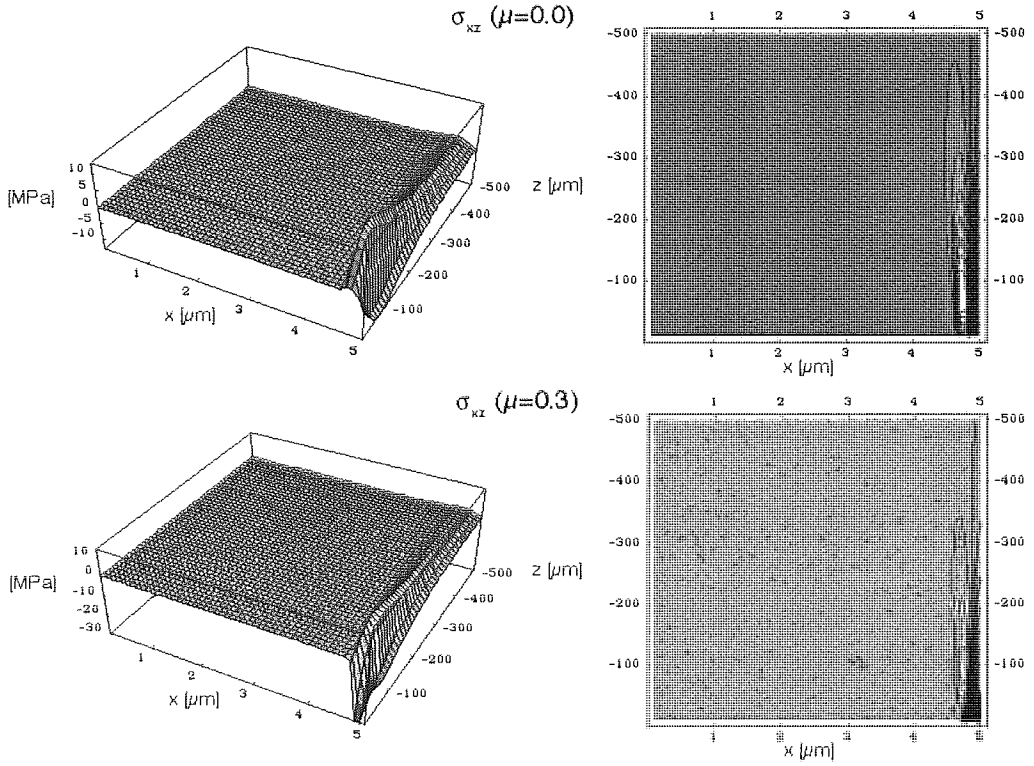

Figure 117. Head subsurface shear stress σ_{xz} for frictionless (μ=0) and frictional (μ=0.3) contact.

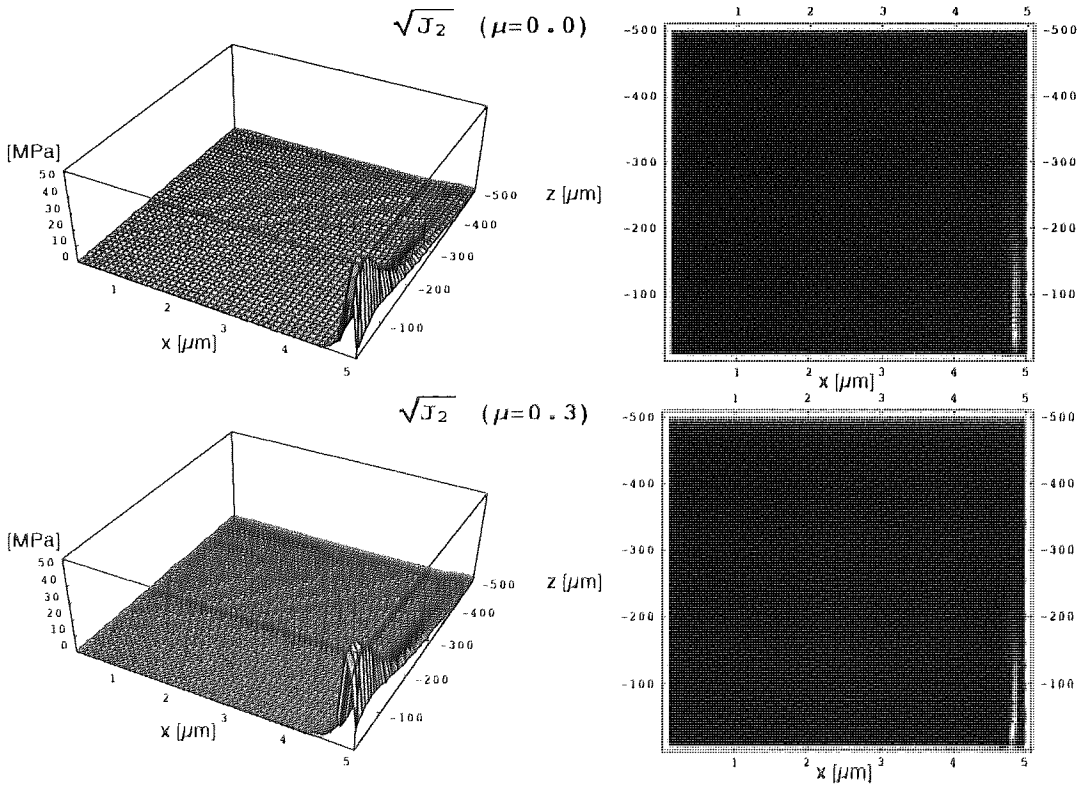

Figure 118. Von Mises stress $\sqrt{J_2}$ for frictionless (μ=0) and frictional (μ=0.3) contact.

5 Chapter V—Discussion

In light of the experimental results presented above, the wear and staining behaviour of ADR standard head and their implications on the signal performance are discussed in this chapter. In accordance, possible solutions to reduce wear and staining—head coating, potentially in combination with a single-phase tape-bearing surface ceramic—, with the purpose of keeping the signal to a maximum are considered.

5.1 Head wear

5.1.1 Al_2O_3-TiC ceramic wear

The first stage of the work covered in this thesis has been to identify the wear and transfer behaviour of the standard heads and understand the mechanisms. Amongst the most striking evidence of wear visible at the surface of worn heads, is a preferential wear affecting the Al_2O_3-TiC tape bearing surface ceramic, which occurred within 20 hours of test. This was regardless of the environmental conditions.

Figure 67 shows views of an ADR head (one selected channel out of eight) obtained using four different imaging techniques: atomic force microscopy (AFM), scanning electron microscopy (SEM), optical microscopy (OM) and Auger electron spectroscopy (AES). The TiC appears as bright spots on the AES Ti map. These spots correspond exactly to the ones appearing on the OM image where (as on the SEM image) both the pole and the TiC region, metal-like materials, are expected to appear clear. Moreover, the patterns seen on the ceramic surface are similar in all respects on the OM and AFM image, and thus clearly indicate that the recessed region (*i.e.* dark on the AFM topographic map) corresponds to the TiC grains.

The bearing ratio curve measured for worn Al_2O_3-TiC tape-bearing surfaces indicated 20 to 30% of the total surface as being recessed. This corresponds to the percentage of TiC in the ceramic. This latter result suggests that after 20 hours on, the whole TiC phase is recessed.

Direct measurement of the TiC intra-grain pullout depth from AFM line scans of the worn heads tested in non-controlled condition is reported in Table 14: the peak to valley was measured as 40 ± 20 nm, and RMS roughness as 21 nm. This latter result compares

to the pullout depth in controlled environment estimated between 20 and 24 nm (± 5 nm) after the bearing ratio (Figure 69), following 500 hours of test and regardless of the atmospheric condition.

The prompt TiC intra-grain pullout process is somewhat unexpected in the sense that the choice of Al_2O_3-TiC is based on its projected outstanding wear resistance. Furthermore, the preferential wear of the harder TiC phase with respect to the softer Al_2O_3 phase is in contradiction with classical formulizations—due to Archard [107] for adhesive wear or Rabinowicz [110] for abrasive wear—which express the wear volume as inversely proportional to the hardness.

Ceramics are normally brittle, with low fracture toughness, and fracture with little or no evidence of plastic flow [226]. Moreover, an interconnection exists between fracture toughness and crack propagation [144]. Thus, a fatigue wear mechanism (relying on material toughness rather that hardness) is likely to govern the TiC intra-grain pullout process. Cyclic stressing of the Al_2O_3-TiC grains from repeated contact with passing tape causes subsurface cracks to propagate parallel to the surface of the ceramic. These cracks will extend until they reach the two-phase boundaries (Al_2O_3-TiC interface). Since TiC grains are embedded in the Al_2O_3 phase, the crack is more likely to section a whole TiC grain and then reach the surface along the boundaries, causing the grain to delaminate.

The above described fatigue wear process relies on subsurface crack creation and propagation. The crack dynamic is driven by the stress field within the material. Moreover, the fatigue crack is assumed to be initiated at the point of maximum von Mises equivalent stress [119, 121].

The stress field at the head subsurface due to the sliding contact with a tape was numerically modelled. The derived real area of contact (where contact pressure at the head-to-tape interface is strictly positive) was found to corroborate the calculation made using a formal model (Table 18): this result is used as an intermediate validation for the modelling. The subsurface stress components σ_{xx} and σ_{yy} were mainly compressive, being tensile at some particular locations such as the trailing edge of contact for σ_{xx} (this is typical in sliding contacts; usually resulting in ring cracks in the trail of an indenter [123]) and 150 nm and 300 nm deep below the contact for σ_{xx} and σ_{yy} respectively. The succession of tensile and compressive stress is likely to weaken the head subsurface and promote a cyclic fatigue process.

The calculated maximum shear stress component σ_{xz} and maximum von Mises equivalent

stress $\sqrt{J_2}$ were respectively located less than 60 nm and between 20 to 30 nm below the surface. Further improvements of the numerical modelling would be required along with a pertinent and thorough interpretation. However, the present result are promising in the sense that they predict a maximum von Mises stress at a depth equivalent to the measured average TiC intra-grain pullout depth: 20 and 24 nm (± 5 nm) after the bearing ratio (Figure 69). This strongly supports the hypothesis of crack propagation at the Mises equivalent stress maximum depth and therefore the fatigue wear mechanism above.

5.1.2 Effect of Al_2O_3-TiC wear on other head elements

In the previous paragraph, the Al_2O_3-TiC wear behaviour (the preferential pullout process of the TiC grain upper part with respect to the Al_2O_3 matrix) was described in an attempt to understand the underlying wear mechanisms (the fatigue fracture of the ceramic sub-surface relying on the propagation of cracks parallel to the surface at a depth equivalent to the maximum Mises equivalent stress). The result of this pullout process is TiC delaminated flakes 20 to 30 nm thick (pullout depth) and with the lateral dimension of the TiC grain they origin from (~ 1 μm). The platelets so produced would fragment immediately to form much smaller particles. TiC is an extremely hard material (the hardest of all materials originally present at the head-to-tape interface), therefore once entrapped between the head and fast sliding tape, is expected to cause significant damages to both head and tape.

Figure 38 shows an AFM image of an ADR head cycled over 10k passes. The debris detached from the Al_2O_3-TiC ceramic at the glue line is believed to have ploughed the pole surface in a single catastrophic event. These exceptional cases rely on the peculiar vulnerability of the ceramic edge at the glue line, but as such are regarded as extreme examples of the general pullout mechanism occurring at the ceramic surface, causing three-body abrasion within the pole-tip recession.

AES maps for O and Ti corresponding to Figure 38 and shown in Figure 43 were converted to bit maps in Figure 44 (white dots indicate the presence of the mapped element). Ti (from TiC) and O (from Al_2O_3) complement each other to cover the whole ceramic surface. O is also present on the insulator surface (SiO_2). More unexpectedly, Ti is found over both the insulator and pole tip surface. The only possible source of Ti is from the ceramic TiC phase: TiC intra-grain pullout particles were therefore trapped within the recessed pole-tip area, were they were likely to produce three-body abrasion effects and be

responsible for an increase in pole-tip recession. This is discussed in more detail later in this chapter.

5.1.3 Other possible forms of wear

Al_2O_3-TiC preferential wear and its probable consequences on the head wear have been discussed. The proposed process involves fatigue wear of the Al_2O_3-TiC ceramic, followed by three-body abrasive wear over the pole-tip due to the TiC delaminated particles. Other possible wear mechanisms and their relative significance are discussed hereafter.

5.1.3.1 Al_2O_3-TiC preferential wear

The first hypothesis put forward to account for the Al_2O_3-TiC preferential wear has been the involvement of two-body abrasion by head-cleaning agents (Al_2O_3) embedded in the tape binder. However, head cleaning agents have the same hardness as the ceramic alumina, but lower than the TiC phase and were therefore unable to explain the observed TiC preferential wear.

Titanium oxidation and subsequent chemical wear has also been considered. The ratio of titanium oxide to titanium carbide measure by XPS on Al_2O_3-TiC dummy heads (Figure 96) was found to decrease over the first 100 hours to increase back as the freshly exposed TiC surface becomes re-oxidized, without further pullout. According to the XPS depth profile of the Al_2O_3-TiC dummy head (Figure 97), the titanium oxide layer is less than 10 nm thick. Chemical wear could induce a progressive wear process where the oxide layer, being softer, is removed and further oxidation takes place followed by removal, etc. This however fails to account for the abrupt TiC phase recession and presence of TiC third-body particles.

5.1.3.2 Pole-tip wear

On standard heads tested at 40°C/80% RH, we observe sliding scratches forming after 20 hours over the pole-tip material (*c.f.* Figure 63 and Figure 64). Similar scratches are not observed at 10°C/10% RH. A possible explanation could be the corrosion at high vapour pressure of the pole Permalloy surface [227]: residual moisture and possible presence of Cl from the binder or handling can form a corrosive environment for Permalloy [228]. Corroded Permalloy is more exposed to abrasion. Corrosion resistance of nickel based Permalloy and Fe based alloys depends to a great extent on the nature and stability of the

passivating oxide films that form on their surfaces [229, 230]. However, presence of third-body particles could remove any passivating oxide film and expose the surface to further corrosion. Isolated, the resulting corrosive wear is expected to be of insignificant consequence on the pole-tip recession, only assisting the three-body abrasive wear.

More generally, calculation of the plasticity index from the Greenwood and Williamson [60] relationship for the head-to-tape interface, by insertion of roughness and elastic parameters for the materials, shows the contact to be almost entirely elastic. Similarly, considering the ultra smooth surfaces and the consequently vanishingly small asperity included angles calculated from Block Halliday, plastic deformation of the pole surface and hence abrasive wear cannot occur. Based on these two criteria two-body abrasion will not occur at the head-to-tape interface.

Adhesive wear occurs at the head-to-tape interface, resulting in material transfer from the tape onto the head surface where it forms stains—this will be discussed in the following section. Adhesive wear may also be responsible for the pitting occasionally observed over the pole-tip surface (*e.g.* in Figure 36). This wear mode has a very limited impact on the pole-tip recession.

Particles released from the tape may possibly cause three-body abrasion, but the analysis has shown that the vast majority of this loose "tape debris" is polymeric in nature and therefore soft compared to the pole materials. Therefore, this effect is small. This, together with the fact that we have shown the overwhelming presence of TiC in recessed pole regions leads us to the conclusion that fractured laminar particles TiC released from ceramic are responsible for the pole-tip recession.

Hence, pole-tip recession is largely due to the mechanism described previously, *i.e.* delamination of TiC particles due to fatigue wear trapped within the pole-tip recession where they would get involved in three-body abrasive wear.

5.2 Stain transfer

5.2.1 Origin, mechanism and location

A first evidence of material transfer onto the head surface is the presence of Fe over the entire surface detected by AES (Figure 39, Figure 45, Figure 48 and Figure 76). This iron concentration clearly cannot be attributed to the NiFe used as a pole tip material (even at the pole tip, the Fe/Ni ratio reaches 4:1, far higher than the 1:4 expected in the Permalloy

used), but must originate in the magnetic pigment—Co-γFe_2O_3—embedded in the tape coating. Similar observations are reported for Travan drives where the poles contain no iron [40].

The highest concentration of Fe is measured above the pole tip—with a notable exception at 40°C/80% RH (Figure 76)—and (to a lesser extent) above the TiC phase of the ceramic. Similarly to actual heads, preferential transfer on TiC grains is observed for Al_2O_3-TiC dummy heads: this can be noticed with the decrease in Ti/Al concentration ratio measured by XPS (Figure 94) at low relative humidity, and simultaneous increase in Fe.

In that respect, heads showing massive transfer are the exception (Figure 48), since Fe found then in particularly high concentration, appears slightly more concentrated over the Al_2O_3 than TiC phase. This latter observation stems possibly from a shadowing effect on the Auger electron beam, related to the TiC recession.

Presence of stain at pole-tips is obvious from AFM topography maps (*c.f.* Figure 46) and OM images (*c.f.* Figure 75)—the stain colour observed by OM is mainly determined by the film thickness and the substrate. On the rest of the head surface, discrete deposits (mainly at low humidity) are visible, whereas stain forms too thin and uniform films (particularly at high humidity) to be immediately identified from the topography map. Temperature has a marked influence on the stain film smoothness, supporting the stain polymeric nature (low melting point). This latter observation combined with the high Fe concentration suggests that stains are mainly constituted of tape binder (polymeric component) loaded with magnetic pigment (iron oxide component).

High temperature and humidity (40°C/80% RH) constitutes a particular case in that despite the presence of a thick transfer film at the pole centre, the Fe concentration is relatively low over the pole, whereas C and O concentration are relatively high (Figure 76). This indicates that the nature of the stain—essentially organic—is different than in other conditions. Re-polymerisation is likely to play a part in producing what has been referred as friction polymer [231].

Analysis of the tape surface points to binder depletion (emergence of iron oxide originally covered with polymeric resin), most probably in connection with the deep grooves ploughed at the tape surface (Figure 51 and Figure 52). The mechanism responsible for the transfer is likely to rely either on ploughing by hard TiC delaminated particles, or adhesive wear, or a combination of both, ploughing (by abrasion) and adhesive wear. Adhe-

sion for polymer/metal contacts would then involve covalent bonding [96] and for polymer/ceramic contacts, ion-dipole bonding [97].

Within the binder, monomers are bound *via* covalent bonding (~ 10 eV/atom) thus forming polymeric chains, which in turn are bound *via* cross-linking (~ 10 eV/atom), hydrogen bonding or dipole-dipole bonding (both ~ 0.1 eV/atom). In favourable conditions, the adhesive strength of the adhesive junctions formed at the binder/head interfaces, may be greater than that of the binder interchain bonds, and lead to adhesive transfer from tape to head. The weakest bonds in the tape magnetic layer are likely to be the binder-pigment bonds. The bond strength here is increased by phosphoric wetting agents, but is lower than the 10 eV or so of the C-H and C-C bonds. This is why separation tends to occur at the binder pigment interface and why stain thickness is roughly equivalent to one particle width (~ 30 nm). Favourable conditions include high temperature (local or atmospheric), low humidity and high conductivity as exposed hereafter.

5.2.1.1 Effect of temperature on head staining

As mentioned earlier, temperature is found to have an influence either locally or globally on the stain transfer. On a close examination, stain deposited on the sides of the pole area, remote from the MR element (shared-pole narrow extremities) appears smoother than at the centre (Figure 46). At high dew point (high temperature, high relative humidity), stain is found only around the MR element, on the pole-tip central area (*c.f.* Figure 75). The energy dissipated by the MR elements is $8RI^2 \sim 48$ mW, which relates to a temperature increase of 5 ~ 6°C. A temperature gradient of ~ 5°C was actually measured between the MRE and EMG (Table 21). This temperature gradient adds up to the environmental high temperature in promoting the formation of adhesive junctions at the pole-tip surface (at high temperature, high humidity) or simply altering the transfer film aspect.

A parallel can be established with experimental observations made on Travan heads [40]: On heads tested with only one of two MR sensors energised, stain was found to form preferentially around the energised MR element. The phenomenon is attributed to the current induced heating effect: the additional heat at the energised sensors would increase any Arrhenius reaction rates, hence increase the probability of covalent bond formation at the metal/tape interface and lead to desorption of water vapour, which might otherwise have saturated surface bonds.

Similarly, atmospheric temperature influences globally the transfer rate: on heads tested at the lowest humidity (10% RH) the rate at which stain forms over the pole increases with temperature (Figure 64). Moreover, spread and flattening of the transfer film seems delayed at low temperature: at 10% RH, the film reaches a steady thickness (~ 20 nm) after 200 hours at low temperature compared with 100 hours at high temperature (Figure 70 (b) vs. (d)).

High resolution AFM scans of the pole-tip (Figure 73 and Figure 74) show smoother transfer film at low temperature: after initial transfer in the early stage of the wear test—in relation to the initial removal of tape higher asperities. The junction strength between the transfer film and the tape binder not sustained by heat, is insufficient to maintain the transfer process, hence the film will become thinner and smoother (homogeneous thickness). This steady state is hardly ever reached at high temperature due to a dynamic process where stain is transferred and removed cyclically. The transfer and removal cycle would eventually reach a permanent state, and the stain—rough due to the dynamic process—will reach a maximum thickness.

5.2.1.2 Effect of humidity on head staining

Humidity normally inhibits conventional stain formation due to water saturation of active sites on the material surface competing with the formation of adhesive junctions. This trend was generally observed over the tape bearing ceramic, showing far less deposit at 35% or 80% RH than at 10% RH (*c.f.* Figure 65 and Figure 66, and Figure 89 to Figure 92):

i. At low humidity (10% RH), small spots on the order of 1 μm appeared on the tape bearing ceramic sprinkled over the entire area of contact (Figure 65). Towards the end of test, these spots became more dispersed, as they supposedly spread, forming a more uniform transfer film.

ii. At higher humidity, 35% RH and 80% RH, vapour pressure seemed the determinant parameter: thus scattered deposits were visible on the tape bearing surface at 25°C/35% RH and 10°C/80% RH (vapour pressure: 730 and 1100 Pa, respectively), while the surface appeared clean at 40°C/80% RH (vapour pressure: 5850 Pa).

On pole-tips, staining is present in any condition (Figure 63 and Figure 64). Assuming that staining involves dipole-dipole interaction over the ceramic, and covalent bonding

over the pole-tips, it may be concluded that high humidity mainly hinders dipole-dipole bonding, possibly in relation to the polar nature of water molecules; covalent bonding is however less affected.

The stain over the pole-tips builds up at slower rate at low humidity, nevertheless, eventually producing thicker films (darker stain over the pole-tip observed under an optical microscope in Figure 75). High humidity makes the polymeric binder softer, less cohesive [152]; weaker binder cohesion would result in production of tape polymeric debris, transferred onto the head surface. For the same reason, debris is expected to show weak cohesion over the head surface at high humidity, hence readily sheared off; the removal may be delayed over the pole-tip, protected by the recession. Thinner transfer films would eventually remain at the end of test due to strong covalent bonding of the transfer film base with the pole-tip surface.

At low humidity, the scraping action by the pole-tip recession edge may help to initiate the transfer process, resulting in the stain growing from the edges.

40°C/80% condition is an exception, probably due to the high vapour pressure combined with the high temperature effect discussed earlier, which could induce re-polymerization producing cohesive tenacious stains of limited spread.

5.2.1.3 Effect of conductivity on head staining

Stain is found in greater quantity over the pole-tip than over any other area on the head surface. This observation must be related to the fact that the poles constitute the most active site at the head surface: electrically or magnetically induced heating is likely to locally increase the temperature. These phenomena would promote adhesive junctions and encourage stain formation. Similarly, electrically induced heat or magnetic field may promote the presence of stain along the buried bias conductors at the insulator surface observed in Figure 46.

The reason for the preferential staining of TiC grains over the Al_2O_3-TiC ceramic is not as clear. Both the pole-tip NiFe and ceramic TiC (refractory metal compound [232]) have high electrical conductivity (Table 4). This suggests a dependency on the electron population of the valence band (VB) and the strength of the bond formed. A greater electron density in the valence band of these materials might allow electron transfer and hence adhesive bond formation. Surface charging cannot be responsible, since if electron density

were high, little charging will occur on these materials. Charging may occur on insulators (alumina for example) and this will lead to electrostatic attractive bonds, but these will almost certainly be very weak and would not under normal circumstances result in transfer.

5.2.2 Effect of stain on the wear mechanism

Transfer of stain builds up a relatively soft thin coating at the head surface, which is expected to influence the head-to-tape interface friction and wear behaviour. The advantages of using soft coatings to reduce friction are well known [65]: soft coatings are expected in particular to decrease the shear strength component of adhesive friction. This is observed on the friction curve deduced from the temperature assessed at the head-to-tape interface throughout the test in Figure 60 and Figure 61: the friction decreases (noticeably for HDL heads) at the beginning of test was due to the transfer of stain at the head-to-tape interface.

The effect of stain on the head / tape friction appeared to be dependent on the temperature: as a general trend, friction decreased with increasing temperature. The friction coefficient was estimated after the temperature measurements to fluctuate between zero and one. This fluctuation is related to the presence of a polymeric transfer film on the head surface (sliding of two polymers—tape coating and head staining—against each other); the temperature dependence of the friction coefficient would then relate to the polymer thermodynamic properties and decrease in shear strength with increasing temperature.

Test on standard heads in controlled environmental conditions showed the TiC intra-grain pullout to reach a steady depth (20 ~ 25 nm) independent of the environmental condition—this is in agreement with the hypothesis of a fatigue wear controlled by the subsurface stress distribution. At an earlier stage, the pullout depth seemed to be affected by the environment, mainly in relation with the presence of stains. At low humidity, stain transfer retarded the pullout "hollow out" in either interfering with the subsurface crack propagation and fatigue wear mechanism or filling up thus formed pullouts:

i. Interference with the subsurface crack propagation may occur as a delay due to the reduction in friction hence in sliding-originated surface tensile stresses [233] or as an initial shift toward the surface due to the additional thickness—comparable to the depth of maximum Mises equivalent stress (20~30 nm). The shear strength of the stain-TiC interface will be far less than the shear strength within the TiC grain. Hence

much of the frictional energy will be dissipated in removing stain. This will be replaced immediately by more stain.

ii. The pullout filling up by transferred stains would decrease the apparent and measured recession; as the stain deposits gradually spreads and form thinner films, the pullout eventually reaches a maximum depth.

iii. An additional effect not directly related to the presence of stain must also be borne in mind: water under hydrostatic pressure may infiltrate the porous sintered ceramics and enhance the crack formation and propagation [22]; this physical effect is due to the non-compressibility of water well known in the pitting of metals [132].

Conversely, at high humidity little stain transfer results in a prompt hollow out.

Comparing the TiC intra-grain pullout depth measured on Greenleaf and Sumitomo Al_2O_3-TiC dummy heads with the one measured on actual heads raises several remarks. On heads tested for 500 hours, the pullout depth remains between 20 and 25 nm—similar to the actual heads. The 10°C/10% RH condition corresponds to the shallowest pullout in all cases whereas, the 40°C/80% RH condition corresponds within the 5 nm error range to the deepest pullouts.

The pullout (or hollow out) characteristic time associated with dummy heads tested at 10°C/10% RH for 200 hours is shorter than in other environmental conditions. The reverse is true for actual heads, tested however for up to 500 hours. Stain, transferred massively at 10°C/10% RH, is expected to spread and decrease in thickness as the test proceeds towards 500 hours. This increases further the pullout depth measured after 200 hours, inducing a further delay hence a characteristic time increase when calculated for 500 hours rather than 200 hours. The measured pullout depth corresponds to the TiC recession depth minus the transfer film thickness. The curve corresponding to a short characteristic time predicts after 500 hours a pullout depth way below the expected one.

The observed spread in pullout depth from one environmental condition to another more marked for Sumitomo (smaller TiC grains) Al_2O_3-TiC may be related to the confinement of stains within smaller pullouts.

5.3 Pole-tip recession and Stain—impact on signal performance

5.3.1 Pole-tip recession and stain transfer: overall mechanism

Following the above discussion, a schematic model for the dominant wear and transfer mechanism at the head-to-tape interface is proposed Figure 119. The TiC phase, embedded in the Al_2O_3 matrix (1), is pulled out from the ceramic surface due to a delaminative fatigue wear process upon sliding contact with a magnetic tape (2). This will result in the production of large laminar particles (order of magnitude: 1 μm by a few 10 nm). These platelets then fragment in smaller particles, which are swept across and entrapped in the recessed poles region where they act as three body abrasive particles (3). Simultaneously, tape material transfers, staining the head surface (the deposit is observed to preferentially cover the recessed pole-tips and TiC grains).

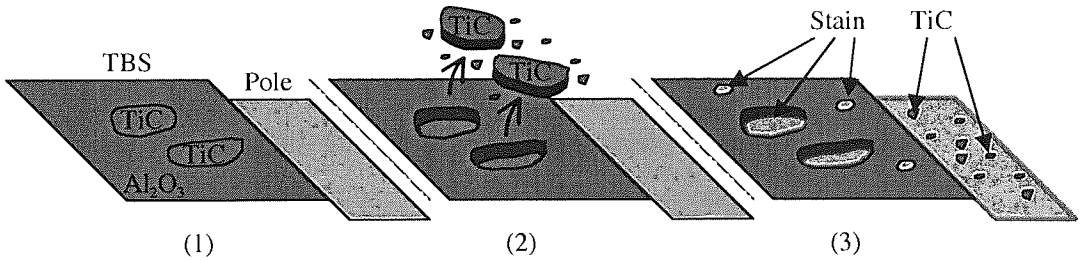

Figure 119. Proposed wear mechanism model for the ceramic part. (1) A tape is in sliding contact against the ceramic surface. (2) The embedded TiC phase wears (delamination) due to a fatigue process. (3) Stain transferred from the tape covers preferentially the TiC recessed phase, with few deposits on the Al_2O_3 phase.

The effect of the three-body abrasion caused by these particles is most pronounced in the softer metal elements of the head (poles and shields) more susceptible to abrasive wear and this is the major factor affecting pole-tip recession. These particles are seen present in the pole regions in Figure 38.

Pole-tip recession, evident at high vapour pressure (40°C/80% RH), is not so apparent at low or intermediate vapour pressures (other environmental conditions). This is partly due to the fact that at low or moderate vapour pressure, TiC abrasive particles are produced at lower rate, but also much more stain (transfer film) is produced. Stain protects the surfaces under these conditions, since contact stresses are confined to the transfer film and are not transmitted to the substrate. Stain, continuously removed and replaced, forms a sacrificial film that protects the surface.

5.3.2 Ultimate effect on signal and errors

The pole-tip recession was measured as 45 ± 10 nm (*c.f.* Table 14) on non-stained poles and ~ 20 nm (*c.f.* 3.1.2.1) on stained poles—the stain was then ~ 20 nm thick, *i.e.* roughly one magnetic particle thickness. This confirms the advantage of staining as long as the pole-tip recession cannot be reduced by other means, such as those discussed later on. The head output loss is proportional to $55\,d/\lambda$ dB [9], where λ is the recording wavelength and d the head-to-tape (magnetic) spacing. The recording wavelength for current ADR systems is $\lambda = 0.7$ µm, therefore a pole-tip recession of 45 ± 10 nm corresponds to a 3 ~ 4 dB output loss. An output loss exceeding 6dB is typically considered as failure [30, 133]: this would correspond to a pole-tip recession of ~ 75 nm. Assuming a change in environmental condition, hence stain transferred to the tape-bearing surface of a non-stained head, the spacing between tape and head could easily attain 75 nm. Moreover, if "spacing" losses could be minimised, then the intensity of the signal per bit could maximized, hence smaller bit sizes and consequently higher data densities could be used.

Additional spacing may come from a magnetic dead layer, air bearing, tenting effect over loose deposits, etc. These observations indicate that an increase in tape linear density keeping the signal loss at an acceptable level would only be possible provided that the pole-tip recession on current heads can be reduced accordingly.

Additional consequences of the described wear mechanism are linked to the degradation of the tape binder, as evidenced by the hollow out of valleys over the tape surface (*c.f.* Figure 51 and Figure 52). Although this is not too important when considering loss of signal, it may become so when considering loss of data and errors.

A last remark concerns the friction and stiction at the head-to-tape interface. Using a temperature model, the friction was found to decrease due to the transfer of stain on the head tape-bearing surface (*c.f.* Figure 61). A close up on the tape-bearing surface reveals the presence of a rippled transfer film, presumably resulting from a stick-slip mechanism or micro-vibrations induced by the sliding process. Effect of that latter phenomenon is difficult to assess, but could perturb the magnetic encoding/decoding process (recording wave length is also in the micro-meter range), as well as again, increase the head-to-tape spacing, hence the signal loss.

5.4 Possible solutions

5.4.1 Head coating

5.4.1.1 DLC coating

DLC coatings from four different suppliers were all found to be worn away after 100 hours. The coating thickness progressive decrease seems to designate either an abrasive or a nano-adhesive wear mechanism. However, considering the hard and very smooth surfaces involved, nano-adhesive wear would be more likely. Presence of patches and stripes over the pole-tip—possibly rests of coating—and pullout observed over the tape-bearing surface, whose depth (~ 10 nm) corresponded to the DLC thickness also pointed to delaminative wear.

Progressive wear and delamination could be involved in a twofold wear mechanism, as illustrated at the sidebar shift where the tape-bearing surface exposed to a load gradient showed a transition from intact to polish-smooth—due to progressive wear—to delaminated. The two mechanisms could be occurring successively—first progressive, and then delaminative—or involved at locations exposed to different contact loads.

The coating delamination may cause extremely hard DLC laminar particles to plough the grooves observed across the tape-bearing surface (Figure 88). In that respect, DLC coating is not only increasing the spacing loss at the head-to-tape interface but threatens to cause severe and permanent catastrophic damage to both the head and the tape.

5.4.1.2 SPL coating

SPL coatings performed markedly better during the wear test than DLC coatings: in all environmental conditions, SPL coatings, either 20 or 40 nm thick, unlike DLC coatings (10 nm thick) resisted to 100 hours of test. After 200 hours, the resistance was still fairly good, whereas after 500 hours, coatings tested in different conditions showed contrasting resistances to wear.

Humidity was found to have a significant influence on the SPL coating resistance: high humidity usually resulted in the most severe wear regardless of the coating thickness. High humidity produced typically less, if any, stains, transferred onto the head surface—this was evident from the Fe concentration measured by AES (Figure 81 and Figure 82). Stain transferred to the head is expected to alter the wear mechanism of the

coating by creating a soft interfacial layer. Soft layers may reduce sliding-originated surface tensile stresses that contribute to subsurface cracking and eventually fatigue wear. Conversely, ingress of water molecules may enhance crack formation and propagation, in the same way as discussed previously for Al_2O_3-TiC tape-bearing ceramic.

Coating wear is furthermore found more severe at low temperature. This is also consistent with the protective action of stains as a soft interfacial layer. Stains are mainly composed of polymeric material, whose shear modulus is expected to decrease with increasing temperature.

It was observed using AES, an increase in Fe at tape takeoff over the tape-bearing surface (Figure 81), where the pressure is up to three times higher than within the contact [165]. Increase in friction hence frictional heat may encourage staining where increase in temperature by as little as 1°C was already found critical on non-coated heads.

Wear of the SPL coated heads produced either pullouts on the tape-bearing surface or scratches on the pole-tip. Scratches were of different nature according to the coating thickness: aligned with the sliding direction in the case of 20 nm thick coatings or replicating the scratches formed during the grinding/lapping process in the case of 40 nm thick coatings. Moreover, 20 nm coating was more prone to wear when located over the TiC than the Al_2O_3 phase, whereas 40 nm coating wore mainly above the poles, to a lesser extent over the insulator, and insignificantly over the tape-bearing surface ceramic.

According to the above results, the wear mechanism is likely to differ for the two coating thicknesses. The 20 nm coating featuring scratches aligned in the sliding direction, above the pole-tip surface, but not above the tape-bearing surface, relies on the substrate mechanical properties (transferring abrasive forces) and particularly the hardness. Besides, the coating overlaying the tape-bearing surface reproduces the uncoated ceramic wear characteristic: therefore, the coating does not "secure" the uncoated tape-bearing surface ceramic wear behaviour, but rather conforms to it. On the other hand, the 40 nm coating wear pattern replicates the interface topography, particularly the flaws created during head machining: therefore, the coating experiences delamination relying on the adhesion failure at the substrate to coating interface. The coating adhesion strength increases in the order: NiFe, SiO_2 and Al_2O_3-TiC. Adhesion failure is found dramatic only in conditions encouraging the coating failure, that is (as observed for 20 nm coatings), high humidity and low temperature.

The divergence in wear behaviour for the two coatings suggests that the forces driving the wear process are acting at a finite depth in the 40 nm range, that is below and at the interface for 20 and 40 nm coatings, respectively. A parallel can be made between this observation and the subsurface maximum van Mises stress calculation presented in Chapter IV for non-coated heads, located about 20~30 nm below the surface. Obviously, a more complex model taking additionally to the substrate both the coating and the interface into account would be required.

Applying a wear resistant hard coating is especially critical in the sense that any worn debris is much harder than the coated head materials or tape binder and may cause particularly severe damage at the head-to-tape interface. This threat together with the spacing loss introduced due to the finite coating thickness is the main drawbacks when applying a coating to the head.

With the current ADR design, the total signal loss of only 1 dB can be tolerated over the lifetime of the head (5000 hrs). With a linear recoding wavelength of ~ 0.5 μm, this limits the suitable coating thickness to approximately 10 nm [165]. Coatings for the future generation high-density recording should furthermore be in the sub-10 nm range. Results on the 20 nm SPL coatings, whose wear resistance conforms to the substrate—uncoated ADR head—suggest therefore that applying a wear resistant sub-10 nm coatings requires looking into and improving the coating / substrate pair wear behaviour.

5.4.2 Single-phase ceramic for improved tape-bearing surface wear resistance

Using single-phase ceramics as an alternative to the original Al_2O_3-TiC ceramic to improve the tape-bearing surface wear behaviour was suggested by observations discussed previously. These observations showed the dramatic consequences on the head wear behaviour of the coexisting two phases within the tape-bearing surface ceramic. Application of a wear resistant hard coating in the sub-10 nm thick range over the whole head surface still relies on the two-phase ceramic wear behaviour, whose improvement is therefore also found necessary.

The following discussion considers two single-phase ceramics dummy head: TiO_x and Al_2O_3.

5.4.2.1 TiO_x dummy heads

According to the environmental condition, more or less material was transferred onto the head surface. Wear was indeed dominated by transfer, as abrasion and fatigue wear were insignificant, as evidenced by the persistence in condition unfavourable to stain transfer (high humidity), of pullout (used in the same way as indentations to assess the extent of wear) appearing in the early stage of the wear test, but also scratches already present on the virgin head.

5.4.2.2 Al_2O_3 dummy heads

Considering the Knoop hardness, Al_2O_3 is almost four times harder than TiO_x. However, no marked difference in wear behaviour was noticed in pseudo-normal condition where transfer masked an insignificant abrasion and fatigue wear—confirmed by the persistence of initial pits at the ceramic surface. Although the single-phase ceramics tested here are also sintered, their improved wear resistance might be related to a better cohesion. Adhesive bonds involving mating surfaces made of the same material may oppose a better resistance to propagating cracks. Homogeneity in mechanical properties could be an additional benefit.

This result is encouraging although may or may not be reproducible once the ceramics applied to actual heads: other unpredictable effects, in particular on the pole-tip recession are possible. Moreover, it is doubtful that all problems inherent to the application of a SPL coating over the tape-bearing surface would be solved this way. Obviously, test on structured actual heads, with and without SPL coating are therefore necessary.

Other single-phase ceramics may also be considered. SiC already used in HD applications could be a good candidate.

6 Chapter VI—Conclusion and further work

This thesis is dedicated to the tribology at the head to tape interface of linear tape recording systems. OnStream ADR system was used as an experimental platform, but most findings apply to all linear tape systems. Combining experimental characterisation with computer modelling, a comprehensive picture of the mechanisms involved in a linear tape recording system was drawn. The work was designed to isolate the mechanisms responsible for the physical spacing between head and tape with the aim of minimising spacing losses and errors and optimising signal output.

Selected heads were tested in controlled environment for up to 500 hours (exceptionally 1000 hours). These heads were standard heads, used in ADR current products and prototype heads: DLC and SPL coated and dummy heads whose contour was homogeneously built from a selected ceramic—Al_2O_3-TiC (standard head tape-bearing surface ceramic) and alternative single-phase ceramics, intended for improved wear resistance.

6.1 Head wear

Evidence of wear on the standard heads were mainly observable as:

i. Preferential wear of the Al_2O_3-TiC tape-bearing surface ceramic resulting in the whole TiC surface of the ceramic being recessed within 20 hours. The TiC grains were delaminated—the Al_2O_3 matrix remaining untouched—due to a fatigue wear mechanism. The former assumption was further confirmed by modelling the subsurface stress, hence locating the von Mises equivalent stress at a depth equivalent to the TiC recession *i.e.* 20~30 nm.

ii. Deep grooves ploughed over the insulator and pole-tip region. TiC delaminated particles were held responsible for this, presumably in a single catastrophic mechanism.

iii. Increase in pole-tip recession. Debris, mainly in form of TiC particle residues found trapped within the pole-tip recession, was assumed thereafter to provide three-body abrasive particles, wearing and increasing the recession of the softer pole material.

Other marginal forms of wear were examined, in relation firstly with the TiC preferential wear over the Al_2O_3-TiC, secondly with the pole-tip recession increase.

1. To account for the TiC preferential wear, two-body abrasion was dismissed because the tape harder particles (Al_2O_3 HCA) are softer; also, this would fail to explain the protrusion of the ceramic Al_2O_3 matrix, softer therefore less resistant to abrasion than the TiC phase. Besides, plastic contacts and hence two-body abrasion is very unlikely to occur. Chemical wear due to oxidation was moreover found too superficial to account for the *instant* TiC recession.
2. Corrosion of the Permalloy pole-tip was estimated too superficial to account for the measured increase in pole-tip recession, but only likely to promote the three-body abrasive wear by the TiC debris. Two-body abrasion by tape hard particles or even three-body abrasion by tape debris, were furthermore dismissed as possible mechanisms. Adhesive wear could only account for the inconsequent pitting observed over the pole-tips.

6.2 Stain transfer

Iron-rich stain was found over the cycled head surface, at any environmental condition except high humidity and high temperature, where mainly organic stains were apparent, most likely produced *via* degradation of the tape surface and re-polymerisation. Iron-rich stain was located preferentially over the pole-tip and, to a lesser extent, over the TiC phase of the tape-bearing ceramic. The influence of temperature, humidity and electric conductivity of the head constituents on stain transfer has been investigated:

i. High temperature was found to promote stain either locally—temperature gradients between the MR vicinity and the pole-tip extremities affected the staining rate and aspect—or globally—high atmospheric temperature resulted in faster staining transfer and spread, in otherwise favourable conditions.

ii. High humidity was found to inhibit stain formation, particularly over the tape-bearing ceramic. Over the pole, stain was found in any condition, however, producing thicker films at a slower rate (possibly in relation with the stronger cohesion of the tape binder) at low humidity.

iii. Stain was generally found to target preferentially head materials with high electrical conductivity: Permalloy and TiC. This observation may be related to a de-

pendency on the electron population of the valence band, thus the strength of the bond formed.

The effect of stain on the head-to-tape interface tribology can be summarised as:

i. Decrease in friction noticed at the head-to-tape interface in relation with the presence of stain, decrease amplified at high temperature.

ii. Delay in the TiC recession hollow-out in relation with either:

   a. the decrease in friction mentioned above, hence in sliding-originated tensile stresses

   b. an initial shift towards the surface of the subsurface von Mises stress maximum due to the stain additional thickness,

   c. stains filling up the recession, later decreasing in thickness.

iii. Fills up the pole-tip recession, acting as a protective soft coating.

6.3 Pole-tip recession, stain and signal performance

The dominant wear mechanisms were confirmed as:

i. TiC grains delaminated of from the Al_2O_3-TiC tape-bearing surface

ii. TiC fragments trapped within the pole-tip recession where they act as erosive or abrasive third-bodies

iii. Transfer of stain mainly in form of tape binder mixed with magnetic pigments

These mechanisms are expected to have a significant impact on the signal performance.

With ADR current recording wavelength ($\lambda = 0.7$ μm), a loss of 6 dB would result from a head-to-tape spacing of ~ 75 nm, possibly reached in adverse circumstances (*e.g.* change in humidity). Additional complications include:

i. The tape degradation and possible inherent loss in data, and

ii. Stick-slip or micro-vibrations at the head-to-tape interface, possibly interfering with the normal signal processing.

6.4 Possible solutions

6.4.1 Head coatings

Two different coatings have been tested:

DLC coating (~ 10 nm thick) was found to disappear within 100 hours, possibly due to a combination of abrasive and fatigue (delaminative) wear, either successively or depending on the contact load.

SPL coating (20 and 40 nm thick): the results illustrated the coating resistance at low humidity and high temperature, probably in relation with stain transferred from the tape, acting as a soft protective regenerative layer. At higher humidity or lower temperature, the coating wore to various degrees.

The fragments pulled out from head surface, either from the DLC or SPL coating and the exposed substrate ceramic (TiC phase) or possibly both together, led to the formation of very hard particles, which may lead to serious damage at the head surface.

i. The 20 nm coatings relied on the substrate wear behaviour, *i.e.* abrasion over the softer pole material and preferential fatigue wear of the TiC phase over the tape-bearing surface. The forces driving the wear process were believed to act within the substrate, that is at a depth over 20 nm below the surface. A parallel was established between this result and the location of the von Mises stress maximum calculated previously for non-coated heads, estimated between 20~30 nm.

ii. The 40 nm coating wear behaviour seemed to rely on the adhesive strength at the coating / substrate interface, hence the depth of the wear process driving forces at about 40 nm below the surface which is still consistent with our previous maximum subsurface stress depth calculation.

From the above observation, it was inferred that for coating less than 30 nm thick—*i.e.* coatings compatible with high-density recording—, the substrate resistance must be taken into account.

6.4.2 Single phase ceramics

Single-phase ceramic—either TiO_x or Al_2O_3—full-contour dummy heads were tested in controlled environmental conditions. Examination of the experimental result led to conclude that:

i. The absence of a second phase eliminates the preferential wear observed at the Al_2O_3-TiC surface, possible due to a better cohesion between adjacent grains and/or more homogeneous mechanical properties

ii. The persistence of scratches at high dew point (40°C/80%) where stain transfer is significantly reduced, indicates a very low wear rate;

iii. No evidence of brittle fracture or preferential wear was disclosed.

Use of real, structured heads would be further necessary to assess the actual impact of single-phase ceramic tape-bearing surface on the pole-tip recession and stain transfer, acknowledged to be the main source of head-to-tape interface gap increase.

6.5 Further Work

ADR is a growing technology and as such is expected to evolve quickly in the coming years. Changes expected to affect the head-to-tape interface wear and staining behaviour include changes in the head profile, contact pressure and the transition from Co-γFe_2O_3 tapes to MP tapes. In that respect, the work exposed in this thesis needs to be verified for those new products. Changes regarding the tape length and width, the track and bit density are also expected [234], however with little impact on the head-to-tape interface tribology.

Another improvement would be the application of a sub-10 nm SPL coating over the full head contour. In light of the exposed results, the wear resistance of a sub-10 nm coating is found particularly critical and would require a further characterization in conjunction with the fine-tuning of the deposition conditions.

As it has been suggested that for such thin coatings, wear properties of the substrate on which the coating is deposited is of crucial importance. Therefore, improvement of these wear properties would still be necessary (*e.g.* using a single phase ceramic tape-bearing surface), while taking into account the presence of the coating. As an extreme case, virtually 0 nm thick SPL coatings, in fact Cr sputtered heads may also be considered.

In addition, the proposed subsurface stress modelling should be modified in order to integrate a hard coating over the head surface, as it would provide a powerful tool for predicting the wear behaviour and advise on directions to take for improving the coating resistance.

Improvements in the stress modelling, could furthermore imply the input of a soft coatings (*e.g.* stain or lubricant), but also refinements and improvements such as the extension of the sampled area to the whole head-to-tape interface simultaneously to a decrease in sample length, using accelerated algorithms (*e.g.* multi-level multi-summation technique [75]). These improvements must be supported by a careful examination of the physical implications.

References

1 V. Poulsen (1900), Das Telegraphon, *Annalen der Physik*, **3**, 754.

2 J.M.D. Coey (2001), "Magnetism in future", *Journal Magnetism and Magnetic Materials*, **226-230**, 2107-2112.

3 J.M.D. Coey (2001), "Magnetic materials", *Journal of Alloys and Compounds*, **326**, 2–6

4 B.R. Acharya, E.N. Abarra, A. Inomata, I. Okamoto (2001), Joint European Magnetism Symposium 2001, Grenoble (France), paper B046.

5 S. Anders, S. Sun, C.B. Murray, C.T. Rettner, M.E. Best, T. Thomson, M. Albrecht, J.-U. Thiele, E.E. Fullerton and B.D. Terris (2002), "Lithography and self-assembly for nanometre scale magnetism", *Microelectronic Engineering*, in press.

6 J.P. Nozières, E. Saporito, B. Viala (2002), "Planar GMR head design for 50+ Gbit/in^2 recording", *Journal of Magnetism and Magnetic Materials*, in press.

7 W.F. Egelhoff, Jr., P.J. Chen, C.J. Powel, R.D. McMichael, M.D. Stiles (2001), "Surface and interface effects in the growth of giant magnetoresistance spin valves for ultrahigh-density data-storage applications", *Progress in Surface Science*, **67**, 355-364.

8 H.J. Borg, R. van Woudenberg (1999), "Trends in optical recording", *Journal of Magnetism and Magnetic Materials*, **193**, 519-525.

9 S.B. Luitjens, W. Folkerts, H.W. Van Kesteren, J.J.M. Ruigrok (1998), "Trends in Digital Magnetic Recording; the Application of Thin-Film heads for Tape Recording", *Philips J. Res.*, **51**, 5-19.

10 G. Cuntze, T. Hughes, S. Magnusson, W. Nichtl-Pechter, D. Norton, M. Pechtold (2001), "Magnetoresistive Read Heads for High-Density Data Applications", *IEEE Transaction on Magnetics*, **37**(5), 3839-3843.

11 K. Muto, K. Majima, R. Taguchi, T. Uehara, H. Okuda, M. Kondo, Y. Shinjo, N. Hasegawa (2001), "High-Density Reproduction characteristics With MR Head for Rotary Drum in Helical-Scan Tape System", *IEEE Transaction on Magnetics*, **37**(4), 1912-1914.

12 T. Ozue, M. Kondo, Y. Soda, S. Fukuda, S. Onodera, T. Kawana (2002), "11.5-Gb/in^2 Recording Using Spin-Valve Heads in Tape Systems", *IEEE Transaction on Magnetics*, **38**(1), 136-140.

13 T. Osaka (2000), "Electrodeposition of highly functional thin films for magnetic recording devices of the next century", *Electrochimica Acta*, **45**, 3311-3321.

14 H. Osaki (2000), "Flexible media – recent developments from the tribology point of view", *Tribology International*, **33**, 373-382.

15 F.J.A.M. Greidanus (1998), "Introduction to the Special Issue on Heads for Magnetic Tape Recording", *Philips J. Res.*, **51**, 1-3.

16 S.B. Luitjens, A.M.A. Rijckaert (1999), "The history of consumer magnetic video tape recording, from a rarity to a mass product", *Journal of Magnetism and Magnetic Materials*, **193**, 17–23.

17 D.P. Gregg (1967), US Patent 3.344.237.

18 C.W.M.P. Sillen, L. Postma, E.A. Draaisma, F.A. Pronk (1998), "Design and Technology of Sensor-Last Thin-film Magnetic Heads", *Philips J. Res.*, **51**, 149-171.

19 J.J.M. Ruigrok, E.A. Draaisma, H.W. Van Kesteren (1998), "Design of Thin-film Tape Heads", *Philips J. Res.*, **51**, 21-57.

20 L.A.M. de Jong (2002), OnStream MST BV, Eindhoven, private communication.

21 H. Jakusch, R.J. Veitch (1993), "Particles for Magnetic Recording", *J. Inf. Rec. Mats.*, **20**, 325-344.

22 J.L. Sullivan (1998), "The Tribology of Flexible Magnetic Recording Media – the Influence of Wear on Signal Performance", *Tribology International*, **31**, 457-464.

23 T. Suzuki, T. Tanaka, K. Ikemizu (2001), "High density recording capability for advanced particulate media", *Journal of Magnetism and Magnetic Materials*, **235**, 159-164.

24 T. Suzuki, *Journal of Magnetism and Magnetic Materials*, **193**, p374.

25 E. Köster, T.C Arnoldussen (1989), "Chap. 3 - Recording Media", in C.D. Mee and E.D. Daniel (Eds.), *Magnetic Recording Handbook - Technology and applications*, McGraw-Hill Publishing Company.

26 B. Bhushan (1996), *Tribology and Mechanics of Magnetic Storage Devices*, 2nd Ed., New York: Springer-Verlag, Inc.

27 E.A. Draaisma, S.R. Cumpson, T.P.H.G. Jansen, P. Hidding, S.B. Luitjens (1999), "Performance of advanced tapes with DigaMax™ thin film heads", *Journal of Magnetism and Magnetic Materials*, **193**, 384–387.

28 B.L. Weick, B. Bhushan (1996), "Characterisation of Magnetic Tapes and Substrates", *IEEE Transaction on Magnetics*, **32**, 3319-3322.

29 Y. Xie, B. Bhushan (1996), "Fundamental wear studies with magnetic particles and head cleaning agents used in magnetic tapes", *Wear*, **202**, 3-16.

30 M.S. Hempstock, J.L. Sullivan (1996), "A study of the mechanical and magnetic performance of metal evaporated tape", *Journal of Magnetism and Magnetic Materials*, **155**, 323-328.

31 F. Roozeboom et P.J.H. Bloemen, W. Klaassens, E.G.J. van de Riet, J.J.T.M. Donkers (1998), *Philips J. Res.*, **51**, p68.

32 J.C.S. Kools, R. Coehoorn, W. Folkerts, M.C. de Nooijer, G.H.J. Somers, "Anisotropic and giant magnetoresistive elements", *Philips J. Res.*, **51**, 125-148.

33 D.J. Mapps (1997), "Magnetoresistive sensors", *Sensors and Actuators*, **A59**, 9-19.

34 R.E. Jones Jr., C.D. Mee (1989), "Chap. 4 - Recording Heads", in C.D. Mee and E.D. Daniel (Eds.), *Magnetic Recording Handbook - Technology and applications*, McGraw-Hill Publishing Company.

35 K. Kryder, W.Messner, L.R. Carley (1996), *J. Appl. Phys.*, **79**, 4485.

36 A.S. Hoagland, J.E. Monson (1994), *Digital Magnetic Recording*, Cambridge University Press, London.

37 R.L. Wallace (1951), "The Reproduction of Magnetically Recorded Signals", *Bell System Technical Journal*, **30**, 1145-1173.

38 R. Dee (1994), "Read Head for Magnetic Tapes", *SPIE*, **2604**, 181-191.

39 J.C.S. Kools, K. Rook, H. Hegde, S.B. Sant, J. Wong, W. Xiong, B. Druz, A. Lam,A. Devayasaham, I. Wagner (2000), "Deposition technology for thin film magnetic recording heads reader fabrication", *Thin Solid Films*, **377-378**, 705-711.

40 E. Sourty, M. Wild, J.L. Sullivan (2002), "Pole tip recession and staining at the head to tape interface of linear tape recording systems", *Wear*, **252**, 276-299.

41 R. Hasegawa (2001), "Application of amorphous magnetic alloys in electronic devices", *Journal of Non-Crystalline Solids*, **287**, 405-412.

42 R. Hasegawa (2001), "Design and synthesis of magnetic structures", *Physica*, **B299**, 199-204.

43 P. Jost (1966), *Lubrication (Tribology) Education and Research*, UK Department of Education and Science, HMSO.

44 J.A. Tichy, D.M. Meyer (2000), "Review of solid mechanics in tribology", *International Journal of Solids and Structures*, **37**, 391-400.

45 I.M. Hutchings (1992), *Tribology: Friction and Wear of Engineering Materials*, CRC Press, Boca Raton.

46 Anonymous (1985), "Surface texture (surface roughness, waviness, and lay)", ANSI/ASME, B46.1, ASME, New York.

47 F. Robbe-Valloire (2001), "Statistical analysis of asperities on a rough surface", *Wear*, **249**, 401-408.

48 A. Broese van Groenou (1991), "Tribology of magnetic storage systems, a short review", *J. Magn. Magn. Mat.*, **95**, 289-312.

49 J.B.P. Williamson (1968), "Topography of solid surfaces", *Interdisciplinary Approach to Friction and Wear*, pp. 82-142, NASA Special Publication, SP-181, NASA, Washington, D.C.

50 P. Luo, S. Tan, H.N. Bertram, G. Hughes, F.E. Talke (2000), "Analysis of Tape Surface Roughness by Magnetic Recording and Mechanical Methods", *IEEE Transactions on Magnetics*, **36**(1), 189-194.

51 International Organisation for Standardisation (ISO), ISO 12085, 1996.

52 Topometrix Technical Brief – SPM overview, Topometrix Corporation (1996), Santa Clara.

53 D.J. Whitehouse, J.F. Archard (1970), "The properties of random surfaces of significance in their contact", *Proc Roy Soc*, **A316**, 97–121.

54 A. Majumdar, C.L. Tien (1990), "Fractal characterisation and simulation of rough surfaces", *Wear*, **136**, 313–327.

55 A. Majumdar, B. Bhushan (1990), "Role of fractal geometry in roughness characterisation and contact mechanics of surfaces", *Trans ASME: J. Tribol.*, **112**, 205–16.

56 A. Majumdar, B. Bhushan (1991), "Fractal model of elastic–plastic contact between rough surfaces", *Trans. ASME: J. Tribol.*, **113**, 1–11.

57 T.L. Warren, D. Krajcinovic (1995), "Fractal models of elastic-perfectly plastic contact of rough surfaces based on the cantor set", *Int. J. Solids Structures*, **32**(19), 2907-2922.

58 T.R. Thomas, B.-G. Rosén (2000), "Determination of the optimum sampling interval for rough contact mechanics", *Tribology International*, **33**, 601–610

59 F.P. Bowden (1957), *Wear*, **1**, 333.

60 J.A. Greenwood, J.B.P. Williamson (1966), "contact of nominally flat surfaces", *Proc. R. Soc. London, Ser. A*, **295**, p. 300.

61 B. Bhushan (1984) "Analysis of the Real Area of Contact Between a Polymeric Magnetic Medium and a Rigid Surface", *J. Trib., Trans. ASME*, **106**, 26-34.

62 T. Baumberger (1997), "Contact dynamics and friction at a solid-solid interface: material versus statistical aspects", *Solid State Communications*, **102**(2-3), 175-185.

63 B. Bhushan (1985) "The Real Area of Contact in Polymeric Magnetic Media – II: Experimental Data and Analysis", *ASLE Trans.*, **28**, 181-197.

64 B. Bhushan, Doerner M.F. (1989), "The Role of Mechanical Properties and Surface Texture in the Real Area of Contact of Magnetic Rigid Disks", *J. Trib. Trans. ASME*, **111**, 452-458.

65 F.P. Bowden, D. Tabor (1950), "Friction and Lubrication of Solids – Part I", Clarendon Press, Oxford.

66 A.H. Uppal, S.D. Probert (1973), "Mean separation and real contact area between surfaces pressed together under high static loads", *Wear*, **23**, 39-53.

67 K.L. Woo, T.R. Thomas (1980), "Contact of rough surfaces: a review of experimental work", *Wear* 58, 331-340.

68 H. Hertz (1882), "Über die berührung fester elastischer körper" ("on the contact of elastic solids"), *J. reine und angewandte Mathematik*, **94**, 156-171.

69 K.L. Johnson, *Contact Mechanics*, Cambridge Univ. Press, Cambridge, 1985.

70 N.P. Suh, *Tribophysics*, Prentice-Hall, Inc., Englewood Cliffs, New Jersey, 1986.

71 C.K. Liu, "Stresses and deformation due to tangential and normal loads on an elastic solid with application to contact stresses", PhD thesis, University of Illinois, 1950.

72 G.G. Adams, M. Nosonovsky (2000), "Contact modelling – forces", *Tribology International*, **33**, 431-442.

73 M.N. Webster, R.S. Sayles (1986), "A numerical model for the elastic frictionless contact of real rough surfaces", *Journal of Tribology*, **108**, 314-320.

74 D.M. Bailey, R.S. Sayles (1991), "Effect of roughness and sliding friction on contact stresses", *Journal of Tribology*, **113**, 729-738.

75 I.A. Polonsky, L.M. Keer (1999), "A numerical method for solving rough contact problems based on the multi-level multi-summation and conjugate gradient techniques", *Wear*, **231**, 206-219.

76 R.S. Sayles (1996), "Basic principles of rough surface contact analysis using numerical methods", *Tribology International*, **29**(8), 639-650.

77 J.J. Kalker, Y. VanRanden (1972), "A minimum principle for frictionless elastic contact with application to non-Hertzian half-space contact problems", *J. Eng. Maths*, **6**, 193-206.

78 X. Tian, B. Bhushan (1996), "A numerical three-dimensional model for the contact of rough surfaces by variational principle", *Journal of Tribology*, **118**, 33-42.

79 W. Peng, B. Bhushan (2001), "Three-dimensional contact analysis of layered elastic/plastic solids with rough surfaces", *Wear*, **249**, 741-760.

80 Q. Tao, H.P. Lee, S.P. Lim, "Contact mechanics of surfaces with various models of roughness descriptions", *Wear*, **249**, 539-545.

81 P.J. Blau (2001), "The significance and use of the friction coefficient", *Tribology International*, **34**, 585-591.

82 B. Bhushan, F.H. Hahn Jr. (1995), "Stain on magnetic tape heads", *wear*, **184**, 193-202.

83 G. Jintang (2000), "Tribochemical effects in formation of polymer transfer film", *Wear*, **245**, 100-106.

84 K. Kato (2000), "Wear in relation to friction—a review", *Wear*, **241**, 151-157.

85 B. Bhushan (1980), "Stick-slip induced noise generation in water-lubricated compliant rubber bearings", *J. Lub. Tech. Trans. ASME*, **102**, 201-212.

86 B. Bhushan, W.E. Jahsman (1978), "Propagation of weak waves in elastic-plastic and elastic-viscoelastic solids with interfaces", *Int. J. Solids and Struc.*, **14**, 39-51.

87 B. Bhushan, W.E. Jahsman (1978), "Measurement of dynamic material behavior under nearly uniaxial strain conditions", *Int. J. Solids and Struc.*, **14**, 739-753.

88 J.S. McFarlane, D. Tabor (1950), "Adhesion of solids and the effect of surface films", *Proc. R. Soc. (Lond.)*, **A202**, 224-243.

89 D.D. Fuller (1984), "Theory and Practice of Lubrication for Engineers", Wiley, New York.

90 K.C. Ludema, D. Tabor (1966), "The friction and viscoelastic properties of polymeric solids", *Wear*, **9**, 329-348.

91 D. Tabor (1975), "Interaction between surfaces: Adhesion and friction", in *Surface Physics of Materials* (J.M. Blakely, ed.), pp. 475-528, Academic Press, New York.

92 M.E. Merchant (1968), "Friction and adhesion", in *Interdisciplinary Approach to Friction and Wear* (D.H. Buckley, ed.), NASA, Cleveland, Ohio.

93 Y.A. Karpenko, A. Akay (2001), "A numerical model of friction between rough surfaces", *Tribology International*, **34**, 531–545

94 B.J. Briscoe, D. Tabor (1978), *Polymer Surfaces*, eds. D.T. Clarke and W.J. Feast, Wiley, New York.

95 B.V. Deryagin and I.I. Abrikosova (1956), *J. Exp. Theor. Phys.*, **3**, 819.

96 D.H. Buckley, W.A. Brainard (1974), *advances in Friction and Wear of Polymers*, **5B**, (Plenum, New York), 315.

97 V.A. Bely (1992), *Friction and Wear of Polymer-based Materials*. Pergamon, Oxford.

98 M.K. Chaudhury (1996), "Interfacial interaction between low-energy surfaces", *Materials Science and Engineering*, **R16**, 97-159.

99 J.L. Sullivan (1996), "The tribology of Flexible Magnetic Recording Media", *Journal of Magnetism and Magnetic Materials*, **155**, 312-317.

100 J. Bos, H. Moes (1995), "Friction heating of tribological contacts", *Journal of Tribology*, **117**, 171-177.

101 J.L. Sullivan, Aston University, Birmingham, private communication.

102 B. Bhushan (1987), "Magnetic head-media interface temperatures part 1–analysis", *J. Trib. Trans. ASME*, **109**, 252-251.

103 B. Bhushan (1987), "Magnetic head-media interface temperatures part 1–application to magnetic tapes", *J. Trib. Trans. ASME*, **109**, 252-256.

104 B. Salti, N. Laraqi (1999), "3-D numerical modeling of heat transfer between two sliding bodies: temperature and thermal contact resistance", *International Journal of Heat and Mass Transfer*, **42**, 2363-2374.

105 D. Meal (1994), "Modelling of the Temperature Effect at a Magnetic Head / Tape Interface", 3M Internal report.

106 J.C. Jaeger (1942), "Moving sources of heat and the temperature at sliding contacts",*Proc. Roy. Soc. N.S.W.*, **76**, 203-224.

107 J.F. Archard (1953) "Contact and rubbing of flat surfaces", *Journal of Applied Physics*, **24**(8), 981-988.

108 J.L. Sullivan, P.J. Sharma, "Factors affecting the durability of repeatedly stressed flexible magnetic recording", *J. Phys. D (Applied Physics)*, **25** (1992) 321-328.

109 I.L. Singer (1996), "Mechanics and chemistry of solids in sliding contact", *Langmuir*, **12**, 4486-4491.

110 E. Rabinowicz (1965), *Friction and wear of materials*, Wiley, New York.

111 J.K. Lancaster (1973), *Plastic and Polymers*, **41**, 112.

112 J.S. Halliday (1955), *Proc. Inst. Mech. Eng.*, **169**, 221.

113 E. Rabinowicz, A. Mutis (1961), *Wear*, **8**, 831.

114 E. Larsen-Basse (1972), *Wear*, **19**, 35.

115 R.O. Ritchie (1999), "Mechanisms of fatigue-crack propagation in ductile and brittle solids", *International Journal of Fracture*, **100**, 55-83.

116 R.O. Ritchie (1988), "Mechanisms of fatigue crack propagation in metals, ceramics and composites: Role of crack-tip shielding", *Materials Science and Engineering*, **A103**, 15–28.

117 R.P. Wahi, B. Lischner (1980), "Fracture and wear behaviour of composites based on Al_2O_3-TiC", *J. Mater. Sci.*, **15**, 875-885.

118 J. Li, D.S. Mao, S.Y. Guo, L.P. Huang, Z.Y. Mao, "A fine Al_2O_3-TiC-Co ceramic and its erosion behaviour", *Journal of Physics D: Applied Physics*, **30** (1997) 2234-2239.

119 G.M. Hamilton, L.E. Goodman (1966), "The Stress Field Created by a Circular Sliding Contact", *Journal of Applied Mechanics, Trasn. ASME*, **33**, 371-376.

120 S. Glodez, Z. Ren (1998), "Modelling of crack growth under cyclic contact loading", *Theoretical and Applied Fracture Mechanics*, *30*, 159-173

121 W. Cheng, H.S. Cheng, T. Mura, L.M. Keer (1994), "Micromechanics modeling of crack initiation under contact fatigue", *ASME J. Tribology*, **116**, 2-8.

122 E. Student, J. Rudzitis (1996), "Contact of surface asperities in wear", *Tribology International*, **29**(4) (1996), 275-279.

123 Y. Yang, S.M. Hsu (1996), "Wear and wear transition mechanisms of ceramics", *Wear*, **195**, 112-122.

124 R.O. Ritchie, C.J. Gilbert, J.M. McNaney (2000), "Mechanics and mechanisms of fatigue damage and crack growth in advanced materials", *International Journal of Solids and Structures*, **37**, 311-329.

125 M.K. Omar, A.G. Atkins, J.K. Lancaster (1986), *J. Phys. D: Appl Phys.*, **19**, 177.

126 M.S. Hempstock, J.L. Sullivan (1998), "Characterization of surface changes to metal evaporated and metal particle media following durability tests in helical scan Hi-8 recorders at ambient and high humidity conditions", *Tribology International*, **31**, 419-424.

127 I.M. Hutchings (1998), "Abrasive and erosive wear tests for thin coatings: a unified approach", *Tribology International*, **31**(1-3), 5-15.

128 I.M. Hutchings, R.E. Winter (1974), "Particle erosion of ductile metals: A mechanism of material removal", *Wear*, **27**, 121-128.

129 I.M. Hutchings, R.E. Winter, J.E. Field (1976), "Solid particle erosion of metals: The removal of surface material by spherical projectiles", *Proc. Roy. Soc. (lond.)*, **A348**, 379-392.

130 I. Finnie (1960), "Erosion of surfaces by solid particles", *Wear*, **3**, 87-103.

131 F.E. Talke (2000), "Tribology in magnetic recording technology", *Industrial Lubrication and Tribology*, **52**(4), 157-164.

132 J.L. Sullivan, M.R. Middleton (1985), *ASLE Trans.*, **28**, 431-438.

133 B. Bhushan, G.S.A.M. Theunissen, X. Li (1997), "Tribological studies of chromium oxide films for magnetic recording applications", *Thin Solid Films*, **311**, 67-80.

134 R.M. Cannon, P.J. Seger, "Chap 4 - Data Storage on Tape", in Mee C.D. and Daniel E.D. (Eds.), Magnetic Recording Handbook - Technology and Applications, Mc Graw-Hill Publishing Company (1989).

135 S.T. Patton, B. Bhushan (1996), "Micromechanical and tribological characterization of alternate pole tip materials for magnetic recording heads", *wear*, **202**, 99-109.

136 B. Bhushan, S.T. Patton (1998), "Tribology in Ultra-High Density Tape Drive Systems: State of the Art and Future Challenges", *IEEE Transaction on Magnetics*, **34**, 1883-1888.

137 W.W. Scott, B. Bhushan (2002), "Micro/nano-scale differential wear of multiphase materials: pole tip recession in magnetic-tape heads", *Wear*, **252**, 103-122.

138 W.W. Scott, B. Bhushan (1999), "Pole tip recession in linear tape heads: measurement technique and influence of head materials, tape speed and tape tension", *Proc. Instn. Mech. Engrs. Part J*, **213**, 139-150.

139 M.J.K. Harrison, J.L. Sullivan, G.S.A.M. Theunissen (1997), "Wear mechanisms of sandwich-type video heads", *Journal of Engineering Tribology*, **211**, 263-277.

140 V. Sharma, F.E. Talke (1997), "Silicon carbide - a potential material for magnetic recording sliders", *Proc. Instn. Mech. Engrs. Part J*, **211**, 317-326.

141 V.N. Koinkar, B. Bhushan (1996), "Microtribological studies of Al_2O_3, Al_2O_3-TiC, polycrystalline and single-crystal Mn-Zn ferrite, and SiC head slider materials", *Wear*, **202**, 110-122.

142 H.H. Gatzen, X. Ma, M. Scherge, M.S. Jhon, C.L. Bauer (1996), "Observations Regarding the Tribological Properties of SiC and AlTiC Sliders", *IEEE Transactions on Magnetics*, **32(5)**, 3783-3785.

143 B. Bhushan, J.A. Lowry (1995), "Friction and Wear Studies of Various Head Materials and Magnetic Tapes in a Linear Mode Accelerated Test Using a New Nano-Scratch Wear Measurement Technique", *Wear*, **190**, 1-15.

144 S. Chandrasekar, B. Bhushan (1990), "Friction and Wear of Ceramics for Magnetic Recording Applications – Part I: A Review", *Journal of Tribology*, **112**, 1-16.

145 B.K Gupta, A.K. Menon (1999), "Characterization of the Head-Disk Interface at Nanometre Dimensions", *IEEE Transactions on Magnetics*, **35(2)**, 764-769.

146 P.H. Clifton (1999), Seagate Technology, N. Ireland, private communication.

147 S.Y. Guo, J. Li, D.S. Mao, M.H. Xu, Z.Y. Mao (1997), "The friction-wear behaviour of Al_2O_3-TiC-Co advanced ceramic during in-situ SEM", *Wear*, **203-204**, 319-324.

148 T.E. Fischer, W.M. Mullins (1992), "Chemical Aspect of Ceramic Tribology", *J. Phys. Chem.*, **96**, 5690-5701.

149 L. Zhang, R.V. Koka (1998), "A study on the oxidation and carbon diffusion of TiC in alumina-titanium carbide ceramics using XPS and Raman spectroscopy", *Material Chemistry and Physics*, **57**, 23-32.

150 H. Ota, K. Namura, N. Ohmae (1991), "Brown Stain on VCR Head Surface Through Contact with Magnetic Tape", *Adv. Info. Storage Syst.*, **2**, 85-96.

151 R. Koka (1995), "Wear of Silicon Carbide in Sliding Contact with Lubricated Thin-Film Rigid Disk", *Tribology Transactions*, **38(2)**, 417-423.

152 E.F. Cuddihy (1976), "Hydroscopic properties of magnetic recording tape", *IEEE Trans. Magn.*, **MAG-12**, 126-135.

153 B. Bhushan, D.V. Khatavkar (1995), "Role of tape abrasivity on friction, wear, staining and signal degradation in audio tapes", *wear*, **190**, 16-27.

154 S.T. Patton, B. Bhushan (1996), "Friction and Wear of Metal Particle, Barium Ferrite and Metal Evaporated Tapes in Rotary Head Recorders", *J. Tribology*, **118**, 21-32.

155 S.T. Patton, B. Bhushan (1996), "Tribological Evaluation of the Streaming Mode Performance of Metal Evaporated and Metal Particle Tapes", *IEEE Trans. Magn.*, **32**, 3684-3686.

156 S.T. Patton, B. Bhushan (1997), "Friction, wear and magnetic performance of metal evaporated and particulate magnetic tapes", *Proc. Instn. Mech. Engrs. - Part J*, **211**, 327-348.

157 M.S. Hempstock, M.A. Wild, J.L. Sullivan, P.I. Mayo (1998), "A study of the durability of flexible magnetic media in a linear tape system", *ibid.*, 435-441.

158 W.W. Scott, B. Bhushan (1999), "Generation of magnetic tape debris and head stain in a linear tape drive", *Proc. Instn. Mech. Engrs. Part J*, **213**,127-138.

159 J. Kelly (1982), "Tape and head wear", in F. Kalil (ed.), *Magnetic Tape Recording for the Eighties*, NASA, Washington D.C., Ref. Pub. 1075, pp 7-22.

160 B.K. Gupta, B.Bhushan, Y. Zhou, N. Winograd, K. Krishnan (1995), "Chemical analyses of stains formed on Co-Nb-Zr metal-in-gap heads sliding against oxide and metal particle tapes", *J. Mater. Res.*, **10**(7), 1795-1810.

161 Y.-F. Liew, J.L. Lauer, F.E. Talke, K. Connel (1995), "Analysis of Deposits from Friction at Head-Tape Interfaces by Raman Spectroscopy", *Tribology Transaction*, **38**(3), 728-732.

162 C.M. Stahle, T.D. Lee (1992), "Characterisation of the Deposits on Helical Scan Heads", *Adv. Info. Storage Syst.*, **4**, 79-86.

163 B.K. Gupta, B. Bhushan (1995), "Mechanical and tribological properties of hard carbon coatings for magnetic recording heads", *Wear*, **190**, 110-122.

164 B. Bhushan, S.T. Patton (1996), "Pole tip recession studies of hard carbon-coated thin-film tape heads", *J. Appl. Phys.*, **79**, 5916-5918.

165 M.D. Bijker, J.J.J. Bastiaens, E.A. Draaisma, L.A.M. de Jong, E. Sourty, S.O. Saied, J.L. Sullivan (2001), "The development of a thin CrO_3 wear protective coating for the Advanced Digital Recording (ADR) system", *Submitted at the TISD'01 conference, Sendai, Japan.*

166 A.K. Menon (2000), "Interface tribology for 100 Gb/in^2", *Tribology International*, **33**, 299 308.

167 K. Homlberg, H. Ronkainen, A. Matthews (2000), "Tribology of thin coating", *Ceramic International*, **26**, 787-795.

168 G.S.A.M. Theunissen (1998), "Wear coatings for magnetic thin film magnetic recording heads", *Tribology International*, **31**(9), 519-523.

169 S.J. Bull, A.M. Korsunsky (1998), "Mechanical properties of thin carbon overcoats", *Tribology International*, **31**(9), 547-551.

170 B. Bhushan (1999), "Chemical, mechanical and tribological characterization of ultra-thin and hard carbon coatings as thin as 3.5-nm: recent developments", *Diamond and Related Materials*, **8**, 1985-2015.

171 Z.H. Liu, J.F. Zhao, J. McLaughlin (1999), "A study of microstructural and electrochemical properties of ultra-thin DLC coatings on AlTiC substrates deposited using the ion beam technique", *Diamond and Related Materials*, **8**, 56-63.

172 B. Bhushan, B.K. Gupta (1995), "Development of Hard Carbon Coatings for Thin-Film Tape Heads", *IEEE Transactions on Magnetics*, **31**(6), 2976-2978.

173 N. Gopinathan, C. Robinson, F. Ryan (1999), "Characterisation and properties of diamond-like carbon films for magnetic recording application", *Thin Solid Films*, **355-356**, 401-405.

174 S. Han, J.H. Lin, X.J. Guo, S.H. Tsai, Y.O. Su (2000), "The effect of Cr interlayer on the microstructure of CrN coatings on steel", *Thin Solid Films*, **377-378**, 578-584.

175 H.-S. Ahn, O.-K. Kwon (1999), "Tribological behaviour of plasma sprayed-chromium oxide coating", *Wear*, **225-229**, 814-824.

176 V. Zieren, M. de Jongh, A. Broese van Groenou, J.B.A. van Zon, P. Lansinski, G.S.A.M. Theunissen (1994), "Ultrathin wear-resistant coatings for the tape bearing surface of thin-film magnetic heads for digital compact cassette", *IEEE Trans. Magn.*, **30**, 340-345.

177 K.E. Kuijk, W.J. van Gestel, F.W. Gorter (1975), *IEEE Trans. Mag.*; **1**, 1215.

178 B. Bhushan, B.K. Gupta, *Handbook of Tribology*, McGraw-Hill, Inc.

179 http://www.hpmetals.com/Nickel.htm

180 CRC Mat. Sci. & Eng. Handbook, p568.

181 Fukuura, Asano, in *Fine Ceramics*, Ed.: Saito, p169.

182 D.D. Tang, "Stable encapsulation Structures for Permalloy Films", IEEE Transactions on magnetics, Vol. 30, No. 6, pp. 5073 – 5078.

183 J. Robertson, M. I. Manning (1990), "Limits to adherence of oxide scales", *Materials Science and Technology*, **6**, 81 - 91.

184 O. Shinoura, T. Koyanagi, "Magnetic thin film head with controlled domain structure by electroplating technology", *Electrochimica Acta*, **Vol. 42**, Nos 20-22, pp. 3361 – 3366.

185 M.D Bijker, E.A. Draaisma, M. Eisenberg, J. Jansen, N. Persat, E. Sourty (2000), "Future Direction in ADR Technology", *Tribology International*, **33**, 383–390.

186 B. Druz, S. DiStefano, A. Hayes, E. Ostan, K. Williams, L. Wang (1996), *Surf. Coat. Tech.*, **86/87**, 708–14.

187 D. Neerinck, P. Persoone, M. Sercu, A. Goel, D. Kester, D. Bray (1998), *Diamond Rel Mat*, **7**, 468–71.

188 V. Zieren, M. De Jongh, M. Broese van Groenou, J.B.A. van Zon, P. Lasinski, G.A.S.M. Theunissen (1994), *and IEEE Trans Mag*; **30**(2), 340–5.

189 G.A.S.M Theunissen, M. De Jongh, V. Zieren (1994), *Philips Res Bull Mat*, **14**, 9–12.

190 http://www.matweb.com/

191 E.A. Draaisma, S.R. Cumpson, T.P.H.G. Jansen, P. Hidding, S.B. Luitjens (1999), "Performance of advanced tapes with DIGAmax thin film heads", *J Mag Magnetic Mat*, **193**, 384–7.

192 P.I. Oden, A. Majumdar, B. Bhushan, A. Padmanabhan, J.J.Graham (1992), "AFM Imaging, Roughness Analysis and Contact Mechanics of Magnetic Tape and Head Surfaces", *J. Tribology*, **114**, 666-674.

193 M.P. Seah, W.A. Dench (1979), *Surf. Interface Anal.*, **1**, 2.

194 G.C. Smith (1991), *Quantitative Surface Analysis for Material Science*, London: The Institute of Metals.

195 M.P. Seah (1990), "Chap 5 - Quantification of AES and XPS", in D. Briggs and M.P. Seah (eds.) *Practical Surface Analysis* (2nd edition), New York: John Wiley and Sons, Inc.

196 D. Briggs, J.C. Rivière (1990), "Chap 3 – Spectral Interpretation", in D. Briggs and M.P. Seah (Eds.) *Practical Surface Analysis* (2nd edition), New York: John Wiley and Sons, Inc.

197 D.A. Shirley (1972), *Phys. Rev.*, **B5**, 4709-4714.

198 J.C. Rivière (1990), "Chap 2 - Instrumentation", in D. Briggs and M.P. Seah (eds.) *Practical Surface Analysis* (2nd edition), New York: John Wiley and Sons, Inc.

199 P.J. Cumpson (1995), "Angle-resolved XPS and AES: depth-resolution limits and a general comparison of properties of depth-profile reconstruction method", *Journal of Electron Spectroscopy and Related Phenomena*, **73**, 25-52.

200 C.D. Wagner, NIST XPS database, version 1.0, 1989.

201 C.D. Wagner, NIST XPS database, version 2.0, 1997.

202 C.D. Wagner *et al.*, Handbook of photoelectron spectroscopy, Perkin Elmer Corporation, Minnesota, 1979.

203 J.H. Schofield, *Journal of Electron Spectroscopy*, **8**, p129, 1979.

204 J.A. Nedler, R. Mead, *Computer Journal*, **7**, p308, 1965.

205 M.D. Bijker (1999), OnStream BV, Eindhoven, private communication.

206 R. van Doorn (1996), "Thermal behaviour of Travan readers", OnStream internal report **MH R-96-32-022 / 1**.

207 J.H. Giusti, J. Fernandez-de-Castro, G.S. Mowry (1997), "Design of High Dual Stripe MR Heads Using Thermal Transmission Line Model", *IEEE Transaction on Magnetics*, **33**, 2920-2922.

208 H.G. Zolla (1997), "Thermal and Electrical Reliability of Dual-Stripe MR Heads", *IEEE Transaction on Magnetics*, **33**, 2914-2916.

209 H. Tian, C.-Y. Cheung, P.-K. Wang (1997), "Non-Contact Induced Thermal Disturbance of MR Head Signals", *IEEE Transaction on Magnetics*, **33**, 3130-3132.

210 B. Bhushan, J.A. Monahan (1995), "Accelerated Friction and Wear Studies of Various Particulate and Thin-Film Magnetic Tapes Against Tape Path Materials in Pure Sliding and Rotary/Sliding Modes", *Tribology Transaction*, **38**, 329-341.

211 A.K. Livesey, G.C. Smith (1994), "The determination of depth profiles from angle-dependent XPS using maximum entropy data analysis", *Journal of Electron Spectroscopy and Related Phenomena*, **67**, 439-461.

212 B.J. Tyler, D.G. Castner, B.D. Ratner (1989), "Regularisation: a stable and accurate method for generating depth profiles from angle-dependent XPS data", *Surf. Interface Anal.*, **14**, 443-450.

213 R.E. Linder, P.B. Mee (1982), "ESCA Determination of Fluorocarbon Lubricant Film Thickness On Magnetic Disk Media", *IEEE Trans. Magn.*, **18**, 1073-1076.0

214 R.A. von Behren, D.P. Smith (1991), "Mechanical Design of a Belt-Driven Data Cartridge", *Adv. Info. Storage Syst.*, **1**, 49-59.

215 FUNCTIONAL SPECIFICATION FOR DIGAMAX 15 GB WIDE BODY MINI CARTRIDGE REV. 01, Verbatim Co., 4060 Sorrento Valley Blvd., San Diego, Ca. 92121.

216 M.D. Bijker (1999), OnStream BV, Eindhoven, private communication.

217 P. Rouws (1999), OnStream BV, Eindhoven, private communication.

218 N.H. Cook, B. Bhushan (1973), "Sliding surface interface temperatures", *J. Lub. Tech., Trans. ASME*, **95**, 59-64.

219 B. Bhushan, N.H. Cook (1973), "On the correlation between friction coefficients and adhesion stresses", *J. Eng. Mat and Tech., Trans ASME*, **97**, 535-536.

220 E.G. Loewen, M.C. Shaw (1954), "On the analysis of cutting tool temperatures", *Trans. ASME*, **76**, 217-231.

221 W.W. Scott, B. Bhushan, A.V. Lakshmikumaran, Abstract book of the 44th Annual Conference on Magnetism and Magnetic Materials (MMM)'99. San Jose, November 15–18, paper EE–15, 1999:244.

222 N. C. da Cruz, E. C. Rangel, J. Wang, B. C. Trasferetti, C. U. Davanzo, S. G.C. Castro, M. A.B. de Moraes (2000), "Properties of titanium oxide films obtained by PECVD", *Surface and Coatings Technology* , **126**, 123-130

223 A.E.H. Love (1929), "The stress produced in a semi-infinite solid by pressure on part of the boundary", *Phil. Trans. Roy. Soc.* (London) Series A., **228**, 377-420.

224 N. Ahmadi, L.M. Keer, T. Mura, V. Vithoontien (1987), "The interior stress field caused by tangential loading of rectangular patch on an elastic half space", *Journal of Tribology*, **109**, 627-629.

225 J.J. Kalker (1986), "Numerical calculation of the elastic field in a half-space", *Communications in Applied Numerical Methods*, **2**, 401-410.

226 D.H. Buckley, K. Miyoshi (1984), "Friction and wear of ceramics", *Wear*, **100**, 333-353.

227 C.H. Bajorek, M.A. Nicolet, C.H. Wilts (1971), "Preferential oxidation of Fe in Permalloy films", *Appl. Phys. Lett.*, **19**, 82–84.

228 L. Nguyentran, K. Sin, J. Hong, P.P. Pizzo,, S.X. Wang (1997), "Corrosion Resistance of Low Coercivity, High Moment FeXN (X= Rh, Mo) Thin Film Head Materials", *InterMag '97*.

229 W.Y. Lee, G. Scherer, C.R. Guarnieri (1979), "Effects of oxidation on the atmospheric corrosion of permalloy films", *J. Electrochem. Soc.*, **126**, 1533–1539.

230 V. Brusic, G. S. Frankel, B. M. Ruth, A. G. Schrott, C. Jahnes, M. A. Russak,, T. Petersen (1990), "Corrosion and Passivation of Iron and FeN Films", *Proceedings of the Symposium on Magnetic materials,*

Processes, and Devices, ed. L. T. Romankiw and Dean A. Herman, Jr., The Electrochemical Society, INC., pp. 325.

231 W.W. Scott, B. Bhushan (2000), "Loose Debris and Head-Stain Generation and Pole-Tip Recession in Modern Tape Drives: A Critical Review", *J. Info. Storage and Proc. Syst.*, Vol.2, 221-254.

232 B. Song, H. Nakamatsu, R. Sekine, T. Mukoyama, K. Taniguchi (1998), "Valence band structures of titanium nitride and titanium carbide calculated with chemically complete clusters", *J. Phys.: Condens. Matter.*, **10**, 9443-9454.

233 T. Spalvins, H.E. Sliney (1994), *Surface and Coating Technology*, **68/69**, 482-488.

234 http://www.onstream.com/ADR_roadmap.pdf

ELSEVIER

Tribology International 33 (2000) 629–637

TRIBOLOGY INTERNATIONAL

www.elsevier.com/locate/triboint

The tribology of advanced digital recording (ADR) systems

E. Sourty [a,*], J.L. Sullivan [a], M.D. Bijker [b]

[a] *Surface Science Research Group, EEAP, Aston University, Birmingham B4 7ET, UK*
[b] *OnStream B.V., Lodewijkstraat 1, 5652 AC Eindhoven, The Netherlands*

ELSEVIER

Tribology International 33 (2000) 383–390

TRIBOLOGY INTERNATIONAL

www.elsevier.com/locate/triboint

Future directions in advanced digital recording technology

M.D. Bijker *, E.A. Draaisma, M. Eisenberg, J. Jansen, N. Persat, E. Sourty

OnStream B.V., Lodewijkstraat 1, 5652 AC Eindhoven, The Netherlands

ELSEVIER

Wear 252 (2002) 276–299

WEAR

www.elsevier.com/locate/wear

Pole tip recession and staining at the head to tape interface of linear tape recording systems

E. Sourty*, M. Wild, J.L. Sullivan

Surface Science Research Group, School of Engineering and Applied Science, University of Aston, Birmingham B4 7ET, UK

Received 3 May 2001; received in revised form 24 October 2001; accepted 5 November 2001

PII: S0043-1648(01)00880-8

ELSEVIER

Tribology International 35 (2002) 171–184

TRIBOLOGY INTERNATIONAL

www.elsevier.com/locate/triboint

Numerical modelling of sub-surface stress in magnetic data tape heads due to the dynamic contact with a tape

E. Sourty [a,*], J.L. Sullivan [a], M.D. Bijker [b]

[a] *School of Engineering and Applied Science, Aston University, Birmingham B4 7ET, UK*
[b] *OnStream B.V., Lodewijkstraat 1, 5652 AC Eindhoven, The Netherlands*

Received 25 May 2001; received in revised form 14 November 2001; accepted 26 November 2001

ELSEVIER

Tribology International XX (2003) XXX–XXX

TRIBOLOGY INTERNATIONAL

www.elsevier.com/locate/triboint

Chromium oxide coatings applied to magnetic tape heads for improved wear resistance

E. Sourty [a,*], J.L. Sullivan [a], M.D. Bijker [b]

[a] *School of Engineering and Applied Science, Aston University, Birmingham B4 7ET, UK*
[b] *OnStream MST B.V., Lodewijkstraat 1, 5652 AC Eindhoven, The Netherlands*

The development of a thin Cr_2O_3 wear protective coating for the Advanced Digital Recording (ADR) system

M..D. Bijker, J.J.J. Bastiaens, E.A. Draaisma, L.A.M. de Jong
OnStream MST B.V. Lodewijkstraat 1, 5652 AC, Eindhoven, The Netherlands

E. Sourty, S.O. Saied, J.L. Sullivan
School of Engineering and Applied Science, Aston University, Birmingham B4 7ET, United Kingdom

Pole Tip Recession in Linear Recording Heads

E. SOURTY, J. L. SULLIVAN, and L. A. M. DE JONG